**University of South-Eastern Norway**
Faculty of Technology, Natural Sciences and Maritime Studies

Doctoral dissertation no. 13
**2018**

Per Morten Hansen

# Experimental and theoretical studies of rapid phase transitions in $CO_2$

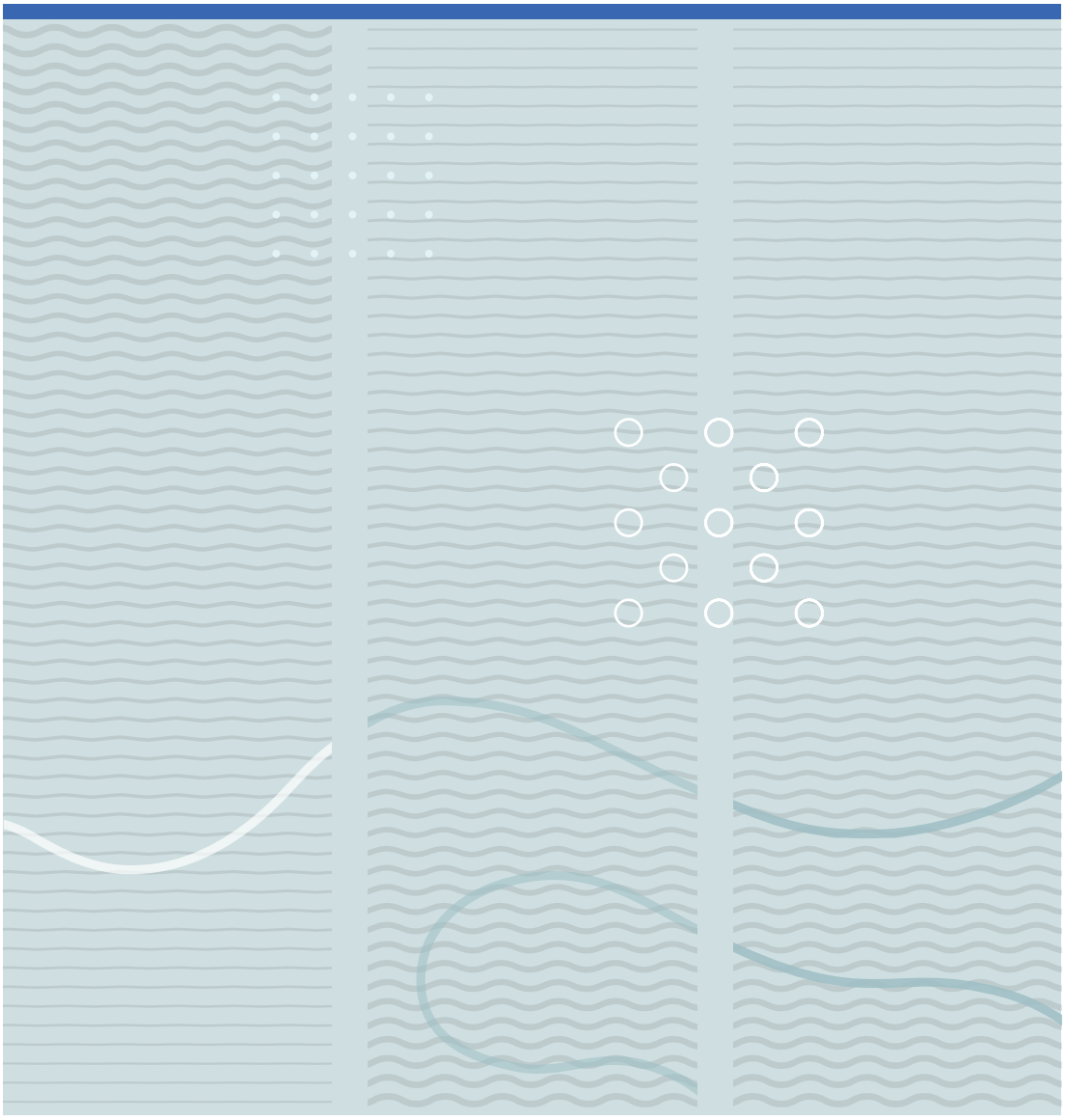

Per Morten Hansen

# Experimental and theoretical studies of rapid phase transitions in $CO_2$

A PhD dissertation in
**Process, Energy and Automation Engineering**

Faculty of Technology, Natural Sciences and Maritime Studies
University of South-Eastern Norway
Porsgrunn, 2018

**Doctoral dissertations at the University of South-Eastern Norway no. 13**

ISSN: 2535-5244 (print)
ISSN: 2535-5252 (online)

ISBN: 978-82-7206-487-6 (print)
ISBN: 978-82-7206-488-3 (online)




Print: University of South-Eastern Norway

*To*

*Marte,*

*Ola,*

*Linus,*

*and Mikkel*

# Preface

This dissertation was submitted in partial fulfillment of the requirements for the degree of doctor of philosophy at the Faculty of Technology, Natural sciences and Maritime sciences. The thesis presents my PhD research work that include a collection of journal papers and conference proceedings. I would like to thank the University of South-Eastern Norway for providing the financial support for this PhD project. The presented work was carried out at campus Porsgrunn between 2014 - 2018. This project is a continuation of the research activities on rapid evaporation of $CO_2$ conducted by the research group Telemark process safety, combustion, and explosion laboratory.

I would especially like to thank my supervisor, Dr. Knut Vaagsaether for the guidance, support, and inspiration from the start of the project all the way to the submission of the thesis. My co-supervisors Professor Dag Bjerketvedt and Dr. André Vagner Gaathaug both deserve big and warm thanks for the encouragement, practical guidance in the lab and all the discussions throughout the project.

My warm gratitude goes to the rest of the research group at USN: Joachim Lundberg, Mathias Henriksen, Samee Maharjan, and Ola Marius Lysaker for offering valuable advice throughout the project and making the days at work both cheerful and inspiring. Sindre Tøsse, which is my predecessor as a PhD student working with $CO_2$ safety at USN, deserves thanks for encouraging discussions and laughs at several social gatherings.

I wish to thank Øyvind Johansen, Eivind Fjelddalen, Jan Gunnar Lode, Fredrik Hansen and Per Otto Ålråk for technical support on the experimental setups and measurement equipment. I would also like to thank my fellow PhD students, and all my colleagues at USN-TNM for the continuing encouragement throughout the project.

My warmest thanks to my family for the support and understanding in these exciting years I have spent as a PhD student. You provide the balance and purpose in my life.

Porsgrunn, June 2018

Per Morten Hansen

# Abstract

Keywords: rapid evaporation, phase transition, evaporation waves, BLEVE, $CO_2$ safety

Rapid depressurization and evaporation of a pressurized liquefied gas are phenomena of relevance to hazard identification and risk analysis in the process industry. Tank explosions and pipeline ruptures are accident scenarios that happen infrequently but have the potential to cause fatalities and significant material damage. This thesis presents results from small-scale experiments and calculations on the rapid depressurization and evaporation of pressurized liquefied carbon dioxide ($CO_2$) in vertical ducts. A motivation was to quantify the damage potential of a sudden $CO_2$ release that originates from scenarios such as a boiling liquid expanding vapor explosion (BLEVE). The primary aim was to describe characteristic velocities and properties behind the evaporation wave as a function of the thermodynamic states ahead of the wave.

The experimental setups in the study included a transparent polycarbonate tube and a rectangular duct. The test sections were filled with pressurized $CO_2$ and sealed with a diaphragm at the upper end. A pulse generator initiated the tests and triggered the diaphragm puncture-device. The instrumentation included pressure sensors, temperature sensors, and high-speed cameras. Upon diaphragm rupture, a rarefaction wave propagated at the local speed of sound into the vapor headspace and further into the liquid phase. Wave reflections occurred at the liquid-vapor interphase and the bottom surface. An evaporation wave followed behind the rarefaction wave. The calculated evaporation wave velocities were in the range 32-42 $ms^{-1}$. Heterogeneous nucleation occurred at the wall surface ahead of the evaporation wave. Neither the transparent polycarbonate tube nor the square-duct glass-window setup provided a sufficiently smooth surface to suppress nucleation and bubble growth at the surface. The evaporation front details were obscured by the vapor bubbles at the glass window. One test campaign focused on the blast from the $CO_2$ released into an openly vented atmospheric chamber. The measured peak overpressure was in the range 15 – 20 kPa. The initial pre-rupture state was saturated $CO_2$ at room temperature (272 ± 1 K). The rapid boiling did not contribute to the initial shock strength in the test geometry. The

evaporation rate was too slow, and the velocity behind the evaporation wave seemed too low to create a shock wave. The heterogeneous wall nucleation seemed to limit the degree of superheat. The tests with a liquid/vapor mixture in the high-pressure reservoir showed a significantly higher impulse compared to the vapor-only tests. Reducing the vent area from 0.1 $m^2$ to 0.01 $m^2$ resulted in a slight increase in the impulse calculated at time $t$ = 100 ms after diaphragm rupture. The experimental results provided reference data that can be used to develop interfacial flux source terms applied in phase transition models. A Rankine-Hugoniot analysis that modeled the phase transition as an evaporation wave calculated the fluid properties behind a CJ wave. Velocities and pressures calculated by model showed good qualitative agreement with the experimental results that were sampled from three separate test setups. The required model inputs were the initial pre-rupture pressure and the pressure of the metastable liquid ahead of the evaporation wave. Typically, the calculated vapor mass fraction behind the evaporation wave was in the range from 0.21 to 0.23. The somewhat limited vapor mass fraction could explain why the rapid evaporation investigations did not produce an observable shock wave. The thesis describe a strategy, which includes the calculated vapor fraction, to predict the mechanical energy released in the rapid depressurization and evaporation processes.

# List of papers

Journal articles. First author:

### A. The behavior of pressurized liquefied $CO_2$ in a vertical tube after venting through the top

Hansen, P.M., Gaathaug, A.V., Bjerketvedt, D., Vaagsaether, K. (2017) Int. J. Heat Mass Transf. 108, pp 2011-2020. doi:10.1016/j.ijheatmasstransfer.2017.01.035.

### B. Blast from pressurized carbon dioxide released into a vented atmospheric chamber

Hansen, P.M., Gaathaug, A.V., Bjerketvedt, D., Vaagsaether, K. (2018) Shock Waves. doi: 1.1007/s00193-018-0819-z.

### C. Rapid depressurization and phase transition of $CO_2$ in vertical ducts – Small-scale experiments and Rankine-Hugoniot analyses

Hansen, P.M., Gaathaug, A.V., Bjerketvedt, D., Vaagsaether, K. Submitted to the Journal of Hazardous Materials May 15, 2018.

Conference Proceedings. First author:

### D. Phase Transition Rate in Rapid Boiling of $CO_2$

Hansen, P.M., Gaathaug, A.V., Bjerketvedt, D., Vaagsaether, K. (2016) Proceedings of the 8$^{th}$ International Seminar on Fire and Explosion Hazards (8$^{th}$ ISFEH). Oral presentation.

### E. Blast from pressurized $CO_2$ released into a vented atmospheric chamber

Hansen, P.M., Gaathaug, A.V., Bjerketvedt, D., Vaagsaether, K. (2017) Proceedings of the 26$^{th}$ International Colloquium on the Dynamics of Explosion and Reactive Systems (26$^{th}$ ICDERS). Oral presentation.

Conference Proceedings. Co-author:

### F. Modelling and Simulation of Phase Transition in Compressed Liquefied $CO_2$

Tosse, S., Hansen, P.M., Vaagsaether, K. (2016) Proceedings of the 9$^{th}$ EUROSIM congress.

# List of figures

# List of tables

# Abbreviations

| | |
|---|---|
| BLEVE | Boiling liquid expanding vapor explosion |
| CCS | Carbon capture and storage |
| CFD | Computational Fluid Dynamics |
| CJ | Chapman-Jouguet |
| $CO_2$ | Carbon dioxide |
| EOR | Enhanced oil recovery |
| EOS | Equation of state |
| fps | Frames per second |
| ICDERS | International Colloquium on the Dynamics of Explosions and Reactive Systems |
| ISFEH | International Seminar on Fire and Explosion Hazards |
| KSL | Kinetic superheat limit |
| NIST | National Institute of Standards and Technology |
| RH | Rankine-Hugoniot |
| PRSV-EOS | Peng-Robinson-Stryjek-Vera equation of state |
| SW-EOS | Span-Wagner equation of state |
| SLT | Superheat limit temperature |
| TSL | Thermodynamic superheat limit |

# Nomenclature

**Roman symbols:**

| Symbol | Description | Unit |
|---|---|---|
| $A$ | Acceleration | $[ms^{-2}]$ |
| $c$ | Speed of sound | $[ms^{-1}]$ |
| $C_p$ | Heat capacity, constant pressure | $[Jkg^{-1}K^{-1}]$ |
| $C_v$ | Heat capacity, constant volume | $[[Jkg^{-1}K^{-1}]$ |
| $E$ | Total energy | [J] |
| $h$ | Enthalpy | $[kJkg^{-1}]$ |
| $P$ | Pressure | [Pa] |
| $S$ | Entropy | $[kJkg^{-1}K^{-1}]$ |
| $T$ | Temperature | [K] |
| $t$ | time | [s] |
| $U$ | Internal energy | $[kJkg^{-1}]$ |
| $u$ | velocity | $[ms^{-1}]$ |
| $V$ | Specific volume | $[m^3kg^{-1}]$ |
| $W_{EW}$ | Evaporation wave velocity | $[ms^{-1}]$ |

**Greek symbols:**

| Symbol | Description | Unit |
|---|---|---|
| $\gamma$ | Heat capacity ratio | [-] |
| $\rho$ | Mass density | $[kgm^{-3}]$ |
| $\chi$ | Vapor mass fraction | [-] |

**Subscripts:**

| Symbol | Description |
|---|---|
| 0 | State 0, pre-rupture state |
| 1 | State 1, ahead of the evaporation wave |
| 2 | State 2, behind the evaporation wave |
| sat | Saturated state |

# Table of contents

# Part I

# Overview

# 1 Introduction

## 1.1 Background

Global warming and climate changes caused by an enhanced greenhouse effect represent some of the most prominent threats to human civilizations in the 21st century. Anthropogenic carbon dioxide ($CO_2$) emissions are identified as major contributors to the enhanced greenhouse effect. An aim presented in the Paris climate agreement is to limit future temperature increases to below 2 K. The establishment of carbon capture and storage (CCS) value chains are a part of the strategy to reduce emissions and mitigate climate changes. It is expected that the annual amount of $CO_2$ being processed at high pressure will increase. The International Energy Agency (IEA) estimated that about 94 Gt of $CO_2$ should be captured and stored by the year 2050 (McCulloch, 2016).

The construction of the necessary infrastructure requires knowledge-based risk assessments to ensure safe operation of the process facilities. The rupture of a vessel, storage tank or pipeline containing a pressurized liquefied gas held at a temperature above its atmospheric pressure boiling point constitutes a hazard that should be included in industrial safety assessments. If the rupture and resulting release take place nearly instantaneously, the explosion can under certain conditions be referred to as a boiling liquid expanding vapor explosion (BLEVE). Three engineers that investigated an explosion in a cast iron vessel coined the BLEVE-term in 1957 (Abbasi and Abbasi, 2008). According to Prugh (1991), the blast energy of a bursting vessel that contains a pressurized liquefied gas is higher than the energy estimated from a vapor-space calculation. Under certain conditions, the rapid evaporation is suspected to contribute to the shock strength. Several BLEVE definitions exist, and this thesis uses the following: "*A BLEVE is the explosive release of expanding vapor and boiling liquid when a container holding a pressure liquefied gas fails catastrophically"* (Birk et al., 2007). Although often associated with fireballs or dispersion of poisonous fumes, BLEVES are also relevant for non-flammable substances such as $CO_2$. Hazards associated with these $CO_2$ releases

relates to both the harmful properties of the fluid (asphyxiation and frost injuries) and the energy release (blast waves, accelerated fragments, and dynamic loads on structures).

This thesis present experimental results and calculations that describe the behavior of rapid depressurization and evaporation of carbon dioxide. The study is limited to the behavior of $CO_2$ because of its relevance to CCS technologies. However, the author believes that the fundamental concepts are transferable to other pressurized liquefied gases, such as ethane, and propane.

This thesis is concerned with the determination of phase transition rates in a BLEVE. The kinetics of the phase transition from liquid to gas will be controlled by the state of the expanded superheated liquid. These rapid evaporation phenomena are not fully understood, and the available experimental data are sparse. Small-scale experiments are presented along with a Rankine-Hugoniot analysis of the evaporation phase change. The modeling of the phase transition could provide a basis for dispersion analyses.

## 1.2 Industrial accidents

Numerous accidents in the process industry and transport sector can be classified as BLEVEs. Possibly the worst industrial BLEVE catastrophe of all time happened at the PEMEX LPG terminal in Mexico City in 1984. The number of causalities were 650, and 6400 people suffered injuries when 3000 tonnes of propane were released and ignited in a succession of BLEVEs (Abbasi and Abbasi, 2007a). Examples of BLEVE accidents with flammable pressurized liquefied gases in the transport sector were presented by Planas et al. (2004, 2015) and Mishra (2016). Although mostly associated with flammable or poisonous substances, BLEVEs are also relevant for “inert” chemicals such as water and carbon dioxide. These physical explosions involve no chemical reactions and no fireballs. The sub-sections below show examples of explosions in tanks that contained pressurized liquefied $CO_2$.

### 1.2.1 Repcelok - Hungary, 1969

In the Hungarian city Repcelok, two $CO_2$ tanks exploded during filling in 1969. Overfilling because of a level indicator failure was the probable cause of the accident that killed nine persons. The tank pressure before the explosion was 15 bar and the temperature was -30 °C. The investigations concluded that the material used to manufacture these tank was not suited for use under low temperature conditions. (Abbasi and Abbasi, 2007a; CCPS, 1994).

### 1.2.2 Haltern – Germany, 1976

In 1976, a pressure vessel mounted on a railroad wagon burst during gravity shunting in Haltern, Germany. One person that worked at the shunting yard died in the accident. Incorrect operation of the wagon brakes provoked two wagons to roll quickly downhill and to crash into a pair of rail brakes placed on the tracks. The leading tank wagon failed catastrophically with large parts of the vessel thrown up to 300 meters away (Häcker, 2014).

### 1.2.3 Worms - Germany, 1988

In the German city of Worms, a 30-tonnes $CO_2$ tank exploded in 1988. The incident took place in a citrus process plant owned by the American company Procter and Gamble. Three persons died in the explosion, and eight persons suffered frost injuries from exposure to the cold $CO_2$. Blast waves destroyed the nearby buildings, and only 20 percent of the tank was recovered just after the explosion. The rest was thrown 300 meters into the nearby river Rhein. The $CO_2$ storage conditions were a pressure of 2.0 MPa and a temperature of 253 K. The tank was equipped with a heater to avoid low temperatures. An investigation concluded that the most probable cause of the accident was a brittle failure because of a previous low temperature (213 K) that resulted from a malfunction of the heater system. The heater was put back in operation but the temperature-high alarm did not work- Overheating occurred that resulted in excessive tank pressure and a pressure relief valve failure (icing). The investigations suggested that the pressure was between 3.5 and 5.1 MPa at tank failure. Procter and Gamble leased

the tank from a $CO_2$ supplier that also made some modifications to the tank just before installation. This accident demonstrated that temporary solutions and modifications could increase the probability of an accident. It also demonstrated potential hazards of installing heaters inside $CO_2$ storage tanks (Clayton and Griffin, 1994).

### 1.2.4 Yuhang - China, 2008

In 2008, a ship in Yuhang, China was docked when a $CO_2$ storage tank exploded. The ship carried 130 $m^3$ of liquid $CO_2$ at initial conditions 2.3 MPa and 258 K. The explosion killed two persons working at the site and sank two nearby ships carrying sulfuric acid and hydrogen peroxide. Modifications to the tank before the accident included work on the level indicator and locking of the relief valve. Primary causes of the accident were brittle fractures and overfilling of the modified $CO_2$ tank (Zhang et al., 2013).

## 1.3 Objectives and scope of the thesis

The primary objective of this study was to describe characteristic velocities and properties behind the evaporation wave as a function of the thermodynamic states ahead of the wave. The results from the presented work reported in three journal articles and two conference papers discuss the behavior of pressurized liquefied $CO_2$ after venting from a saturated state to atmospheric conditions. Figure 1.1 illustrates the main contributions of these publications.

Also, one co-authored conference paper (paper F) demonstrates a model for rapid phase transition in compressed liquefied gases (Tosse et al., 2016). Tosse (2017) describes this model in detail. The work presented in the current thesis is a continuation of the research activities on rapid evaporation of $CO_2$ performed by the research group Telemark process safety, combustion, and explosion laboratory. The emphasis is on experimental studies to determine velocities and thermodynamic states in rapid evaporation of $CO_2$. Rankine-Hugoniot analyses of the evaporation front and state calculations supplement the results from the small-scale experiments.

The experimental work is based on shock tube methods. The pressurized $CO_2$ is introduced into a vertical high-pressure vessel, tube or duct that is sealed with a diaphragm at the upper end. The puncture of the diaphragm results in an expansion fan that propagates through the vapor and liquid phases. A phase transition process occurs behind the rarefaction fan. The characteristic waves are recorded with a setup consisting of a high-speed camera and an illumination system. High-speed videos combined with pressure and temperature measurements recorded along the duct make it possible to determine how the kinetics in the phase transition process depends on the thermodynamic states.

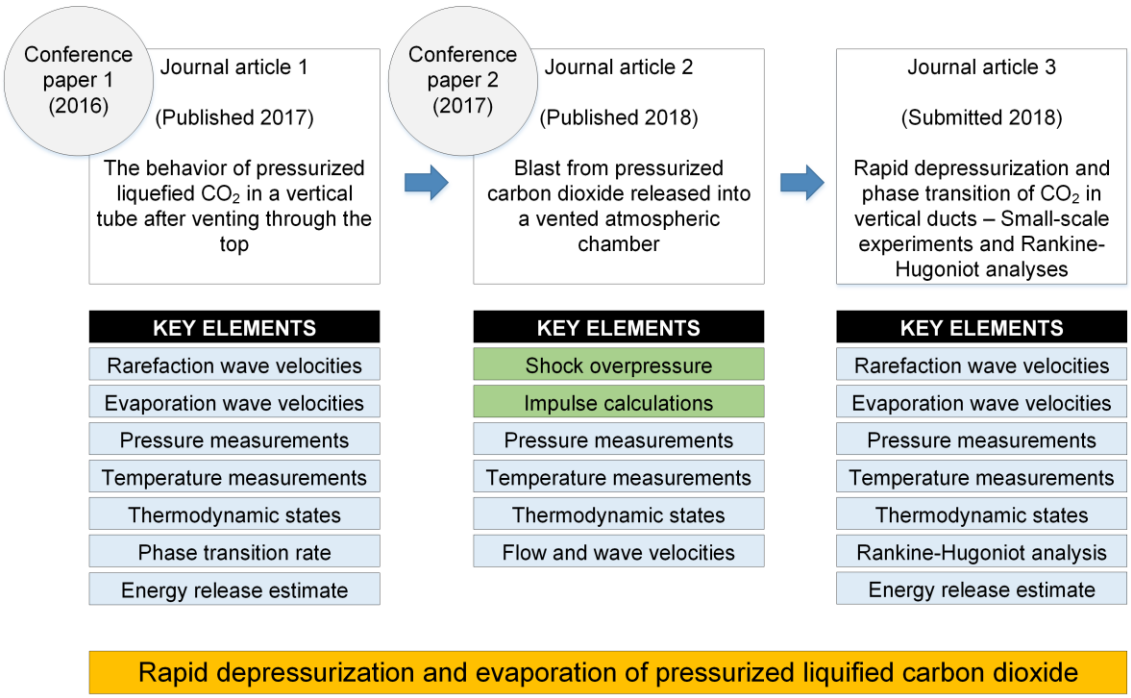


**Figure 1.1: Illustration that shows the main contents of the publications that are included in the thesis.**

The results from the experimental work performed by Tosse (2017) showed some promising results. High-speed images from the test setup captured the propagation of evaporation waves and contact surfaces inside the tube. Because there were no pressure measurements inside the tube, the thermodynamic states ahead of and behind the phase change front could not be determined. The upgrades in the current study

include pressure sensors and temperature sensors installed along the sidewall inside the pressurized duct.

An experimental determination of the velocities and state parameters in the rapid evaporation process represent the novelty of the project. High-speed videos, pressure histories, and temperature histories provide the state information at defined positions in the test setup. The experimental data describe the flow and wave velocities that could be used as inputs to phase-transition rate models. However, the development of a mechanistic phase- transition rate model is outside the scope of the current study.

## 1.4 Thesis structure

A literature overview in Chapter 2 follows the introduction in Chapter 1. The literature study presents relevant publications on BLEVEs, rapid evaporation, and evaporation waves. Chapter 3 contain a description of the materials and methods in the study. The aim is to present the setups and equipment that were used in the experiments. Chapter 4 presents the primary results from the articles. Chapter 5 discuss the implications of the main findings and contributions to the existing research. Chapter 6 summarize the conclusions and offer suggestions on elements that could be included in future studies. Part II contains the journal papers and manuscripts that form the basis of this article-based thesis.

# 2 Literature study on superheated liquids and BLEVE

This chapter presents a selection of previous work on superheated liquids, rapid evaporation and BLEVEs that are relevant to the present study. The ability of a superheated liquid to temperately store internal energy in a metastable liquid state and then to release it rapidly in an evaporation process is relevant to the situation in tank explosion scenarios. Such phase transitions, which take place at non-equilibrium conditions, are different from "ordinary" nucleate boiling at thermodynamic equilibrium. The chapter starts with a description of basic terms and concepts and continues with a discussion of the superheat limit theory. A sub-chapter then describes rapid evaporation of droplets at the superheat limit. The next subsection discusses evaporation waves and boiling front propagation. A brief presentation then follows on experimental and numerical studies that aim to predict the initiation and behavior of a BLEVE. The section closes with a short presentation on thermodynamic equations of state that are used in selected publications and the current study.

## 2.1 Definitions and fundamental terms

In a rapid expansion of a pressurized liquefied gas toward atmospheric pressure, the substance could cross the saturation line without undergoing a phase transition (Skripov, 2010). The absence of available nucleation sites can suppress the bubble formation. The liquid then becomes superheated (or metastable). Debenedetti (1996) defined a superheated liquid as follows: " A liquid that is exposed to a pressure lower than its vapor pressure at the given temperature, or to a temperature higher than the boiling temperature at the prevailing pressure is called superheated." Hence, a saturated liquid can become superheated in the following ways: By lowering the pressure, or increasing the temperature, as illustrated in Figure 2.1. There is a limit to the degree of superheat that a metastable liquid can obtain. This limit can be examined from either a thermodynamic or kinetic nucleation theory (Reid, 1976; Reid, 1978 a-c).

The thermodynamic stability limit is given by the expression $(\partial P/\partial V)_T = 0$. The locus of states that satisfies this criterion is called the spinodal curve.

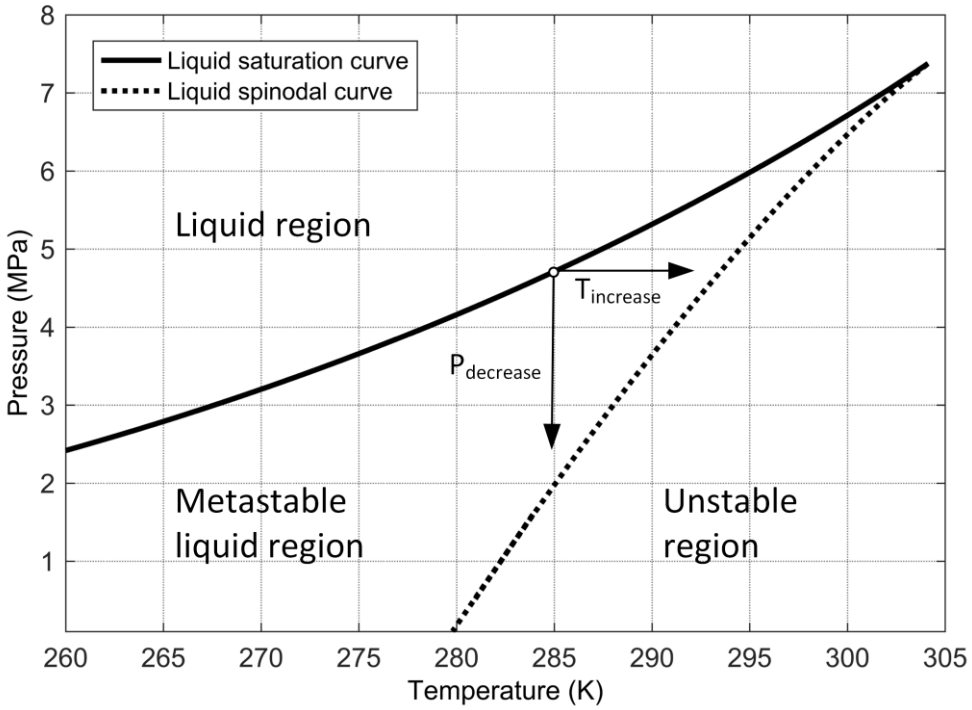


**Figure 2.1: p-T diagram of carbon dioxide. A saturated liquid can become superheated by decreasing the pressure or increasing the temperature.**

The slope of an isotherm in a p-V diagram is equal to zero at the intersections with the spinodal curves, as illustrated in Figure 2.2. The temperature at the intersection with the liquid spinodal curve can be referred to as the thermodynamic superheat limit or TSL (Xie, 2013). In an isobaric process, this temperature is the upper limit of stability for a pure liquid. The foundation of the thermodynamic theories were developed by Gibbs (1875-1876, 1877-1878, 1961). Gibbs discussed criteria for phase equilibrium and stability limits of substances.

Any cubic equation of state (EOS) can be used to predict the TSL by application of the criterion for the spinodal state. However, the correlations between P-V-T in an EOS are developed for equilibrium conditions and do not usually extrapolate well into the metastable region (Reid, 1976). Kraska (2004) investigated the stability limit of pure substances based on their EOS and proposed strategies to reduce the disagreement between calculations and experiments.

A kinetic approach can also be used to discuss the stability of superheated liquids

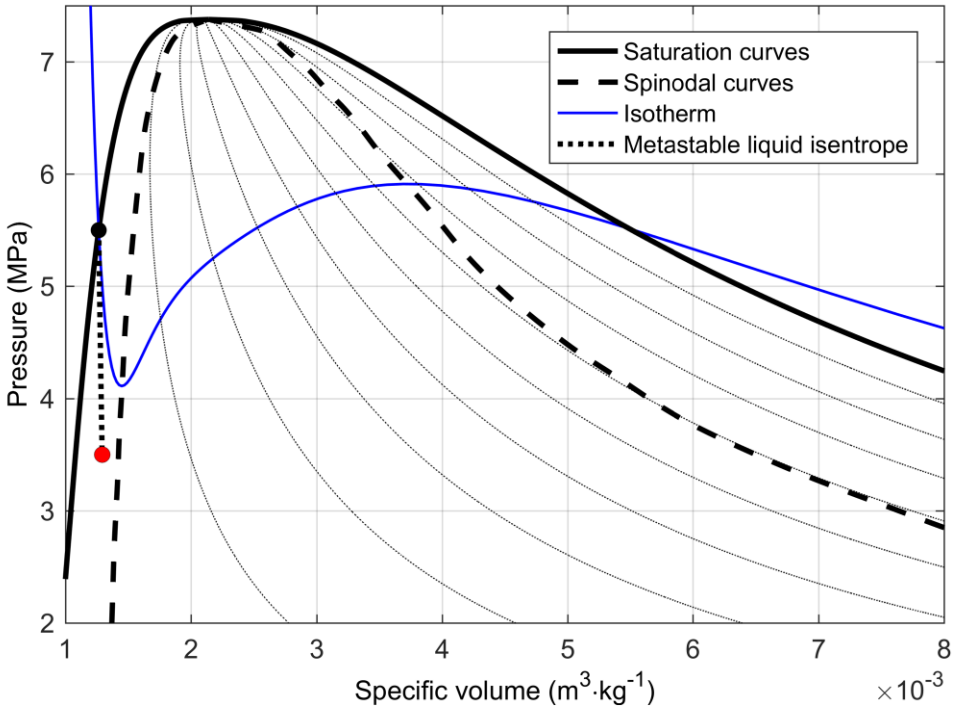


**Figure 2.2: p-V diagram of carbon dioxide. The diagram shows the saturation curves, the spinodal curves, an isotherm, and a metastable liquid isentrope.**

This treatment is based on kinetic nucleation theory and deals with probability and how rapidly the visible vapor bubbles form in a superheated liquid (Reid, 1976). Based on this approach, the kinetic superheat-limit or KSL is derived (Xie, 2013). According to Xie (2013), a superheat limit temperature that is determined by experiments will always be the KSL. Skripov (1974, 2010) studied the reduced superheat limit temperature ($T_C / T$) for a wide range of substances. He reported that most values of the atmospheric superheat limit were found within the interval 0.89 - 0.91.

The evaporation at moderate degrees of superheat process usually starts by heterogeneous nucleation on a solid surface, on particle impurities, or inside microscopic gas cavities found on the solid surface. Suppression of heterogeneous nucleation can support a highly superheated state close to the liquid spinodal. Homogeneous nucleation takes place close to the thermodynamic superheat limit. It appears spontaneously in the liquid bulk and differs from heterogeneous nucleation; it does not require a solid surface to form gas bubbles. The study of homogeneous

nucleation involves estimation of free energy and calculation of critical bubble size. The nucleation rates are found to be sensitive to small changes in conditions such as temperature and pressure (Oxtoby, 1992).

The x-t diagram in Figure 2.3 illustrates the wave patterns and phase transition that follows a rapid depressurization of a saturated liquid. An initial shock wave propagates outward, and a rarefaction wave (or fan) propagates through the fluid. A contact surface that initially separated liquid and vapor propagates behind the shock wave. At a range of superheats close to the superheat limit, an evaporation wave can propagate behind the rarefaction fan through the metastable liquid (Simões-Moreira and Shepherd, 1999).

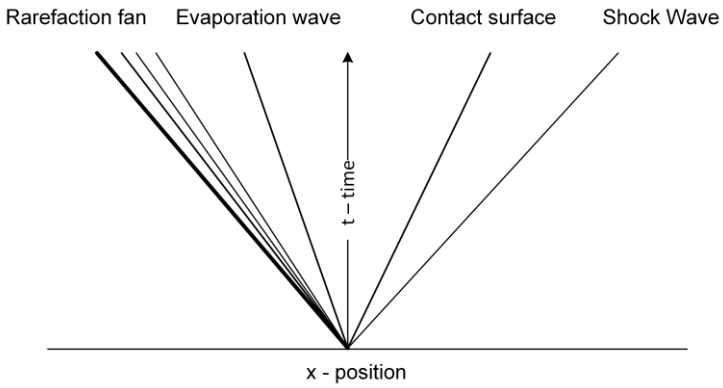


**Figure 2.3: x-t diagram that illustrates wave patterns in a rapid depressurization of a liquid. The diagram shows a shock wave; contact surface; rarefaction wave, and an evaporation wave. Reproduced from Saurel (2008).**

## 2.2 The superheat limit theory as a trigger for the BLEVE

Reid (1979, 1980) proposed a hypothesis that is referred to as the superheat limit theory. The hypothesis suggested that a BLEVE is initiated by homogeneous nucleation at the superheat limit. Vapor bubbles are then spontaneously formed within the bulk fluid. A rapid depressurization of a saturated liquid could result in an explosion if specific condition requirements were fulfilled. The pre-rupture temperature of the liquid must be higher than the superheat-limit temperature (or homogeneous nucleation temperature) at 1 atm. Moreover, the pressure drop must be very rapid (Reid, 1979, 1980). Figure 2.4 shows a p-T diagram that illustrates the depressurization of saturated

$CO_2$ from two initial conditions. According to the hypothesis, a BLEVE could only occur if the liquid spinodal curve is reached during the liquid depressurization.

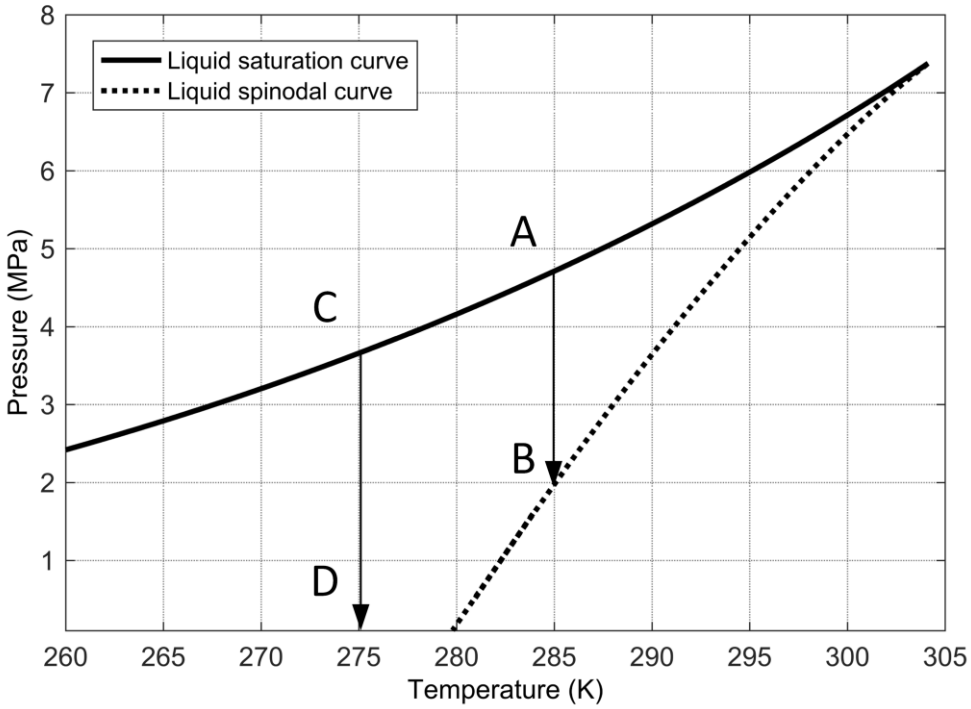


**Figure 2.4: p-T diagram of $CO_2$. Depressurization above (A-B), and below (C-D) the superheat limit.**

The depressurization from state A to B could result in a BLEVE because it is possible to reach the liquid spinodal state at atmospheric pressure. On the other hand, a depressurization from state C to D would provoke rapid boiling, but no BLEVE, because the temperature is below the atmospheric pressure superheat limit.

At first, the superheat limit theory aimed to explain the mechanism for explosions in tank trucks and railroad cars. These tanks carried pressurized liquefied gases such as propane. This class of explosions can be referred to as BLEVEs because the event includes both a rapid boiling of the liquid and an expansion of the vapor contained in the vessel before the tank rupture. The spinodal curve in Figure 2.4 was calculated with the Span-Wagner technical equation of state (SW-EOS). No equilibrium liquid phase exist in $CO_2$ below the triple point at 0.518 MPa (only solid and vapor phase). Then, an extrapolation of the liquid spinodal line from the triple point to atmospheric pressure

gave the superheat limit temperature estimate of *T* =280 K. Other EOS´s would provide different predictions.

Salla et al. (2006) analyzed seven methods for calculating the superheat limit temperature of 22 substances. An estimated TSL in $CO_2$, which was based on the energy balance in the initial liquid mass just before the explosion, was T = 289.7 K.

Abbasi and Abbasi (2007b) presented estimates for the TSL in $CO_2$ that originated from a selection of EOS´s. The estimates varied in the range between 257 and 283 K. The same authors presented a temperature measurement from experiments that was *T* = 267 K. This estimate represents a prediction of the kinetic superheat limit (KSL).

According to the superheat limit theory, maintaining the $CO_2$ below *T = 267 K* could prevent the occurrence of a BLEVE in case of a rapid depressurization. This temperature corresponds to a saturation pressure of *P* = 3.0 MPa. Investigation reports from previous tank explosions show only partial agreement with this hypothesis. The findings after the explosion in Worms concluded that the tank pressure was between 3.5 - 5.1 MPa. This pressure corresponded to at saturation temperature in the range 273 - 288 K at the time of rupture (Clayton et al., 1994). However, the accident reports from Yuhang (Zhang et al., 2013) and Repcelok (CCPS, 1994), which reported storage temperatures of 258 K and 233 K, demonstrate that a BLEVE could occur even if the initial temperature is below the superheat limit temperature (Zhang et al., 2013). This conclusion was supported by Bjerketvedt et al. (2011), and Ke (2009) in their work with small-scale $CO_2$ BLEVE experiments. The initial temperatures in these tests were below the superheat limit at 1 atm. Birk et al. (2007) doubted the role of homogeneous nucleation altogether as a trigger for the onset of BLEVEs. Van der Voort et al. (2013) concluded from their experimental work with 40-liter $CO_2$ cylinders that BLEVE blasts did not disappear abruptly below the homogeneous nucleation temperature but showed a gradual decay. These previous results suggest that homogenous bulk nucleation at the superheat limit might not be the only trigger for a BLEVE. Preventative measures should always be taken to avoid hazardous conditions such as overfilling, rapid pressure reductions and operation at temperatures outside the material specification limits.

## 2.3 Rapid evaporation of droplets at the superheat limit

The rapid evaporation of single droplets at the superheat limit has been studied in numerous publications since the 1950s. Moore (1956, 1959) presented experimental results from a bubble column setup. No bubble-forming nuclei were present, and the test liquid could achieve a highly superheated state. Figure 2.5 illustrates the basic principles that were explained by Reid (1976). A vertical glass column is filled with a host fluid that is immiscible with the test fluid. The column is heated so that the temperature is significantly higher at the top than at the bottom. A syringe introduces a droplet of the test fluid, which has a diameter of about 1 mm, into the bottom of the column. The droplet rises because it has a lower density than the host fluid. At the same time, the host liquid transfers heat to the test liquid at constant pressure. The temperature increases as the droplet move up toward the top of the column. At a certain height, the droplet reaches the homogeneous nucleation temperature (KSL) and evaporates explosively. This technique, which measures the superheat limit temperature by isobaric heating, has shown high reproducibility for the same test fluid in different columns (Reid, 1976).

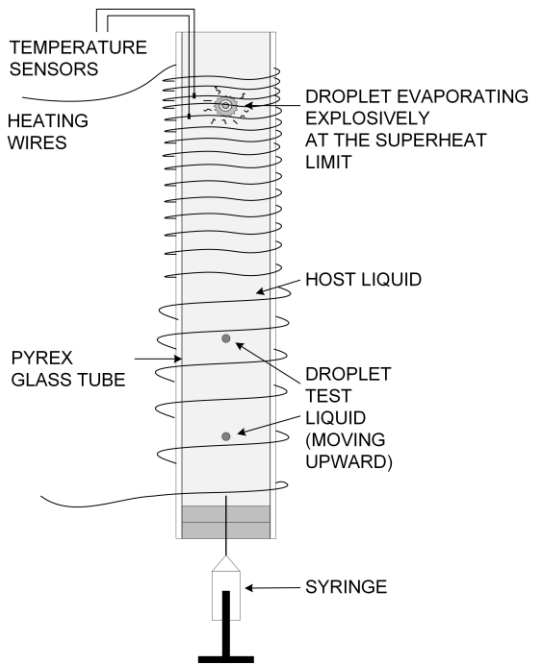


**Figure 2.5 Schematic of a bubble column setup that measures the superheat limit temperature of droplets at constant pressure. Reproduced from Reid (1976).**

Shepherd (1981), and Shepherd and Sturtevant (1982) studied the rapid evaporation of butane droplets at the superheat limit. The experiments were carried out at atmospheric pressure. They observed that nucleation started from a single nucleation site on the droplet. They suggested that the Landau mechanism of instability, originally associated with roughening of laminar flames, applies to rapid evaporation. They observed that the bubble was Rayleigh-Taylor unstable and disintegrated into a cloud of tiny bubbles.

Frost (1985, 1988), and Frost and Sturtevant (1986) continued the work by Shepherd on rapid evaporation of droplets at the superheat limit. Three other fluids (pentane, isopentane, and ether) were tested and confirmed the generality of the phenomena observed by Shepherd. The effect of ambient pressure was examined in the range between 0.025 and 0.45 MPa. An interesting observation was that the vaporization rate decreased when the ambient pressure was raised. The explanation was that an increase in pressure resulted in a degree of lower superheat attained at the superheat limit.

Avedisian (1985) measured superheat limit temperatures of 90 pure substances and 28 mixtures. The tests did not include pure $CO_2$.

Nguyen et al. (1988) presented a model that estimates the mass transfer flux in rapid evaporation at the superheat limit. The model, which was applied to the case of a butane droplet, was compared to the work by Shepherd and Sturtevandt (1982). The authors stated that the simulation results were in “general agreement” with measurements.

McCann et al. (1989) studied evaporation of butane droplets at the superheat limit temperature. The experimental study was conducted to test the model proposed by Nguyen et al. (1988). The predicted values was about 50 % larger than experimentally observed values

Park et al. (2005) measured the superheat limit temperature of four pure hydrocarbons, which included pentane, hexane, cyclohexane and benzene, and a selection of binary mixtures.

## 2.4 Evaporation waves and boiling front propagation

Experimental small-scale investigations of rapid evaporation in superheated liquids can be separated into those concerning single droplets (section 2.3) and those involving volumes up to a few liters. The latter category includes studies of evaporation waves that propagate through metastable liquids below the superheat limit. It is a phenomenon distinctly different from homogenous bulk nucleation at the superheat limit or heterogeneous nucleation on solid surfaces or particle impurities. The degree of superheat has to be above a certain level, but below the superheat limit. (Simões-Moreira and Shepherd, 1999). Instead of being heated at constant pressure, the liquid is now subject to a rapid depressurization. Figure 2.6 shows a simplified illustration of a rapid depressurization and evaporation process. After the initial rupture, a rarefaction wave propagates through the saturated liquid. If heterogeneous nucleation is suppressed, the liquid becomes superheated. A phase change process happens behind the initial depressurization. The phase change can under certain conditions be restricted to a narrow region called an evaporation wave that is traveling through the expanded metastable liquid state at a nearly constant velocity (Simões-Moreira and Shepherd, 1999).

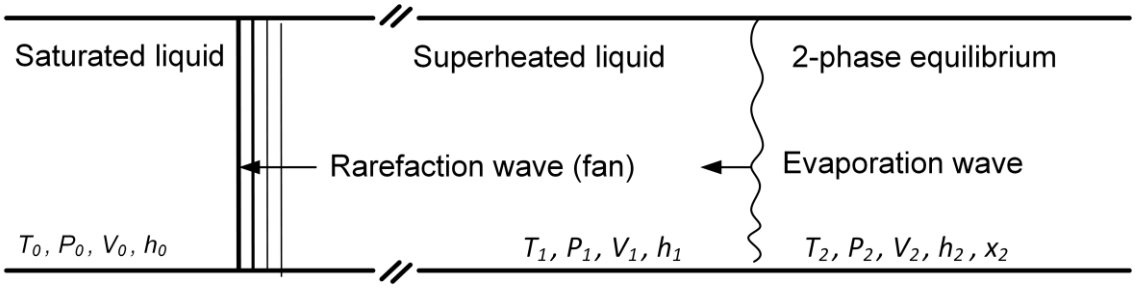


**Figure 2.6: Illustration of an evaporation wave propagating into a superheated liquid.**

The evaporation wave can be treated as a jump between a superheated liquid state and a liquid-vapor two-phase equilibrium state. According to Hill (1991), this analysis is analog to the investigation of propagating deflagration waves described in premixed combustion studies. Figure 2.7 shows an x-t diagram of the depressurization and phase change process with more details than the diagram presented in Figure 2.3.

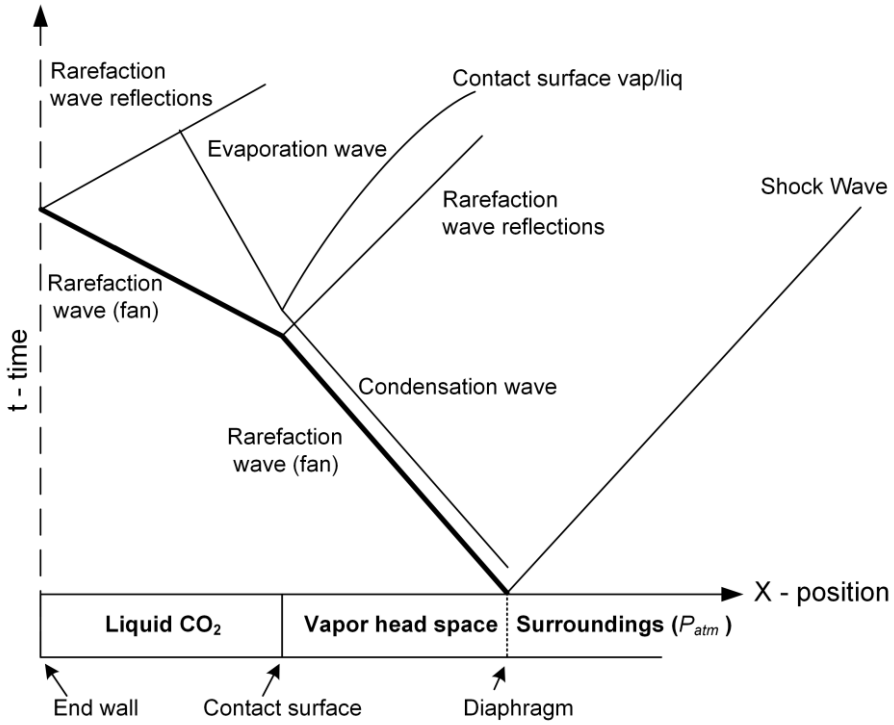


**Figure 2.7: x-t diagram of a depressurization and phase change processes in a channel that is filled with a pressurized liquefied gas and sealed with a diaphragm.**

The channel, which initially contains a pressurized liquefied gas with a vapor headspace, is sealed with a diaphragm at one end. The state behind the evaporation wave is usually a liquid-vapor two-phase mixture, but could theoretically consist of pure vapor in the rare case of complete evaporation waves in retrograde liquids (Simões-Moreira and Shepherd, 1999). The primary relevance of evaporation waves to the current study is through the possibilities to estimate phase transition rates in a one-dimensional BLEVE model. These phase transition rate estimates are calculated by evaporation front velocities and estimates of the density in the liquid ahead of the wave. The propagation of adiabatic evaporation waves is well documented. Considerable preparations are usually necessary to suppress heterogeneous nucleation on the walls ahead of the evaporation wave. Examples include the use of freshly drawn glass tubes and low-volatile buffer liquids at the bottom section. In most studies, the downstream fluid is ejected into a low-pressure reservoir with an adjustable pressure to control the degree of superheat. In some studies, the contents are ejected to atmospheric pressure to resemble conditions of industrial relevance.

Numerous terms have been used to name the phenomenon of a boiling front propagation into a superheated liquid. Examples include free surface boiling, evaporation waves, boiling discontinuities, and boiling fronts.

Terner (1962) described phase changes observed in shock tube experiments with rapid depressurization of water. It was concluded that the phase change process (vaporization) proceeded at a slow rate compared to the initial rarefaction waves.

Gromles and Fauske (1974) studied depressurization and evaporation of water, R-11, and methyl alcohol in tubes with diameters from 0.2 to 15 inches. They reported that the onset of propagation was dependent on the degree of initial superheat and the tube diameter.

Chaves (1984), Chaves et al. (1985), and Thompson et al. (1987) performed experimental studies on the retrograde substance perfluoro-n-hexane. The rupture of a diaphragm initiated the experiments. These phenomena were described as wave splitting. An initial pressure-release wave split into a forerunner acoustic expansion wave and a phase change wave. The initial temperature and consequently the nucleation rate had to be sufficiently high to produce evaporation waves. The upstream state, which is the state ahead of the evaporation wave contained gas bubbles. Hence, this was not a pure liquid phase. A Rankine-Hugoniot analysis of the evaporation wave was presented, suggesting an analogy to premixed combustion waves. It was proposed that the downstream velocity, which is the velocity behind the evaporation wave, will be governed by the lower branch Chapman-Jouguet (C-J) condition.

Das et al. (1987) studied evaporation of water by rapid depressurization. They concluded that the boiling front velocity increased with increased degree superheat and test section diameter. The velocity also increased with lower water contamination levels. The latter observation was explained by the inhibiting effect of impurities on bubble-formation and heat transfer at the evaporating surface.

Shepherd et al. (1990) presented an evaporation wave model based on the jump relations discussed by Chaves (1984) and Thompson et al. (1987). The model involved a

retrograde liquid capable of producing complete evaporation waves characterized by a pure vapor state behind the wave.

Hill (1990), and Hill and Sturtevant (1991) described evaporation waves in superheated refrigerants R12 (Dichlorodifluoromethane) and R114 (dichlorotetrafluoroethane). A distinct wavefront with a leading edge bubble layer was observed. Detailed still photographs of the wavefront region revealed bubble-like structures. A jump condition model, which was based on an analysis of the experimental results, was presented. The authors concluded that a unique evaporation wave velocity, which corresponded to the C-J point, could not be defined without specifying an additional rate relation.

Barbone (1994) and Barbone et al. (1995) presented experimental results from the depressurization of liquefied R-22 (chlorodifluoromethane). The study included a glass tube and a steel vessel. It was demonstrated that the propagation of evaporation waves could be inhibited if the wall surface was not sufficiently smooth to suppress heterogeneous nucleation.

Simões-Moreira (1994) studied the propagation of adiabatic evaporation waves in superheated dodecane. Similar to work by Chaves (1984), a retrograde fluid was chosen to obtain complete evaporation waves. The maximum estimated vapor quality behind the evaporation wave was above 90%. These calculations were based on the measured data from tests carried out at a temperature of 300 °C. In comparison, the estimated vapor quality at 180 °C was 25%.

Reinke (1997), and Reinke and Yadigaroglu (2001) presented experimental studies on explosive vaporization of propane, n-butane, refrigerant R-134a (tetrafluoroethane), and water. The test setup used circular glass pipes with length 500 mm and diameter up to 80 mm. A range of superheat conditions was examined in the pressure range of 1 - 10 bar and temperature range - 4 °C to 150 °C. It was observed that the front-velocity of the evaporation wave was not influenced by the pipe diameter in the range from 14 - 80 mm. The authors suggested that this observation could be caused by the larger diameters used and a complete absence of wall nucleation sites. The effect of

superheating degree on front propagation velocity was similar to earlier studies. The study presented detailed images of the boiling front propagation. The boiling front velocity varied for the most part linearly with the liquid superheat. The boiling front showed a bubbly appearance with smaller bubbles appearing inside larger ones. The authors suggested that the phase change propagated too slow to be described as an isentropic process.

Simões-Moreira and Shepherd (1999) presented evaporation wave characteristics and a jump condition analysis for a retrograde fluid (dodecane) at various degrees of superheat. The initial temperatures were in the range 453 - 573 K. Complete evaporation waves were approached but could not be obtained. The reported reason was an unexpected increase in liquid pressure that limited the superheat degree.

Hahne and Barthau (2000) observed evaporation waves in adiabatic flashing processes, characterized by a low degree of superheat and small depressurization rates. They also found that the presence of metal/liquid contacts decreased the necessary superheat for the formation of evaporation waves.

Kuznetsov et al. (2007, 2012) conducted experimental investigations of adiabatic evaporation waves in R11 (Trichlorofluoromethane). They reported on highly irregular heat transfer to the interphase surface with phase transition occurring in conditions of developing multiscale turbulence.

Tosse et al. (2014) and Tosse (2017) presented experimental results from the rapid boiling of pressurized liquefied $CO_2$ in a polycarbonate tube. The saturated liquid that was initially at room temperature was rapidly expanded to atmospheric pressure. Evaporation waves that propagated with a velocity of 20 - 30 $ms^{-1}$ were observed.

Ciccarelli et al. (2017) presented a study on the rapid boiling of $CO_2$, from a polycarbonate tube (driver section) into a steel pipe (driven section). No evaporation waves were observed in the expansion and phase change process. The pressure histories showed that the initial stage of the driver expansion was governed by the vapor expansion. The evaporation did not influence the initial shock wave in the driven section.

## 2.5 Numerical modeling and calculations

This thesis aims to provide reference data for the source terms in rapid phase transition models. Several published models claim to predict the physical behavior of BLEVES and phase transitions in pressurized liquefied gases. Some models are limited to describe the energy release of the BLEVE blast only, and others present estimates of the initial shock wave, bubble nucleation, the evaporation wave velocity and blast effects. Both the thermodynamics and the kinetics needs considering. BLEVE simulation models are valuable tools in safety assessments because it is difficult to achieve representative measurement results from full-scale BLEVE experiments. This section contains a brief presentation of numerical modeling and calculations on BLEVES and related phenomena.

### 2.5.1 One-dimensional phase transition models

Pinhasi et al. (2007) proposed a one-dimensional (1D) numerical model that describes the thermodynamic and the dynamic states in a BLEVE. The model predicts the bubble growth process, the front velocity of the expanding liquid and the shock wave pressure formed by the liquid expansion through the air. The model does not predict nucleation but assumes that nucleation sites are already present. The nucleation site density is a model input. Two models were combined, with the coupling between the models taking place at the interphase (moving boundary). One model describes the expanding two-phase mixture, and the other describes air. The equal velocities unequal temperatures (EVUT) description of the Euler equations describes the flow of the rapidly vaporizing liquid. Non-slip conditions and no interfacial friction are among the assumptions. The model uses the particle-path algorithm method of characteristics to solve the governing equations.

Xie (2013) developed a model that predicts whether a BLEVE will occur based on homogeneous nucleation and a prediction of the shock strength when a BLEVE does occur. The TUD-NET model was based on the work by Pinhasi but offers a predictive sub-model for homogeneous bubble nucleation and an improved thermodynamic basis. The

modified Peng Robinson equation of state proposed by Stryjek and Vera (PRSV-EOS) describes the relationship between the thermodynamic variables. The heat and mass transfer models incorporated non-equilibrium thermodynamics (NET). Xie claimed that the simulations conducted with the TUD-NET model revealed that homogeneous bubble nucleation is the primary trigger of a BLEVE.

Saurel et al. (1999, 2008) and Le Métayer et al. (2005) proposed a Godunov method for compressible multiphase flow capable of handling phase transition in metastable liquids. The model used a Riemann solver on a system of hyperbolic partial differential equations capable of predicting evaporation waves.

Tosse (2017) presented a 1D numerical solver for two-phase metastable flow governed by the van der Waals equation of state. The model was capable of predicting phase transition and evaporation rates. However, the author considered the model as a "proof of concept." A potential improvement to the model is to include a more accurate thermodynamic basis. The model could not predict the onset of nucleation. Strong points in the model included the incorporation and further development of the HLLC Riemann solver.

### 2.5.2 BLEVE blast estimation

A safety assessment of a BLEVE scenario often includes a calculation of the mechanical energy released from the potential explosion and the estimated peak overpressure from the burst. The scatter in the results calculated by the existing methods suggests the presence of significant uncertainties. As a consequence, a conservative estimate is often preferred. This estimate represents a "safe estimate," but could potentially result in unnecessary costs. The released mechanical energy is divided into several parts. One part is associated with the vessel opening, one part is associated with propelling the vessel fragments, and a third part generates the blast wave (Abbasi and Abbasi, 2007a).

Prugh (1991) proposed a method for estimating the potential energy release in a BLEVE. The method calculates the TNT equivalent of the released energy. The method assumes isentropic expansion of an ideal gas at constant heat capacity ratio. The volume

generated by the rapid evaporation of a fraction of the liquid is added to the tank volume. The main attraction of Prugh's method can be attributed to its simplicity.

Planas et al. (2004) proposed a method that claims to be more accurate than Prugh's because it treats the vapor as a real-gas and the expansion as an irreversible adiabatic process. Prugh method tends to overestimate the energy released, hence produces conservative estimates (Planas et al., 2004)

Van den Berg et al. (2004, 2006) presented a method to calculate the BLEVE blast from an exploding vessel of liquefied gas. The proposed estimate includes the assumption that the evaporation of the superheated liquid happens infinitely fast. The evaporation rate is expansion-controlled. The study proposed that rupture of a pressure vessel generate significant blast only in case of a nearly instantaneous disintegration of the vessel.

Abbasi and Abbasi (2007b) offer a comparative discussion of the models proposed by Prugh (1991), Planas et al. (2004), and Van den Berg et al. (2004, 2006).

Yakush (2016) presented a model that calculates blast waves in BLEVEs. The model assumes that the mixture in the two-phase cloud stays in thermodynamic equilibrium during expansion. The structure of superheated liquid expansion was divided into two zones. An inner zone included the superheated liquid and a two-phase cloud. The outer zone is the ambient atmospheric in which shock waves can be generated. Simulations revealed a multi-shock structure of BLEVE blast waves. Over-expansion of the two-phase cloud explained the occurrence of secondary pressure peaks.

Hemmatian (2016) and Hemmatian et al. (2017a) presented a prediction method that specifies the vessel liquid fraction and the temperature at failure as inputs to estimate the mechanical energy release and resulting overpressure. This linear regression method offers a quick estimate with a minimum of required information.

Hemmatian et al. (2017b) published a comparative analysis of mechanical energy and overpressure modeling. The study included ten different substances and six different

thermodynamic assumptions. The thermodynamic assumptions of the models dictate the way the methods compute the mechanical energy. This observation could explain the scattering in calculated energy results.

### 2.5.3 Rankine-Hugoniot analysis of an adiabatic evaporation wave.

There is an analogy between the evaporation waves in superheated liquids and deflagration waves in premixed combustible gas-mixtures. Hill (1991) stated that the jump conditions for conserved quantities, which include mass, momentum, and energy, are similar. Most studies on evaporation waves described in section 2.4 included attempts to model the evaporation wave by the Rankine-Hugoniot relations. The references include but are not limited to the following publications: (Labuntsov and Avdeev, 1981); (Chaves, 1984); (Chaves et al., 1985); (Thompson, 1987); Shepherd et al., 1989); (Hill, 1991), (Frost et al., 1991); (Simões-Moreira, 1994, 2000); (Reinke, 1997), (Simões-Moreira and Shepherd, 1999); (Angelo et al., 2005); (Avdeev, 2016).

## 2.6 Experimental studies on BLEVEs

This section introduces experimental studies that describe small-scale and medium-scale BLEVE tests. A common motivation in most studies was to investigate the validity of the superheat limit theory.

Kim-E (1978), and Kim-E and Reid (1983) performed a series of rapid venting experiments with pressurized liquefied $CO_2$ in a 7-liter vessel. A motivation for the study was to validate the superheat limit theory as a trigger for a BLEVE. None of the thirteen experiments resulted in a vessel rupture. An explanation offered for the discrepancy between theory and experiments was the occurrence of heterogeneous nucleation on the wall or plunger rod. Another explanation was that the reflected shock resulting from the breaking of the burst disc led to vapor formation in the partially superheated liquid.

Pettersen (2002) carried out experimental investigations on boiling liquid expansion in a test $CO_2$ vessel. As cited by Zhang (2013), the main aim was to clarify the possible

occurrence of BLEVE in $CO_2$ systems. None of the experiments showed signs of BLEVE. No re-pressurization to a level above the initial pressure was observed.

Birk et al. (2007) measured blast overpressures from medium-scale BLEVE tests. The experimental results came from nearly 20 catastrophic failures in 0.4 and 2 $m^3$ propane tanks. The authors claimed that the mechanical energy released by the rapid evaporation did not create a shock wave in the near or far field.

Bjerketvedt et al. (2011) carried out a series of small-scale BLEVE tests in transparent plastic tubes. The tubes, which had a length of 60 or 100 mm and an inner-diameter of 30 mm, were filled with solid phase $CO_2$. The internal pressure increased until the tubes ruptured at pressures between 3.0 - 4.5 MPa. The authors proposed that the decompression of the vapor phase generate the shock waves in the experiments.

Van der Voort et al. (2012, 2013) conducted modeling and experimental work with 40-liter $CO_2$ cylinders. The overpressures from the experiments were measured and compared with simulations. Modeled results were conservative (produced higher overpressure) compared to the experimental results. The model assumes that the explosive evaporation process is limited by the inertia of the expanding liquid/vapor mixture into the surroundings. BLEVE experiments performed at initial temperatures both above and below the superheat limit temperature showed that BLEVE blast did not abruptly disappear below the SLT but followed a gradual decay. The results showed that low $CO_2$ storage temperatures should not exclude BLEVE scenarios from hazard assessments.

Laboureur et al. (2015) investigated the overpressure from BLEVES blasts in mid-scale and small-scale experiments. They found from shadowgraph images that a second shock wave was caused by the fast evaporation of the fluid.

Birk et al. (2018) carried out small-scale experiments with weakened 0.6-liter aluminum tubes. A flame heated the tubes until the internal pressure led to the catastrophic rupture. Measured overpressures were compared with numerical results generated

from a prediction model. The model was named a “shock start model.” The authors suggested that the lead shock was primarily generated by the vapor space.

Further references on BLEVEs include the following publications: (Casal et al., 2001); (Eckhoff, 2014); (Ibarreta, 2016); (Abbasi and Abbasi,2007a, 2008); (Armstrong, 2004); (Clifford, 2008); (Mcdevitt et al. (1990); (Stawczyk, 2003); (Yu and Venart et al., 1996).

## 2.7 Equations of state (EOS)

The determination of state properties and the change from one state to another require measurements or a thermodynamic equation of state. Because of the difficulties to obtain reliable experimental measurements in the metastable region, the state information is often obtained from an EOS. The validity of most equations of state are typically limited to equilibrium conditions, and extrapolation is necessary to calculate state values in the metastable region. The chosen EOS influence the calculated results. In principle, any cubic EOS that describes the P-V-T relations for the fluid through the metastable and unstable region can be chosen. However, the scatter of calculated results can be significant. Examples of EOS used in dynamic simulations of rapid depressurization and phase transition include the stiffened gas (Tosse, 2017) and (Saurel, 2008); van der Waal (Tosse, 2017); Peng-Robinson Stryjek-Vera (Xie, 2013); and Span-Wagner (Giljarhus, 2012).

The Span-Wagner technical EOS (Span and Wagner, 1996) claims to provide reliable results for $CO_2$ in the range from the triple-point up to 800 MPa. The SW-EOS is a multiparameter equation of state explicit in the Helmholtz free energy. This EOS and later versions (Span and Wagner 2003 a,b) specify the reduced density and temperature as inputs.

Giljarhus et al. (2011) presented the use of the Span-Wagner equation of state in fluid-dynamic simulations of $CO_2$ behavior. Two case studies, which included simulations of tank depressurization and pipe transport, demonstrated the method.

Munkejord et al. (2016) reviewed data and models for $CO_2$ transport. They concluded that conservative designs and operational decisions must be made because of a lack of quantitative validated models.

The state calculations in the current thesis use the Span-Wagner EOS (Span and Wagner, 1996) and table values from the National Institute of Standards and Technology (NIST) that were found in Lemmon et al. (2018).

# 3 Experimental setup and methods

The thesis includes results from experimental work carried out on two independent setups that are denoted A and B. Hansen (2018) describes the design and assembly of setup A. Setup B, which was constructed by Tosse, was described in Tosse et al. (2015) and Tosse (2017). A third setup C, which was built by Ke (2009) and described in Bjerketvedt et al. (2011), is briefly presented in Appendix A. No experimental work was carried out on setup C in the current study. However, the pressure histories from one previous test were compared with the pressure calculated by the Rankine-Hugoniot model. This chapter presents test setups A and B, and the methods that accompanied the experimental work and the calculations in the thesis.

## 3.1 Setup A - Rectangular duct with glass and stainless steel

Setup A was designed to study the behavior of pressurized liquefied $CO_2$ released from a high-pressure reservoir into an atmospheric vented chamber. The construction of this test rig represents an essential contribution to the current study. Figure 3.1 shows a schematic diagram of the experimental setup that consisted of the following main parts: (1) a stainless steel high-pressure reservoir; (2) an atmospheric chamber with an adjustable open vent; (3) a cross-shaped knife with a pneumatic plunger actuator; (4) an aluminum foil diaphragm, and (5) a $CO_2$ supply-system with two industry grade cylinders. The two cylinders supplied liquid-phase and vapor-phase feed. Pressure sensors and temperature sensors were installed at defined positions on the experimental setup. The setup was designed to study $CO_2$ but can easily adapt to other substances such as propane.

The high-pressure reservoir was a custom-designed level gauge manufactured by PresSure Products Company and rated at 10 MPa. The vessel height from the bottom up to the diaphragm was 450 mm. A bottom section, which was a rectangular duct with volume 320 × 16 × 25.4 $mm^3$, had borosilicate glass windows that offered imaging possibilities. A circular section, which had a height of 130 mm, was located between the rectangular duct and the diaphragm. The aluminum foil diaphragm was circular with a

34-mm opening diameter. The total vessel volume was 190 $cm^3$ with the possibility of a 130-$cm^3$ liquid volume. Temperature sensor ports (T1-T6) and pressure sensor ports (P1-P6) were installed on the two stainless-steel sidewalls. The vertical spacing between two adjacent sensors was 50.8 mm.

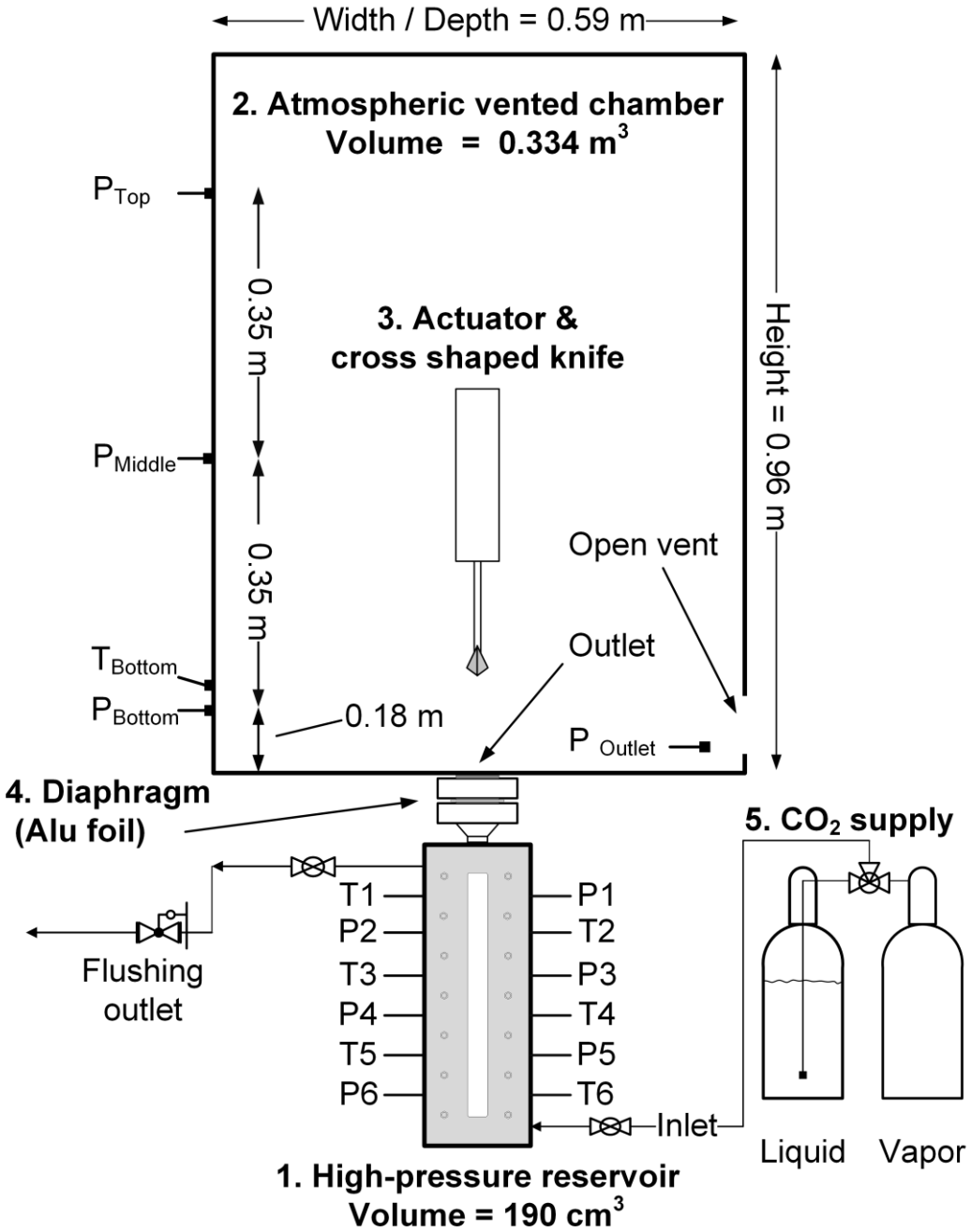


**Figure 3.1: Schematic that shows the main components of setup A.**

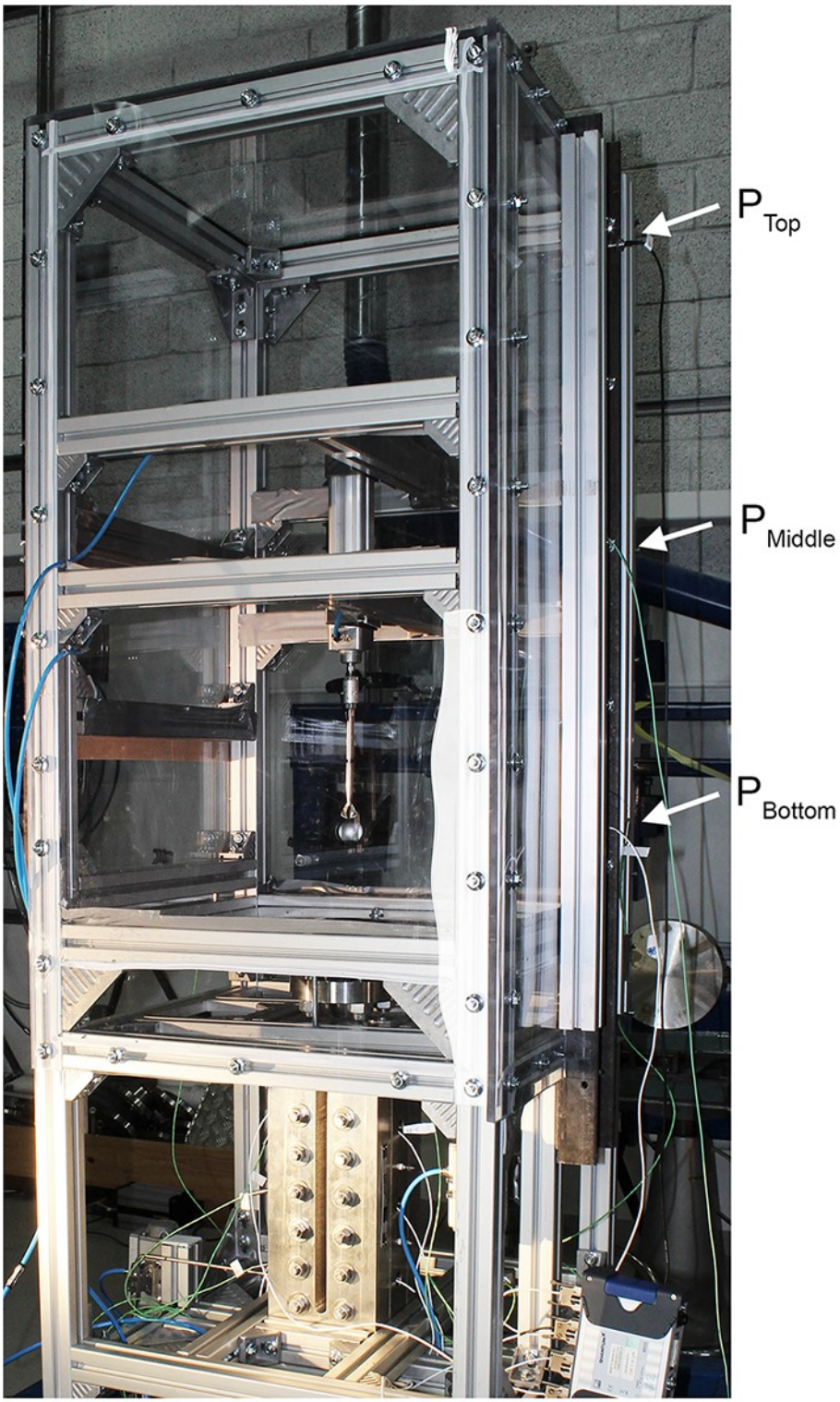


**Figure 3.2: Photograph that shows the high-pressure reservoir and the vented chamber.**

The atmospheric chamber volume was 0.334 $m^3$. The support-frame, which consisted of 45 × 45 $mm^2$ Rexroth aluminum profiles, determined the chamber size. Transparent 10-

mm polycarbonate panels covered all six surfaces and enabled visual observation of the $CO_2$ release. The chamber dimensions were 0.59 × 0.59 × 0.96 $m^3$. The high-pressure reservoir and the atmospheric chamber had a volume ratio of about 1750. This ratio was similar to the release from a 1-$m^3$ $CO_2$ storage tank into a 1750-$m^3$ factory hall. Placement of the vent at the bottom of the right sidewall, which is illustrated in Figure 3.1, prevented the long term accumulation of $CO_2$. The vent area $A_v$ was fully open at all times.

### 3.1.1 Diaphragm material and puncture device

The puncture device consisted of a Bosch Rexroth actuator and a custom-made cross-shaped knife. The actuator was a Series 167 tie rod pneumatic cylinder. Four 0.65-mm thick Stanly blade parts that were soldered onto a pointy rod ensured a complete rupture of the diaphragm.

The diaphragm consisted of a 6-layer arrangement of aluminum foil originating from soda cans. Such products are typically manufactured from 3004 - 19 or 3104 - H19 aluminum alloys. The thickness of each layer was approximately 100 µm. A series of tests determined the number of layers necessary. A decreased pressure difference between the high-pressure reservoir and the atmospheric pressure surroundings would require fewer aluminum foil layers.

### 3.1.2 Instrumentation

Four pressure sensors were installed in the atmospheric chamber. Three sensors (bottom, middle and top) were flush-mounted to the wall on a vertical U-channel steel beam at the left sidewall. The last sensor was placed on the front sidewall perpendicular to the vent opening. One Kulite-XTM-190-100G piezoresistive transducer with a measuring overpressure range of 0-0.7 MPa and a natural frequency of 95 kHz was installed at the steel beam bottom position. The sensor accuracy was about ± 1% of the measurement range. Pressure results from a test series gave an uncertainty estimate of ± 2 kPa.

The remaining three sensors in the vented chamber were Kistler 7001 piezoelectric transducers with a measuring overpressure range of 0-25 MPa and a natural frequency of 70 kHz. The pressure transducers in the high-pressure reservoir were Kulite-XTM-190-2000G piezoresistive sensors with a measuring range of 0-14 MPa, and a natural frequency of 410 kHz. The accuracy was ± 1% of the measurement range, and the thermal sensitivity shift was ± 2% per 100 K. All temperature sensors were fast-response Cromel-Alumel, K-type thermocouples with an accuracy of ± 1 K and a bead size diameter in the order of 0.1 mm. An Ametek Jofra CTC140A unit calibrated the temperature sensors before the start of the test series.

### 3.1.3 High-speed camera and illumination setup

Two high-speed cameras recorded the behavior of the $CO_2$ release upon diaphragm rupture. Figure 3.3 shows a schematic of the visualization setup. A Photron Fastcam SA-1 operating at 5,000 frames per second (fps), which used front lightning, captured the $CO_2$ expansion in the vented chamber. The light-source for this camera consisted of 400-Watt DEB400D Dedolight and one 250-Watt Dedocool tungsten light head.

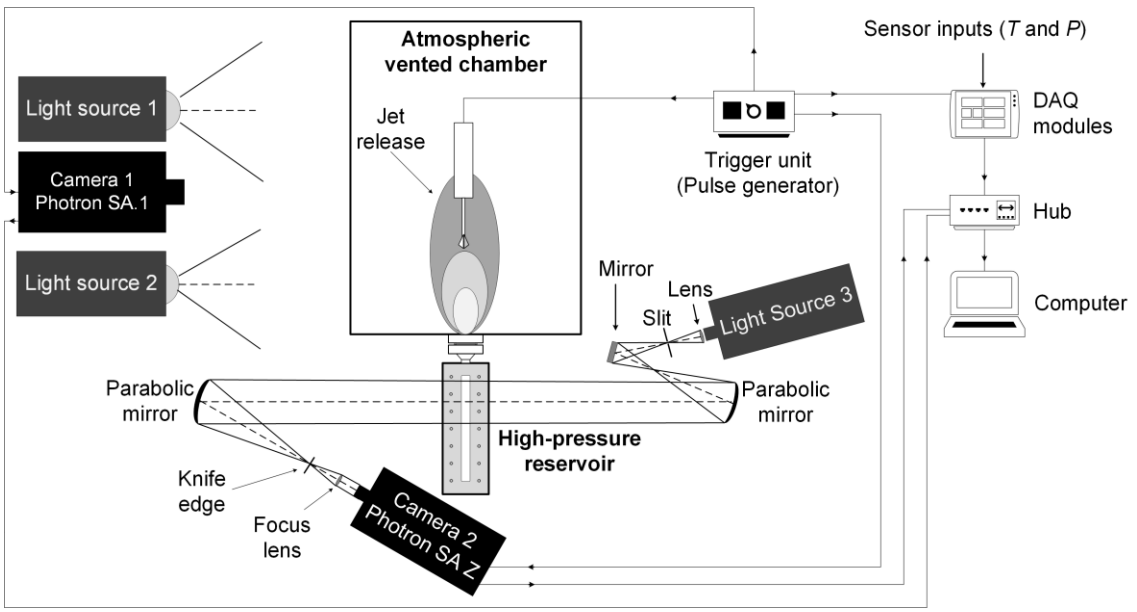


**Figure 3.3: Schematic of the visualization setup and the experiment control setup. Camera 1 captured the jet-release into the atmospheric vented chamber while camera 2 captured the depressurization inside the high-pressure reservoir.**

A Photron Fastcam SA-Z camera operating at 75,000 fps, which was a part of a z-type schlieren setup, captured the expansion and phase transition processes inside the high-pressure reservoir. The schlieren technique is described in Settles (2001). Two parabolic mirrors combined with a focus lens covered a 0.127-m section of the vessel height.

### 3.1.4 Test procedure and experiment control

A Quantum Composers 9500 series pulse generator initiated the experiments. A 5 volt signal triggered the knife actuator, the high-speed cameras, and the DAQ system simultaneously. The DAQ setup consisted of two HBM Quantum MX410 modules, an HBM MX440B module, and a Sigma LDS Nicolet digital oscilloscope. The trigger signal opened the valve that filled the pneumatic actuator with pressurized air. The piston-movement of the actuator lasted about 0.4 s before the cross-shaped knife punctured the diaphragm completely and with high reproducibility. A shock wave then propagated outward (into the atmospheric chamber), while a rarefaction wave propagated downward (into the high-pressure reservoir). A multiphase $CO_2$ jet followed the initial shock wave.

The high-speed images, the temperature histories, and the pressure histories were stored and then analyzed in MATLAB. High-speed videos with sensor data included were prepared. A comparison of the image observations with the sensor measurements provided a basis for the interpretation of the experimental results.

Before each test, the high-pressure reservoir was flushed three times with pressurized vapor-phase $CO_2$ at 1 MPa. Then, the chamber was slowly filled with either vapor-phase or liquid-phase $CO_2$ to the desired liquid level. The pre-rupture liquid level was obtained from the high-speed images. A ten minute idle period, between the filling stage and the test initiation, provided thermal equilibrium and stable sensor measurements. The pre-rupture state was saturated $CO_2$ at room temperature.

## 3.2 Setup B - Polycarbonate tube

Setup B was built by Tosse and described in Tosse et al. (2015), Tosse et al. (2016), and Tosse (2017). A modified setup was used to produce a part of the experimental results presented in Hansen et al. (2016; 2017) and the current thesis. The modifications included the addition of a temperature sensor close to the bottom position and a LED illumination system.

Figure 3.4a shows a schematic diagram of the rig that included the following main parts: (1) a vertically oriented transparent polycarbonate plastic tube; (2) a Rexroth pneumatic plunger actuator with a cross-shaped arrow that punctured the diaphragm; (3) a diaphragm arrangement that consisted of two layers of PET polymer film. Figure 3.4b shows a photograph of the test setup. The polycarbonate tube and attached flanges were mounted on to a single vertically oriented 45 × 45 mm Rexroth profile

The polycarbonate tube had a visible section of 32 cm, and the total high-pressure section height was 43.5 cm. The inner-diameter was 9 mm, and the wall thickness was 1.5 mm. In most comparable studies, the preferred material is glass because the smooth surface suppresses heterogeneous nucleation. In the current study, testing with pre-rupture pressures up to 6.2 MPa excluded the use of glass tubes because of insufficient mechanical strength. An objective of the current study was to investigate whether polycarbonate tubes would offer both a sufficiently smooth surface and the necessary mechanical strength.

The experimental work included tests with both pure vapor and liquid/vapor mixtures. The pre-rupture condition was saturated liquid/vapor at room temperature. A 40-liter industry grade cylinder that contained an internal riser pipe supplied the liquefied $CO_2$. A needle valve at the inlet and a relief valve at the outlet evacuated the air initially present in the polycarbonate tube, and carefully filled it with pressurized $CO_2$. The liquid level was determined by visual inspection. An emergency valve installed at the bottom of the rig safely released the pressure and evacuated the $CO_2$ inside the test section in case of an instrument air failure.

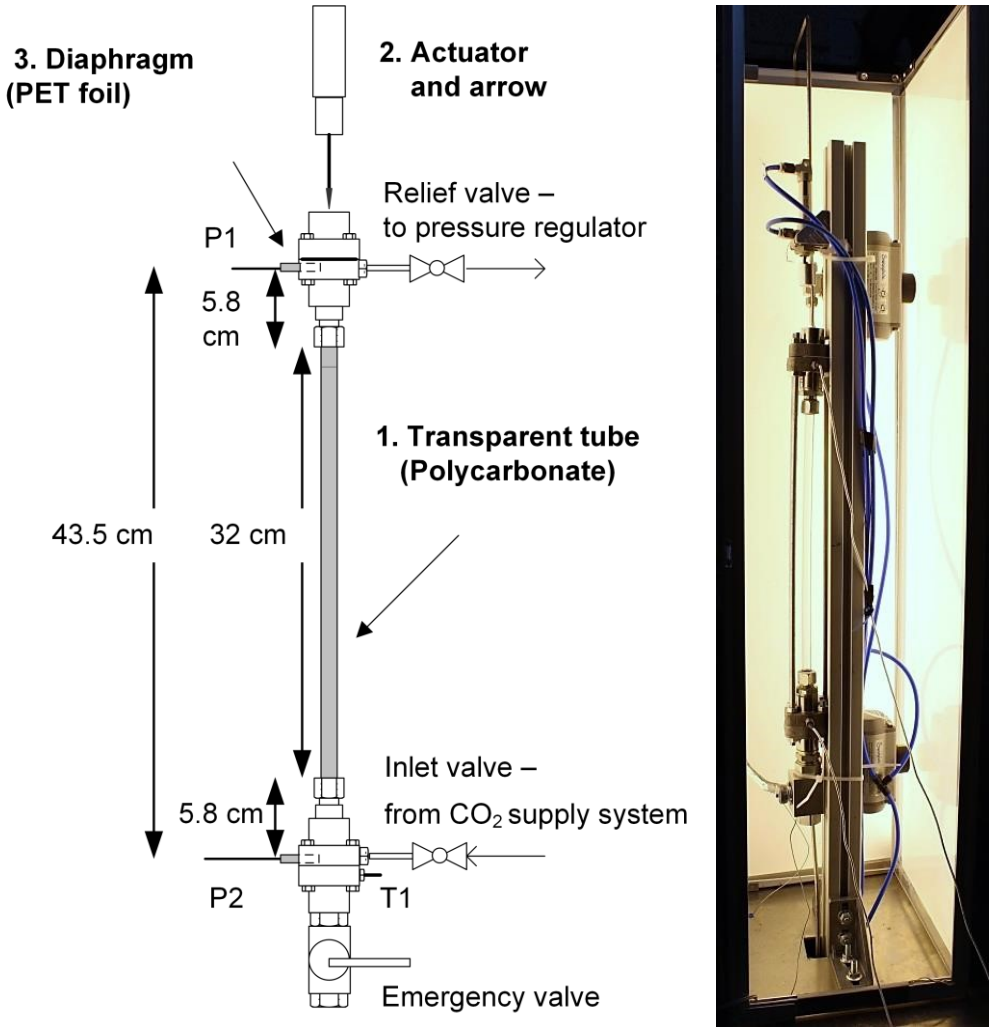


**Figure 3.4: Setup B (Polycarbonate tube). (a) A schematic that describes the main parts. (b) A photograph that shows the test setup and two of the LED panels.**

### 3.2.1 Instrumentation

The instrumentation included two Kulite XTM-190-1000G pressure sensors (P1, P2), and one temperature sensor (T1). The spacing between the top and bottom pressure sensor was 43.5 cm. The pressure range was 0 - 7 MPa, and the natural frequency was 290 kHz. The thermal sensitivity shift was typically ± 2% per 100 deg F. The sensors were calibrated before the start of the test series. According to the manufacturer, the piezoresistive operation makes these pressure sensors less sensitive towards thermal

shocks than piezoelectric sensors. No shielding measures were performed because of the short timescales of the experiment (about 10 ms).

The temperature sensor was a thermocouple type-K (Cromel/Alumel) with a measurement error limit of ±1.5 K. The sensor/transmitter had a time constant of 150 ms. Hence, only the initial (pre-rupture) temperature measurement was reported. The sensor was calibrated with an external calibrator (Ametek Jofra CTC140A) before the start of the test series.

The data acquisition (DAQ) unit, which was an HBM QuantumX MX410 amplifier, recorded the temperature and pressure histories at a 96 kHz sample frequency.

### 3.2.2 High-speed camera and illumination setup

A Photron Fastcam APX RS digital high-speed camera and a 50-mm Nikkor lens recorded the rapid depressurization and phase transition processes. The camera frame rate was 3000 frames per second (fps) at full resolution (1024 × 1024 pixels). The cropped image size was 1024 × 128 pixels. The recorded frame-rate (cropped image size) was 20,000–30,000 fps and the shutter-speed was 1/62,000 s. The primary light source was 3 LED panels (20W each) with diffusers that provided uniform illumination. Figure 3.4b shows two of the LED panels behind the polycarbonate tube setup. A pair of 250W Dedocool tungsten light heads provided secondary lighting that was used in some front-lit tests.

### 3.2.3 Test procedure and experiment control

The tube was slowly filled with $CO_2$ at the start of each test run. An idle period of 5 - 10 min provided stable test conditions. The initial pre-rupture state was a saturated liquid/vapor mixture at room temperature ($T_0$ = 293 ± 2 K). The manual operation of a Quantum Composers 9500 series pulse generator initiated the tests. A 5V signal triggered the arrow actuator, the high-speed camera, and the DAQ unit simultaneously. The pressurized polycarbonate tube contents, which were released directly into the test hall, produced a multi-phase jet upon diaphragm rupture.

### 3.2.4 Image processing method

The high-speed images from each test run were imported into MATLAB and stacked next to each other to produce position-time (x-t) plots. The resolution of the high-speed images were 1024 x 128 pixels; the tube diameter typically accounted for 35-40 pixels. The resulting resolution was approximately 3 pixels per mm. Figure 3.5 shows a series of cropped high-speed images stacked next to each other.

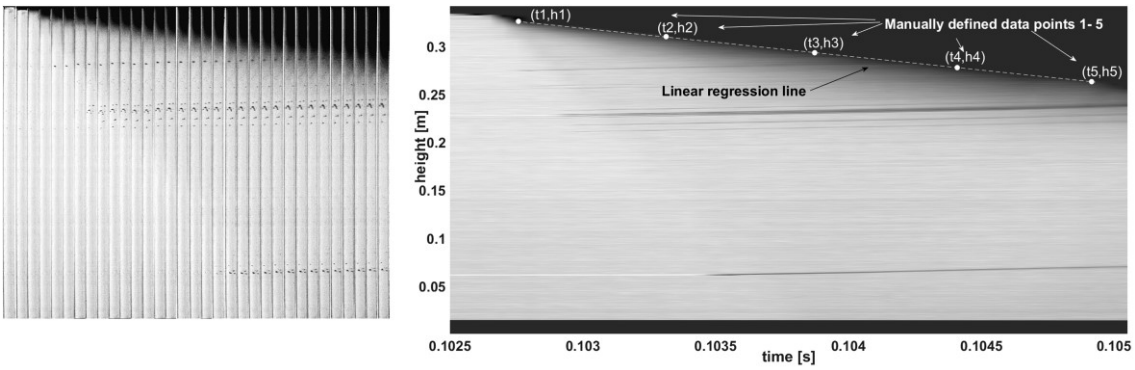


**(a)** **(b)**

**Figure 3.5: Time series. (a) A series of cropped high-speed images stacked together. (b) High-speed images imported and processed in MATLAB.**

The following image processing method was used to interpret the information from the high-speed images and to calculate wave and flow velocities. The gray-scale values of each pixel in the x-direction were added together in MATLAB and used to present the entire tube diameter. The image dimensions were reduced from 1024 × 128 pixels to 1024 × 1 pixels. Hence, a visualization of the expansion and boiling process was reduced to a 1D phenomenon evolving in time, as illustrated in Figure 3.5b. This averaging method was used to calculate characteristic velocities. A disadvantage associated with this method was a loss in the ability to resolve flow details.

The processed high-speed images were matched with the pressure histories and plotted together to interpret the data and to calculate average velocities. The wave and the fluid flow velocities were calculated by linear regression as illustrated in Figure 3.5b. In this example, five discrete data points 1 -5 were manually identified on the x-t diagram in MATLAB. The slope of the regression line then gave an estimate of the velocity. The on-

screen plot in MATLAB allowed significantly higher precision than what is reproduced in Fig 3.5. The following procedure describes the method that was used to calculate the flow velocities: (1) Define from the x-t plot the velocity that should be calculated; zoom in on the region of interest. (2) manually define 3 to 10 points that follow the wave or fluid flow of interest. (3) Arrange the x-t data into an array with time and spatial position. (4) Use the least squares method to calculate the velocity from the slope of the discrete data points regression line.

The sensitivity to measurement errors increased with increasing velocities and decreasing height differences. The largest uncertainty in the velocity calculations corresponded to time measurement error for high velocities. At 20,000 frames per second, the time difference between two images was 0.05 ms. An error estimate for a rarefaction wave propagating at 300 $ms^{-1}$ measured along the total tube length gave ± 13.4 $ms^{-1}$, or 4.5%. The measurement error in the y-axis contributed considerably less at these velocities, giving a total error estimate of ± 13.7 $ms^{-1}$, or 4.6%. Evaporation wave velocities were typically calculated at the upper section of the tube. A total velocity error estimate (both x and y-direction) of an evaporation wave propagating at 30 $ms^{-1}$ through a 0.1 m section was ± 0.5 $ms^{-1}$, or 1.8%.

## 3.3 Rankine-Hugoniot calculation method

The propagation of adiabatic evaporation waves was modeled by the Rankine-Hugoniot relations that treats the wave as a jump between a superheated liquid state and a 2-phase equilibrium state. This section describes the calculation method that was used. The method incorporates the ideas previously discussed by Chaves (1984), Thompson et al. (1987), Shepherd et at. (1989), Hill (1991), Frost et al. (1991), Simões-Moreira and Shepherd (1999), Reinke (1997), Reinke and Yadigaroglu (2001), Simões-Moreira (1994, 2000), Angelo et al. (2005), and Stutz and Simões-Moreira (2013). The analysis defines three states, separated by a rarefaction wave (or fan), and an evaporation wave, see Figure 3.6. State 0 (saturated liquid) is the initial pre-rupture state, located in front of the rarefaction wave. State 1 (superheated liquid) is the metastable liquid state, located behind the rarefaction wave but ahead of the evaporation wave. State 2 (two-phase equilibrium mixture) is located behind the evaporation wave. In Figure 3.7 $T$ is the temperature, $P$ is the pressure, $V$ is the specific volume, $h$ is the enthalpy, $u$ is the velocity, and $\chi$ is the vapor mass fraction. A control volume that includes state 1 and state 2 is drawn around the evaporation wave. The evaporation wave is restricted to a narrow region (Simões-Moreira and Shepherd, 1999). The enthalpy used to evaporate a fraction of the liquid originates from the rapid depressurization from the saturated liquid state to the superheated state.

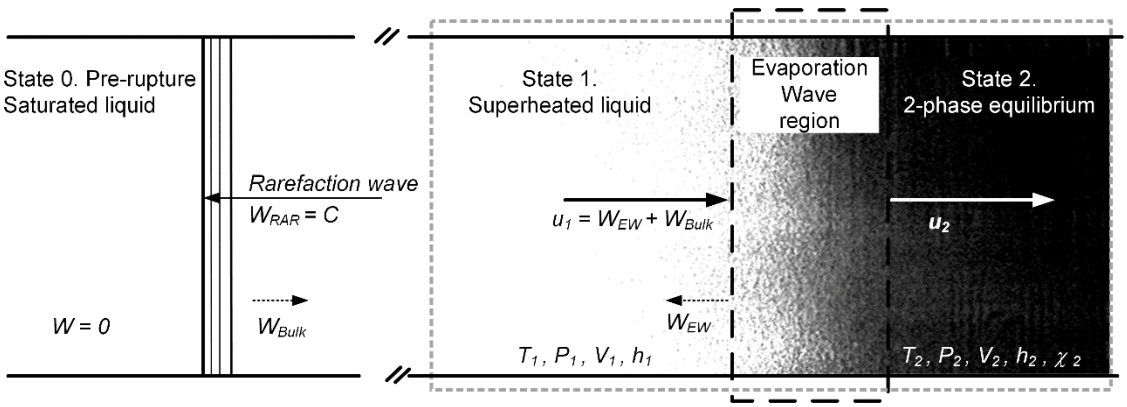


**Figure 3.6: Control volume that is used in the Rankine-Hugoniot calculations.**

The following assumptions were used in the calculations. The evaporation wave is modelled as a jump from a superheated liquid state to a two-phase equilibrium state. One-dimensional inviscid fluid flow is assumed with no heat transfer from the walls (adiabatic conditions). Heterogeneous nucleation on the wall surface ahead of the evaporation wave is neglected. Also, the gravitation force effects are neglected. The method assumes both mechanical equilibrium (no slip between vapor and liquid), and phase equilibrium (saturated vapor and liquid mixture) at state 2. The integral form of the conservation equations of mass, momentum, and energy for steady, one-dimensional flow can be formulated as:

$$\rho_1 u_1 = \rho_2 u_2 \tag{3.1}$$

$$P_1 + \rho_1 u_1^2 = P_2 + \rho_2 u_2^2 \tag{3.2}$$

$$h_1 + \frac{1}{2}u_1^2 = h_2 + \frac{1}{2}u_2^2 \tag{3.3}$$

The velocities $u_1$ and $u_2$ are defined relative to the evaporation wave (from the wave frame of reference). Whereas, the evaporation wave velocity $W_{EW}$ and the liquid bulk velocity $W_{Bulk}$ ahead of the evaporation wave are obtained from the experiment in a stationary laboratory frame of reference (see Fig. 3.7). Then the velocity $u_1$ can be calculated by the following expression:

$$u_1 = W_{Bulk} + W_{EW} \tag{3.4}$$

$W_{Bulk}$ is approximated by the difference in liquid-phase speed of sound that results from the density ratio $\rho_0/\rho_1$ across the rarefaction wave. The Rayleigh line (equation 3.5) relates the velocity $u_1$ to the change in pressure and specific volume across the wave. A combination of equation 1 and 2 eliminates the velocity $u_2$:

$$u_1 = V_1\left(\frac{P_2 - P_1}{V_1 - V_2}\right)^{1/2} \tag{3.5}$$

The solving for pressure $P_2$ gives a linear relation that connects $V_2$ and $P_2$ for a specific velocity $u_1$ and specified state 1. The negative slope of the Rayleigh line represents the

mass flux squared, expressed by the squared ratio between the velocity $u_1$ to the specific volume $V_1$:

$$P_2 = -\left(\frac{u_1}{V_1}\right)^2 V_2 + \left[P_1 + \frac{u_1^2}{V_1}\right] \tag{3.6}$$

The Hugoniot curve (or evaporation adiabat) represents a locus of possible states behind the evaporation wave. The curve combines the conservation of mass, momentum, and energy in equations 3.1-3.3 to eliminate both the velocities $u_1$ and $u_2$:

$$h_2 - h_1 = \frac{1}{2}(P_2 - P_1)(V_2 + V_1) \tag{3.7}$$

The enthalpy available for adiabatic evaporation is the enthalpy difference between the expanded and saturated liquid at pressure $P_1$. If $u_2$ is assumed to be sonic, corresponding to the Chapman-Jouguet solution, the maximum mass flux is obtained. If state 2 is assumed to be at phase equilibrium, the mixture properties specific volume enthalpy are related to the saturation state values by the following equations:

$$V_2 = \left(1 - \chi_2\right)V_{l,2} + \chi V_{v,2} \tag{3.8}$$

$$h_2 = \left(1 - \chi_2\right)h_{l,2} + \chi h_{v,2} \tag{3.9}$$

The subscripts *l,2* and *v,2* denotes saturated liquid and vapor at state 2. A combination of equations 3.7-3.9 produces the vapor mass fraction $\chi_2$ at state 2:

$$\chi_2 = \frac{2\left(h_1 - h_{l,2}\right) + \left(V_1 + V_{l,2}\right)(P_2 - P_1)}{2\left(h_{v,2} - h_{l,2}\right) - \left(V_{v,2} - V_{l,2}\right)(P_2 - P_1)} \tag{3.10}$$

State 2 correspond to the intersection between the Rayleigh line and the Hugoniot curve that are shown in p-V diagram Fig. 3.8. The thermodynamic properties are calculated by the Span-Wagner technical equation of state (Span and Wagner, 1996) and saturation properties from NIST (Lemmon et al., 2018). The parameter inputs taken from the experimental results are the pre-rupture pressure $P_0$, the superheated liquid pressure $P_1$, and the velocity $u_1$. State 1 is calculated as an isentropic expansion from $P_0$ to $P_1$.

Figure 3.7a shows a p-V diagram that includes two Rayleigh lines, corresponding to two evaporation wave velocities. The initial temperature at state 0 is $T_0$ = 293 K. The two solutions are one non-CJ solution ($u_1$ = 30 $ms^{-1}$), and one CJ solution ($u_1$ = 36.5 $ms^{-1}$) where the Rayleigh line is tangent to the Hugoniot curve. The specified pressures at states 0 and 1 are 5.7 MPa and 4.9 MPa, respectively.

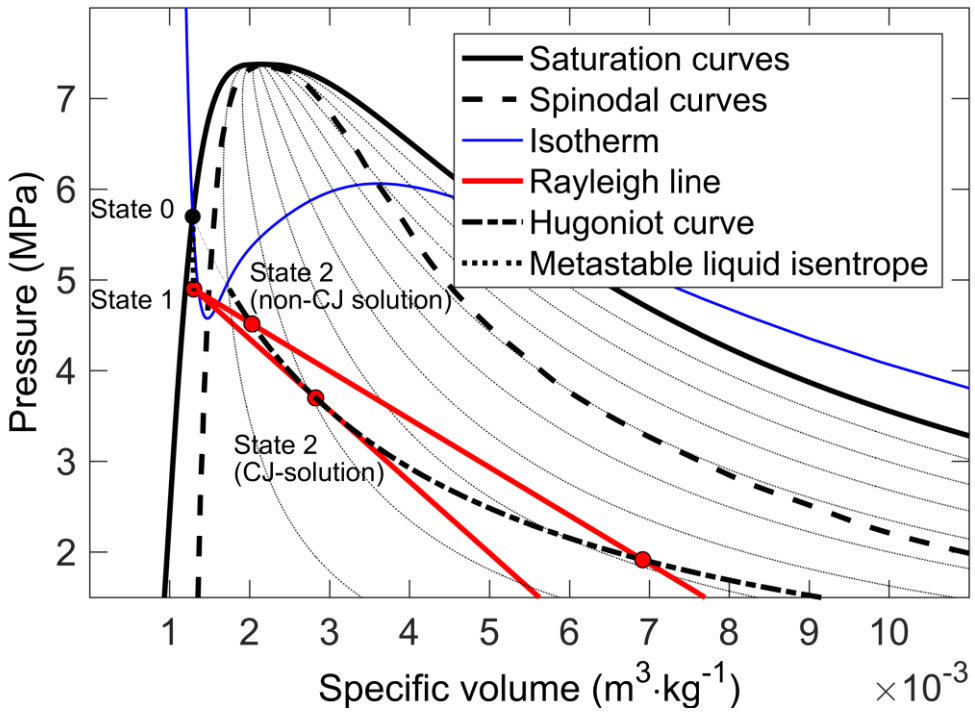


**Figure 3.7: p-V diagram of $CO_2$ that shows the saturation curves, the spinodal curves, the T = 293 K isotherm, an isentrope, the Rayleigh line, and the Hugoniot curve from the Rankine-Hugoniot analysis.**

The subsonic solution is named the non-CJ solution in Figure 3.7. Figure 3.8 shows a p-V diagram that provides a close-up of the area of interest. The plot contains the CJ solution only.

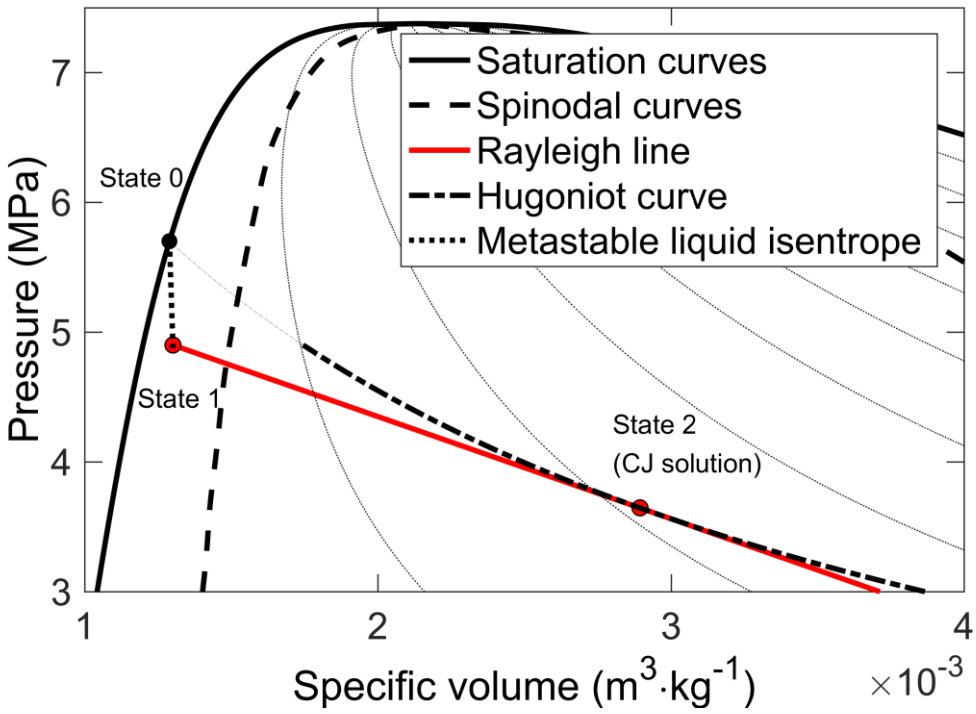


**Figure 3.8: p-V-diagram of $CO_2$ that provides a close-up of the region of interest. The diagram shows the CJ solution with the Rayleigh line being tangent to the Hugoniot curve.**

# 4 Summary of the articles

This chapter presents the primary results from the three journal papers that were publishes as a part of this study. The complete paper manuscripts, which includes journal papers and conference proceedings, are included in part II of the thesis.

## 4.1 Paper A. "The behavior of pressurized liquefied $CO_2$ in a vertical tube after venting through the top"

### 4.1.1 Introduction

This paper presents results from small-scale experiments on the rapid depressurization and boiling of saturated carbon dioxide at room temperature. Tosse et al. (2015) presented results from the same test rig and observed evaporation waves propagating at a near constant velocity of 20-30 $ms^{-1}$ inside a half-filled transparent tube. This study represents a continuation of the experimental work. New contributions includes additional testing with liquid contents of 0, 50, and 95 vol% in the tube, a phase transition rate estimate, and an energy release estimate. The number of publications that describe evaporation waves and rapid phase transition in carbon dioxide are limited. Hence, it is of interest to increase the number of experimental data sets. The saturation pressure of $CO_2$ at room temperature is 5.5-5.7 MPa. This is significantly higher than that of comparable studies performed with other substances. The experimental setup includes a polycarbonate tube. The surface properties of polycarbonate tubes causes heterogeneous nucleation in the superheated liquid ahead of the evaporation wave. One of the objectives was to determine if these plastic tubes offer both a sufficiently smooth surface, and the necessary mechanical strength. The relevance of experimental data on $CO_2$ is high for safety assessments of process equipment used in carbon capture and storage technologies. An application of the experimental results is to provide reference data for the source terms used in 1D phase transition models. Several such models currently exist, that are capable of predicting the blast wave pressure and dynamics in a BLEVE, e.g., Pinhasi et al. (2007), Xie (2013), and

Tosse (2017). The study is restricted to the phenomena occurring inside the tube. Effects imposed on the surroundings, such as blast overpressure measurements are essential parts of BLEVE studies and will be discussed in article B. The explosions from this study may not be considered as true BLEVEs according to the definition proposed by Birk et al. (2007), since the test rig does not shatter. However, the depressurization and boiling mechanisms are believed to be transferable to a real BLEVE.

### 4.1.2 Results

Paper A presents three tests that are denoted as TR1 to TR3. Table 4-1 summarizes the initial conditions and the calculated velocities. Figure 4.1 shows a schematic x-t diagram of the expansion and evaporation of $CO_2$. A vapor head-space is located above the liquid level. The physical phenomena appeared similar to the observations discussed by Hill (1991), and Pinhasi et al. (2007). The tests were initiated by puncturing the diaphragm that separated the tube contents from the surrounding atmospheric air. Rarefaction waves then propagated through the tube. What seems to be the middle or the tail of the expansion fan (A) was observed propagating with constant velocity through the liquid phase. When the rarefaction fan interacted with the liquid/vapor interphase, it was partially reflected and then propagated through the liquid phase. The wave then reflected at the tube bottom flange. The saturated vapor partially condensed (E) because of the isentropic expansion and entered the two-phase envelope. The liquid became superheated because of the sudden pressure reduction that followed the passage of the rarefaction wave. Then boiling started at the phase boundary. In most but not all cases, an evaporation wave (B) was observed propagating downward into the liquid phase, resulting in a two-phase vapor/liquid mixture behind the evaporation wave. The details in the boiling front could be observed in these tests. One reason was the low resolution (about 3 pixels per mm). Another reason was the observation of heterogeneous nucleation that occurred in the superheated liquid ahead of the evaporation wave.

**Table 4-1: Initial conditions, measured properties, and calculated properties. Results from tests TR1-TR3 in Paper A.**

| Description | Wave ID | Unit | TR1 | TR2 | TR3 |
|---|---|---|---|---|---|
| Initial liquid level, | | % | 0 | 58 | 95 |
| Initial temperature, $T_0$ | | °C | 21.6 | 19.5 | 19.7 |
| Initial pressure (bottom), $P_2$ | | barg | 57 | 56 | 57 |
| Rarefaction wave velocity (Average - both gas and liquid phase) based on pressure sensors P1 and P2. | | $ms^{-1}$ | 192 | 240 | 280 |
| Rarefaction wave velocity, liquid phase, from bubble condensation, based on high-speed camera images | | $ms^{-1}$ | N/A | 318 | 302 |
| Velocity - middle or tail of the expansion fan | A | $ms^{-1}$ | N/A | 235 | 240 |
| Evaporation wave velocity | B | $ms^{-1}$ | N/A | 32 | 32 |
| Gas bubble velocity (indicate liquid bulk flow when assuming no slip) | C | $ms^{-1}$ | N/A | 5.2 | 5.4 |
| Average bulk flow velocity | D | $ms^{-1}$ | 171-66 | 77 | N/A |
| Condensation wave velocity, Vapor phase | E | $ms^{-1}$ | 192 | 190 | N/A |
| Contact surface velocity, vapor-vapor/liquid, upper 6 cm | F | $ms^{-1}$ | N/A | 95 | N/A |
| Liquid layer front velocity | G | $ms^{-1}$ | N/A | 8.0 | N/A |

The evaporation wave was more defined in the upper part of the tube before the propagation was disturbed by rarefaction waves reflected from the tube bottom. In some test runs, gas bubbles (C) were observed moving upward and accelerated after the passage of the rarefaction wave. Visual observations of the tube during the experiments showed that these bubbles were situated in the bulk and not at the tube wall. A contact surface (F) between the vapor and the vapor-liquid/vapor two-phase mix

was observed, accelerating towards the outlet of the tube. A liquid layer front (G), which originated at the liquid/vapor interface, moved upward at a constant velocity. At the center of the tube, an annular bulk flow (D) with significantly higher velocity than the liquid layer at the tube wall (G) was observed. The velocity of D did not remain constant but decreased gradually with decreasing pressure as time evolved. At a later stage, when the pressure was below the triple point at 5.2 bar, the remaining $CO_2$ was expected to consist of a mixture of vapor and dry ice particles.

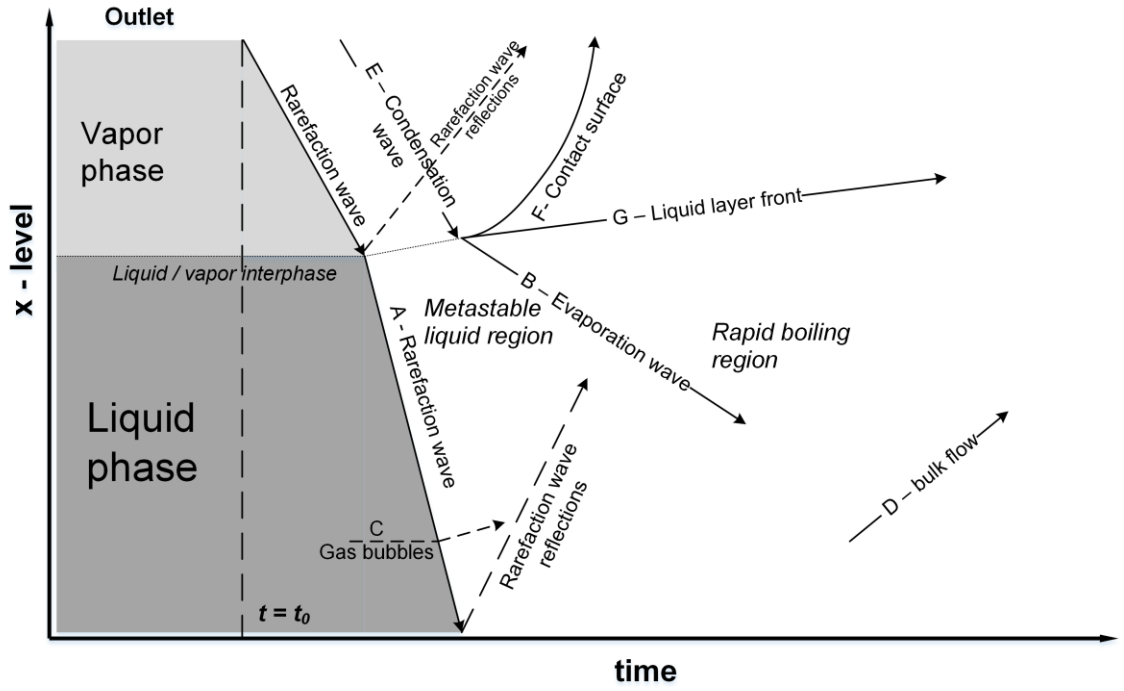


**Figure 4.1: Schematic x-t diagram that presents the overall wave and fluid flow phenomena in a vertical tube that contains liquefied $CO_2$ and a vapor headspace.**

In TR2, the initial visual level of the saturated liquid $CO_2$ was 58%. Figure 4.2 shows an x-t plot of the processed high-speed images and a p-t plot from pressure sensors P1 (top) and P2 (bottom). The full paper manuscript presents similar plots from TR1 and TR3. The arrows labeled A-G indicate the velocities of the waves and the fluid flows in the x-t diagram. The numbering corresponds to the characters used in Figure 4.1 The observations in TR2 were similar to the experimental results reported by Tosse et al. (2015).

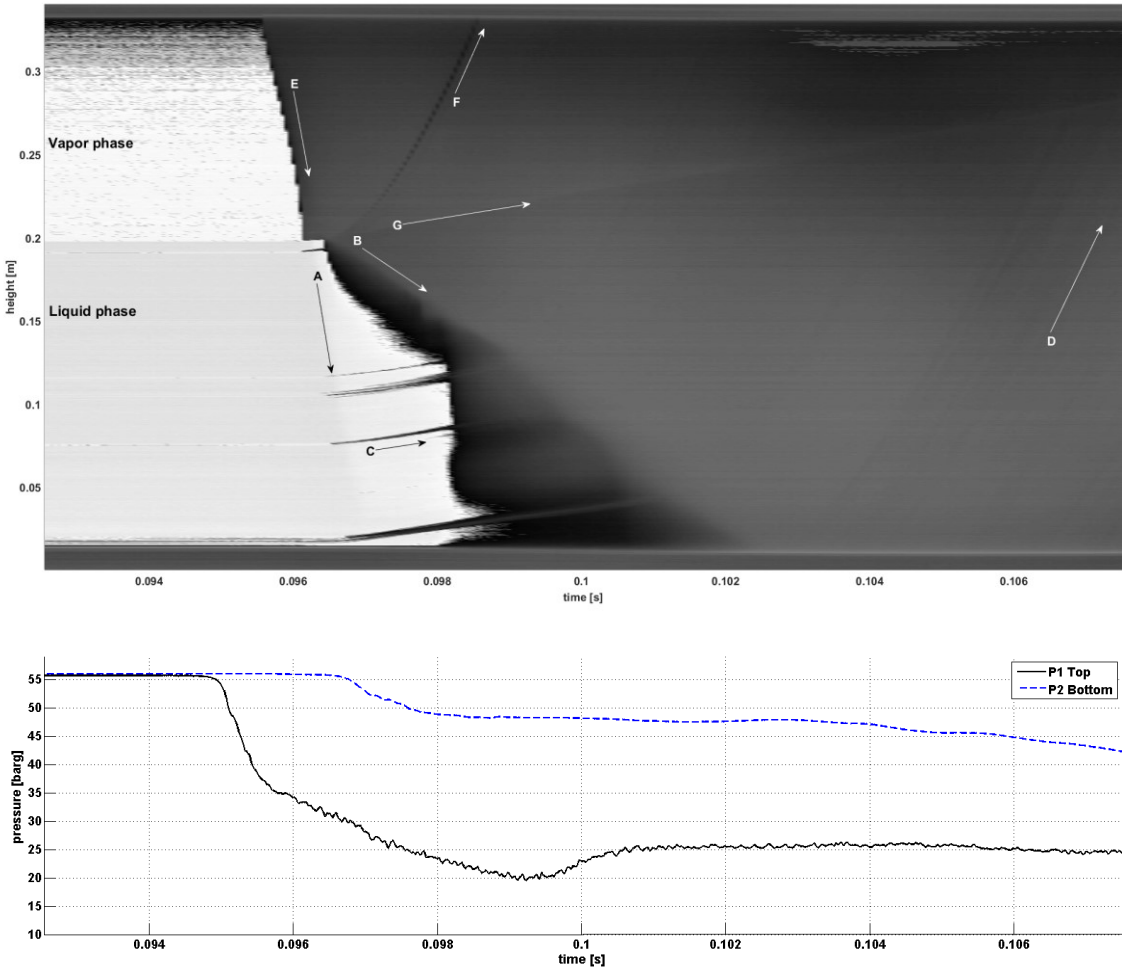


**Figure 4.2: Experimental results from TR2 (58 vol % liquid level). Top: x-t plot of the processed high-speed images. Bottom: a p-t plot from pressure sensors P1 (top) and P2 (bottom).**

The pressure P1 started to drop at time t = 95 ms from an initial value of 5.6 MPa to a temporary minimum of 2.0 MPa. After a 1.81 ms delay, the pressure P2 (bottom) started to decrease. The average rarefaction wave velocity was 240 ± 13 $ms^{-1}$ that is similar to the velocity 238 ± 12 $ms^{-1}$ calculated by Tosse et al. (2015). The average speed of sound, based on interpolated values from the Span-Wagner equation of state (1996) with saturated $CO_2$ at 19.4 °C, was 258 $ms^{-1}$ (196 $ms^{-1}$ in the vapor phase and 344 $ms^{-1}$ in the liquid phase). At time t = 95.5 ms, the first visual changes were observed. Because of the rapid expansion of the saturated vapor, a condensation wave (E) propagated in the vapor bulk downward to the vapor/liquid interface with an average velocity of 190 ± 7 $ms^{-1}$.

A front (A) was observed that propagated with a constant velocity of 235 ± 13 $ms^{-1}$. This velocity was considered too slow to represent the head of the expansion fan. Later studies concluded that these observations originated from heterogeneous nucleation at the tube wall in front of the evaporation wave.

### 4.1.3 Conclusions

Paper A presented experimental results from three test runs, denotes as TR1-TR3. The tests described rapid phase transition of pressurized liquefied carbon dioxide in a vertical tube. The experimental setup that included a high-speed camera and two pressure sensors was able to successfully identify the expected phenomena such as the acoustic rarefaction waves, the evaporation wave, and a liquid/liquid-vapor surface. Calculated wave propagation velocities were presented. The evaporation wave velocity was constant in the upper part of the tube. No evaporation front details could be observed. The transparent polycarbonate tube did not provide a sufficiently smooth surface to suppress heterogeneous wall nucleation. A phase transition rate estimate was calculated based on the net evaporation wave velocity and the density in the expanded liquid. The presented experimental results could be used as reference data for the interfacial flux source terms in 1D phase transition models.

## 4.2 Paper B. "Blast from pressurized $CO_2$ released into a vented atmospheric chamber"

### 4.2.1 Introduction

Paper B describes the blast from pressurized carbon dioxide ($CO_2$) released from a high-pressure reservoir into an openly vented atmospheric chamber. Small-scale experiments with pure vapor and liquid/vapor mixtures were carried out and compared with simulations. A motivation was to investigate the effects of vent-size and liquid content on the peak overpressure and impulse response in the atmospheric chamber. An additional objective was to study if the volume production resulting from the rapid boiling would contribute to the shock strength in the current test geometry. The results included both experimental work and numerical simulation of the $CO_2$ release. The CFD model described the gas dynamics in a closed chamber and did not include any phase transitions. The experimental parameters included two different vent areas (0.1 and 0.01 m2) and three different liquid fractions (0, 32, and 68 vol %). The vent-opening areas were selected based on a series of tests. Experimental work describing the depressurization and release of $CO_2$ from a high-pressure reservoir has previously been published, but not with a test geometry identical to the setup in the current study. Examples of complementary publications include the work by Tosse et al. (2015), Hansen et al. (2017), Bjerketvedt et al. (2011), Ciccarelli et al. (2017), Voort et al. (2012) and Li et al. (2016; 2018). Li et al. described tests carried out in a comparable high-pressure section, but their studies were mainly limited to the behavior inside the high-pressure vessel.

### 4.2.2 Results

Paper B presents results from five tests that are denoted as TR1 to TR5. Table 4-2 summarizes the test parameters and main results. The initial pre-rupture state was saturated $CO_2$ at room temperature (292 K). Figure 4.3 shows selected high-speed video images of the $CO_2$ jet from TR1 (vapor-only) captured at specified times after diaphragm-rupture. The jet diameter and height was significantly reduced after 10 ms.

Table 4-2: Initial conditions, measured properties, and calculated properties. The table shows results reproduced from tests TR1-TR5 and simulations in paper B.

| **Description** | **Unit** | **TR1** | **TR2** | **TR3** | **TR4** | **TR5** | **Sim** |
|---|---|---|---|---|---|---|---|
| Initial pressure $P_0$ | MPa | 5.5 ± 0.1 | 5.3 ± 0.1 | 5.6 ± 0.1 | 5.6 ± 0.1 | 5.6 ± 0.1 | 5.5 |
| Initial temp. $T_0$ | K | 292 ± 1 | 292 ± 1 | 292 ± 1 | 292 ± 1 | 292 ± 1 | 292 |
| Open vent area $A_v$ | $m^2$ | 0.1 | 0.01 | 0.1 | 0.01 | 0.01 | 0 |
| Liquid volume $V_{L,HP}$ | $cm^3$ | 0 | 0 | 130 | 130 | 70 | 0 |
| Vapor volume $V_{V,HP}$ | $cm^3$ | 190 | 190 | 60 | 60 | 120 | 176 |
| Liquid fraction | vol % | 0 | 0 | 68 | 68 | 37 | 0 |
| Mass of $CO_2$ $m_{CO2}$ | g | 36 | 36 | 113 | 113 | 77 | 33 |
| Peak overpressure $P_{peak, Bottom}$ | kPa | 15 ± 2 | 17 ± 2 | 20 ± 2 | 15 ± 2 | 18 ± 2 | 12 |
| Impulse at 100 ms $J$ | kPa·ms | 55 | 149 | 326 | 426 | 206 | - |

Figure 4.4 shows selected high-speed video images of the jet release in TR3 (68 vol% liquid). The vertical jet velocity at the early stage was equal to TR1.

The jet release period was increased from ≈ 20 ms (vapor-only) to ≈ 40 ms (liquid/vapor mixture). After 50-100 ms, the vented chamber was filled with a white mist.

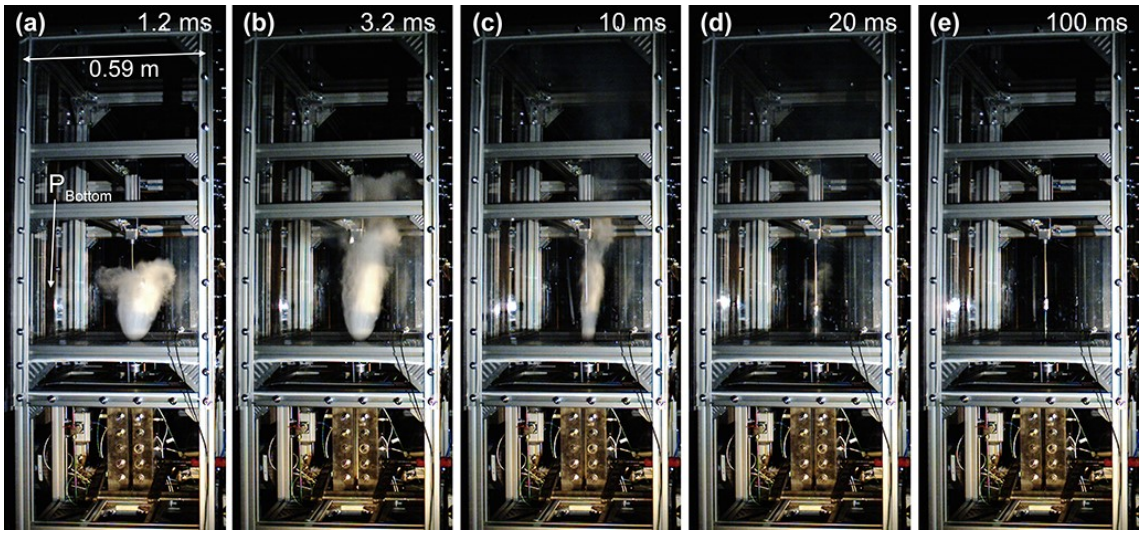


**Figure 4.3: Selected video frames that show the release of $CO_2$ vapor into the open vent chamber. TR1 (vapor-only).**

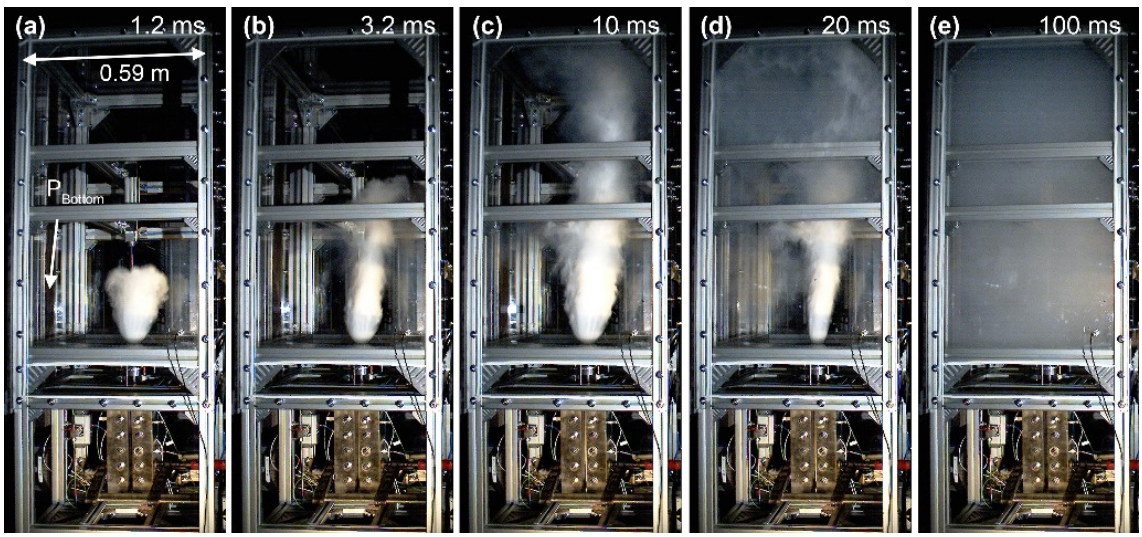


**Figure 4.4: Selected video frames that show the release of a liquid/vapor mixture into the open vent chamber. TR3 (68 vol % liquid).**

Figure 4.5 shows that the rapid evaporation did not contribute to the shock strength in the current geometry. The pressure measurements and impulse calculations of pure vapor and liquid/vapor mixtures were almost identical up to about 7.5 ms.

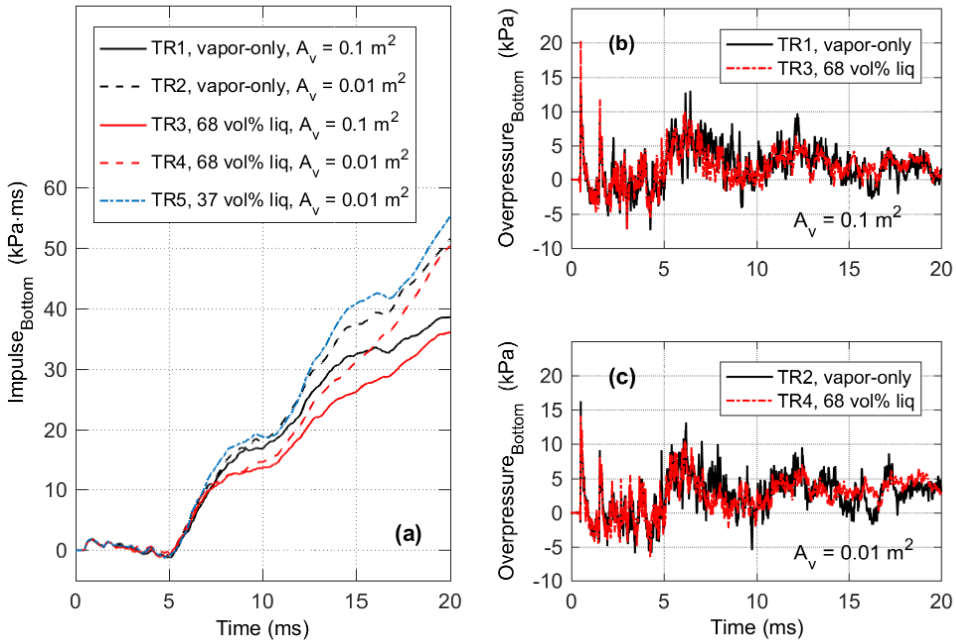


**Figure 4.5: (a) Impulse calculations, and (b - c) pressure measurements from the vented chamber bottom sensor. From 0 - 20 ms after diaphragm rupture.**

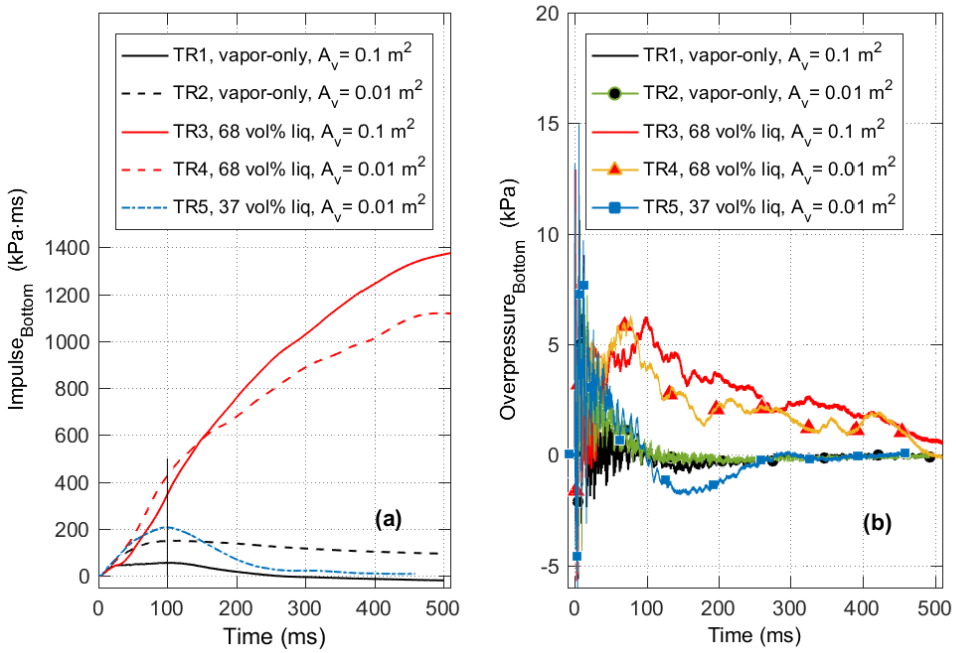


**Figure 4.6: (a) Impulse calculations, and (b) pressure measurements from the vented chamber bottom sensor. From 0-500 ms after diaphragm rupture.**

Figure 4.6 shows that the calculated impulse was significantly higher when the high-pressure reservoir contained a large liquid/vapor fraction, as compared to pure vapor. The duration of the liquid/vapor test was longer than 100 ms, because of the extra time needed to push the $CO_2$ cloud through the vent opening.

3D simulations of the $CO_2$ release were performed with the USN in-house CFD code. The experimental impulse histories and pressure histories in Figure 4.7 showed a good qualitative agreement with the simulations. The numerical results reproduced both the incident shock wave and the main shock reflections inside the atmospheric chamber. During the 0 - 20 ms period, the pressure response in the atmospheric chamber was governed by the rapid expansion of vapor-phase $CO_2$ from the pre-rupture state to atmospheric pressure.

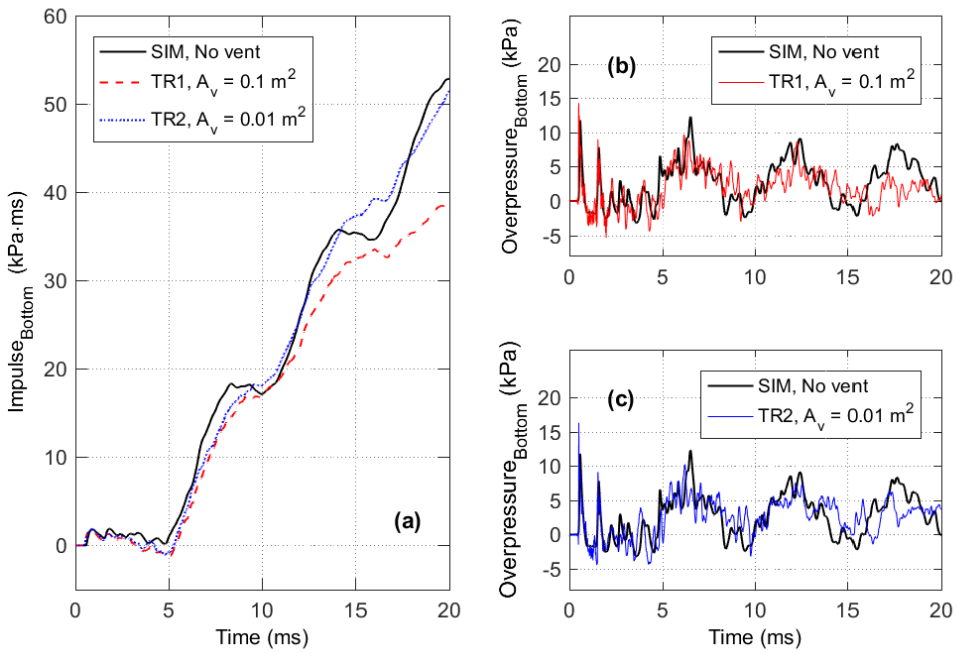


**Figure 4.7: Comparison of simulations and experimental results from the vented chamber bottom sensor. (a) Impulse histories, and (b - c) pressure histories.**

### 4.2.3 Conclusion

Paper B investigated the release of pressurized $CO_2$ from a high-pressure reservoir into a vented chamber. The comparison of vapor-phase $CO_2$ test results with simulations

showed good agreement. The numerical code (Vaagsaether, 2010) modeled the single-phase gas dynamics inside of a closed chamber, i.e, phase transition was not considered in the simulations. Hence, the simulations described a vapor-only test into an unvented chamber. Nevertheless, the simulations reproduced both the incident shock wave, the shock reflections, and the jet release inside the atmospheric chamber. In the experiments, the rapid phase transition did not contribute to the initial shock strength in the current test geometry. The evaporation rate was too low to contribute to the measured peak pressure that was in the 15-20 kPa range. The simulation results produced a calculated peak overpressure of 12 kPa. The liquid tests showed a significantly higher impulse compared to tests with pure vapor. Reducing the vent opening from 0.1 $m^2$ to 0.01 $m^2$ resulted in a slightly higher impulse calculated at 100 ms. The effects of the vent area size on the impulse were evident in the vapor-only tests, but not so clear in the liquid/vapor mixture tests.

## 4.3 Paper C. "Rapid depressurization and phase transition of $CO_2$ in vertical ducts – small-scale experiments and Rankine-Hugoniot analyses"

### 4.3.1 Introduction

Paper C discusses the rapid expansion and phase transition of pressurized liquefied $CO_2$ in vertical ducts. Results from small-scale experiments in three test setups (A, B, and C) were compared with a Rankine-Hugoniot model that treats the phase transition as an adiabatic evaporation wave of constant thickness. The model calculates the fluid properties behind the evaporation wave. The motivation was to quantify hazards and energy-release in tank explosions such as a boiling liquid expanding vapor explosion. Table 4-3 presents the initial conditions, measured, and calculated properties. The pressures at state 0 (saturated liquid), at state 1 (metastable liquid), at state 2 (two-phase equilibrium), and the evaporation wave velocity ($W_{EW}$) were measured.

### 4.3.2 Results

**Table 4-3: Initial conditions, measured properties, and calculated properties. The table shows results reproduced from tests TR1-TR4 in paper C.**

| | State | Symbol | Unit | Test 1 Setup A | Test 2 Setup A | Test 3 Setup B | Test 4 Setup C |
|---|---|---|---|---|---|---|---|
| **Measured properties** | | | | | | | |
| Pressure | *0* | $P_0$ | MPa | 5.84 | 6.27 | 5.70 | 3.40 |
| | *1* | $P_1$ | MPa | 5.05 | 5.60 | 4.90 | 2.00 |
| | *2* | $P_2$ | MPa | 3.6-3.8 | 4.15 | 3.5 | 1.2-1.4 |
| Velocity | *1* | $W_{EW,m}$ | $ms^{-1}$ | 35-40 | 42.4 | 32 | ~ 10* |
| **Calculated properties** | | | | | | | |
| Pressure | *2* | $P_2$ | MPa | 3.74 | 4.27 | 3.64 | 1.29 |
| Temperature | *0* | $T_0$ | K | 294.0 | 297.0 | 292.9 | 272.2 |
| | *1* | $T_1$ | K | 292.5 | 295.5 | 291.5 | 270.9 |
| | *2* | $T_2$ | K | 275.9 | 281.0 | 274.9 | 240.2 |
| Density | *0* | $\rho_0$ | $kgm^{-3}$ | 764.4 | 726.6 | 775.6 | 932.5 |
| | *1* | $\rho_1$ | $kgm^{-3}$ | 756.7 | 718.6 | 768.5 | 928.0 |
| | *2* | $\rho_2$ | $kgm^{-3}$ | 345.6 | 372.6 | 345.5 | 141.5 |
| Enthalpy | *0* | $h_0$ | $kJkg^{-1}$ | 258.7 | 270.2 | 255.2 | 197.3 |
| | *1* | $h_1$ | $kJkg^{-1}$ | 257.6 | 269.3 | 254.1 | 195.9 |
| | *2* | $h_2$ | $kJkg^{-1}$ | 254.9 | 266.6 | 251.5 | 193.0 |
| Velocity | *0* | $W_{Bulk}$ | $ms^{-1}$ | 3.3 | 3.2 | 3.1 | 2.6 |
| | *1* | $W_{EW,c}$ | $ms^{-1}$ | *35* | *41.4* | 33.4 | 9.1 |
| | *1* | $u_1$ | $ms^{-1}$ | 38.1 | 44.6 | 36.5 | 11.7 |
| | *2* | $u_2$ | $ms^{-1}$ | 83.5 | 86.1 | 81.2 | 76.9 |
| Vapor mass fraction | *2* | $\chi_2$ | - | 0.217 | 0.227 | 0.209 | 0.213 |
| Mass flux | | | $kgm^{-2}s^{-1}$ | 28 855 | 32 066 | 28 073 | 10 877 |
| **Deviation (Meas-Calc)** | | | | | | | |
| Pressure difference | *2* | $\Delta P_{2,dev}$ | MPa | *0.1* | *0.12* | *0.14* | *0.1* |
| Velocity difference | *1* | $\Delta W_{EW,dev}$ | $ms^{-1}$ | *< 5* | *1.0* | *1.4* | *~ 1.0* |

* *In the order of*

The Rankine-Hugoniot jump condition model produced the calculated properties.

The available superheat energy caused by the rapid depressurization resulted in a calculated vapor mass fraction $\chi_2$ in the range 0.21 - 0.23 at state 2.

Upon diaphragm rupture, a shock wave propagated outward from the opening (not visible in Figure 4.8). At the same time, a rarefaction wave propagated downward through the vessel. A series of schlieren images (Figure 4.8b) captured the expansion wave that propagated at the speed of sound (typically 300 - 360 $ms^{-1}$) through the liquid phase. A jet of partially condensed $CO_2$ vapor followed the shock wave. Figure 4.8a shows the jet that propagated with an initial velocity of about 190 $ms^{-1}$.

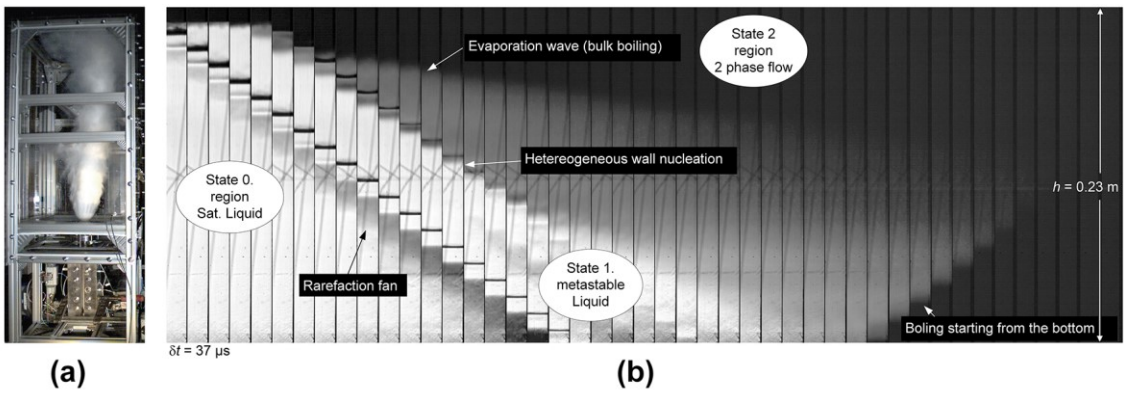


**Figure 4.8: High-speed images that originated from tests with setup B. (a) $CO_2$ jet from the high-pressure vessel. (b) Image-series from the schlieren setup that shows 1.5 ms of the rapid expansion and boiling process inside the vertical duct.**

A contact surface that initially separated the liquid phase and the vapor headspace accelerated toward the high-pressure vessel exit plane (not visible in Figure 4.8). Because of the 0.7 - 0.9 MPa pressure reduction across the rarefaction fan, the liquid became superheated. After an induction time, rapid boiling started at the liquid/vapor interphase and continued downward into the superheated liquid. Heterogeneous nucleation propagated at a velocity of 240 - 260 $ms^{-1}$ downward at the glass window surface. The wall nucleation that occurred in front of the evaporation wave limited the degree of superheat in the current test setup. The rarefaction wave induced an upward flow on the liquid bulk that started to flow with a velocity $W_{Bulk}$ of about 3-5 $ms^{-1}$. An evaporation wave propagated downward from the liquid/vapor interphase with a velocity $W_{EW}$ of about 32-42 $ms^{-1}$.

### Rankine-Hugoniot analysis versus experimental results

Figures 4.9-4.11 shows results from the Rankine-Hugoniot analysis and the experimental pressure histories in tests 1, 3 and 4. The three test setups (A, B and C) offered a range of initial conditions.

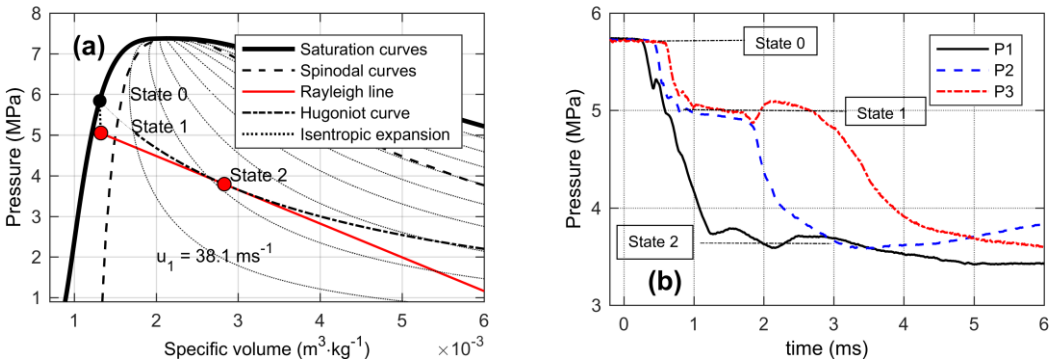


**Figure 4.9: (a) calculated state data; (b) experimental results from Test1, setup A.**

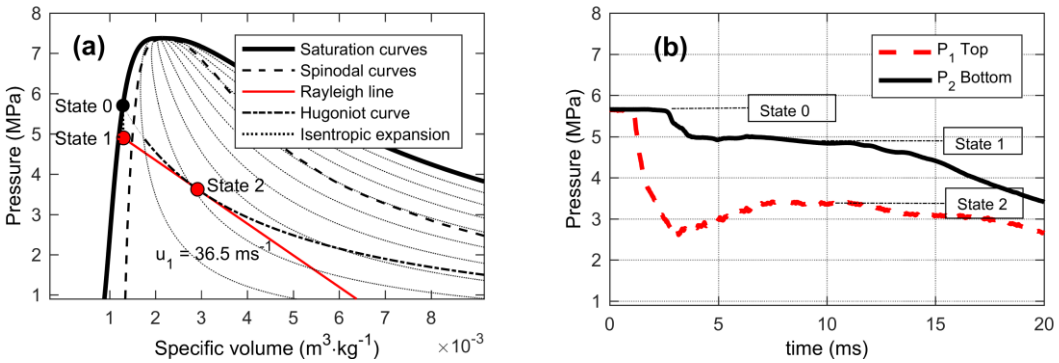


**Figure 4.10: (a) calculated state data; (b) experimental results from Test3, setup B.**

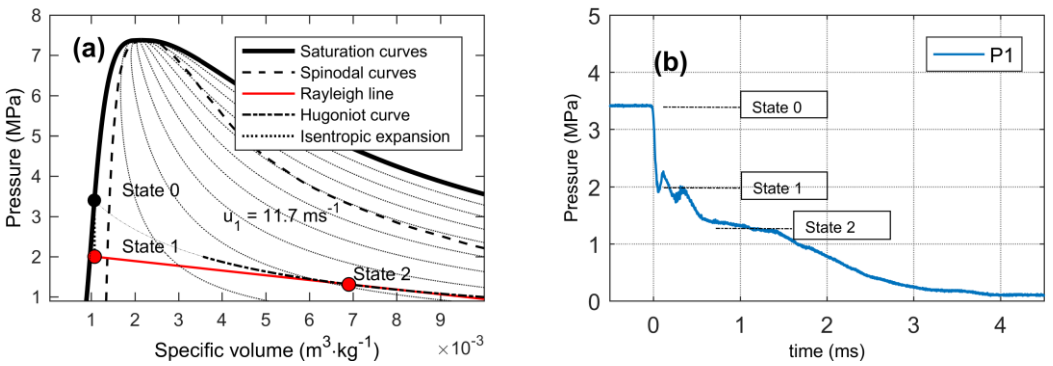


**Figure 4.11: (a) calculated state data; (b) experimental results from Test4, setup C.**

The results suggested that the Rankine Hugoniout relations could be used to model the rapid boiling of $CO_2$ as an evaporation wave.

**Chapman Jouguet (CJ) solutions**

Figure 4.12 shows calculated properties ahead of, and behind the evaporation wave. The plots show results from the Rankine-Hugoniot calculations that satisfy the CJ-solution for a range of pre-rupture pressures $P_0$ and superheat pressure drop ($P_0$-$P_1$).

The plots in Figure 4.12 provide calculation results that can be used in simple flow and state predictions. For example, if saturated liquefied $CO_2$ at 5.5 MPa expands to a superheated state at 4.0 MPa in a rapid isentropic process, the calculated evaporation wave velocity is approximately 27 $ms^{-1}$ (Figure 4.12a). The pressure drop across the evaporation wave accelerates the flow to a velocity of ~ 90 $ms^{-1}$ relative to the wave (Figure 4.12b). The expansion across the wave decreases the density from ~ 790 to 230 $kgm^{-3}$ (Figure 4.12c and d). Figure 4.12e shows that the calculated pressure behind the wave is ~ 2.7 MPa. The calculated vapor mass fraction behind of the wave is ~ 0.26 (Figure 4.12f).

It is important to note that these calculations do not guarantee that the phase transition will occur as an evaporation wave in reality. The calculations solve the conservation equations at idealized, stationary conditions. The influence of heterogeneous nucleation is restricted to determine the superheat pressure ($P_1$). Homogeneous nucleation close to the superheat limit, which Reid (1979, 1980) proposed as the primary trigger for a BLEVE, is not considered here.

It is proposed that the calculated vapor mass fraction $\chi_2$ from the Rankine-Hugoniot analysis can be used to estimate the mechanical energy released in a tank explosion.

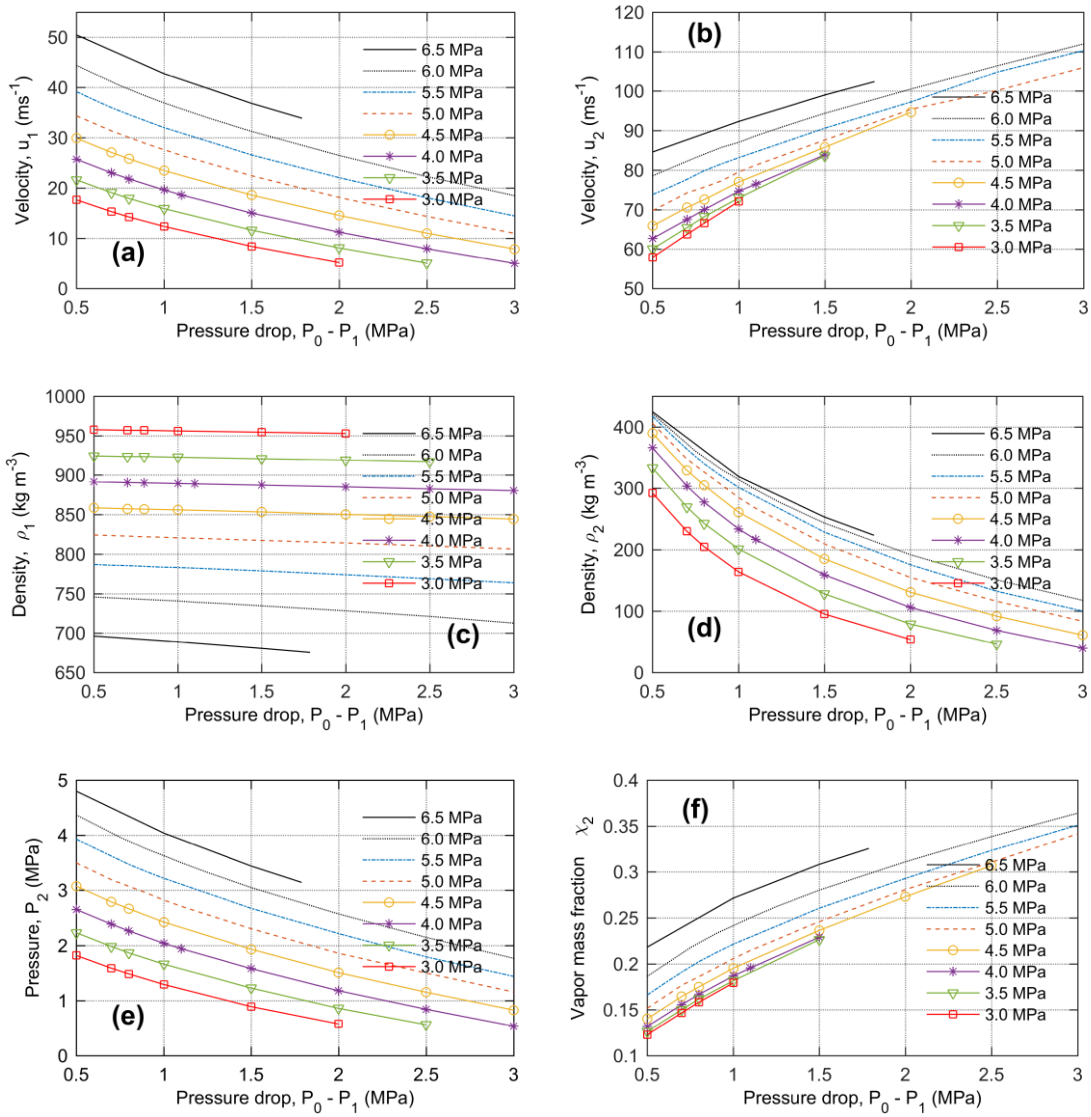


**Figure 4.12: Calculated CJ-solutions from the Rankine-Hugoniot analysis. Each line represents an initial pre-rupture pressure P0. Six properties were plotted as a function of the superheat pressure drop $P_0$ - $P_1$. (a) velocity $u_1$. (b) velocity $u_2$. (c) density $\rho_1$. (d) density $\rho_2$. (e) pressure $P_2$. (f) vapor mass fraction $\chi_2$.**

The method proposed by Prugh (1991), which calculates the isentropic expansion of an ideal gas at constant specific heat ratio, is the starting point of the present calculation. Figure 4.13 shows results from a calculation example with a 1-$m^3$ storage tank filled with pressurized liquefied $CO_2$. The liquid volume fraction was 85%, and the pre-rupture pressure was $P_0$ = 5.5 MPa.

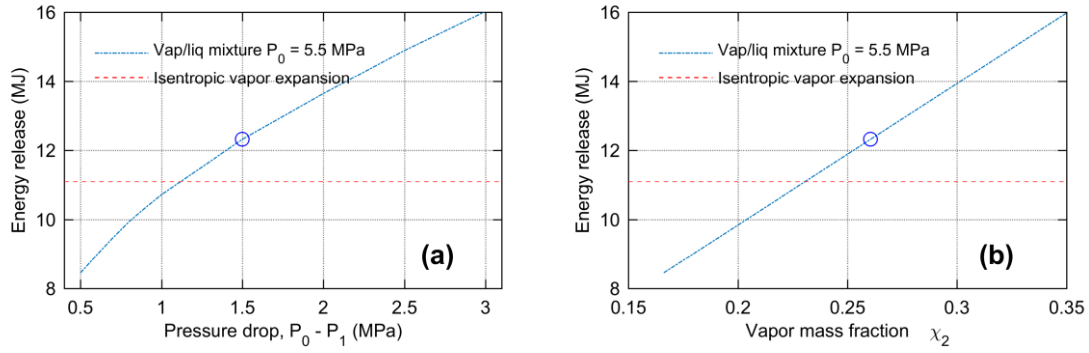


**Figure 4.13: The estimated mechanical energy released in an explosion of a vessel with a tank volume $V_T$ = 1 m$^3$ as a function of the superheat pressure drop. (a) Energy release as a function of the superheat pressure drop. (b) Energy-release as a function of the vapor mass fraction $\chi_2$.**

The calculated mechanical energy-release was 12.4 MJ. In comparison, isentropic expansion of a pure vapor produced an estimate of 11.1 MJ. The calculated vapor mass fractions $\chi_2$ had to be higher than 0.229 to produce total vapor volumes $V^*$ larger than the volume calculated from a pure vapor expansion.

### 4.3.3 Conclusion

Paper C investigated the rapid expansion and phase transition of carbon dioxide ($CO_2$) in vertical ducts. The motivation was to quantify damage potential in scenarios such as $CO_2$ tank explosions. Results from small-scale experiments were compared with calculations from a Rankine-Hugoniot analysis. The Rankine-Hugoniot relations modeled the phase transition as an evaporation wave and calculated the fluid properties behind the wave. The model showed a good qualitative agreement with the experimental results that were sampled from three separate test setups. The measured evaporation wave velocities were 32 – 42 ms$^{-1}$ (setup A and B), and ~ 10 ms$^{-1}$ (setup C). The experimental results seemed to correspond with a Chapman Jouguet solution. At a specific CJ solution, the required model inputs were the initial pre-rupture pressure and the pressure of the metastable liquid ahead of the evaporation wave. Typically, the estimated vapor mass fraction behind the evaporation wave was in the range from 0.21 to 0.23. The paper presents a strategy to predict the energy released in a tank explosion based on the calculated vapor mass fraction behind the evaporation wave.

# 5 Discussion

The findings in the thesis provide a new set of results on the behavior of pressurized liquefied $CO_2$ expanded from a saturated state to atmospheric pressure. The phase transitions in the current study were too slow to produce a shock wave. Pressure histories from the experiments suggested that expansion of the vapor head-space governed the initial shock strength. The test results were compared with simulations of a pressurized $CO_2$ vapor released from a high-pressure reservoir into an atmospheric vented chamber. A plausible explanation for these findings was a small vapor mass fraction behind the evaporation wave. The estimated values were $\chi_2 \approx 0.2$. These findings support the observations published by Birk et al. (2007, 2018) that stated: *"the liquid energy content did not contribute to the shock overpressures. The lead shock was primarily generated by the vapor space".* However, the observations in the current study do not rule out that rapid evaporation can produce a shock in other situations.

Test results from the current study showed a limited degree of superheat. Heterogeneous wall nucleation ahead of the evaporation wave prevented a further pressure reduction. The Rankine-Hugoniot model was used to describe the behavior of the evaporation wave. The evaporation wave represents a different phase change mode compared to homogeneous nucleation that is expected to occur close to the spinodal. The pressure histories show that homogeneous nucleation did probably not take place in the current test series. The wall nucleation propagated as a front ahead of the evaporation wave at a velocity of 240 - 260 $ms^{-1}$. The time series in Figure 5.1 shows that the bubble growth was rapid ($t_{bubble\ growth} < 1$ ms), and that the average bubble size was small. The diameter increased from < 5µm to about 60 µm in less than 1 ms. A rough estimate of the number of nucleation sites based on the images in Figure 5.1 suggested 300-500 bubbles per $mm^2$. These images were captured with a high magnification lens from Navatar. The wall effects in the small-scale setups influenced outcomes from the current study. Polycarbonate does not offer a sufficiently smooth surface for homogeneous nucleation to occur. Borosilicate glass would also require additional treatment to provide the necessary surface properties.

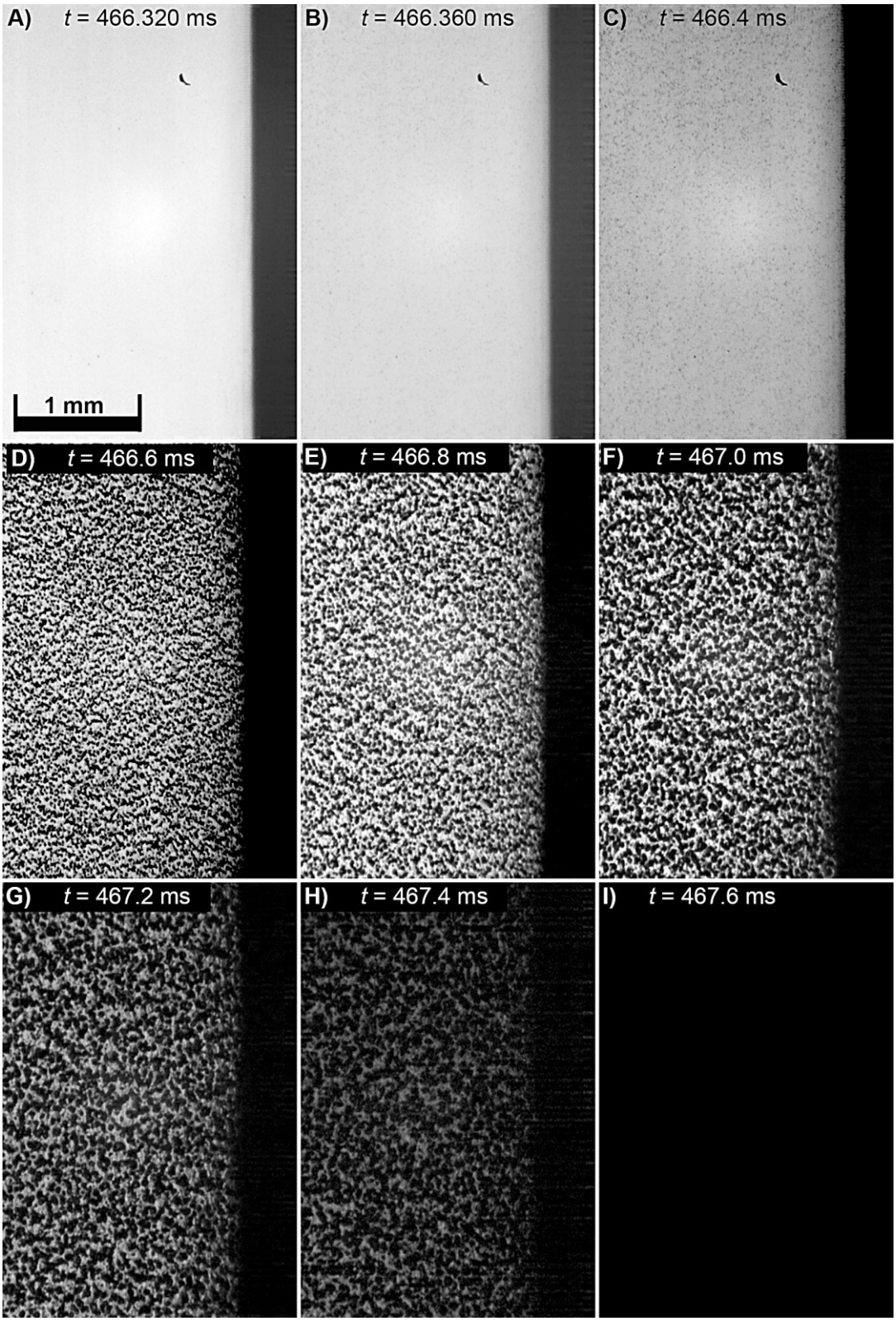


**Figure 5.1: Time series that shows heterogeneous bubble nucleation at the front glass. Image size: 2.3 × 3.4 mm. Backlit camera setup. The test was initiated at *t* = 0 ms.**

It would be of interest to reduce the wall-effects by an upscaling of the test setups. The upscaling would produce a higher volume/area ratio. The construction of a test setup that eliminates wall nucleation, which was successfully achieved by Fauske et al. (1974), Hill (1991), Simões-Moreira (1994) and Reinke (1997), represent an important objective in future studies.

Evaporation waves were observed, and the velocities were calculated. According to Simões-Moreira and Shepherd (1999)**,** it is expected that the velocity depends on both the initial state and the degree of superheat. These statements agree with the results from the Rankine-Hugoniot calculations in the current study. The Rankine-Hugoniot analysis calculated the properties behind the evaporation wave and provided simple phase transition rate estimates. These numerical results, which were verified by small-scale experiments, could be used as inputs to estimate the source terms in a phase transition model.

The one dimensional Rankine-Hugoniot calculation method described in the current study should be further developed and adapted to three-dimensional geometries. Such a model could predict the expansion in tank explosion scenarios such as a BLEVE. Angelo et al. (2005) discuss a generalization of the jump equations from one to three-dimensional scenarios.

The experimental results were approximated by a CJ solution of the Rankine-Hugoniot relations. The CJ-solution could imply chocked flow conditions in the two-phase mixture after the evaporation wave, relative to the wave. These findings do not exclude other solutions. Figure 5.2 shows Rankine-Hugoniot calculations with one pre-rupture pressure $P_0$ = 5.5 MPa and a range of $u_1$ velocities. Six parameters were plotted as a function of possible $u_1$ velocities in the range from zero up to the velocity at the CJ solution. Each line represents a different degree of superheat caused by the pressure drop $(P_0 - P_1)$.

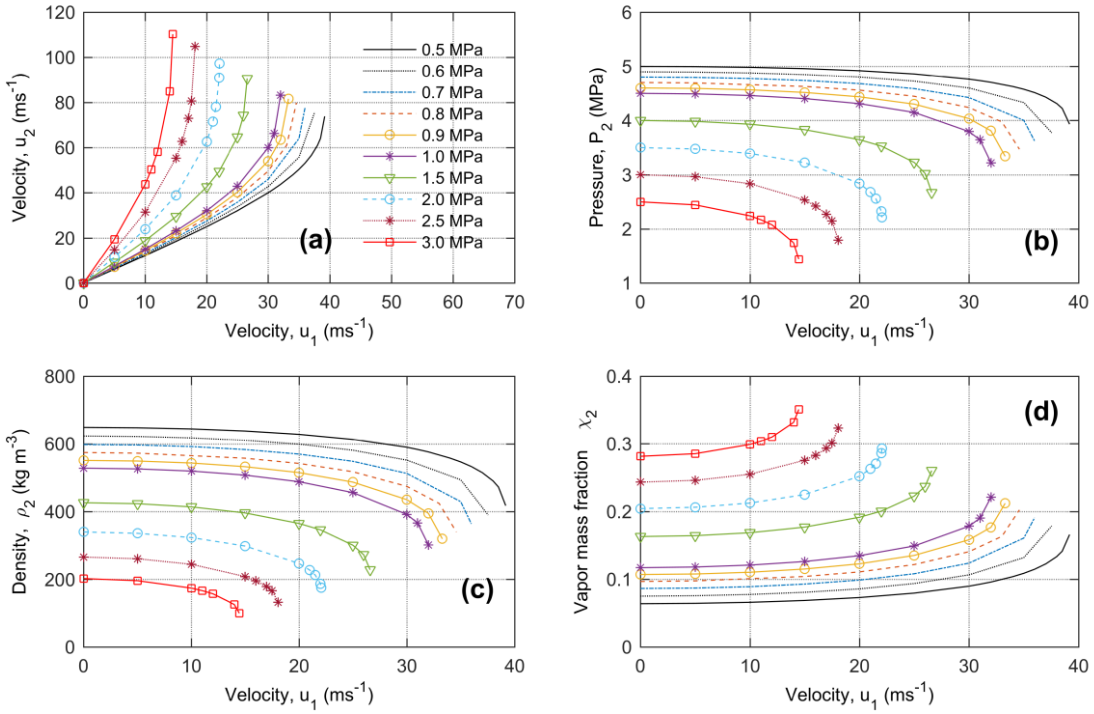


**Figure 5.2: Calculated R-H solutions with pre-rupture pressure $P_0$ = 5.5 MPa. Each line represents a ($P_0$ -$P_1$) superheat pressure drop. $u_1$ is varied from 0 up to the CJ-velocity.**

Changes in $u_1$ velocities result in larger changes in properties at state 2 as the CJ velocity.

These plots show the behavior of the Rankine-Hugoniot calculations that include both CJ solutions and non-CJ solutions. It is important to note that not all of these solutions are expected to be physically valid. For instance; the lower degrees of superheat would probably not result in CJ solutions. The validity range of the Rankine-Hugoniot model should be explored further in experimental investigations that include a broader range of test conditions.

# 6 Conclusions

This PhD thesis presented a study on the rapid depressurization and evaporation of pressurized liquefied $CO_2$ in vertical ducts. Experimental work and theoretical calculations were carried out to determine characteristic velocities and properties behind the evaporation wave as a function of the thermodynamic states ahead of the wave. The primary motivation was to quantify the damage potential in scenarios such as tank explosions of pressurized liquefied gas. Three journal papers, which include two accepted and one submitted manuscript, document the main results. Also, one co-authored paper points at an application of the findings that is input to numerical simulations of a $CO_2$ BLEVE. This chapter summarizes the contributions from the project and offers suggestions for future research work.

Main observations and conclusions

- Upon diaphragm rupture, a rarefaction wave propagated at the local speed of sound into the vapor headspace and the liquid phase. Wave reflections occurred at the liquid-vapor interphase and the bottom surface. These observations verify previous work. By Tosse et al. (2015).
- High-speed videos showed that an evaporation wave followed behind the rarefaction wave. These observations verify previous work.
- The calculated evaporation wave velocities were in the range 32-42 $ms^{-1}$.
- Heterogeneous nucleation occurred ahead of the evaporation wave. Neither the transparent polycarbonate tube nor the square-duct glass-window setup provided a sufficiently smooth surface to suppress nucleation and bubble growth at the surface.
- The evaporation front details were obscured by vapor-bubbles at the glass window.
- One test campaign focused on the blast from saturate $CO_2$ at room temperature (T = 292 ± K) released into an openly vented atmospheric chamber. The measured peak pressure was in the range 15 – 20 kPa.

- The rapid boiling did not contribute to the initial shock strength in the test geometry. The evaporation rate was too slow, and the velocity behind the evaporation wave seemed too low to create a shock wave. The heterogeneous wall nucleation seemed to limit the degree of superheat.
- The tests with a liquid/vapor mixture in the high-pressure reservoir showed a significantly higher impulse compared to the vapor-only tests. Reducing the vent area from 0.1 $m^2$ to 0.01 $m^2$ resulted in a slight increase in impulse calculated at 100 ms.
- An application of the experimental test results is to represent reference data that describe the interfacial flux source terms in phase transition models.
- A Rankine-Hugoniot analysis that modeled the phase transition as an evaporation wave calculated the fluid properties behind the wave. The model showed a good qualitative agreement with the experimental results that were sampled from three separate test setups.
- The experimental results seemed to correspond with a Chapman Jouguet solution. At a given CJ solution, the required model inputs were the initial pre-rupture pressure and the pressure of the metastable liquid ahead of the evaporation wave.
- Typically, the estimated vapor mass fraction behind the evaporation wave was in the range from 0.21 to 0.23. The somewhat limited vapor mass fraction could explain why the rapid evaporation investigations did not produce an observable shock wave.
- The thesis presents a strategy, which includes the calculated vapor mass fraction, to predict the mechanical energy released in the rapid depressurization and evaporation processes. The vapor mass fraction is then used in the method presented by Prugh (1991).

## 6.1 Recommendations for future research

- Most studies prefer a higher degree of superheat and a nearly instantaneous release of liquid-phase $CO_2$ from the high-pressure reservoir. Placing the

diaphragm and outlet section at the bottom could make the vapor headspace act as a piston to push the liquid-phase $CO_2$ out through the reservoir exit plane. These modifications could improve the study on the effect of the rapid boiling on the blast wave pressure and calculated impulse.

- Further studies should include tests with a minimized vapor headspace and a liquid volume-fraction closer to 100%.
- Reducing the volume of the atmospheric chamber could be favorable when studying the effect of vent area on the measured pressure response. The possible generation of a shock wave would probably also require a high-pressure reservoir with a diverging/conical geometry.
- Further studies should extend the 1D Rankine-Hugoniot model to 3-D geometry. The modification would increase the relevance to realistic tank explosion scenarios.
- A high-pressure reservoir that has a cone-shaped cross-section could avoid choking conditions in the test setup. Increased the expansion and the degree of superheat could promote the generation of shock waves.
- Future studies should reduce the influence of wall effects. It would be of interest to implement the necessary precautions that eliminate heterogeneous nucleation ahead of the evaporation wave.

# References

Abbasi, T. and Abbasi, S. A. (2007) 'The boiling liquid expanding vapour explosion (BLEVE): Mechanism, consequence assessment, management', Journal of Hazardous Materials, 141(3), pp. 489-519.

Abbasi, T. and Abbasi, S. A. (2007) 'Accidental risk of superheated liquids and a framework for predicting the superheat limit', Journal of Loss Prevention in the Process Industries, 20(2), pp. 165-181.

Abbasi, T. and Abbasi, S. A. (2008) 'The boiling liquid expanding vapour explosion (BLEVE) is fifty … and lives on!', Journal of Loss Prevention in the Process Industries, 21(4), pp. 485-487.

Angelo, E., Simões Moreira, J. R. and Barrios, D. B. (2005) 'Theory and occurrence of evaporation waves', Proceedings of COBEM 2005, 18th International Congress of Mechanical Engineering, Ouro Preto, MG.

Armstrong, G. M. (2004) 'The mystery of the BLEVE', Journal of Failure Analysis and Prevention, 4(1), pp. 6-7.

Avdeev, A. A. (2016) 'Theory of Boiling Shock', Bubble Systems. Cham: Springer International Publishing, pp. 265-327.

Avedisian, C. T. (1985) 'The Homogeneous Nucleation Limits of Liquids', Journal of Physical and Chemical Reference Data, 14(3), pp. 695-729.

Barbone, R. (1994), ´Explosive boiling of a depressurized volatile liquid´, MSc thesis, McGill University, Montreal, Quebec, Canada.

Barbone, R., Frost, D. L., Makris, A. and Nerenberg, J. (1995) 'Explosive Boiling of a Depressurized Volatile Liquid', in Morioka, S. & Van Wijngaarden, L. (eds.) IUTAM Symposium on Waves in Liquid/Gas and Liquid/Vapour Two-Phase Systems: Proceedings of the IUTAM Symposium held in Kyoto, Japan, 9–13 May 1994. Dordrecht: Springer Netherlands, pp. 315-324.

Birk, A. M., Davison, C. and Cunningham, M. (2007) 'Blast overpressures from medium scale BLEVE tests', Journal of Loss Prevention in the Process Industries, 20(3), pp. 194-206.

Birk, A. M., Heymes, F., Eyssette, R., Lauret, P., Aprin, L. and Slangen, P. (2018). ´Near-field BLEVE overpressure effects: The shock start model´, Process Safety and Environmental Protection, 116, pp. 727-736.

Bjerketvedt, D., Egeberg, K., Ke, W., Gaathaug, A., Vaagsaether, K. and Nilsen, S. H. (2011) 'Boiling liquid expanding vapour explosion in $CO_2$ small scale experiments', Energy Procedia, 4, pp. 2285-2292.

Casal, J., Arnaldos, J., Montiel, H., Planas-Cuchi, E. and Vilchez, J. A. (2001) 'Modelling and understanding BLEVEs'. In: FINGAS, M. (ed.) Handbook of Hazardous Spills. New York: McGraw Hill.

CCPS, (1994) 'Guidelines for evaluating the characteristics of vapor cloud explosions, flash fires, and BLEVEs' New York, NY: Center for Chemical Process Safety of the American Institute of Chemical Engineers.

Chaves, H. (1984) ´Phasenübergänge und wellen bei der entspannung von fluiden hoher spezifischer wärme´ PhD thesis, Georg-August-Universität, Göttingen,

Chaves, H., Lang, H., Meier, G. E. A. and Speckmann, H. D. (1985) 'Adiabatic phase transitions and wavesplitting in fluids of high specific heat', in Meier, G.E.A. & Obermeier, F. (eds.) Flow of Real Fluids. Berlin, Heidelberg: Springer Berlin Heidelberg, pp. 115-124.

Chiccarelli, G., Melguizo-Gavilanes, J. and Shepherd, J. E. (2017) 'Pressure-field Produced by the Rapid Vaporization of a $CO_2$ Liquid Column', Proceedings of the 30th International Symposium on Shock Waves, Tel-Aviv, Japan. Springer International publishing, pp. 1293-1297.

Clayton, W. E. and Griffin, M. L. (1994) 'Catastrophic failure of a liquid carbon dioxide storage vessel', Process Safety Progress 4(13), pp. 202-209.

Clifford, A. A. (2008) 'BLEVE: Theory and Importance in Oil Recovery', The open Thermodynamics Journal, 2, pp. 89-94.

Das, P. K., Bhat, G. S. and Arakeri, V. H. (1987) 'Investigations on the propagation of free surface boiling in a vertical superheated liquid column', International Journal of Heat and Mass Transfer, 30(4), pp. 631-638.

Debenedetti, P. G. (1996) ´Metastable Liquids: Concepts and Principles´. Princeton University Press.

Eckhoff, R. K. (2014) 'Boiling liquid expanding vapour explosions (BLEVEs): A brief review', Journal of Loss Prevention in the Process Industries, 32, pp. 30-43.

Frost, D. L. (1985) ´Effects of ambient pressure on the instability of a liquid boiling explosively at the superheat limit´, PhD thesis, California institute of technology, Pasadena, California.

Frost, D. L. (1988) 'Dynamics of explosive boiling of a droplet', The Physics of Fluids, 31(9), pp. 2554-2561.

Frost, D. L., Lee, J. H. S. and Ciccarelli, G. (1991) 'The use of Hugoniot analysis for the propagation of vapor explosion waves', Shock Waves, 1(2), pp. 99-110.

Frost, D. L. and Sturtevant, B. (1986) 'Effects of Ambient Pressure on the Instability of a Liquid Boiling Explosively at the Superheat Limit', Journal of Heat Transfer, 108(2), pp. 418-424.

Gibbs, J. W. (1875-1876 and 1877-1878) On the Equilibrium of Heterogeneous Substances. Transactions of the Connecticut Academy, III, pp. 108-248 (Oct. 1875-May 1876), and pp. 343-524 (May 1877 - July 1878).

Gibbs, J. W. (1961) The scientific papers of J. Willard Gibbs, PhD, LL.D. I. Thermodynamics, pp 219-331. Dover Publications. New York.

Giljarhus, K. E. T., Munkejord, S. T. and Skaugen, G. (2012) 'Solution of the Span–Wagner Equation of State Using a Density–Energy State Function for Fluid-Dynamic Simulation of Carbon Dioxide', Industrial & Engineering Chemistry Research, 51(2), pp. 1006-1014.

Gromles, M. A. and Fauske, H. K. (1974) 'Axial propagation of free surface boiling into superheated liquids in vertical tubes'. Fifth International Heat Transfer Conference, Tokyo, The heat transfer society of Japan, pp. 30-34.

Hahne, E. and Barthau, G. (2000) 'Evaporation waves in flashing processes', International Journal of Multiphase Flow, 26(4), pp. 531-547.

Hansen, P. M., Gaathaug, A. V., Bjerketvedt, D. and Vaagsaether, K. (2016) 'Phase transition rate in rapid boiling of $CO_2$'. In Proceedings of the Eighth International Seminar on Fire and Explosion Hazards, Hefei, China, University of Science and Technology of China Press, pp. 547-557.

Hansen, P. M., Gaathaug, A. V., Bjerketvedt, D. and Vaagsaether, K. (2017) 'The behavior of pressurized liquefied $CO_2$ in a vertical tube after venting through the top', International Journal of Heat and Mass Transfer, 108, Part B, pp. 2011-2020.

Hansen, P. M., Gaathaug, A. V., Bjerketvedt, D. and Vaagsaether, K. (2018) 'Blast from pressurized carbon dioxide released into a vented atmospheric chamber', Shock Waves. doi: 10.1007/s00193-018-0819-z

Hemmatian, B. (2016) 'Contribution to the study of boiling liquid expanding vapor explosions and their mechanical effects´, PhD thesis, Universitat Politècnica de Catalunya, Barcelona, Catalonia, Spain

Hemmatian, B., Casal, J and Planas, E. (2017) 'Comparative analysis of BLEVE mechanical energy and overpressure modelling´, Process Safety and Environmental Protection, 106, pp.138-149.

Hemmatian, B., Planas, E. and Casal, J. (2017) 'Comparative analysis of BLEVE mechanical energy and overpressure modelling´, Process Safety and Environmental Protection, 106, pp.138-149.

Hill, L. G. (1991) An experimental study of evaporation waves in a superheated liquid. PhD thesis, California Institute of Technology, Pasadena, California.

Hill, L. G. and Sturtevant, B. (1990) 'An Experimental Study of Evaporation Waves in a Superheated Liquid', in Meier, G.E.A. & Thompson, P.A. (eds.) Adiabatic Waves in Liquid-Vapor Systems: IUTAM Symposium Göttingen, 28.8.–1.9.1989. Berlin, Heidelberg: Springer Berlin Heidelberg, pp. 25-37.

Häcker, R. (2014) 'Failure of a pressure vessel for rail transport of fluid carbon dioxide', Engineering Failure Analysis, 43, pp. 92-106.

Ibarreta, A., Biteau, H. and Sutula, J. (2016) 'BLEVES and Fireballs', in Hurley, M.J., Gottuk, D.T., Hall Jr, J.R., Harada, K., Kuligowski, E.D., Puchovsky, M., Torero, J.L., Watts Jr, J.M. & Wieczorek, C.J. (eds.) SFPE Handbook of Fire Protection Engineering. New York, NY: Springer New York, pp. 2792-2816.

Ke, W. (2009) ´$CO_2$ BLEVE (Boiling Liquid Expanding Vapor Explosion)´. MSc thesis, Telemark University College, Norway.

Kim-E, M. (1981) ´The possible consequences of rapidly depressurizing a fluid´, MSc thesis, Massachusetts Institute of Technology, Massachusetts Institute of Technology, Cambridge, Massachusetts.

Kim-E, M. and Reid, R. C. (1983) 'The rapid depressurization of hot high pressure liquids or supercritical fluids', In Chemical engineering at supercritical fluid conditions, Paulantis, M.E., Penninger, J.M.L., Gray, R.D., Jr & Davidson, P. (eds.), chapter 3, Ann Arbor Science, pp. 81-100.

Kraska, T. (2004) 'Stability Limits of Pure Substances: An Investigation Based on Equations of State', Industrial & Engineering Chemistry Research, 43(19), pp. 6213-6221.

Kuznetsov, V. V., Kozulin, I. A. and Vitovsky, O. V. (2012) 'Experimental investigation of adiabatic evaporation waves in superheated refrigerants', Journal of Engineering Thermophysics, 21(2), pp. 136-143.

Kuznetsov, V. V., and Vitovskii, O. V. (2007) 'Evaporation waves in a metastable single-component liquid', Journal of Engineering Thermophysics, 16(3), pp. 169-174.

Laboureur, D., Birk, A. M., Buchlin, J. M., Rambaud, P., Aprin, L., Heymes, F. and Osmont, A. (2015) 'A closer look at BLEVE overpressure', Process Safety and Environmental Protection, 95, pp. 159-171.

Labuntsov, D. A., and Avdeev, A. A. (1981) 'Theory of boiling discontinuity', Teplophizika Vysokikh Temperatur, 19(3), pp. 552-556.

Le Métayer, O., Massoni, J., and Saurel, R. (2005) 'Modelling evaporation fronts with reactive Riemann solvers', Journal of Computational Physics, 205(2), pp. 567-610.

Lemmon E. W., McLinden W. O., and Friend D.G., ´Thermophysical Properties of Fluid Systems´ in NIST Chemistry WebBook, NIST Standard Reference Database Number 69, P.J. Linstrom and W.G. Mallard (Eds.), National Institute of Standards and Technology, Gaithersburg MD, 20899, doi:10.18434/T4D303, (accessed 3 January 2018).

Li, M. z., Huang, Q., Liu, Z. y., and Zhao, Y. (2016) 'Experimental study on solid $CO_2$ BLEVE based on the superheat limit theory'. 2016 Annual Reliability and Maintainability Symposium (RAMS), 25-28 Jan. 2016, 1-7.

Li, M., Liu, Z., Zhou, Y., Zhao, Y., Li, X. and Zhang, D. (2018) 'A small-scale experimental study on the initial burst and the heterogeneous evolution process before $CO_2$ BLEVE', Journal of Hazardous Materials, 342(Supplement C), pp. 634-642.

McCann, H., Clarke, L. J. and Masters, A. P. (1989) 'An experimental study of vapour growth at the superheat limit temperature', International Journal of Heat and Mass Transfer, 32(6), pp. 1077-1093.

McCulloch, S, Keeling, S., Malischek, R, Stanley, T. (2016) '20 years of carbon capture and storage; accelerating future developments', Report prepared by the CCS unit of the International Energy Agency (IEA), (online), Available from:https://webstore.iea.org/20-years-of-carbon-capture-and-storage/ , (accessed 12th April 2018).

McDevitt, C. A., Chan, C. K., Steward, F. R. and Tennankore, K. N. (1990) 'Initiation step of boiling liquid expanding vapour explosions', Journal of Hazardous Materials, 25(1–2), pp. 169-180.

Mishra, K. B. (2016) 'Multiple BLEVE's and fireballs of gas bottles: Case of a Russian road carrier accident', Journal of Loss Prevention in the Process Industries, 41, pp. 60-67.

Moore, G. R. (1956) ´Vaporization of superheated drops in liquids´, PhD thesis, University of Wisconsin, Madison, Wisconsin.

Moore, G. R. (1959) 'Vaporization of superheated drops in liquids', AIChE Journal, 5(4), pp. 458-466.

Munkejord, S. T., Hammer, M. and Løvseth, S. W. (2016) '$CO_2$ transport: Data and models – A review', Applied Energy, 169, pp. 499-523.

Nguyen, V. T., Furzeland, R. M. and Ijpelaar, M. J. M. (1988) 'Rapid evaporation at the superheat limit', International Journal of Heat and Mass Transfer, 31(8), pp. 1687-1700.

Oxtoby, D. W. (1992) 'Homogeneous nucleation: theory and experiment', Journal of Physics: Condensed Matter, 4(38), pp. 7627.

Park, H.-C., Byun, K.-T., and Kwak, H.-Y. (2005) 'Explosive boiling of liquid droplets at their superheat limits', Chemical Engineering Science, 60(7), pp. 1809-1821.

Pettersen, J. (2002) ' Experimental study on boiling liquid expansion in a $CO_2$ vessel', 5th IIR Gustav Lorentzen Conference on Natural Working Fluids, Guangzhou, China, September 2002

Pinhasi, G. A., Ullmann, A., and Dayan, A. (2007) '1D plane numerical model for boiling liquid expanding vapor explosion (BLEVE)', International Journal of Heat and Mass Transfer, 50(23–24), pp. 4780-4795.

Planas, E., Pastor, E., Casal, J. and Bonilla, J. M. (2015) 'Analysis of the boiling liquid expanding vapor explosion (BLEVE) of a liquefied natural gas road tanker: The Zarzalico accident', Journal of Loss Prevention in the Process Industries, 34, pp. 127-138.

Planas-Cuchi, E., Gasulla, N., Ventosa, A. and Casal, J. (2004) 'Explosion of a road tanker containing liquified natural gas', Journal of Loss Prevention in the Process Industries, 17(4), pp. 315-321.

Planas-Cuchi, E., Salla, J. M. and Casal, J. (2004) 'Calculating overpressure from BLEVE explosions', Journal of Loss Prevention in the Process Industries, 17(6), pp. 431-436.

Prugh, R. W. (1991) 'Quantitative Evaluation of "Bleve" Hazards', Journal of Fire Protection Engineering, 3(1), pp. 9-24.

Reid, R. C. (1976) 'Superheated liquids', American Scientist, 64(2), pp. 146-156.

Reid, R. C. (1978a) 'Superheated liquids a laboratory curiosity and, possibly, an industrial curse. Part 1: Laboratory studies and theory ', Chemical Engineering Education, 12(2), pp. 60-69.

Reid, R. C. (1978b) 'Superheated liquids: a laboratory curiosity, and possibly, an industrial curse. Part 2: Industrial vapor explosions.', Chemical Engineering Education, 12(3), pp. 108-114.

Reid, R. C. (1978c) 'Superheated liquids: a laboratory curiosity, and possibly, an industrial curse. Part 3: Discussion and conclusions.', Chemical Engineering Education, 12(9), pp. 194-202.

Reid, R. C. (1979) 'Possible mechanism for pressurized-liquid tank explosions or BLEVE's', Science, 203(4386), pp. 1263-5.

Reid, R. C. (1980) 'Some theories on boiling liquid expanding vapour explosions', Fire, (March), pp. 525-526.

Reinke, P. (1997) ´Surface Boiling of Superheated Liquid´, PhD thesis, Energy Technique Institute, Zürich.

Reinke, P. and Yadigaroglu, G. (2001) 'Explosive vaporization of superheated liquids by boiling fronts', International Journal of Multiphase Flow, 27(9), pp. 1487-1516.

Salla, J. M., Demichela, M. and Casal, J. (2006) 'BLEVE: A new approach to the superheat limit temperature', Journal of Loss Prevention in the Process Industries, 19(6), pp. 690-700.

Saurel, R., and Abgrall, R. (1999) 'A Multiphase Godunov Method for Compressible Multifluid and Multiphase Flows', Journal of Computational Physics, 150(2), pp. 425-467.

Saurel, R., Petitpas, F., and Abgrall, R. (2008) 'Modelling phase transition in metastable liquids: application to cavitating and flashing flows', Journal of Fluid Mechanics, 607, pp. 313-350.

Settles, G. S. (2001) 'Schlieren and Shadowgraph Techniques: Visualizing Phenomena in transparent Media. Springer-Verlag Berlin Heidelberg New York GmbH & Co.

Shepherd, J. E. (1981) Rapid evaporation at the superheat limit. PhD thesis, Caltech Institute of Technology, Pasadena, California.

Shepherd, J. E., McCahan, S. and Cho, J. (1990) 'Evaporation Wave Model for Superheated Liquids', in Meier, G.E.A. & Thompson, P.A. (eds.) Adiabatic Waves in Liquid-Vapor Systems: IUTAM Symposium Göttingen, 28.8.–1.9.1989. Berlin, Heidelberg: Springer Berlin Heidelberg, pp. 3-12.

Shepherd, J. E., and Sturtevant, B. (1982) 'Rapid evaporation at the superheat limit', Journal of Fluid Mechanics, 121, pp. 379-402.

Simões-Moreira, J. R. (1994) ´Adiabatic evaporation waves´, PhD thesis, Rensselaer Polytechnic Institute, Troy, New York.

Simões–Moreira, J. R. and Shepherd, J. E. (1999) 'Evaporation waves in superheated dodecane', Journal of Fluid Mechanics, 382, pp. 63-86.

Simões-Moreira, J. R. (2000) 'Oblique evaporation waves', Shock Waves, 10(4), pp. 229-234.

Skripov, V. P. (1974) ´Metastable liquids´, Israel program for scientific translations, Jerusalem, J. Wiley, New York.

Skripov, P. V., and Skripov, A. P. (2010) 'The Phenomenon of Superheat of Liquids: In Memory of Vladimir P. Skripov', International Journal of Thermophysics, 31(4), pp. 816-830.

Span, R. and Wagner, W. (1996) 'A New Equation of State for Carbon Dioxide Covering the Fluid Region from the Triple-Point Temperature to 1100 K at Pressures up to 800 MPa', Journal of Physical and Chemical Reference Data, 25(6), pp. 1509-1596.

Span, R. and Wagner, W. (2003a) 'Equations of State for Technical Applications. I. Simultaneously Optimized Functional Forms for Nonpolar and Polar Fluids', International Journal of Thermophysics, 24(1), pp. 1-39.

Span, R. and Wagner, W. (2003b) 'Equations of State for Technical Applications. III. Results for Polar Fluids', International Journal of Thermophysics, 24(1), pp. 111-162.

Stawczyk, J. (2003) 'Experimental evaluation of LPG tank explosion hazards', Journal of Hazardous Materials, 96(2–3), pp. 189-200.

Stutz, B. and Simões-Moreira, J. R. (2013) 'Onset of boiling and propagating mechanisms in a highly superheated liquid - the role of evaporation waves', International Journal of Heat and Mass Transfer, 56(1–2), pp. 683-693.

Terner, E. (1962) 'Shock-Tube Experiments Involving Phase Changes', Industrial & Engineering Chemistry Process Design and Development, 1(2), pp. 84-86.

Thompson, P. A., Chaves, H., Meier, G. E. A., Kim, Y. G. and Speckmann, H. D. (1987) 'Wave splitting in a fluid of large heat capacity', Journal of Fluid Mechanics, 185, pp. 385-414.

Tosse, S., Vaagsaether, K. and Bjerketvedt, D. (2015) 'An experimental investigation of rapid boiling of $CO_2$', Shock Waves, 25(3), pp. 277-282.

Tosse, S., Hansen, P.M, Vaagsaether, K. (2016) ´ Modelling and Simulation of Phase Transition in Compressed Liquefied $CO_2$´, The 9th EUROSIM congress on modelling and simulation, Oulu, Finland September 2016.

Tosse, S. (2017) 'The rapid depressurization and evaporation of liquified carbon dioxide'. PhD thesis, University College of Southeast Norway, Norway.

Vaagsaether, K. (2010) 'Modelling of gas explosions' PhD thesis, Telemark University College / NTNU, Norway.

van den Berg, A. C., van der Voort, M. M., Weerheijm, J. and Versloot, N. H. A. (2004) 'Expansion-controlled evaporation: a safe approach to BLEVE blast', Journal of Loss Prevention in the Process Industries, 17(6), pp. 397-405.

van den Berg, A. C., van der Voort, M. M., Weerheijm, J. and Versloot, N. H. A. (2006) 'BLEVE blast by expansion-controlled evaporation', Process Safety Progress, 25(1), pp. 44-51.

van der Voort, M. M., van der Berg, A. C., Roekaerts, D. J. E. M., Xie, M. and de Bruijn, P. C. C. (2012) 'Blast from explosive evaporation of carbon dioxide: experiment, modeling, and physics', Shock Waves, 22, pp. 129-140.

van der Voort, M. M., van Wees, R. M. M., Ham, J. M., Spruijt, M. P. N., van den Berg, A. C., de Bruijn, P. C. J. and van Ierschot, P. G. A. (2013) 'An experimental study on the temperature dependence of $CO_2$ explosive evaporation', Journal of Loss Prevention in the Process Industries, 26(4), pp. 830-838.

Xie, M. (2013) ´Thermodynamic and gasdynamic aspects of a boiling liquid expanding vapour explosion´. Ph.D. thesis, Delft University of Technology, The Netherlands.

Yakush, S. E. (2016) 'Model for blast waves of Boiling Liquid Expanding Vapor Explosions', International Journal of Heat and Mass Transfer, 103, pp. 173-185.

Yu, C. M., and Venart, J. E. S. (1996) 'The boiling liquid collapsed bubble explosion (BLCBE): A preliminary model', Journal of Hazardous Materials, 46(2–3), pp. 197-213.

Zhang, Y., Schork, J. and Ludwig, K. 'Revisiting the Conditions for a $CO_2$ Tank Explosion'. AIChE Spring Meeting and Ninth Global Congress on Process Safety, San Antonio, Texas: Curran Associates, pp. 109-120.

# Appendix A. Setup C – PMMA tube

A previous study on small-scale BLEVEs included the construction of setup C. Ke (2009), and Bjerketvedt et al. (2011) published detailed information about the test setup and the experimental results. No experimental work was carried out on setup C as a part of the current thesis work. However, the apparatus is briefly described below because pressure histories from one previous test were compared with the pressures calculated by the Rankine-Hugoniot model.

The setup, which is illustrated in Fig. 1, used a transparent Polymethylmethacrylate (PMMA) plastic tube with length 100 mm and an inner diameter of 30 mm that was placed between two flanges. The test-cell volume was 70 $cm^3$. A gasket and an O-ring sealed the tube contents from the surroundings and prevented leakage. The small-scale BLEVE tests were conducted with liquid and solid phase $CO_2$ that was heated until the tube ruptured. The heating system consisted of a Beru GN 857 glow plug, which is commonly used in diesel engines, and a power supply. The internal pressure in the tube at the time of rupture was in the range between 3.3 - 4.2 MPa.

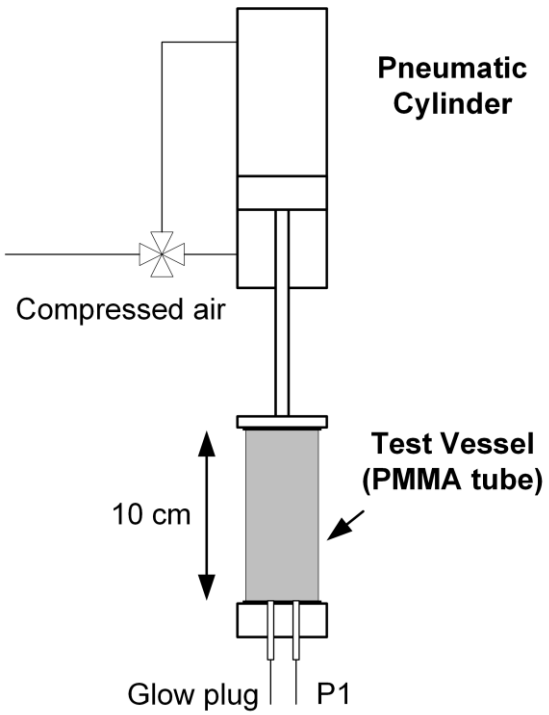


**Figure 1: A schematic that describes the main components in setup C.**

# Part II

# Published and submitted papers

# Paper A

# The behavior of pressurized liquefied $CO_2$ in a vertical tube after venting through the top

This paper is published in International Journal of Heat and Mass Transfer. Accepted 11 January 2017. https://doi.org/10.1016/j.ijheatmasstransfer.2017.01.035.

International Journal of Heat and Mass Transfer 108 (2017) 2011–2020

Contents lists available at ScienceDirect

International Journal of Heat and Mass Transfer

journal homepage: www.elsevier.com/locate/ijhmt

# The behavior of pressurized liquefied $CO_2$ in a vertical tube after venting through the top

Per Morten Hansen *, Andre Vagner Gaathaug, Dag Bjerketvedt, Knut Vaagsaether

*University College of Southeast Norway, Kjolnes Ring 56, 3918 Porsgrunn, Norway*

ARTICLE INFO

*Article history:*
Received 13 October 2016
Received in revised form 23 December 2016
Accepted 11 January 2017

*Keywords:*
BLEVE
Carbon dioxide
Phase transition rate
Evaporation waves

ABSTRACT

This paper presents results from small-scale experiments on the rapid phase transition of pressurized liquefied carbon dioxide in a vertical tube. The main motivation for the study was to provide reference data for the source terms in 1-D phase transition models. In addition a phase transition rate estimate and an energy estimate is presented. To initiate the test runs, a diaphragm was ruptured which led to the expansion toward atmospheric pressure and rapid boiling of the superheated liquid. The main contributions were the calculated front velocities and bulk flow velocities. Evaporation waves were observed, propagating with a velocity of 30 ± 0.5 m/s into the superheated liquid. The initial pre-rupture condition was saturated liquid at ambient temperatures (19–21 °C). The pressure reduction in the bottom during the boiling period was typically 8 bar (reduction from 56 to 48 barg). Due to the high pre-rupture pressure, the tube was made of polycarbonate. High speed images showed that the tube surface was not sufficiently smooth to suppress heterogeneous nucleation entirely. Consequently, the evaporation wave front was rather diffuse, mainly caused by upstream wall nucleation. This limited the degree of superheat, hence homogenous bulk nucleation was not observed. A contact surface between the vapor and vapor-liquid phases was observed, accelerating out of the tube with a velocity of 90 ± 5 m/s. A liquid layer front propagated with a constant velocity of 8.0 ± 0.1 m/s. Gas bubbles in the upstream liquid bulk moved with a constant velocity of about 5 m/s after passage of the rarefaction wave.



## 1. Introduction

Rapid phase transition of a pressurized liquefied gas due to a sudden rupture and depressurization of the confining container is a violent physical phenomenon of relevance in industrial safety assessments. Under certain conditions this phenomenon can be referred to as a boiling liquid expanding vapor explosion (BLEVE). Several definitions for a BLEVE exists. Birk et al. [1] proposed the following, which is used in the current publication: "*A BLEVE is the explosive release of expanding vapor and boiling liquid when a container holding a pressure liquefied gas fails catastrophically*". Although often associated with fireballs or dispersion of poisonous fumes, non-flammable substances such as water and carbon dioxide has also been involved in violent explosions initiated by rapid depressurization and boiling. Previous incidents, including a 2008 ship accident in Yuhang, China [2] and a 1988 accident at a process plant in Worms, Germany [3] demonstrate how $CO_2$ BLEVEs can result in human casualties and significant material damage. According to Zhang et al. [2], the transport ship in Yuhang, Hangzhou, carried 130 $m^3$ of liquid $CO_2$ at initial conditions of 23 bar and −15 °C. The ship was in dock when the $CO_2$ storage tank exploded, killing two workers and sinking two nearby ships carrying sulfuric acid and hydrogen peroxide. A brittle fracture and overfilling of the modified $CO_2$ tank were believed to be the causes of the accident. Modifications to the tank included work on the level indicator and locking of the relief valve [2]. The BLEVE is a safety hazard that must be considered when designing and operating process equipment for pressure liquefied $CO_2$, such as transportation lines and storage systems. It is important that the designers have sufficient knowledge of the BLEVE mechanism and potential consequences to reduce the risk of future incidents. Accurate modeling of the phase transitions and possible accidental dispersion is a part of the risk evaluation, and requires knowledge of the thermodynamic states and kinetics related to the phase transition.

The superheat limit theory proposed by Reid [4–6] has been the standard theory to explain what triggers a BLEVE. Reid suggested that a BLEVE is initiated by homogenous nucleation at the superheat limit with vapor bubbles being spontaneously formed within the bulk fluid. This theory and its validity has later been discussed by others [1,7–11]. In studies of metastable liquids close to the

* Corresponding author.
*E-mail address:* perha@usn.no (P.M. Hansen).

http://dx.doi.org/10.1016/j.ijheatmasstransfer.2017.01.035
0017-9310/

superheat limit, the evolving of steady evaporation waves have been observed propagating from the phase boundary into the superheated liquid phase [12–22].

This article presents results from small-scale experiments on the rapid depressurization and boiling of saturated carbon dioxide at room temperature. Tosse et al. [23] presented results from the same test rig and observed evaporation waves propagating at a near constant velocity of 20–30 m/s inside a half-filled transparent tube. The present paper continues the experimental work, with new contributions such as varied liquid content in the tube, a phase transition rate estimate and an energy estimate. The number of publications describing evaporation waves and rapid phase transition in carbon dioxide is limited, hence it is of interest to increase the number of experimental data available. The saturation pressure at room temperature is 55–57 barg, significantly higher than those of comparable studies performed with other substances, which excluded the use of glass tubes. Polycarbonate tubes are used in the current publication, with the potential risk of experiencing heterogeneous nucleation in the upstream metastable liquid. An objective is then to investigate if these plastic tubes offer both a sufficiently smooth surface and the necessary mechanical strength. The relevance of experimental data on $CO_2$ is high for safety assessments of process equipment used in carbon capture and storage technology. An application of these experimental results on $CO_2$ evaporative front propagation is to provide reference data for the source terms in a one-dimensional (1-D) phase transition model. Several such models currently exist, that are capable of predicting the blast wave pressure and dynamics in a BLEVE. The work of Pinhasi et al. [24] and Xie [25] serves as relevant references on the subject. Xie offers the most recent model among these two, with the stated ability to predict the onset of a BLEVE based on homogenous bubble nucleation. He build on the work of Pinhasi, with improvements such as a model for nucleation, and an improved thermodynamics basis. In addition, the work of Xie contains an extensive review of BLEVE related literature up to 2013. The current study is mostly restricted to fundamental phenomena occurring inside the tube. Effects imposed on the surroundings, such as blast waves, overpressure estimates, dynamic loads and acceleration of container fragments are essential parts of BLEVE studies, but will not be discussed here. Relevant references on these topics include the BLEVE review article of Abbasi and Abbasi [8], the work of Yakush [26], of Van der Voort et al. [27] and Chicarelli et al. [28]. Chicarelli et al. presented experimental results with rapid vaporization of $CO_2$ in a shock tube with a polycarbonate driver section and a stainless steel driven section. The experiments described in the current paper may not be considered as true BLEVEs according to the definition in [1], since the test rig does not shatter during the test runs. However, the fundamental depressurization and boiling mechanisms are believed to be transferable to a real BLEVE.

## 2. Experimental setup and test procedure

### 2.1. Apparatus

Fig. 1 shows a schematic diagram of the tube (a), a photograph of the experimental setup (b) and a high speed camera image of the tube filled with $CO_2$ (c). The test setup consisted of following main parts (1–8): (1) a Rexroth pneumatic plunger actuator with an arrow to puncture the diaphragm; (2) a diaphragm consisting of two layers of PET polymer film; (3) a vertically oriented transparent polycarbonate tube with a visible region 32 cm long, an inner diameter of 9 mm, and a wall thickness of 1.5 mm; (4) a relief valve to evacuate air and carefully raise the liquid $CO_2$ level inside the tube; (5) two Kulite XTM-190 piezo resistive pressure (P1 = top, P2 = bottom, spacing 43.5 cm); (6) an inlet valve to fill the rig from an external $CO_2$ cylinder; (7) an emergency valve to safely release the pressure and empty the test rig in case of malfunction of the actuator device; and (8) a temperature sensor mounted at the bottom flange to measure the initial temperature.

The liquid $CO_2$ was supplied from a 40 l industry grade cylinder with an internal riser pipe. A needle valve at the inlet and a pressure regulator at the outlet ensured controlled filling of the rig. A Quantum Composers 9500 series pulse generator was used to trigger the experiment, while the temperature and pressure measurements were saved using a HBM QuantumX MX410 data acquisition module. Upon diaphragm rupture, the contents of the pressurized tube was released to atmospheric pressure. The initial pre-rupture conditions were limited to ambient room temperature (19–21 °C), since the current experimental setup had no temperature control possibilities.

The transparent tube was made of polycarbonate. In most comparable studies, the standard material of choice is glass, due to the smooth surface providing an ability to suppress heterogeneous nucleation. Carbon dioxide stored at room temperature has a saturation pressure of 55–57 barg, which is significantly higher than the pressure in comparable studies. This fact excluded the use of glass pipes due to their insufficient mechanical properties. The use of plastic tubes increased the probability of experiencing heterogeneous nucleation in the upstream superheated liquid. However, the high initial pressure resulted in significantly higher velocities and shorter timescales than most comparable studies, limiting the time available for heterogeneous nucleation to evolve. An objective of the current study was then to investigate whether polycarbonate tubes would offer both a sufficiently smooth surface and the necessary mechanical strength. The diaphragm rupture device was an arrow with a cross shaped tip driven by a pneumatic piston. Two layers of 100 μm PET film was used as a diaphragm.

### 2.2. Instrumentation

The pressure sensors (Kulite XTM-190) had a natural frequency of 290 kHz and a measuring range of 0–1000 psig. The sensors were calibrated with an external device (GE Druck calibrator) before the start of the test series. The thermal sensitivity shift was ±2%/100°. The piezoresistive operation makes these sensors less sensitive toward thermal shocks and more suitable for dynamic measurements than piezoelectric sensors. No shielding measures were performed due to the short timescales of the experiment (about 10 ms). However, as indicated by the thermal sensitivity shift, an effect by temperature changes on pressure (about 3.6% per 100 °C) was to be expected.

The temperature sensor was a thermocouple type-K (Cromel/Alumel) with a measurement error limit of ±1.5 °C. Only the initial (pre-rupture) temperature measurement was used, due to a time constant of about 150 ms. The sensor was calibrated with an external calibrator (Ametek Jofra CTC140A) before the start of the test series.

A Photron Fastcam APX RS digital high-speed camera with a 50 mm Nikkor lens was used to record the rapid expansion and boiling process. The framerate was 20,000–30,000 frames per second and the typical shutter speed was 1/62,000 s. The image resolution was typically 1024 × 128 pixels. The primary light source was 3 LED panels (20 W each) with diffusors that provided uniform illumination without distracting glare reflections. In addition, a pair of 250 W Dedocool tungsten light heads were used as a secondary front light source in some test runs.

### 2.3. Test procedure

At the start of each test run, the tube was slowly filled with liquid $CO_2$. Then, a time period of 5–10 min was added to provide

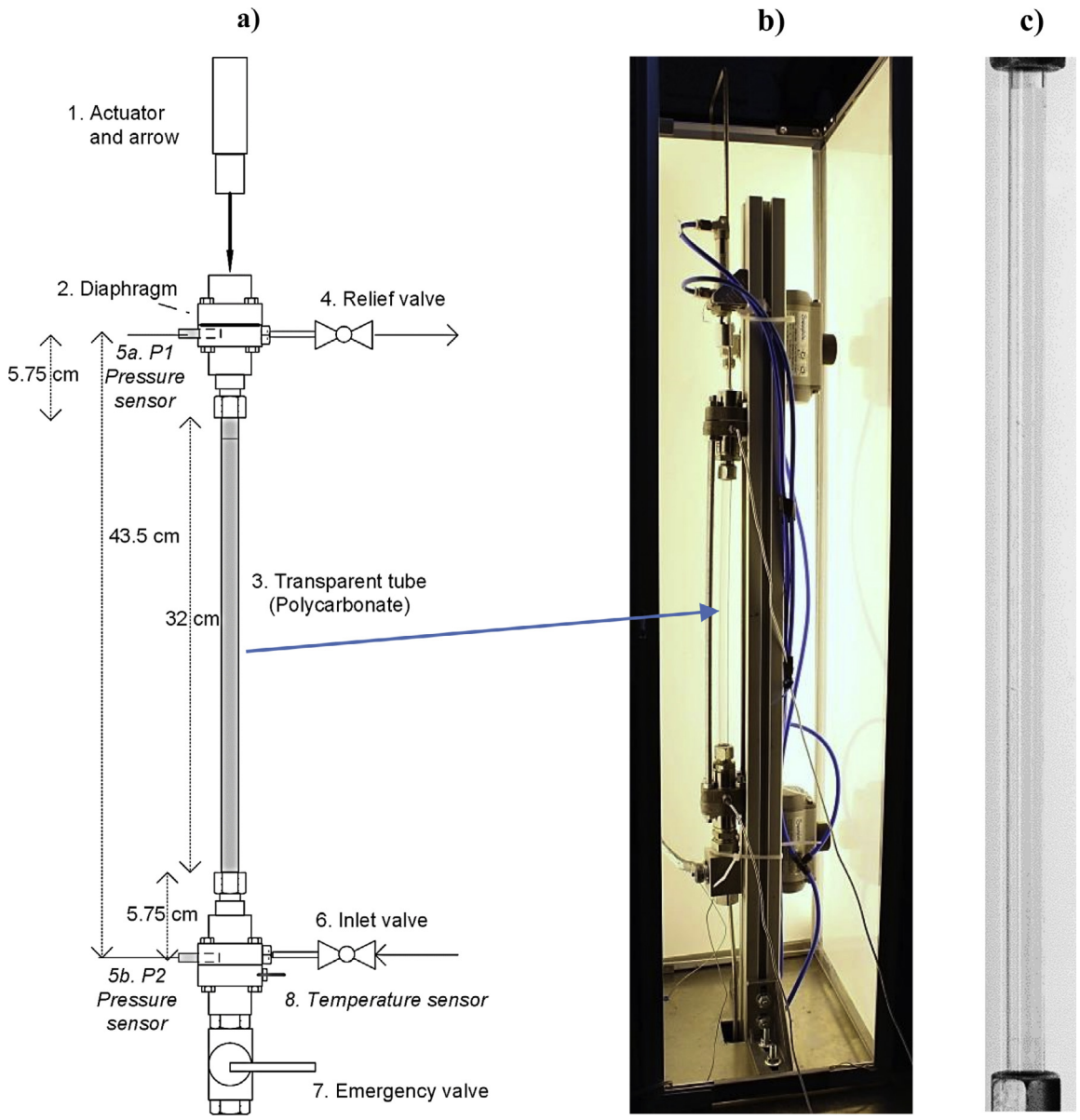


**Fig. 1.** (a) Schematic diagram of the tube, (b) photograph of the experimental setup, (c) high-speed camera image.

thermal equilibrium by letting the temperature and pressure readings stabilize. The initial pre-rupture state was then saturated liquid at room temperature. The experiments were initiated by simultaneously triggering the arrow actuator, the high-speed camera and the data acquisition module. Time $t_0 = 0$ s denotes the initial trigger time. A time delay of typically 100 ms followed before any changes were detected due to the pneumatic operation of the diaphragm rupture device.

The high-speed images from each test run were imported into MATLAB and stacked next to each other to produce a position-time (x-t) plot. The original dimensions of the high-speed images were $1024 \times 128$ pixels where the tube diameter typically accounted for 35–40 pixels. This gave a resolution of about 3 pixels per mm. Fig. 2a shows a series of cropped high speed images stacked next to each other. Following image processing method was used to interpret the information from the high-speed images and to calculate relevant velocities. The values of each pixel along the image width were added together in MATLAB, so that one combined pixel per image in the x-axis represented the entire tube diameter. The image dimensions were then reduced from $1024 \times 128$ pixels to $1024 \times 1$ pixels. Hence, a visualization of the expansion and boiling process was reduced to a 1-D phenomenon evolving in time, as illustrated in Fig. 2b. This averaging method was used in the results section to emphasize and calculate characteristic velocities. A disadvantage was loss in the ability to photographically resolve flow details.

The processed high-speed images were matched and plotted together with the pressure measurements to interpret the data and calculate typical velocities. The wave and the fluid flow velocities were calculated by linear regression as illustrated in Fig. 2b. In this example, five discrete data points 1–5 were defined manually on the x-t diagram in MATLAB. The slope of the regression line then gave an estimate of the velocity. The on-screen plot in MATLAB allowed significantly higher precision than what is reproduced in Fig. 2b. The following procedure serve as an example of the method used to calculate the flow velocities: (1) Define from the x-t plot which velocity should be calculated and zoom in on the region of interest; (2) Define manually 3–10 $(t_i, h_i)$ points following the wave

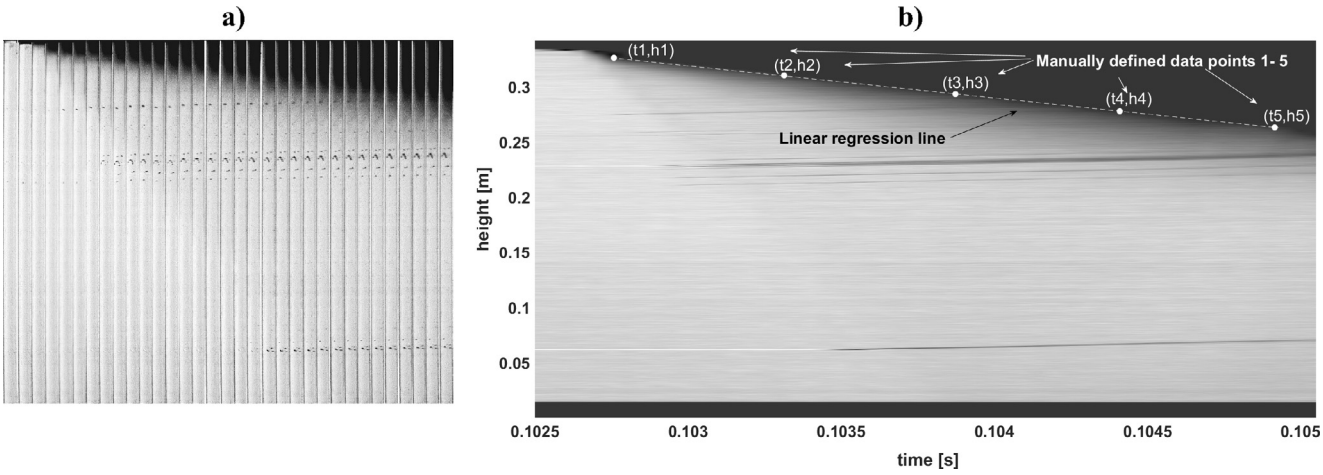


**Fig. 2.** Left: a series of cropped high-speed images stacked together; Right: high-speed images imported and processed in MATLAB; the dimension is reduced to 1024 × 1 pixels, letting one combined pixel represent the entire tube diameter. Discrete data points and a dashed regression line are added to illustrate the method for calculating the velocities.

or fluid flow of interest. The number of extracted data points are dependent on the spatial distribution span; (3) Arrange the x-t data into an array with time and spatial position; (4) Use the least squares method to calculate the velocity from the slope of the discrete data points regression line.

The sensitivity toward measurement errors increased with increasing velocities and decreasing height differences. The largest uncertainty in the velocity calculations corresponded to measurement errors in the x-axis (time measurements) at high velocities. At 20,000 frames per second, the time difference between two images is 0.05 ms. An error estimate for a rarefaction wave propagating at 300 m/s measured along the total tube length gives ±13.4 m/s or 4.5%. The measurement errors in the y-axis contributed less at these velocities, giving a total error estimate of ±13.7 m/s or 4.6%. Evaporation wave velocities were typically calculated at the upper section of the tube. A total velocity error estimate (both x and y direction) of an evaporation wave propagating at 30 m/s through a 10 cm section gave ±0.5 m/s or 1.8%.

## 3. Experimental results

### 3.1. Overall description

The study consisted of thirteen test runs in total. Three test runs is presented here, denoted as TR1 to TR3. The initial conditions and calculated velocities are summarized in Table 1. Fig. 3 shows a schematic x-t diagram of the expansion and evaporation process with $CO_2$ vapor above the liquid level. The physical phenomena was similar to what have been previously reported by other authors such as Hill [16,17], and Pinhasi et al. [24]. The test runs was initiated by puncturing the diaphragm separating the contents of the tube from the ambient air at atmospheric pressure. Isentropic rarefaction waves then propagated through the tube. What seems to be the middle or the tail of the expansion fan (A) was observed propagating with a constant velocity through the liquid phase. When the head of the rarefaction fan hit the liquid/vapor interphase, it was partially reflected and partially transmitted into the liquid phase, then reflected again at the tube bottom flange. The saturated vapor partially condensed (E) due to the isentropic expansion and entered the two-phase envelope. Due to the sudden pressure reduction, the liquid was temporarily superheated and in a metastable state for a few milliseconds after the passage of the first rarefaction wave. Then boiling started at the phase boundary. In most but not all cases, an evaporation wave (B) was observed propagating downward into the liquid phase, resulting in a two-phase vapor/liquid mixture downstream region. In the current experiments, no clear boiling front was observed. This fact is partially due to the low resolution (about 3 pixels per mm) and partially due to the observation of heterogeneous nucleation occurring in the upstream superheated liquid in front of the evaporation wave. The evaporation wave was more evident in the upper part of the tube, before its propagation was disturbed by reflections of the rarefaction wave and possible wall nucleation. In some test runs, gas bubbles (C) were observed moving upward and accelerated after the passage of the rarefaction wave. Visual observations of the tube during the experiments showed that these bubbles were situated in the bulk and not at the tube wall. A

**Table 1**
Initial conditions and calculated wave velocities from the experiments TR1-TR3.

| Description | Wave ID | – | TR1 | TR2 | TR3 |
|---|---|---|---|---|---|
| Initial liquid level | | [%] | 0 | 58 | 95 |
| Initial temperature | | [°C] | 21.6 | 19.5 | 19.7 |
| Initial pressure P2 (bottom) | | [barg] | 57 | 56 | 57 |
| Rarefaction wave velocity (average - both gas and liquid phase) based on pressure sensors P1 and P2 | | [m/s] | 192 | 240 | 280 |
| Rarefaction wave velocity, liquid phase, from bubble condensation, based on high-speed camera images | | [m/s] | N/A | 318 | 302 |
| Velocity - middle or tail of the expansion fan | A | [m/s] | N/A | 235 | 240 |
| Evaporation wave velocity | B | [m/s] | N/A | 32 | 32 |
| Gas bubble velocity (indicate liquid bulk flow when assuming no slip) | C | [m/s] | N/A | 5.2 | 5.4 |
| Average bulk flow velocity | D | [m/s] | 171–66 | 77 | N/A |
| Condensation wave velocity, vapor phase | E | [m/s] | 192 | 190 | N/A |
| Contact surface velocity, vapor-vapor/liquid, upper 6 cm | F | [m/s] | N/A | 95 | N/A |
| Liquid layer front velocity | G | [m/s] | N/A | 8.0 | N/A |

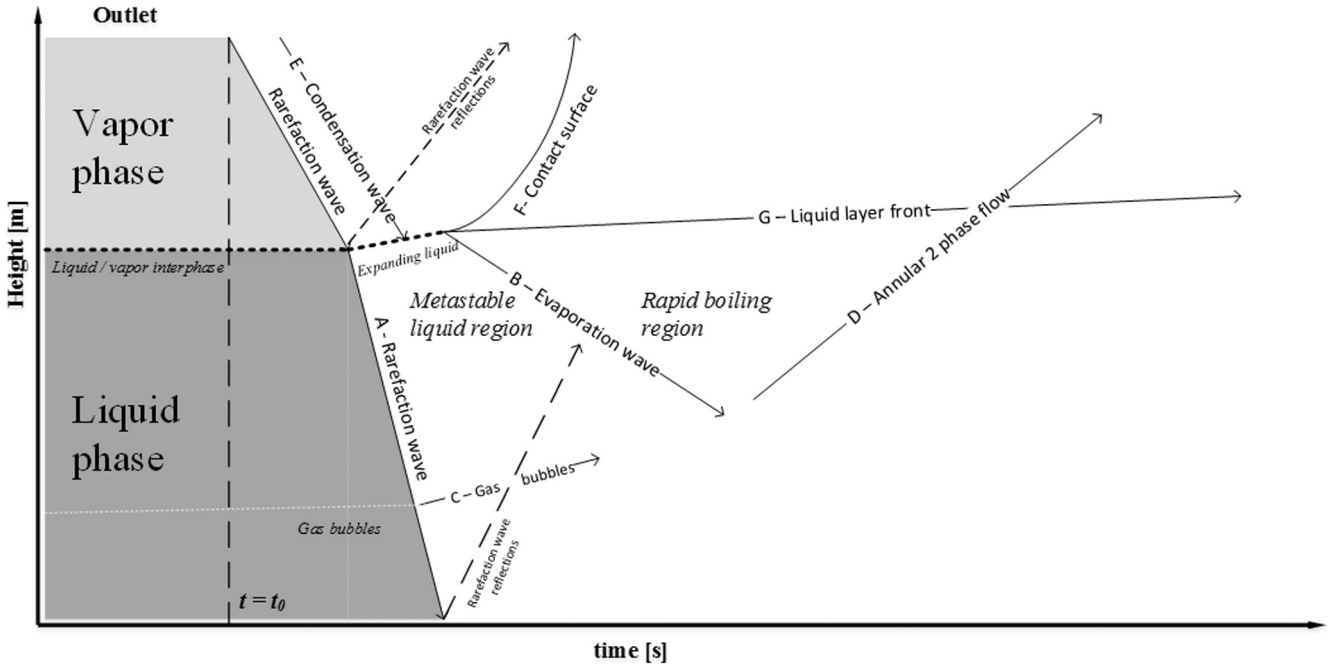


**Fig. 3.** A typical schematic x-t diagram of the expansion & evaporation process with a partially filled tube.

contact surface (F) between the vapor and the vapor-vapor/liquid two phase mix was observed, accelerating toward the outlet of the tube. Originating at the liquid – vapor interphase, a liquid layer front (G) attached to the tube wall was observed, moving upward at a constant velocity. At the center of the tube, an annular two phase spray flow (D) with significantly higher velocity than the liquid layer at the tube wall (G) was observed. The velocity of D did not remain constant, but decreased gradually with decreasing pressure as time evolved. At a later stage, when the pressure was below the triple point at 5.2 bar, the remaining $CO_2$ consisted of a mixture of vapor and dry ice particles.

Table 1 shows the initial values and calculated wave velocities for TR1-TR3. Blank cells labeled "N/A-" in the data table denote that the wave or fluid flow velocity was either not observed or was not relevant for the given test run. Deviations between measured values and literature values could be due to measurement uncertainties as discussed in Section 2.2. In TR1, the tube initially contained pure gas phase $CO_2$. In TR 2 and TR3, the liquid level was 58% and 95% respectively.

### 3.2. Test run 1: vapor phase $CO_2$ only

Fig. 4 shows an x-t plot of the processed high-speed images combined with a p-t plot from pressure sensors P1 (top) and P2 (bottom) in TR1. Initially, the tube contained saturated $CO_2$ vapor at pressure p = 57 barg. The diaphragm ruptured at time $t_0$ = 93.3 ms. After the pressure P1 started to drop there was a 1.6 ms delay before any visual changes were observed. At time t = 94.9 ms, a condensation wave appeared at the top, propagating downward with a velocity of 192 ± 11 m/s. Calculations showed that the velocities of the condensation wave and the head of the rarefaction fan were almost identical, with a time delay of ~0.4 ms between the waves.

With the current test setup, further changes in the bulk caused by propagation of the rarefaction wave through the vapor phase could not be observed. When the condensation wave (E) approached the bottom of the tube, the velocity was no longer linear but had a "discontinuous" propagation, as seen in the region marked "x" in Fig. 4. This was probably caused by the interaction with the reflected rarefaction fan and collision with expanding vapor flowing toward the outlet. The velocity of the bulk transport is indicated with four white arrows, labeled $D_1$ to $D_4$ in Fig. 4. The calculated bulk flow velocities ($D_1$ - $D_4$) were, in descending order, 141, 121, 86, and 66 m/s. The pressure P1 (top) decreased from 57 barg to 25 barg in about 3 ms, stayed nearly constant for about 4 ms, and then continued to decrease toward atmospheric pressure. The pressure P2 (bottom) decreased steadily from the initial state of 57 barg down to atmospheric pressure. The local pressure minimum at time ≈97.0 ms could have been due to the wave reflection at the bottom of the tube.

### 3.3. Test run 2: initial liquid $CO_2$ level 58%

In TR2, the visual level of the saturated liquid $CO_2$ was initially 58%. Fig. 5 shows an x-t plot of the processed high-speed images and a p-t plot from pressure sensors P1 (top) and P2 (bottom). The arrows labeled A-G indicate the velocities of the waves and the fluid flows in the x-t diagram. The observations in TR2 were similar to the experimental results previously published by Tosse et al. [23].

The pressure P1 started to drop at time t = 95 ms from an initial value of 56 barg to a temporary minimum of 20 barg. After a 1.81 ms delay, the pressure P2 (bottom) started to decrease. This gave an average rarefaction wave velocity of 240 ± 13 m/s, which is similar to the velocity 238 ± 12 m/s calculated by Tosse et al. [23]. The average speed of sound, based on interpolated values from the Span-Wagner equation of state [29] with saturated $CO_2$ at 19.4 °C, was 258 m/s (196 m/s in the vapor phase and 344 m/s in the liquid phase). At time t = 95.5 ms, the first visual changes was observed. Due to the rapid expansion of the saturated vapor, a condensation wave (E) propagated in the vapor bulk downward to the vapor/liquid interface with an average velocity of 190 ± 7 m/s.

A front (A) was observed that propagated with a constant velocity of 235 ± 13 m/s. This is to slow to represent the head of the expansion fan but could be changes happening in the bulk or at the tube surface closer to the tail of the expansion fan.

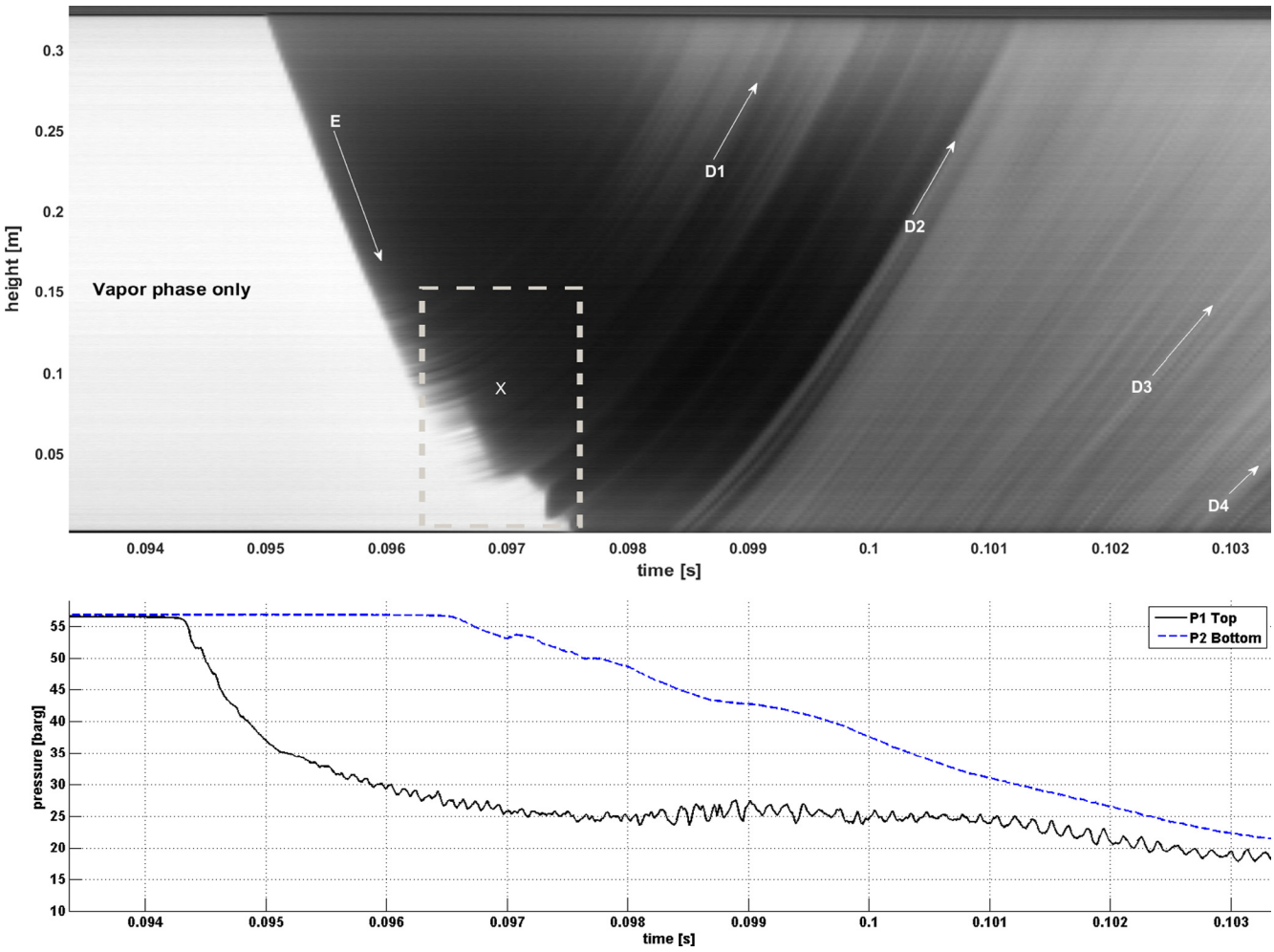


**Fig. 4.** Experimental results from TR1 with vapor phase $CO_2$ only, showing an x-t plot of the processed high-speed film and a p-t plot from pressure sensors P1 (top) and P2 (bottom); the box marked "x" shows where the condensation wave is discontinuous and the arrows $D_1$-$D_4$ indicate the bulk flow velocities.

Some gas bubbles were originally present in the liquid phase. Visual observations during the conduct of experimental work showed that the bubbles were located in the bulk moving upwards and not stuck at the tube wall. Initially, the bubbles propagated with a velocity of <0,1 m/s, driven by buoyancy forces. As the rarefaction wave passed the bubbles, they began to condense and then entered the two-phase region due to the rapid expansion. The condensing gas bubbles (C) accelerated and moved toward the tube outlet with a constant velocity of 5.2 m/s. Assuming no velocity slip between the gas and the liquid phase, this velocity could also represent an estimate of the bulk flow velocity in the expanded liquid. In this region, after the head of the rarefaction fan passed by and before the boiling started, the liquid bulk was in a metastable state. A rough estimate of the rarefaction wave velocity in the expanded liquid phase gave 318 ± 13 m/s. This calculation was based on position vs. time observations of the gas bubble condensation in the original high speed movie. The recorded time of condensation inside the gas bubbles was compared with the distance between the bobbles. The resulting velocity estimate was then calculated as $v = \Delta x/\Delta t$.

After an induction time of 0.3 ms from when the condensation wave (E) reached the liquid/vapor interface, boiling was observed at the interface at time t = 96.4. An evaporation wave (B) was formed, propagating into the liquid phase. The evaporation wave front was rather diffuse, probably due to heterogeneous nucleation in the upstream liquid. The current experimental setup did not permit the visualization of front details. The velocity of the evaporation front was not constant throughout the tube, but seemed to accelerate. At a 0.1 m section below the liquid/vapor interphase, the calculated evaporation wave velocity was 32 ± 0.5 m/s. At time t = 98.2 ms, the boiling front accelerated. It is believed that the acceleration was caused by an interaction with the reflection of the first downward rarefaction wave. There were no sensors along the transparent tube, but the pressure level in this section was assumed to be between the pressures measured by sensors P1 and P2. As the liquid started to boil at the interface, two additional wave fronts were detected. First, a front (F) was observed that was the contact surface between the vapor and the vapor/liquid phase. It started at the interface, and then it accelerated upward with a velocity 96 ± 9 m/s in the upper region. Second, a liquid layer front (G), propagated with a constant velocity of 8.0 ± 0.1 m/s toward the outlet. The annular two-phase flow (D) seemed to accelerate toward the outlet. A calculated bulk velocity at time t = 105.7 ms increased from 60 ± 4 m/s near the bottom to about 90 ± 8 m/s close to the outlet. The velocities of D and G were calculated following the procedure described in Section 2.3 by manually selecting position versus time data points (x,t) and then calculating the slope by linear regression. In Fig. 5, the features of lines D and G are not so easily seen. However, the on-screen plots in MATLAB provided better contrast and visibility. Techniques were used to enhance the subtle differences needed to make calculations with sufficient accuracy. Plotting the gradient is one example. This

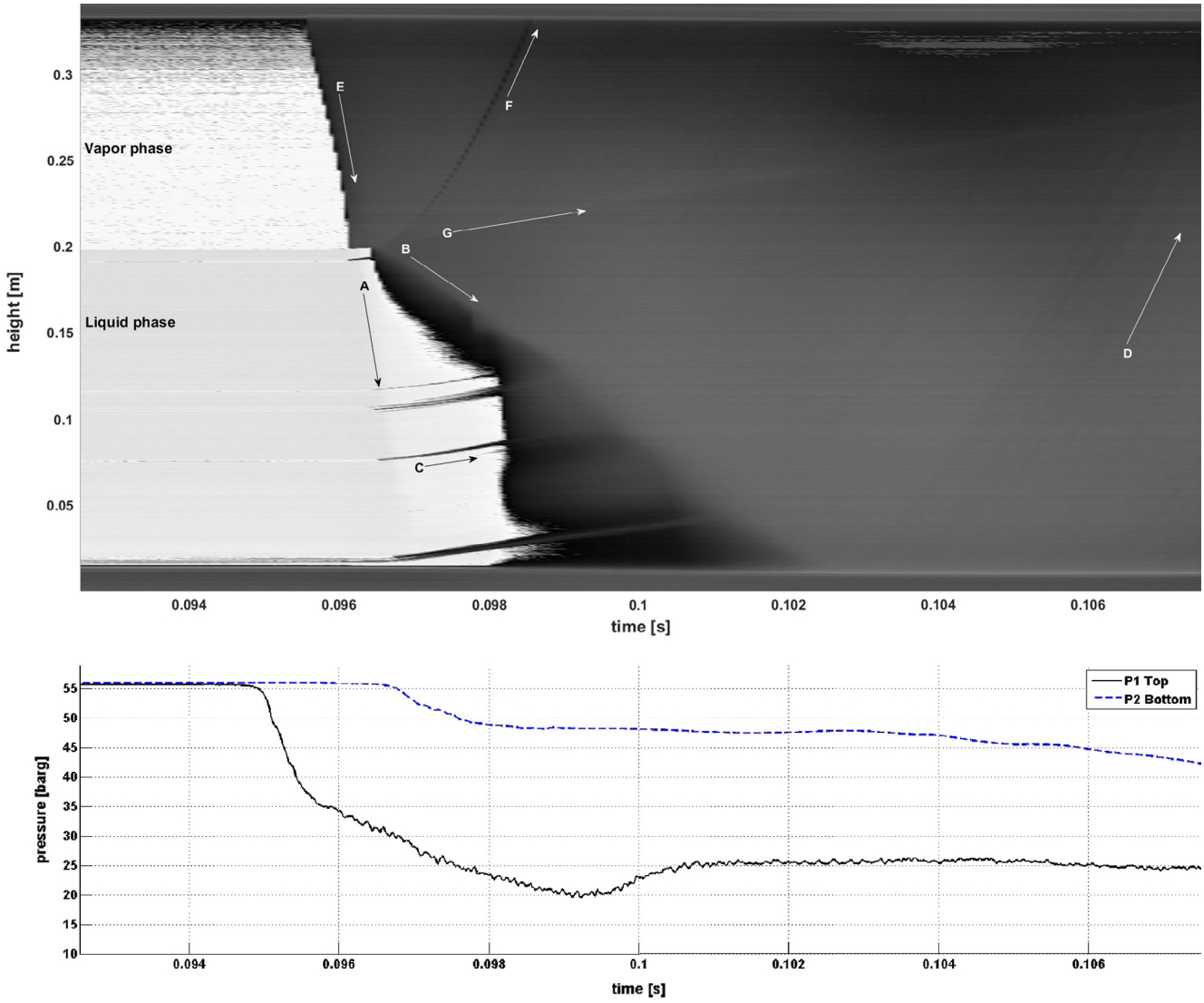


**Fig. 5.** Experimental results from TR2 with 58% liquid level, showing an x-t plot of the processed high-speed film and a p-t plot from pressure sensors P1 (top) and P2 (bottom). The arrow A shows changes observed in front of the evaporation wave, B shows propagation of the evaporation wave, C represent the gas bubble velocity in the superheated liquid phase, E represents the condensation wave, F is the contact surface between vapor and liquid/vapor, G is a liquid layer front at the tube wall, and D represents annular two-phase bulk flow.

increased the contrast, but also amplified the image noise, making these plots less suitable for presentation in the printed paper.

By plotting the gradient background subtraction that will increase the visibility of the lines and also the accuracy of the calculations. The pressure P1 (top) decreased rapidly upon diaphragm rupture from 56 to 20 barg. Then a pressure increase was observed (about 5 bar), caused by passing of the contact surface (F) The pressure P2 (bottom) decreased by about 8 bar to 48 barg and remained nearly constant during a 8 ms boiling period.

### 3.4. Test run 3: initial liquid $CO_2$ level 95%

Fig. 6 shows an x-t plot of the processed high-speed film and a p-t plot from the pressure sensors in TR3. The initial liquid level was 95%. Additional front illumination (Dedolight) was used compared to TR2, to provide more image details. The wave velocities in TR2 and TR3 were similar. The results are presented in Table 1.

## 4. Discussion

Evaporation waves were observed and the velocities were calculated. From results published by others, it is expected that the velocity (32 m/s) is not unique, but will depend on the initial temperature [19], the depressurization rate [20], the degree of superheat [14,21], and possibly but not necessarily on the test section diameter [14,21].

The high speed images revealed that wall nucleation occurred after the passage of the rarefaction wave. The polycarbonate tube did not provide a necessarily smooth surface, probably due to the availability of nucleation sites. The degree of superheat was then limited, meaning that homogenous bulk nucleation did not take place in the current test series. In Fig. 7, the pressure-volume diagram shows that isentropic expansion from 56 barg would intersect the liquid spinodal curve at about 18 barg. It would then be expected that homogenous nucleation could take place at about 20–25 barg.

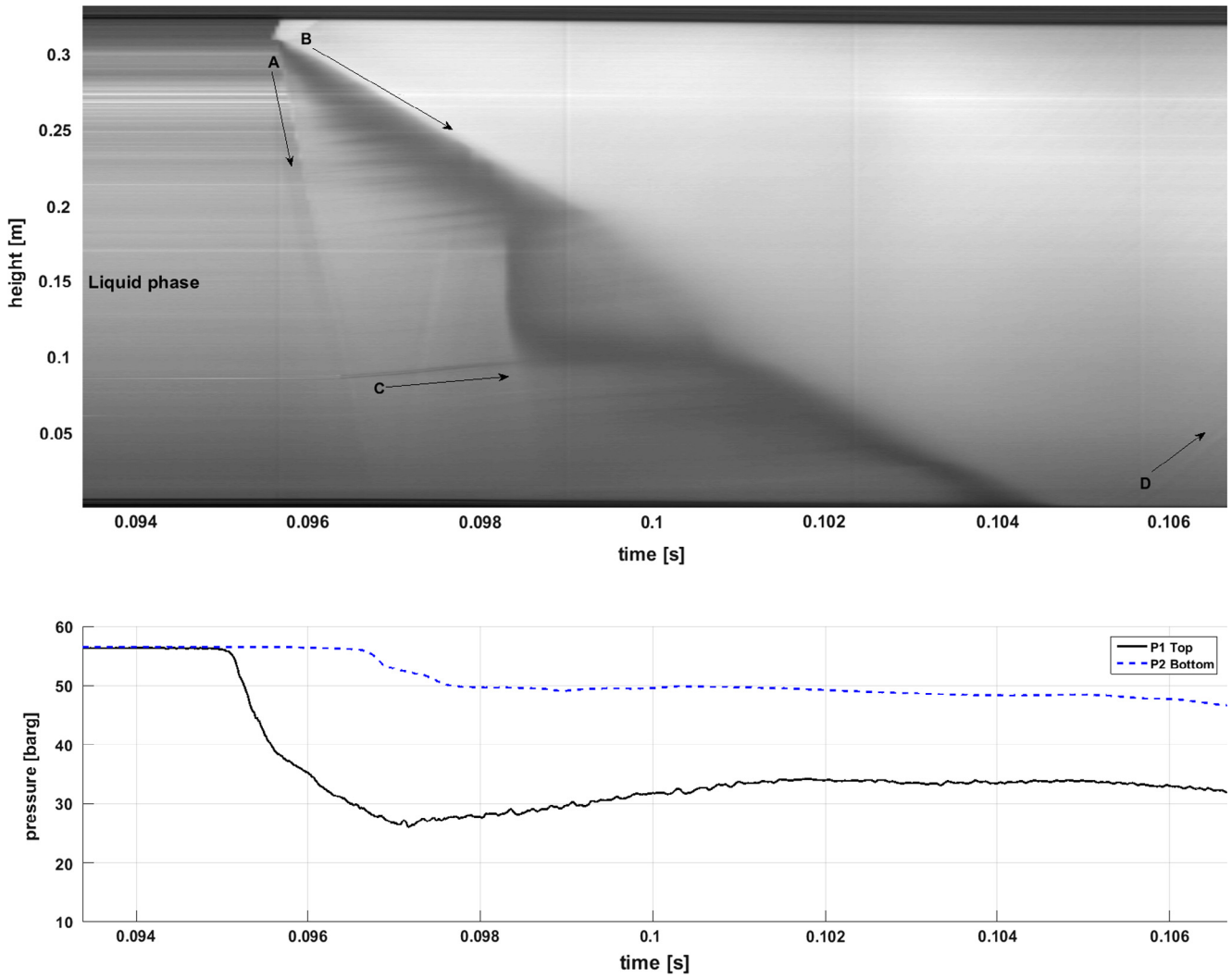


**Fig. 6.** Experimental results from TR2 with 95% liquid level, showing an x-t plot of the processed high-speed film (MATLAB) and a p-t plot from pressure sensors P1 (top) and P2 (bottom). The arrow A shows changes observed in front of the evaporation wave; B represent the evaporation wave velocity; C is the velocity of bubbles in the upstream liquid phase; D indicate two-phase bulk flow.

### 4.1. Phase transition rate and energy estimate

This section presents a simple phase transition rate estimate and an estimate of the energy potentially released if the $CO_2$ is allowed to expand from the initial state (saturated liquid at $T_0 = 19.5\ °C$, $P_0 = 56$ barg) to the end state ($T_2 = -78.9\ °C$, $P_2 = 1$ atm). This would be the case, for instance in a tank rupture. The states 0, 1 and 2 are identified in the pressure-temperature diagram in Fig. 7 Isentropic expansion is assumed from the initial state (0) to the metastable state (1), where rapid boiling is initiated. Assuming adiabatic phase change, the latent heat of vaporization is supplied from the energy stored in the metastable liquid [5]. As the expansion continues below the triple point ($T_{tr} = -56.6\ °C$, $P_{tr} = 5.18$ bar), the $CO_2$ in the end state (2) will consist of a mixture of gas and dry ice. The vapor fraction at the end state and energy release will depend on whether the adiabatic evaporation is assumed reversible or irreversible. In these simplified calculations, the process is assumed isentropic (adiabatic, reversible), which probably will result in an overestimation of the energy release [12,19]. Fig. 8 shows a sketch of the control volume as the evaporation wave is propagating through the liquid phase.

The velocity calculated in Eq. (1) is the calculated net velocity upstream $v_1$:

$$v_1 = s_1 + v_B = 32 + 5.2 = 37.2\ \left[\frac{\mathrm{m}}{\mathrm{s}}\right] \tag{1}$$

where $v_B$ (m/s) is the liquid phase bulk flow velocity and $s_1$ (m/s) is the evaporation wave velocity. The estimated phase transition rate $\dot{m}''$ presented in Eq. (2) is:

$$\dot{m}'' = \rho_1 \cdot v_1 = 768 \cdot 37.2 \approx \underline{28,570}\left[\frac{\mathrm{kg}}{\mathrm{m^2\ s}}\right] \tag{2}$$

where $\rho_1$ (kg/m$^3$) is an estimate of the density in the expanded, metastable liquid state ($T_1 = 18.5\ °C$, $P_1 = 48$ barg) calculated using the Span Wagner technical equation of state [29]. These numbers could be used as inputs in the validation of the source terms in a 1-D BLEVE model.

An estimate of the energy potentially released if the $CO_2$ is allowed to expand from the initial state to the end state is presented in Eq. (3):

$$E_v = m \cdot (u_0 - u_2) = 0.017 \cdot (467 - 371) = 1.6\ \mathrm{kJ} \tag{3}$$

where $m$ (kg) is the mass of $CO_2$ originally present in the test rig, $u_0$ (kJ/kg) is the estimated internal energy at the initial state and $u_2$ (kJ/kg) is the estimated internal energy at the end state.

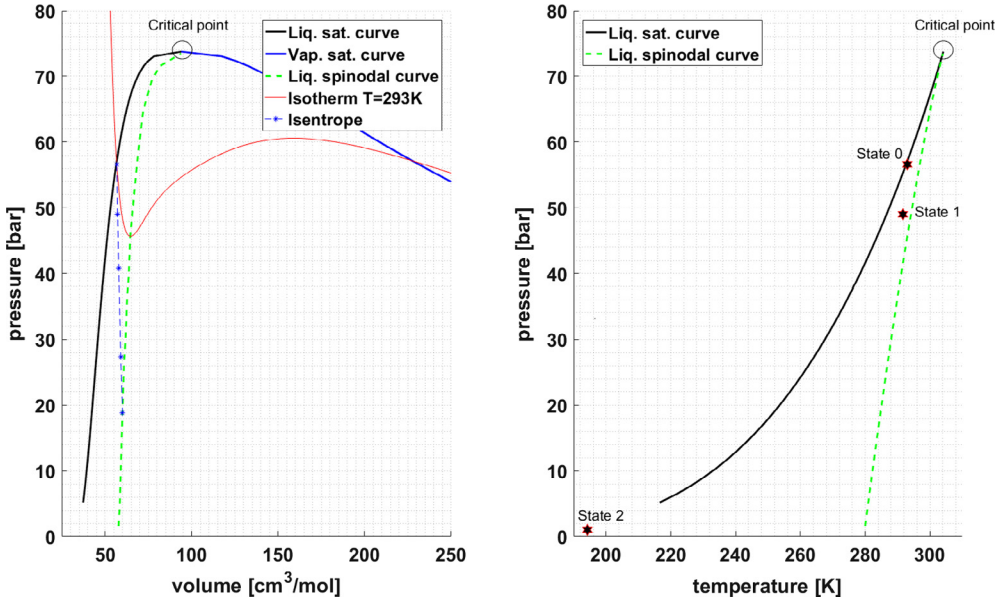


**Fig. 7.** Left: p-V diagram of $CO_2$ using the Span Wagner technical equation of state. The figure shows the 293 K isotherm and isentropic expansion from the liquid saturation curve at 293 K down to the spinodal curve. Right: p-T diagram of $CO_2$ identifying the states 0, 1 and 2 in the analysis presented in Section 4.1.

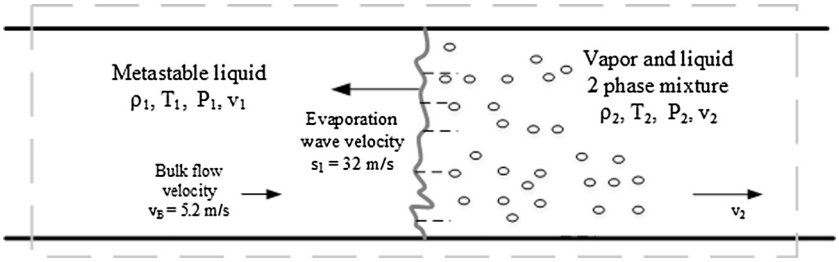


**Fig. 8.** Control volume used in the calculations.

An estimate of the energy flux potentially released if the $CO_2$ is allowed to expand from the initial state to the end state is presented in Eq. (4):

$$\dot{E}'' = \dot{m}'' \cdot (u_0 - u_2)28,570 \cdot 95 = \underline{2714}\left[\frac{\mathrm{MJ}}{\mathrm{m^2\ s}}\right] \tag{4}$$

where $\dot{m}''$ (kg/m$^2$ s) phase transition rate, $u_0$ (kJ/kg) is the estimated internal energy at the initial state and $u_2$ (kJ/kg) is the estimated internal energy at the 1 atm end state. In comparison, an estimate of the energy release in detonation with 30 vol% hydrogen in air gave 4300 MJ/m$^2$ s.

The calculations and results from the phase transition rate and energy estimations are summarized in Table 2.

**Table 2**
Data, phase transition rates and energy estimations.

| Description | TR2 |
|---|---|
| Initial mass of $CO_2$, $m$ (g) | 17 |
| Density, expanded liquid state, $\rho_1$ (kg/m$^3$) | 768 |
| Net evaporation wave velocity, $v_1$ (m/s) | 37.2 |
| Internal energy, initial state, $u_0$ (kJ/kg) ($T_0$ = 19.5 °C, $P_0$ = 56 barg) | 467 |
| Internal energy, end state, $u_0$ (kJ/kg) ($T_2$ = 19.5 °C, $P_2$ = 1 atm) | 371 |
| Phase transition rate, $\dot{m}''$ (kg/m$^2$ s) | 28,570 |
| Energy potentially released in the expansion, $E_v$ (kJ) | 1.6 |
| Energy flux, potentially released in the expansion, $\dot{E}''$ (MJ/m$^2$ s) | 2714 |

## 5. Conclusions

This article presents experimental results from three test runs, TR1-TR3, with rapid phase transition of pressurized liquefied carbon dioxide in a vertical tube. The experimental setup that included a high speed camera and two pressure sensors was able to successfully identify the expected phenomena such as the acoustic rarefaction waves, the evaporation wave and a liquid/liquid-vapor surface. Calculated wave propagation velocities were presented. The evaporation wave velocity was constant in the upper part of the tube. No evaporation front details could be observed with the current setup. The transparent polycarbonate tube did not provide a sufficiently smooth surface to suppress heterogeneous wall nucleation. A phase transition rate estimate was calculated based on the net evaporation wave velocity and the density in the expanded liquid. An application of the presented experimental results would be as reference data for the interfacial flux source terms in a 1-D phase transition model.

## References

[1] A.M. Birk, C. Davison, M. Cunningham, Blast overpressures from medium scale BLEVE tests, J. Loss Prev. Process Ind. 20 (2007) 194–206.
[2] Y. Zhang, J. Schork, K. Ludwig, Revisiting the conditions for a $CO_2$ tank Explosion, in: Proceedings of the 2013 AIChE Spring Meeting and Ninth Global Congress on Process Safety, Curran Associates, San Antonio, Texas, 2013, pp. 109–120.
[3] W.E. Clayton, M.L. Griffin, Catastrophic failure of a liquid carbon dioxide storage vessel, Process Saf. Prog. 13 (4) (1994) 202–209.

[4] R.C. Reid, Possible mechanism for pressurized-liquid tank explosions or BLEVE's, Science 203 (4386) (1979) 1263–1265.
[5] R.C. Reid, Some theories on boiling liquid expanding vapour explosions, Fire (1980) 525–526.
[6] R.C. Reid, Superheated liquids, Am. Sci. 64 (2) (1976) 146–156.
[7] T. Abbasi, S.A. Abbasi, Accidental risk of superheated liquids and a framework for predicting the superheat limit, J. Loss Prev. Process Ind. 20 (2007) 165–181.
[8] T. Abbasi, S.A. Abbasi, The boiling liquid expanding vapour explosion (BLEVE): mechanism, consequence assessment, management, J. Hazard. Mater. 141 (2007) 489–519.
[9] D. Bjerketvedt, K. Egeberg, W. Ke, A. Gaathaug, K. Vaagsaether, Boiling liquid expanding vapor explosion in $CO_2$ small scale experiments, Energy Proc. 4 (2011) 2285–2292.
[10] W. Ke, $CO_2$ BLEVE (Boiling Liquid Expanding Vapor Explosion), Master's thesis, Telemark University College, Porsgrunn, Norway, 2009.
[11] M.M. van der Voort, R.M.M. van Wees, J.M. Ham, M.P.N. Spruijt, A.C. van den Berg, P.C.J. de Bruijn, P.G.A. van der Ierschot, An experimental study on the temperature dependence of $CO_2$ explosive evaporation, J. Loss Prev. Process Ind. 26 (2013) 830–838.
[12] M.A. Gromles, H.K. Fauske, Axial propagation of free surface boiling into superheated liquids in vertical tubes, in: Proceedings of the Fifth International Heat Transfer Conference, Tokyo, 1974, vol 4, pp. 30–34.
[13] R.J. Peterson, S.S. Grewal, M.M. El-Wakil, Investigations of liquid flashing and evaporation due to sudden depressurization, Int. J. Heat Mass Transf. 27 (2) (1984) 301–310.
[14] P.K. Das, G.S. Bhat, V.H. Arakeri, Investigations on the propagation of free surface boiling in a vertical superheated liquid column, Int. J. Heat Mass Transf. 30 (4) (1987) 631–638.
[15] P.A. Thompson, H. Chaves, G.E.A. Meier, Y.G. Kim, H.D. Speckmann, Wave splitting in a fluid of large heat capacity, J. Fluid Mech. 185 (1987) 385–414.
[16] L.G. Hill, B. Sturtevant, An experimental study of evaporation waves in a superheated liquid, in: G.E.A Meier, P.A Thompson (Eds.), Proceedings of the ITUAM Symposium on Adiabatic Waves in Liquid-Vapor Systems, Springer Science & Business Media, Göttingen, 1989, pp. 25–37.
[17] L.G. Hill, An experimental study of evaporation waves in a superheated liquid, PhD thesis, California Institute of Technology, Pasadena, CA, 1991.
[18] R. Barbone, D.L. Frost, A. Makris, J. Nerenberg, Explosive boiling of a depressurized volatile liquid, in: D. Morioka, L. van Wijngaarden (Eds.), Proceedings of the ITUAM Symposium on Waves in Liquid/Gas and Liquid/Vapor Two-phase Systems, Springer, Netherlands, Kyoto, 1994, vol. 31, pp. 315–324.
[19] J.E. Shepherd, J.R. Simões-Moreira, Evaporation waves in superheated dodecane, J. Fluid Mech. 382 (1999) 63–86.
[20] E. Hahne, G. Barthau, Evaporation waves in flashing processes, Int. J. Multiph. Flow 26 (2001) 531–547.
[21] P. Reinke, G. Yadigaroglu, Explosive vaporization of superheated liquids by boiling fronts, Int. J. Multiph. Flow 27 (2001) 1487–1516.
[22] V.V. Kuznetsov, I.A. Kozulin, O.V. Vitovsky, Experimental investigation of adiabatic evaporation waves in superheated refrigerants, J. Eng. Thermophys. 21 (2) (2012) 136–143.
[23] S. Tosse, K. Vaagsaether, D. Bjerketvedt, An experimental investigation of rapid boiling of $CO_2$, Shock Waves 25 (2015) 277–282.
[24] G.A. Pinhasi, A. Ullmann, A. Dayan, 1D plane numerical model for boiling liquid expanding vapor explosion (BLEVE), Int. J. Heat Mass Transf. 50 (2007) 4780–4795.
[25] M. Xie, Thermodynamic and gasdynamic aspects of a boiling liquid expanding vapour explosion (PhD Thesis), Delft University of Technology, The Netherlands, 2013.
[26] S.E. Yakush, Model for blast waves of boiling liquid expanding vapor explosions, Int. J. Heat Mass Transf. 103 (2016) 173–185.
[27] M.M. van der Voort, A.C. van den Berg, D.J.E.M. Roekaerts, M. Xie, P.C.J. de Bruijn, Blast from explosive evaporation of carbon dioxide: experiment, modeling and physics, Shock Waves 22 (2012) 129–140.
[28] G. Chiccarelli, J. Melguizo-Gavilanes, J.E. Shepherd, Pressure-field produced by the rapid vaporization of a $CO_2$ liquid column, in: Proceedings of the 30th International Symposium on Shock Waves, Tel-Aviv, 2015.
[29] R. Span, W. Wagner, A new equation of state for carbon dioxide covering the fluid region from the triple-point to 1100 K at pressures up to 800 MPa, J. Phys. Chem. Ref. Data 25 (6) (1996) 1509–1596.

# Paper B

# Blast from pressurized carbon dioxide released into a vented atmospheric chamber

This paper is published in Shock Waves. Accepted 17 March 2018.

https://doi.org/10.1007/s00193-018-0819-z.

Shock Waves
https://doi.org/10.1007/s00193-018-0819-z

ORIGINAL ARTICLE

# Blast from pressurized carbon dioxide released into a vented atmospheric chamber

P. M. Hansen[1] · A. V. Gaathaug[1] · D. Bjerketvedt[1] · K. Vaagsaether[1]

Received: 31 October 2017 / Revised: 8 March 2018 / Accepted: 17 March 2018


**Abstract**
This study describes the blast from pressurized carbon dioxide ($CO_2$) released from a high-pressure reservoir into an openly vented atmospheric chamber. Small-scale experiments with pure vapor and liquid/vapor mixtures were conducted and compared with simulations. A motivation was to investigate the effects of vent size and liquid content on the peak overpressure and impulse response in the atmospheric chamber. The comparison of vapor-phase $CO_2$ test results with simulations showed good agreement. This numerical code described single-phase gas dynamics inside a closed chamber, but did not model any phase transitions. Hence, the simulations described a vapor-only test into an unvented chamber. Nevertheless, the simulations reproduced the incident shock wave, the shock reflections, and the jet release inside the atmospheric chamber. The rapid phase transition did not contribute to the initial shock strength in the current test geometry. The evaporation rate was too low to contribute to the measured peak overpressure that was in the range of 15–20 kPa. The simulation results produced a calculated peak overpressure of 12 kPa. The liquid tests showed a significantly higher impulse compared to tests with pure vapor. Reducing the vent opening from 0.1 to 0.01 $m^2$ resulted in a slightly higher impulse calculated at 100 ms. The influence of the vent area on the calculated impulse was significant in the vapor-phase tests, but not so clear in the liquid/vapor mixture tests.

**Keywords** Blast wave · Carbon dioxide · Rapid phase transition · Rapid evaporation · Vented explosion

## 1 Introduction

Accidental releases of carbon dioxide ($CO_2$) from a high-pressure reservoir into a confined space include complete tank ruptures and BLEVEs. Hazards associated with these $CO_2$ releases are related to both the harmful properties of the fluid (asphyxiation and frost injuries) and the energy release (blast waves, accelerated fragments, and dynamic loads on structures). The peak pressure and the impulse will be influenced by the initial state of the fluid, the degree of superheat, the amount of mass released, the vent opening area, and the structure geometry. Studies by Zhang et al. [1] and Clayton and Griffin [2] discuss the possible catastrophic consequences of previous $CO_2$ tank explosions.

In a rapid expansion of a pressurized liquefied gas toward atmospheric pressure, the liquid could cross the saturation line without any boiling taking place. The liquid becomes superheated as it enters the metastable region, which is situated between the saturation line and the liquid spinodal line, inside the two-phase envelope. Eventually, the evaporation process will start, usually by heterogeneous nucleation on a solid surface, on particle impurities, or in microscopic gas cavities found on the surface. If heterogeneous nucleation is suppressed, the fluid could reach a highly superheated state close to the liquid spinodal. According to Reid [3,4], the possible generation of a shock wave caused by explosive evaporation could occur by homogeneous nucleation at the superheat limit. At this locus of states, the evaporation rate is very high. However, discussions in the published literature present divergent opinions as to what extent a rapid evaporation process is capable of producing a shock wave [5].

This paper presents small-scale experiments and simulations that describe the release of saturated pressurized $CO_2$ from a high-pressure reservoir at room temperature (292 K) into an openly vented atmospheric chamber. The primary aim

Communicated by G. Ciccarelli.

✉ P. M. Hansen
perha@usn.no

[1] Faculty of Technology, Natural Sciences and Maritime Sciences, University College of Southeast Norway, Kjolnes ring 56, 3918 Porsgrunn, Norway

Published online: 30 March 2018

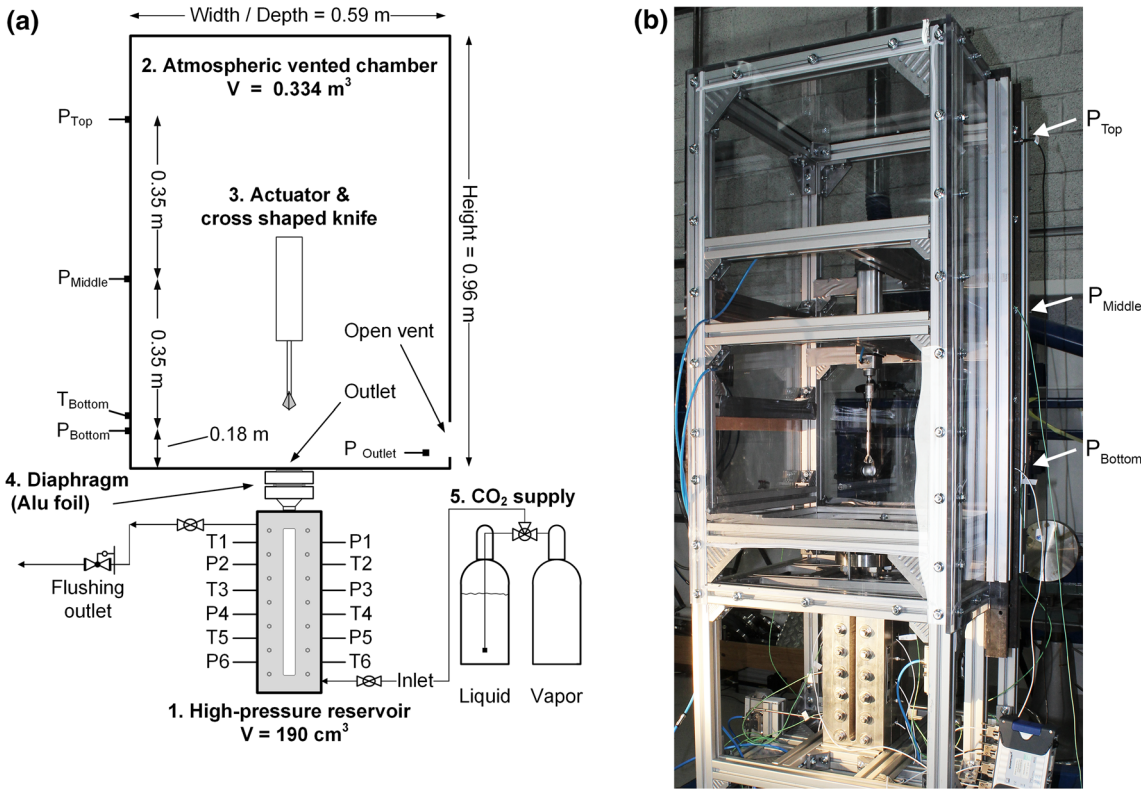


**Fig. 1** **a** Schematic showing the experimental setup, **b** photograph of the high-pressure reservoir and the vented chamber

was to investigate the effects of vent opening size and initial liquid content on the measured pressure and calculated impulse response in the atmospheric chamber. An additional objective was to study whether the volume production resulting from the rapid boiling would contribute to the shock strength in the current test geometry. The results included both experimental work and a numerical simulation of the $CO_2$ release. The CFD model described the gas dynamics in a closed chamber and did not include any phase transitions. The experimental parameters included two different vent areas (0.1 and 0.01 $m^2$) and three different liquid fractions (0, 32, and 68 vol%). The vent opening areas were selected based on a series of tests. Experimental work describing the depressurization and release of $CO_2$ from a high-pressure reservoir has previously been published [6–11], but not with a test geometry identical to the setup in the current study. Li et al. [11] describe tests in a comparable high-pressure section, but their study was mainly limited to the behavior inside the high-pressure vessel.

## 2 Experimental setup and methods

### 2.1 Apparatus

A new test setup was designed and built to study the behavior of pressurized $CO_2$ upon a rapid expansion toward atmospheric pressure. Figure 1 shows a schematic diagram (a) and a photograph (b) of the experimental setup that consisted of the following main parts: (1) a stainless steel high-pressure reservoir, (2) an atmospheric chamber with an adjustable open vent, (3) a cross-shaped knife with a pneumatic plunger actuator, (4) an aluminum foil diaphragm, and (5) a $CO_2$ supply-system with two industry-grade cylinders. The two cylinders supplied liquid-phase and vapor-phase feed. Pressure sensors and temperature sensors were installed at defined positions on the experimental setup.

The high-pressure reservoir was a custom-designed level gauge rated at 10 MPa. The vessel height from the bottom up to the diaphragm was 450 mm. A bottom section, which was a rectangular duct with volume 320 × 16 × 25.4 $mm^3$, had borosilicate glass windows that offered imaging possibilities. A circular section, which had a height of 130 mm, was located between the rectangular duct and the diaphragm. The aluminum foil diaphragm was circular with a 34-mm opening diameter. The total vessel volume was 190 $cm^3$ with the possibility of a 130-$cm^3$ liquid volume. Temperature sensor ports (T1–T6) and pressure sensor ports (P1–P6) were installed on the two steel sidewalls. The vertical spacing between two sensors was 50.8 mm.

The atmospheric chamber volume was 0.334 $m^3$. The support frame, which consisted of Rexroth aluminum profiles, determined the chamber size. Transparent 10-mm polycar-

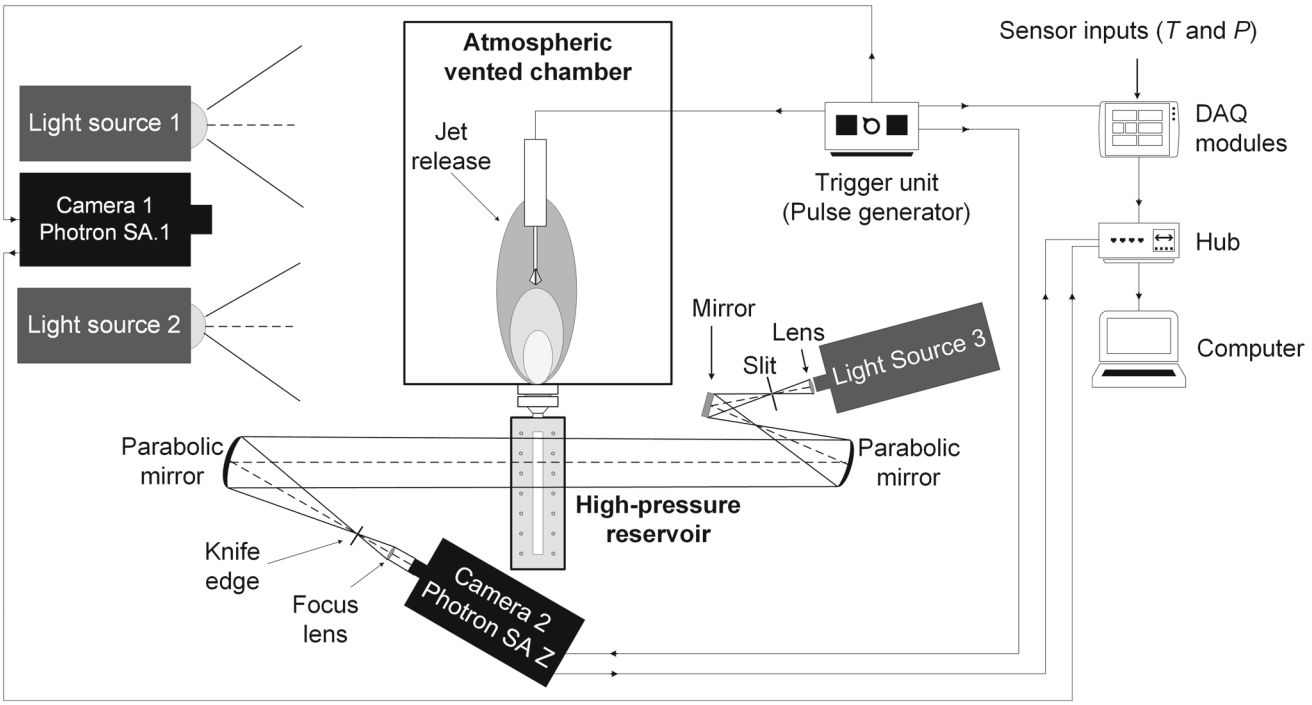


**Fig. 2** Schematic of the visualization setup and the experiment control setup. Camera 1 captured the jet release into the atmospheric vented chamber while camera 2 captured the depressurization inside the high-pressure reservoir

bonate panels covered all six surfaces and enabled visual observation of the $CO_2$ release. The chamber dimensions were $0.59 \times 0.59 \times 0.96\,m^3$. The high-pressure reservoir and the atmospheric chamber had a volume ratio of about 1750. This resembled the release from a 1-$m^3$ $CO_2$ storage tank into a 1750-$m^3$ factory hall. Placing the vent at the bottom of the right sidewall, which can be seen in Fig. 1a, avoided accumulation of $CO_2$. The vent area $A_v$ was fully open at all times.

## 2.2 Instrumentation

Four pressure sensors were installed in the atmospheric chamber. Three sensors (bottom, middle, and top) were mounted flushed to the wall on a vertical U-channel steel beam at the left sidewall. The last sensor was placed on the front sidewall perpendicular to the vent opening. One Kulite-XTM-190-100G piezoresistive transducer with a measuring overpressure range of 0–0.7 MPa and a natural frequency of 95 kHz was installed at the steel beam bottom position. The sensor accuracy was about ± 1% of the measurement range. Pressure results from a test series gave an uncertainty estimate of ± 2 kPa.

The remaining sensors in the vented chamber were Kistler 7001 piezoelectric transducers with a measuring overpressure range of 0–25 MPa and a natural frequency of 70 kHz. The pressure transducers in the high-pressure reservoir were Kulite-XTM-190-2000G piezoresistive sensors with a measuring range of 0–14 MPa and a natural frequency of 410 kHz. The accuracy was ± 1% of the measurement range, and the thermal sensitivity shift was ± 2% per 100 K. All temperature sensors were fast-response Chromel–Alumel, K-type thermocouples with an accuracy of ± 1 K. An Ametek Jofra CTC140A unit calibrated the temperature sensors before the start of the test series.

## 2.3 Camera setup and experiment control

Two high-speed cameras recorded the behavior of the $CO_2$ release upon diaphragm rupture in these experiments. Figure 2 shows a schematic of the visualization setup. A Photron Fastcam SA-1 operating at 5000 frames per second (fps), which used front lighting, captured the release from the high-pressure reservoir into the vented chamber. The light source was one 400-W DEB400D Dedolight and one 250-W Dedocool tungsten light head. A Photron Fastcam SA-Z operating at 75,000 fps, which was combined with a Z-type schlieren setup, captured the expansion and phase transition processes inside the high-pressure reservoir. Two parabolic mirrors combined with a focus lens covered a 0.127-m section of the vessel height.

## 2.4 Test procedure

Before each test, the high-pressure reservoir was flushed three times with pressurized vapor-phase $CO_2$ at 1 MPa. Then, the chamber was slowly filled with either vapor-phase

(TR1 and TR2) or liquid-phase $CO_2$ (TR3–TR5) to the desired liquid level. Visual estimations, which consisted of pixels-to-length conversion of calibrated high-speed images, provided the liquid level data. A 10 min idle period between the filling stage and the test initiation provided thermal equilibrium and stable sensor measurements. The pre-rupture state was saturated $CO_2$ at room temperature. A Quantum Composers 9500 series pulse generator initiated the experiments. A 5-V voltage signal simultaneously triggered the knife actuator, the high-speed cameras, and the two data acquisition systems (HBM Quantum X modules and a Sigma LDS Nicolet digital oscilloscope). The trigger signal opened the valve that filled the pneumatic knife actuator with pressurized air. The piston movement of the actuator lasted about 0.4 s, before the cross-shaped knife punctured the diaphragm completely and with high reproducibility. A shock wave then propagated outward (into the atmospheric chamber), while a rarefaction wave propagated downward (into the high-pressure reservoir). A multiphase $CO_2$ jet followed the initial shock wave.

The high-speed images and the sensor data were stored and then analyzed in MATLAB. High-speed videos with sensor data included were prepared. A comparison of the image observations with the sensor measurements provided a basis for the interpretation of the experimental results.

## 2.5 Simulation method

The 3D simulations of the $CO_2$ release were performed with the USN in-house CFD code [12–14]. Figure 3 shows an illustration of the simulation volume and the computational mesh. The mesh was Cartesian with one mesh length (2.5 mm) in all three directions. The simulation domain had two vertical symmetry planes to reduce computational effort. The symmetry indicated in Fig. 3 was both in the $x$–$z$ and $y$–$z$ planes. Hence, the simulation volume was one quarter of the full volume.

The simulation method is based on a second-order flux limiter centered (FLIC) TVD method. In addition to the mass, momentum, and energy equations, one-species transport equation is solved for $CO_2$ into air. The ideal gas law is used for both the gases ($CO_2$ and air) in the model. The governing equations are:

$$\frac{\partial \boldsymbol{U}}{\partial t} + \frac{\partial}{\partial x}\left(\boldsymbol{F}\left(\boldsymbol{U}\right)\right) + \frac{\partial}{\partial y}\left(\boldsymbol{G}\left(\boldsymbol{U}\right)\right) + \frac{\partial}{\partial z}\left(\boldsymbol{H}\left(\boldsymbol{U}\right)\right) = \boldsymbol{0} \tag{1}$$

$$\boldsymbol{U} = \begin{bmatrix} \rho \\ \rho u \\ \rho v \\ \rho w \\ E \\ \rho Y \end{bmatrix}, \quad \boldsymbol{F}\left(\boldsymbol{U}\right) = \begin{bmatrix} \rho u \\ \rho u^2 + p \\ \rho uv \\ \rho uw \\ u\left(E + p\right) \\ \rho uY \end{bmatrix},$$

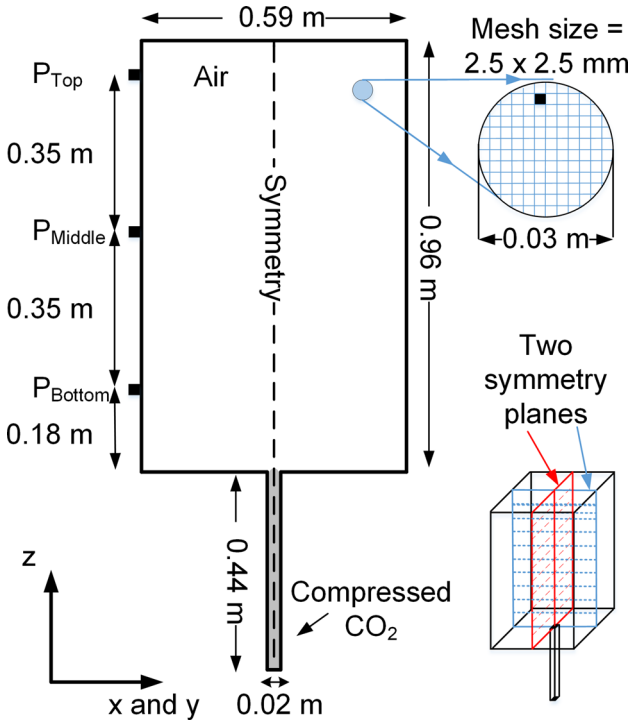


**Fig. 3** Illustration of the simulation geometry and the computational mesh

$$\boldsymbol{G}\left(\boldsymbol{U}\right) = \begin{bmatrix} \rho v \\ \rho vu \\ \rho v^2 + p \\ \rho vw \\ v\left(E + p\right) \\ \rho vY \end{bmatrix}, \quad \boldsymbol{H}\left(\boldsymbol{U}\right) = \begin{bmatrix} \rho w \\ \rho wu \\ \rho wv \\ \rho w^2 + p \\ w\left(E + p\right) \\ \rho wY \end{bmatrix} \tag{2}$$

$$E = \frac{p}{\gamma - 1} + \frac{1}{2}\rho\left(u^2 + v^2 + w^2\right) \tag{3}$$

Equations (1)–(3) show the three-dimensional inviscid transport equations for mass, momentum, energy, and one species. These equations were solved by the second-order accurate, centered FLIC scheme [15] and the fractional step method [16]. The first-order fractional step method solves the transport equations in one direction at a time in sequence as one-dimensional hyperbolic equations. The Courant–Friedrich–Levy (CFL) criterion controls the time-step in the simulation for a CFL number of 0.9, meaning that the fastest wave in the domain can only propagate 90% of the mesh length in one time-step. The inviscid transport equations are chosen because the simulation results should capture the blast wave structures and the main jet-behavior. Even if the viscous stresses become large, they will not influence the wave propagation significantly in this study.

The atmospheric chamber simulation volume, which was modeled as an empty chamber, did not include any vent opening. The numerical code described single-phase gas

**Table 1** Test parameters and results from the five presented test runs and the simulation

| Test number | Initial pressure $P_0$ (MPa) | Initial temp. $T_0$ (K) | Open vent area $A_v$ ($m^2$) | Liquid volume $V_{L,HP}$ ($cm^3$) | Vapor volume $V_{V,HP}$ ($cm^3$) | Liquid fraction (vol%) | Mass of $CO_2$ $m_{CO_2}$ (g) | Peak overpressure $P_{peak,Bottom}$ (kPa) | Impulse at 100 ms $J$ (kPa ms) |
|---|---|---|---|---|---|---|---|---|---|
| TR1 | $5.5 \pm 0.1$ | $292 \pm 1$ | 0.1 | 0 | 190 | 0 | 36 | $15 \pm 2$ | 55 |
| TR2 | $5.3 \pm 0.1$ | $292 \pm 1$ | 0.01 | 0 | 190 | 0 | 36 | $17 \pm 2$ | 149 |
| TR3 | $5.6 \pm 0.1$ | $292 \pm 1$ | 0.1 | 130 | 60 | 68 | 113 | $20 \pm 2$ | 346 |
| TR4 | $5.6 \pm 0.1$ | $292 \pm 1$ | 0.01 | 130 | 60 | 68 | 113 | $15 \pm 2$ | 426 |
| TR5 | $5.6 \pm 0.1$ | $292 \pm 1$ | 0.01 | 70 | 120 | 37 | 77 | $18 \pm 2$ | 206 |
| Simulation | 5.5 | 292 | 0 | 0 | 176 | 0 | 33 | 12 | – |

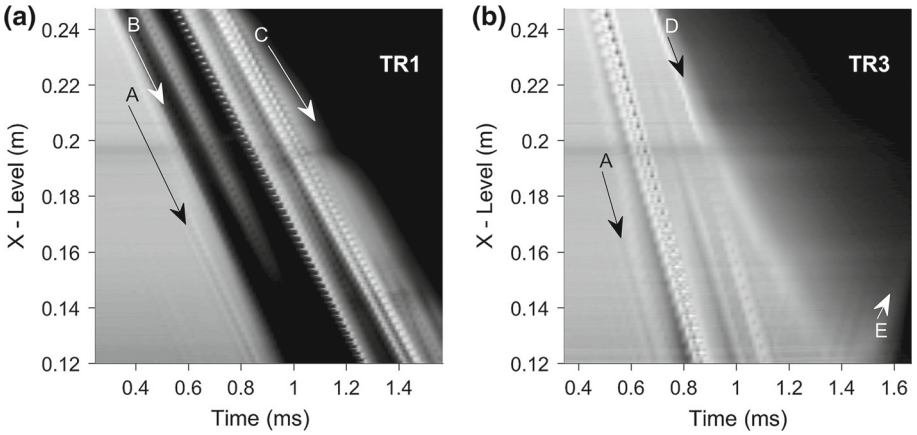


**Fig. 4** $x$–$t$ plots showing processed schlieren images recorded at 75,000 fps. **a** TR1—vapor-only, **b** TR3—68 vol% liquid. Arrows $A$–$E$ indicate slope and position of wave phenomena. $A$, head of the rarefaction fan; $B$, $C$, condensation waves; $D$, heterogeneous nucleation at the glass surface; $E$, rapid boiling propagating from the duct bottom

dynamics and did not model any phase transitions. Consequently, the simulation results were only compared with vapor-only test results. Constant heat capacity ratios of $\gamma_{CO_2} = 1.28$ and $\gamma_{air} = 1.4$ were chosen. This simplification (constant gamma values) would not be valid if the primary aim was to provide accurate numerical simulations of the depressurization in the high-pressure reservoir. Because the simulations primarily focused on the blast waves and the jet release into the atmospheric chamber, this simplification could be justified. In that case, the heat capacity ratio of air would be dominant. A calculated average of $C_p/R$ values from Masi and Petkof [17] gave the $CO_2$ gamma value.

## 3 Results and discussion

Table 1 shows test parameters and results from five presented test runs (TR1–TR5) and one simulation. The open-vent area $A_v$ and the liquid fraction in the high-pressure reservoir were the main parameters. The initial pre-rupture state was saturated $CO_2$ at room temperature (292 K).

The results and discussion section was divided into the following subsections: high-pressure reservoir (Sect. 3.1), atmospheric chamber (Sect. 3.2), simulations (Sect. 3.3), and a brief comparison of experiments and simulations (Sect. 3.4).

### 3.1 High-pressure reservoir

This study focused on the blast wave and the jet released into the atmospheric chamber. Nevertheless, a complete experiment description required some key results from the high-pressure reservoir. Figure 4 shows two $x$–$t$ plots of TR1 (a) and TR3 (b). These $x$–$t$ plots represent 100 processed high-speed schlieren images each that captured the initial stage of depressurization up to about 1.6 ms. Hansen et al. [7] described the preparation method that used an averaging technique to emphasize the characteristic velocities. The main disadvantage compared with stacked image series was a loss in the ability to resolve flow details. The $y$-axis was the visual level range in the high-pressure reservoir, starting from a position $x = 0.12$ m above the duct bottom. Upon diaphragm rupture, defined as time $t_0 = 0$ ms, a rarefaction fan propagated through the duct at the local speed of sound. Arrows ($A$–$E$) in Fig. 4a, b indicate the slope and position of the wave phenomena.

Arrows $A$ in Fig. 4 locate the head of the rarefaction fan. The visually estimated gas-phase sound speed ($200 \pm 10$ m/s) in Fig. 4a corresponded with the speed of sound calculated

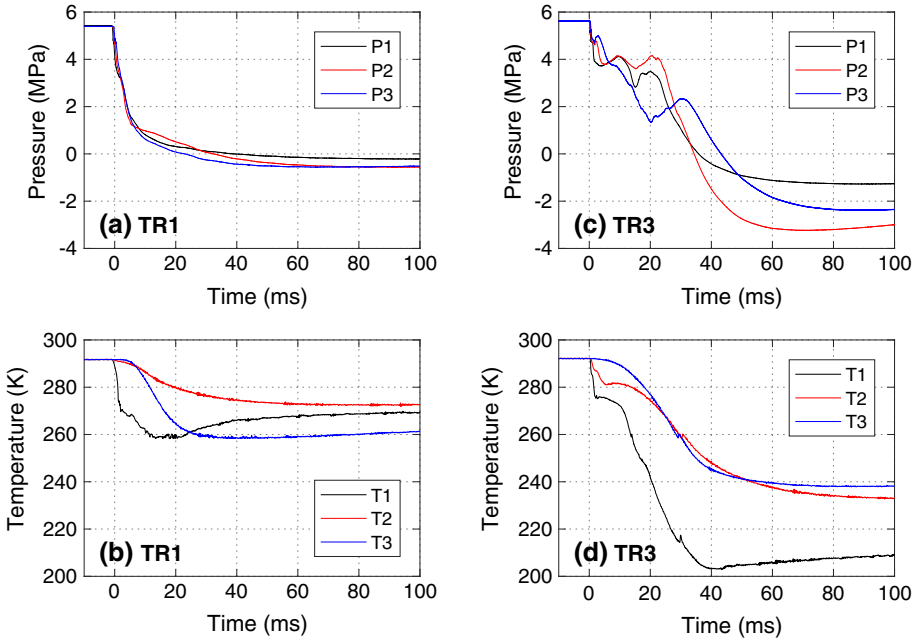


**Fig. 5** Pressure-time histories and temperature-time histories from the three upper sensor ports in the high-pressure reservoir. TR1 (vapor-only) and TR3 (liquid/vapor mixture). **a** TR1 pressure, **b** TR1 temperature, **c** TR3 pressure, **d** TR3 temperature

by the Span Wagner (SW-EOS) technical equation of state (197 m/s). Likewise, a visually estimated liquid-phase sound speed ($344 \pm 10$ m/s) in Fig. 4b corresponded with the calculated SW-EOS value (348 m/s). Arrows *B* and *C* in Fig. 4a showed the condensation waves that followed the sudden depressurization. Arrow *D* indicated the creation of micro-size gas bubbles (heterogeneous nucleation) on the glass surface. Arrow *E* showed rapid boiling that started from the duct bottom.

The pressure traces in Fig. 5a, c showed that the duration of the expansion process depended on the initial liquid fraction. The time period increased from about 20 ms (vapor-only) to about 40 ms (68 vol% liquid). As expected, the measured temperature drop caused by the evaporation (Fig. 5d) was significantly larger than the temperature drop caused by just the vapor-expansion (Fig. 5b). At equilibrium states with pressure below the triple point ($T = 217$ K, $P = 0.518$ MPa), only solid-phase and vapor-phase $CO_2$ exist. Temperature measurements below 217 K in Fig. 5d suggested a solid-particle fraction greater than zero. A significant difference in temperature histories of T1 compared to T2 and T3 was observed in Fig. 5d. A possible reason could be that T1 was placed 1–2 mm into the duct, whereas T2 and T3 were placed flushed to the wall.

In Fig. 5c, the pressure decrease from the pre-rupture state at 5.6 MPa to the onset of boiling was about 0.8 MPa. Heterogeneous nucleation on the duct surfaces limited the degree of superheat that was achieved in the current test setup. According to Reid [3,4], the evaporation rate would then be too low to produce a shock wave. To achieve a higher degree of superheat in the rapid depressurization process, a smoother surface and an absence of nucleation sites would be required. Examples of such test setups were presented by Shepherd and Simões-Moreira [18], Hill [19], Reinke [20], and Simões-Moreira [21].

### 3.2 Atmospheric vented chamber

All the jets observed in this study were non-stationary with an outflow duration from the high-pressure reservoir less than 100 ms. Upon diaphragm rupture, the front-lit high-speed camera did not capture the propagation of the initial blast wave into the atmospheric chamber. Moreover, the $CO_2$ jet was only visible when it consisted of a liquid/vapor mixture or contained solid particles. Pure $CO_2$ vapor would be transparent, whereas multiphase compositions appeared as an opaque white cloud.

Figure 6 shows selected high-speed video images of the $CO_2$ jet from TR1 (vapor-only) captured at specified times after diaphragm rupture. In Fig. 6a, a jet of partially condensed vapor was observed propagating into the atmospheric vented chamber at a vertical velocity of about 190 m/s. The knife actuator and its support frame acted as an obstacle, which is illustrated in Fig. 6b, that restricted a free jet propagation. At about 6 ms, the jet hit the top surface and was reflected downward (not visible in Fig. 6). After 10 ms, the jet diameter and height were significantly reduced. The maximum jet-diameter in the vapor-only tests was 0.11 m. Hence, the minimum distance from the pressure sensors to the edge of the jet was 0.24 m. Figure 5a shows that the high-pressure reservoir approached an atmospheric pressure after about 20 ms. These pressure measurements corresponded with the disappearance of the $CO_2$ cloud observed in Fig. 6c, d.

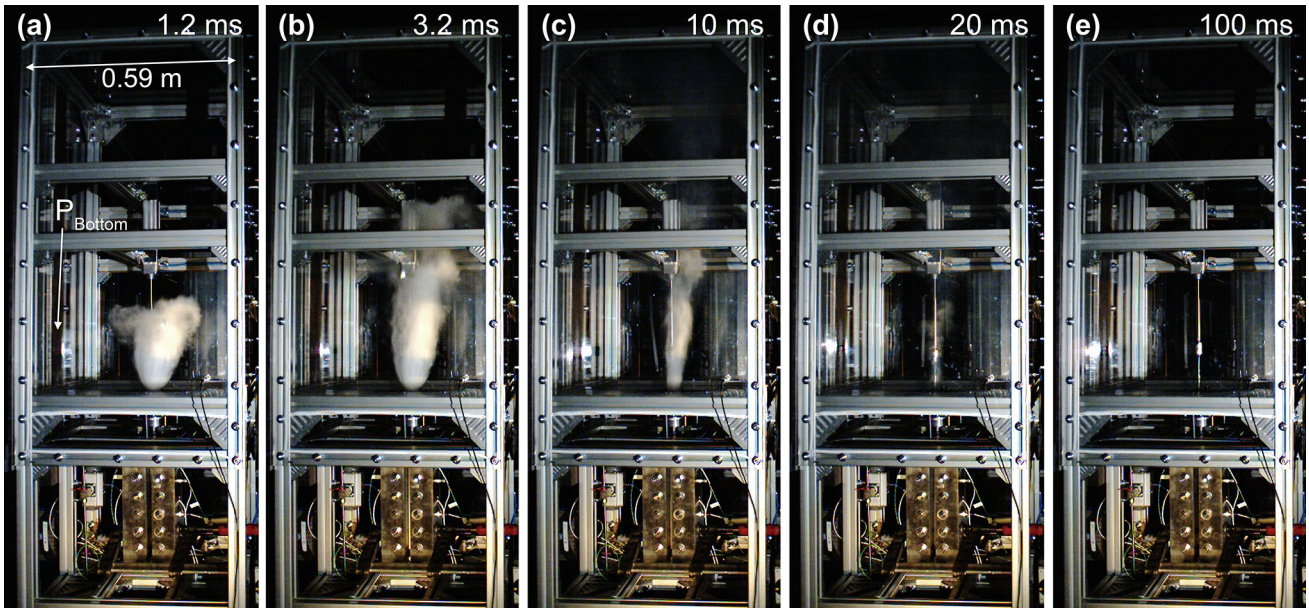


**Fig. 6** Selected video frames showing the release of $CO_2$ vapor into the open vent chamber. TR1 (vapor-only)

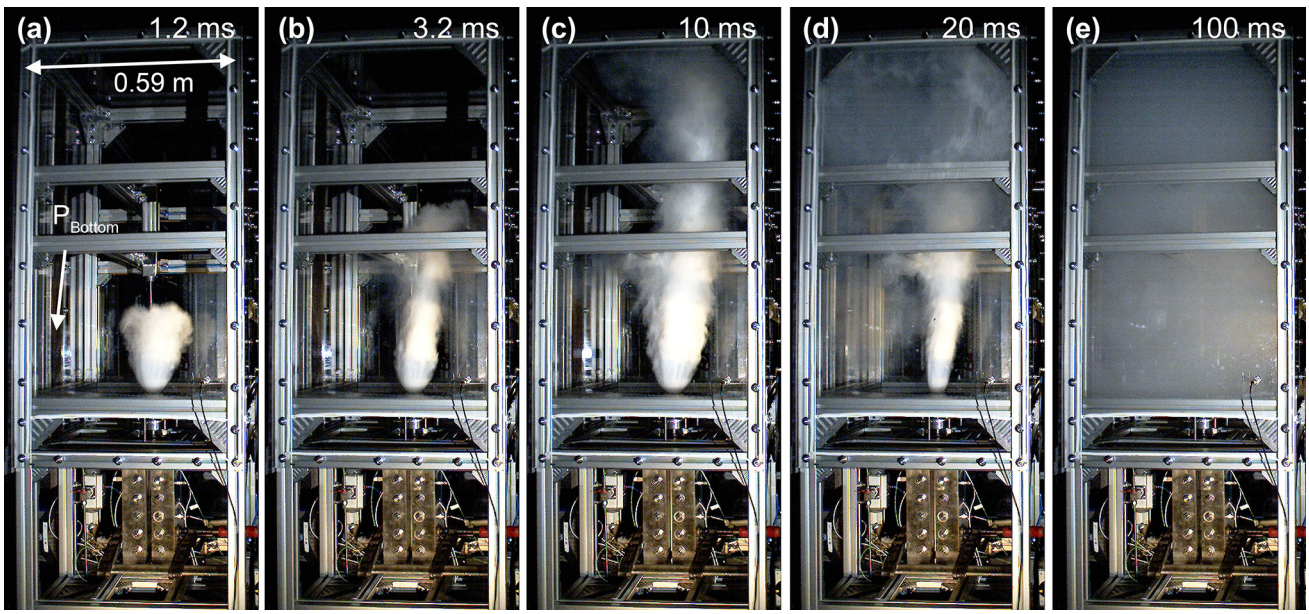


**Fig. 7** Selected video frames showing the release of a liquid/vapor mixture into the open vent chamber. TR3 (68 vol% liquid)

Figure 7 shows selected high-speed video images of the jet release in TR3 (68 vol% liquid). The vertical jet velocity at the early stage was equal to TR1. In the first 3 ms after diaphragm rupture, the jet release in TR1 and TR3 appeared almost identical. No contribution from the liquid fraction in the high-pressure reservoir was observed. During this period of time, the jet behavior was governed by the expansion of the vapor headspace.

After 3.2 ms, the jet suddenly appeared more energetic, and the outflow seemed to increase (see Fig. 7c). The jet-plume diameter increased from 0.09 to 0.18 m. According to earlier work [6,7] and tests not included in this article, this observation would correspond with the arrival of the liquid/vapor interphase (contact surface) at the reservoir exit plane. After 8–10 ms, the jet reached the top surface (see Fig. 7c) and was reflected downward. The video frames in Fig. 7c, d, and the pressure measurements in Fig. 5a, c show that a larger initial liquid fraction in the high-pressure reservoir resulted in a $CO_2$ jet with longer duration and a more vigorous appearance. The jet release period was increased from $\approx$20 ms (vapor-only) to $\approx$40 ms (liquid/vapor mixture). After 50–100 ms, the vented chamber was filled with

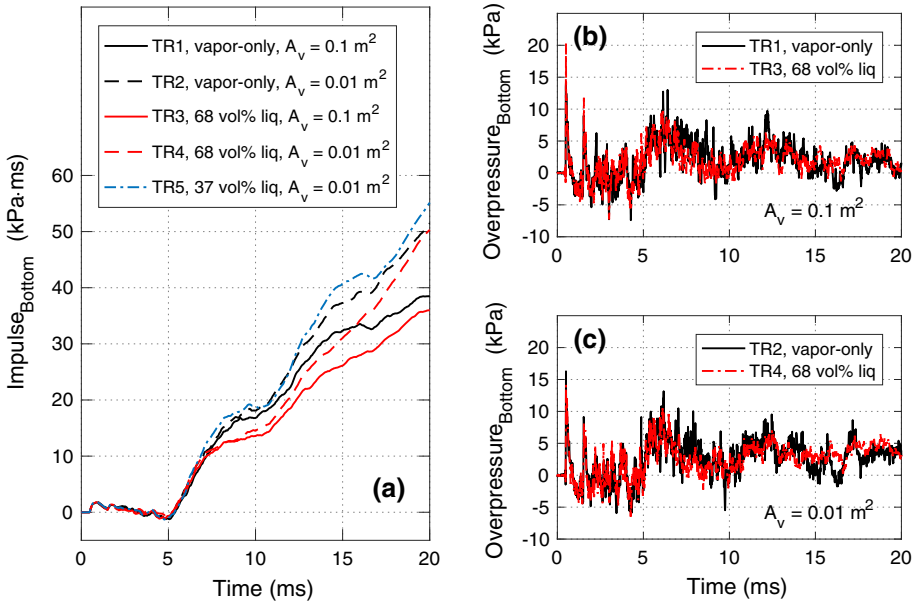


**Fig. 8** **a** Impulse calculations, **b**, **c** pressure measurements from the vented chamber bottom sensor. 0–20 ms after diaphragm rupture. Five tests (TR1–TR5), two vent areas (0.1 and 0.01 $m^2$), and three liquid ratios (0, 37, and 68 vol% liquid)

a white mist (Fig. 7e). The sudden temperature decrease ($\Delta T \approx 16$ K) could condense some of the water in the air that was originally present in the atmospheric chamber. Hence, a fraction of the observed mist could originate from micro-size water droplets.

The high-speed videos showed periodic wall oscillations inside the vented chamber because of multiple shock reflections (not seen in Figs. 6, 7). High-frequency vibrations originating from the initial shock wave propagated along the U-channel steel beam. These vibrations were more dominant in the middle and top sensor positions. The Kulite sensor (bottom position) seemed less sensitive to these vibrations than the Kistler sensors (top, middle, and outlet) in the present experimental study. In addition, it could provide measurements for a longer time period because of the piezoresistive operation. For these reasons, the presented pressure histories from the vented chamber originated from the Kulite bottom sensor.

The measured peak overpressure from the initial blast wave in TR1–TR5 was in the range from 15 to 20 kPa. Figure 8 shows one impulse plot and two pressure plots from the first 20-ms period. The pressure histories in the atmospheric chamber suggested the evaporation process was too slow in the current test geometry to contribute to the initial shock strength. In this study, the gas dynamics dominated the pressure response in the atmospheric chamber. No additional peaks or pressure increase could be related to the boiling liquid released from the high-pressure reservoir in the period from 0 to 20 ms. Figures 4b and 5c in Sect. 3.1 showed that the degree of superheat achieved in the high-pressure reservoir was limited by heterogeneous nucleation. These observations suggested that adiabatic evaporation at a more moderate degree of superheat would not contribute to the shock wave.

The calculated impulses in Fig. 8a were almost identical up to about 7 ms. Then, the impulse in the tests with lowest liquid fractions (TR1, TR2, and TR5) showed a larger increase rate than the tests with the highest liquid fractions (TR3 and TR4).

Figure 9 shows an impulse plot and a pressure plot from the 0–500-ms period. The pressure response in the atmospheric chamber seemed to coincide with the liquid content in the high-pressure reservoir. In TR3 and TR4, an increase from zero to 5–7 kPa was observed at the bottom pressure-sensor, starting at about 30 ms. A larger liquid content resulted in a longer time period at a positive overpressure. Consequently, the calculated impulses were significantly higher when the high-pressure reservoir contained a large liquid/vapor fraction, as compared to pure vapor. The duration of the liquid/vapor test was longer than 100 ms, because of the extra time needed to push the $CO_2$ cloud through the vent opening.

An unexpected crossover in the impulse histories of TR3 and TR4 was observed in Fig. 9 at $t = 150$ ms. One would expect that the smallest vent opening area ($A_v = 0.01\ m^2$) would result in the highest impulse because of a larger pressure buildup. A reason for the crossover could be the influence of the temperature drop on the pressure measurements in the chamber. As a conservative estimation, the impulses reported in Table 1 were calculated at 100 ms. A permanent offset originating from a thermal zero shift would result in a significant error contribution to the impulse calculations. Because of the rapid expansion and evaporation processes, the temperature decreased significantly both inside the high-pressure reservoir and in the vented chamber.

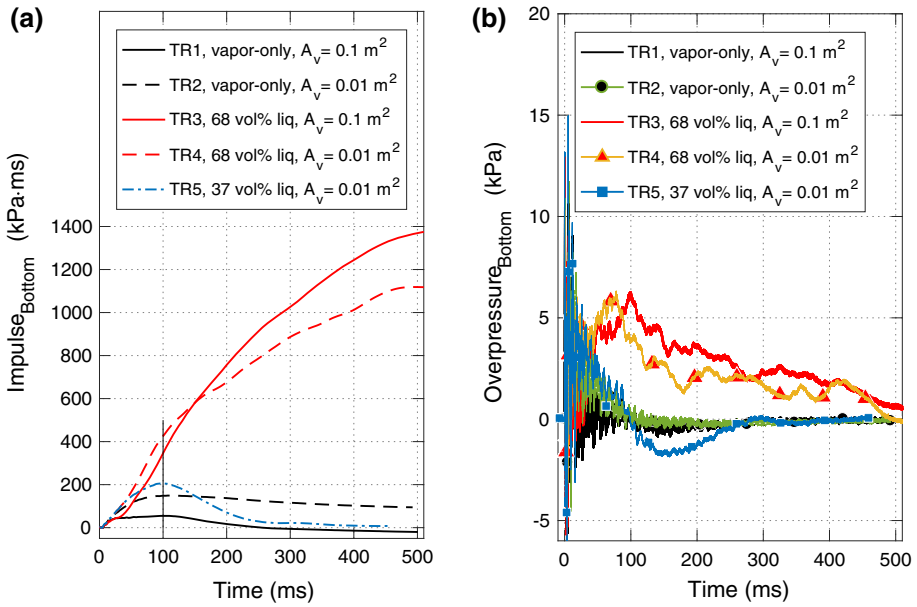


**Fig. 9** **a** Impulse calculations, **b** pressure measurements from the vented chamber bottom sensor. 0–500 ms after diaphragm rupture. Five tests (TR1–TR5), two vent areas (0.1 and 0.01 $m^2$), and three liquid ratios (0, 37, and 68 vol% liquid)

The following suggestions apply to future studies. It would be preferable to secure a nearly instantaneous release of liquid-phase $CO_2$ into the vented chamber, as recommended by Voort et al. [10]. This would improve the investigations concerning the effect of the rapid boiling on the blast wave pressure and calculated impulse. Further investigations should involve tests with a minimized vapor headspace that give a liquid content closer to 100%. Reducing the volume of the atmospheric chamber could be favorable when studying the effect of vent area on the measured pressure response. The possible generation of a shock wave would probably also require a high-pressure reservoir with a diverging/conical geometry.

### 3.3 Simulations of the $CO_2$ release (vapor-only, no vent)

The 3D simulations covering the 0–20-ms period were performed with the USN in-house CFD code. This numerical work reproduced the behavior of vapor-only $CO_2$ (no phase transitions) released into a closed chamber (no vent). The initial state was $P = 5.5$ MPa and $T = 292$ K. Because the chamber walls produced a multiple of shock reflections, these simulations provided a useful aid to interpret the experimental pressure histories presented in Fig. 8. A time-series of numerical schlieren images that represented scaled density gradients is shown in Fig. 10. These time-series reproduced the incident shock wave, the shock reflections, and the $CO_2$ jet release. The time specified in the image frames, which covered the period from 0.6 to 18.9 ms, corresponded with the simulated pressure-time histories and impulse-time histories presented in Fig. 11. The incident shock wave, which was observed at $t = 0.6$ ms in Fig. 10, gave the first overpressure peak in Fig. 11b–d.

The reflected shock shown at $t = 1.3$ ms in Fig. 10 gave the second overpressure peak in Fig. 11b–d. The upper surface and the sidewalls formed compression corners that produced the multiple of pressure peaks observed in Fig. 11b. The pressure wave then propagated in a vertical periodic pattern as shown in Figs. 10 and 11. The $CO_2$ jet interacted with the reflected shock wave at a time between 3.2 and 3.9 ms in Fig. 10. However, the reflected shock did not seem to influence the progression of the jet. Between the numerical images at 4.6 and 5.4 ms, the jet reached the top surface and was reflected downward. At 8.1 ms, the reflected $CO_2$ jet and a reflected shock (second cycle) arrived at the top pressure-sensor position almost simultaneously. It seemed that both the jet and the shock contributed to the pressure increase observed in Fig 11b.

### 3.4 Comparison: simulations and experimental results

The experimental impulse histories and pressure histories in Fig. 12 showed a good qualitative agreement with the simulations. The numerical results reproduced both the incident shock wave and the main shock reflections inside the atmospheric chamber. During the 0–20-ms period, the pressure response in the atmospheric chamber was governed by the rapid expansion of vapor-phase $CO_2$ from the pre-rupture state to atmospheric pressure. The simplified simulation geometry, which did not include a vent opening nor obstacles, contributed to some discrepancies in pressure histories observed in the 14–20-ms period. The gradual pressure decrease observed in the experimental results was not present

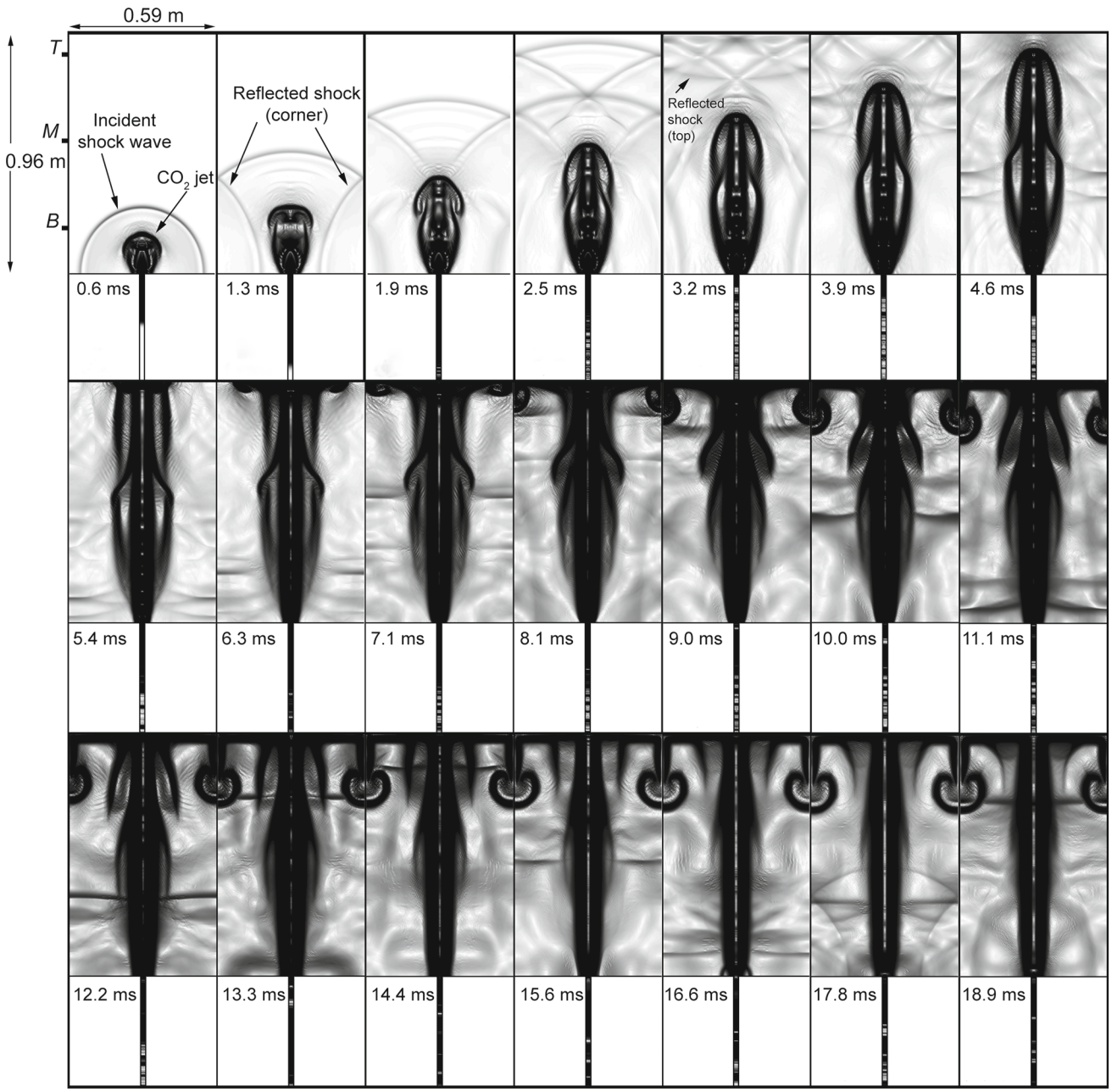


**Fig. 10** Numerical schlieren time-series (0.6–18.9 ms) that represents scaled density gradients. Letters $T$, $M$, and $B$ show pressure-time history positions. Simulations of $CO_2$ (vapor-only) released from a high-pressure reservoir into a closed atmospheric chamber. The numerical schlieren reproduces the incident shock wave, the shock reflections, and the jet progression

in the simulations, because the simulation volume was a closed chamber.

Although the simulation code predicted the behavior of the $CO_2$ release in this study, it did not model phase transitions. Hence, it is not designed to model a true BLEVE. Examples of such models, which also take into account the contribution from rapid evaporation of superheated liquids, include the work by Tosse [22] and Xie [23].

## 4 Conclusions

This study investigated the release of pressurized $CO_2$ from a high-pressure reservoir into an openly vented atmospheric chamber. The pressure response was studied in a combination of small-scale experiments and simulation work. The rapid boiling did not contribute to the initial shock strength in the current test geometry. The evaporation rate was too low to contribute to the measured peak pressure that was

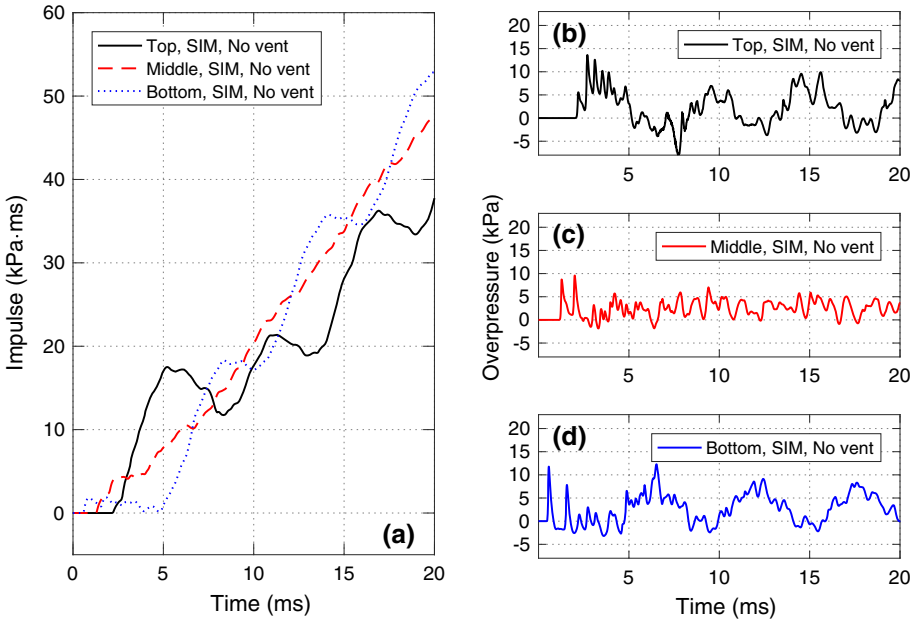


**Fig. 11** Simulation results from the 0–20-ms period. Top, middle, and bottom sensor position. **a** Impulse histories, **b** top position pressure history, **c** middle position pressure history, **d** bottom position pressure history

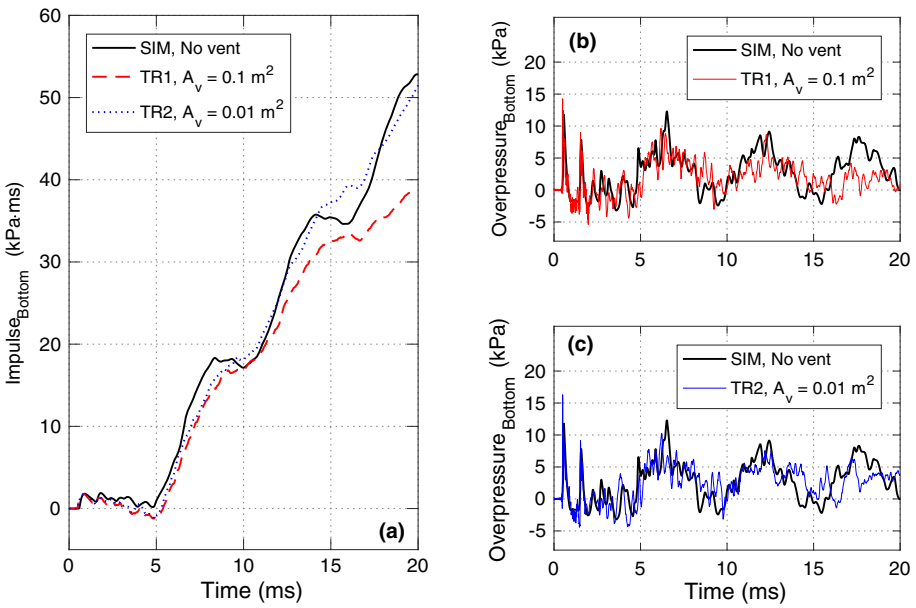


**Fig. 12** Comparison of simulations and experimental results from the vented chamber bottom sensor. **a** Impulse histories, **b**, **c** pressure histories

in the 15–20 kPa range. Simulations of the vapor-only $CO_2$ release into a closed atmospheric chamber gave a calculated overpressure of 12 kPa. The tests with a liquid/vapor mixture in the high-pressure reservoir showed a significantly higher impulse compared to the vapor-only tests. Reducing the vent area from 0.1 to 0.01 $m^2$ resulted in a slight increase in impulse calculated at 100 ms. The effects of the vent area size on the impulse was evident in the vapor-only tests, but not so clear in the liquid/vapor mixture tests.

## References


1. Zhang, Y., Schork, J., Ludwig, K.: Revisiting the conditions for a $CO_2$ tank explosion. Paper presented at the AIChE 2013 Spring Meeting, San Antonio, Texas, 28 April–2 May 2013. ISBN: 9781627484480
2. Clayton, W.E., Griffin, M.L.: Catastrophic failure of a liquid carbon dioxide storage vessel. Process Saf. Prog. **13**(4), 202–209 (1994). https://doi.org/10.1002/prs.680130405
3. Reid, R.C.: Superheated liquids. Am. Sci. **64**, 146–156 (1976)
4. Reid, R.C.: Possible mechanism for pressurized-liquid tank explosions or BLEVE's. Science **203**(4386), 1263–1265 (1979). https://doi.org/10.1126/science.203.4386.1263
5. Birk, A.M., Davison, C., Cunningham, M.: Blast overpressures from medium scale BLEVE tests. J. Loss Prev. Process Ind. **20**(3), 194–206 (2007). https://doi.org/10.1016/j.jlp.2007.03.001

6. Tosse, S., Vaagsaether, K., Bjerketvedt, D.: An experimental investigation of rapid boiling of $CO_2$. Shock Waves **25**(3), 277–282 (2015). https://doi.org/10.1007/s00193-014-0523-6
7. Hansen, P.M., Gaathaug, A.V., Bjerketvedt, D., Vaagsaether, K.: The behavior of pressurized liquefied $CO_2$ in a vertical tube after venting through the top. Int. J. Heat Mass Transf. **108**, 2011–2020 (2017). https://doi.org/10.1016/j.ijheatmasstransfer.2017.01.035
8. Bjerketvedt, D., Egeberg, K., Ke, W., Gaathaug, A., Vaagsaether, K., Nilsen, S.H.: Boiling liquid expanding vapor explosion in $CO_2$ small scale experiments. Energy Proced. **4**, 2285–2292 (2011). https://doi.org/10.1016/j.egypro.2011.02.118
9. Ciccarelli, G., Melguizo-Gavilanes, J., Shepherd, J.E.: Pressure-field produced by the rapid vaporization of a $CO_2$ liquid column. In: Proceedings of the 30th International Symposium on Shock Waves, Tel-Aviv (2015). https://doi.org/10.1007/978-3-319-44866-4_87
10. Voort, M.M., Berg, A.C., Roekaerts, D.J.E.M., Xie, M., Bruijn, P.C.C.: Blast from explosive evaporation of carbon dioxide: experiment, modeling and physics. Shock Waves **22**, 129–140 (2012). https://doi.org/10.1007/s00193-012-0356-0
11. Li, M., Liu, Z., Zhou, Y., Zhao, Y., Li, X., Zhang, D.: A small-scale experimental study on the initial burst and the heterogeneous evolution process before $CO_2$ BLEVE. J. Hazard. Mater. **342**, 634–642 (2018). https://doi.org/10.1016/j.jhazmat.2017.09.002
12. Vaagsaether, K., Knudsen, V., Bjerketvedt, D.: Simulation of flame acceleration and DDT in $H_2$-air mixture with a flux limiter centered method. Int. J. Hydrog. Energy **32**(13), 2186–2191 (2007). https://doi.org/10.1016/j.ijhydene.2007.04.006
13. Gaathaug, A.V., Vaagsaether, K., Bjerketvedt, D.: Experimental and numerical investigation of DDT in hydrogen–air behind a single obstacle. Int. J. Hydrog. Energy **37**(22), 17606–17615 (2012). https://doi.org/10.1016/j.ijhydene.2012.03.168
14. Vaagsaether, K.: Modelling of gas explosions. PhD Thesis, Telemark University College/NTNU (2010). http://hdl.handle.net/11250/2437792
15. Toro, E.F.: Riemann Solvers and Numerical Methods for Fluid Dynamics: A Practical Introduction. Springer, Berlin (2009). https://doi.org/10.1007/b79761
16. LeVeque, R.J.: Finite Volume Methods for Hyperbolic Problems. Cambridge Texts in Applied Mathematics. Cambridge University Press, Cambridge (2002). https://doi.org/10.1017/CBO9780511791253
17. Masi, J.F., Petkof, B.: Heat capacity of gaseous carbon dioxide. J. Res. Natl. Inst. Bur. Stand. **48**(3), 179–187 (1952). https://doi.org/10.6028/jres.048.025
18. Shepherd, J.E., Simões-Moreira, J.R.: Evaporation waves in superheated dodecane. J. Fluid Mech. **382**, 63–86 (1999). https://doi.org/10.1017/S0022112098003796
19. Hill, L.G.: An experimental study of evaporation waves in a superheated liquid. PhD Thesis, California Institute of Technology (1991)
20. Reinke, P.: Surface boiling of superheated liquid. PhD Thesis, ETH Zürich (1997)
21. Simões-Moreira, J.R.: Adiabatic evaporation waves. PhD Thesis, Rensselaer Polytechnic Institute (1994)
22. Tosse, S.: The rapid depressurization and evaporation of liquefied carbon dioxide. PhD Thesis, University College of Southeast Norway (2017)
23. Xie, M: Thermodynamic and gasdynamic aspects of a boiling liquid expanding vapour explosion. PhD Thesis, Delft University of Technology (2013)

# Paper C

# Rapid depressurization and phase transition of $CO_2$ in vertical ducts – Small-scale experiments and Rankine-Hugoniot analyses

This paper is submitted to Journal of Hazardous Materials. (Submitted 15 May 2018).

# Rapid depressurization and phase transition of $CO_2$ in vertical ducts – small-scale experiments and Rankine-Hugoniot analyses

Per Morten Hansen[a,*]. André Vagner Gaathaug[a]. Dag Bjerketvedt[a]. Knut Vaagsaether[a].

[a]University of South-Eastern Norway, Kjolnes ring 56, 3918 Porsgrunn, Norway

* Corresponding Author. Email: perha@usn.no . Orchid: https://orcid.org/0000-0001-7048-9137

## Abstract

This study discusses the rapid expansion and phase transition of liquefied carbon dioxide ($CO_2$) in vertical ducts. Results from small-scale experiments in three test setups (A, B, and C) were compared with a Rankine-Hugoniot model that treats the phase transition as an adiabatic evaporation wave of constant thickness. The model calculates the fluid properties behind the evaporation wave. The motivation was to quantify hazards and energy-release in tank explosions such as a boiling liquid expanding vapor explosion. The experimental results corresponded with a Chapman Jouguet (CJ) solution. The contributions include a mapping of CJ solutions calculated from a range of pre-rupture conditions. The puncture of a diaphragm (setup A, and B), or complete test section rupture (setup C) initiated the tests. The three test setups provided a range of pressures for the model. Evaporation waves were observed, propagating with velocities of 35-42 $ms^{-1}$ (setup A, and B), and ~ 10 $ms^{-1}$ (setup C) into the superheated liquid. The calculated vapor mass fraction behind of the evaporation wave was in the range 0.21-0.23. The study presents a strategy, which incorporates the calculated vapor mass fraction, to predict the energy released in a tank explosion.

**Keywords:** Carbon dioxide; Rankine-Hugoniot analysis; rapid evaporation; evaporation wave; BLEVE

## 1. Introduction

The hazards of pressurized liquefied gases such as ammonia, propane, and carbon dioxide ($CO_2$) include loss of containment and tank explosions. A blast wave and a nearly instantaneous venting of the vapor head-space is followed by rapid evaporation of the liquid phase. Previous studies show that the evaporation process could increase the duration of the blast wave. $CO_2$ is often stored and transported as a pressurized liquefied gas. The establishment of carbon capture and storage (CCS) value chains is a part of the strategy to mitigate greenhouse gas emissions. An aim in the Paris climate agreement is to limit future temperature increases to below 2 K. It is expected that the annual amount of $CO_2$ being processed at high pressure will increase. The International Energy Agency (IEA) estimated that about 94 Gt of $CO_2$ must be captured and stored by the year 2050 [1]. To deliver on these ambitions, a step-change in the number of large scale-projects is needed, as compared to the 15 facilities operating in 2016 [1,2]. The design and construction of the necessary infrastructure require risk assessments to ensure safe operation of the process facilities. Hazard identification is a part of the risk assessment and includes the study of previous incidents, identifying the primary causes and mitigating measures. The sudden rupture of a pressure vessel, storage tank or pipeline containing dense phase $CO_2$ poses a hazard that has resulted in some industrial accidents in modern time. Three fatal accidents that all resulted in human fatalities and significant material damage were the incidents in Repcelak, Hungary [3], Worms, Germany [4] and Yuhang, China [5]. The identified main reasons for these tank failures included overfilling, overheating that caused excessive pressure, and brittle failure. The mitigation of future accidents requires sufficient knowledge about the physics of the rapid expansion and phase transition phenomena.

In a rapid depressurization process, a pure liquid substance can under certain conditions reach its boiling point without the initiation of a phase change. The substance remains in a superheated liquid state as it transgresses the liquid saturation line and enters the metastable region inside the two-phase. The area between the liquid saturation curve and the liquid spinodal curve form the metastable liquid region. As the liquid continues to expand, the degree of superheat increases until the evaporation process eventually starts. Under certain conditions, the phase change can be restricted to a narrow region. A name of this phase transition mode is an evaporation wave that propagates through the expanded liquid. The evaporation wave represents a jump between a superheated liquid state and a liquid-vapor two-phase equilibrium state. This analysis is analog to the investigation of deflagration waves described in premixed combustion studies. Previous studies [6-25] discuss experimental investigations of evaporation waves. These publications describe the analogy to the propagation of deflagration waves in premixed reactive flows, and the use of a Rankine-Hugoniot analysis to model the wave propagation. The importance of the Chapman Jouguet (CJ) solution as an upper limit of the evaporation wave velocity and mass flux in choked flow conditions is often discussed. Thompson et al. [8] suggested that the CJ condition for deflagration governed the evaporation wave velocity. On the other hand, Shepherd and Simões-Moreira [12] stated that the evaporation wave velocity depends on the pressure drop across the wave and the degree

of superheat in the liquid in front of the wave. They observed that evaporation waves took place at "moderate" superheats. At high superheats, heterogeneous nucleation was observed ahead of the wave [12].

When the vessel contains a pressurized liquefied gas kept at a temperature higher than its atmospheric pressure boiling point, a catastrophic failure resulting from loss of containment can be referred to as a boiling liquid expanding vapor explosion (BLEVE). The definition proposed by Birk et al. [26] is used in the current publication: "A BLEVE is an explosive release of expanding vapor and boiling liquid when a container holding a pressure liquefied gas fails catastrophically." This definition does not put restrictions on what triggers the explosion or the underlying boiling mechanisms (heterogeneous or homogeneous nucleation). Two requirements are however that the container opens completely in the catastrophic failure, and that the contents are released nearly instantaneous [26]. Reid [27-29] suggested that a BLEVE is initiated by homogeneous nucleation at the kinetic superheat limit. Gas bubbles are then spontaneously created in the liquid bulk and do not require a solid surface as in heterogeneous nucleation. Incident reports suggested however that the consequences could be severe also below the superheat limit [3-5].

This paper presents results from small-scale experiments with rapid expansion and phase transition of pressurized liquefied $CO_2$. A Rankine-Hugoniot model that use an integral form of the conservation equations, the Span-Wagner technical equation of state [30] and saturated $CO_2$ state data from NIST [31] is presented. This study aims to model evaporation waves in $CO_2$ by the jump conditions in a Rankine-Hugoniot analysis. The study includes a comparison of calculated results and experimental values. Three different test designs offer a range of initial conditions for the model. An objective is to calculate realistic flow velocities and thermodynamic states behind the evaporation wave. This information is valuable from a process safety perspective. Previously published studies presented theoretical and experimental work with similar scenarios [32-46]. To the author's knowledge, no other works exist that use a Rankine-Hugoniot analysis to model the evaporation waves in $CO_2$.

## 2. Experimental setup and methods

This study incorporates experimental results from three test setups, denoted A, B and C. Figure 1 shows three schematics that include the main components. Sub-section 2.1 describes setup A in brief. This test setup is identical to the high-pressure section of the rig that was presented in [37]. Sub-sections 2.2 and 2.3 contain a short description of the test setups B and C that were presented in the publications [32-36]. Setup C resembled a tank explosion with a vessel (plastic tube) that ruptured completely during the test.

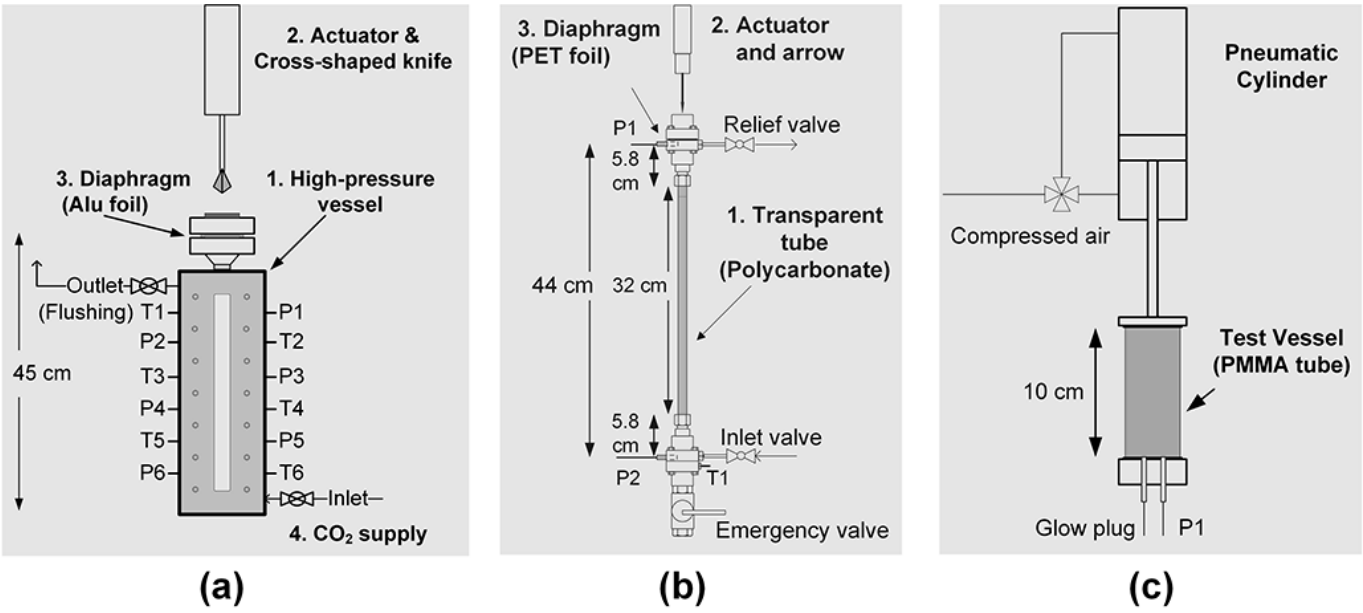


**Fig. 1.** Schematic diagrams that show the three experimental setups included in the study. (a) Setup A, stainless steel square channel with glass windows. (b) Setup B, polycarbonate tube. (c) Setup C, polymethyl methacrylate PMMA tube.

### 2.1 Experimental setup A

Test setup A (see Fig 1a) included the following main parts: (1) a stainless steel high-pressure vessel with a volume of 190 $cm^3$; (2) a cross-shaped knife driven by a pneumatic plunger actuator; (3) an aluminum foil diaphragm; and (4) a $CO_2$ supply system that consisted of two industry grade cylinders (liquid and vapor phase). Temperature sensor ports (T1-T6) and pressure sensor ports (P1-P6) were installed on the two steel side-walls. Hansen et al. [37] described further details about the apparatus and the instrumentation.

A Photron Fastcam SA-Z high-speed camera operating at frame-rates between 27,000 and 75,000 frames per second (fps) recorded the expansion and phase transition processes inside the high-pressure channel. The test campaign included high-speed imaging techniques such as front-lit, back-lit, and z-schlieren arrangements. Figure 2 shows schematics of two visualization setups. A z-schlieren setup (Fig 2a and Fig 5b) covered a 0.23-m section of the vessel height. A back-lit setup that used a Navitar 12 × zoom lens captured images with high magnification (Fig 2b and Fig 6).

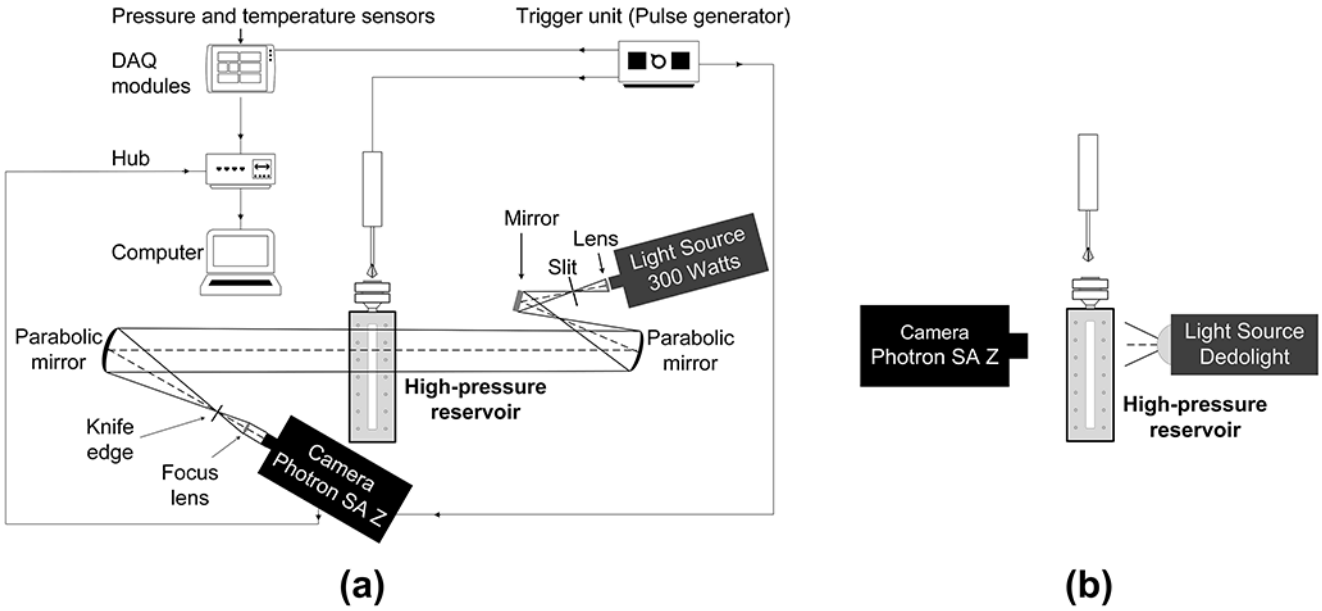


**Fig. 2.** Schematics of the high-speed imaging arrangements and the experimental control setup in test setup A. (a) Z-schlieren setup. (b) Back-lit zoom-lens setup. Hansen et al. [37] described the experimental setup and test procedure.

### 2.2 Experimental setup B

Setup B (see Fig 1b) used a transparent polycarbonate tube with a length 435 mm and a 9-mm inner diameter. The tube volume was 28 $cm^3$. Rapid boiling tests were performed with pressurized liquefied $CO_2$ supplied from a cylinder. The pre-rupture states were saturated liquid at room temperature ($P_0 \approx 5.5$ MPa and $T_0 \approx 293$ K). The burst of a PET polymer diaphragm resulted in the rapid depressurization and phase transitions. Additional information about these experiments, such as the test setup, and the results were published in Tosse et al. [34], Tosse [35], and Hansen et al. [36].

### 2.3 Experimental setup C

Setup C (see Fig 1c) used a transparent Polymethylmethacrylate (PMMA) plastic tube with length 100 mm and an inner diameter of 30 mm that was placed between two flanges. The volume was 70 $cm^3$. A gasket and an o-ring sealed the tube contents from the surroundings and prevented leakages. Small-scale BLEVE tests were conducted with liquid and solid phase $CO_2$ that was heated until the tube ruptured. The internal pressure in the tube at the time of rupture was in the range from 3.3 MPa to 4.2 MPa. Ke [32] and Bjerketvedt et al. [33] published detailed information about the test setup and the results from these small-scale BLEVE experiments.

### 2.4 Rankine-Hugoniot analysis

This subsection describes the Rankine-Hugoniot calculation method that incorporates the ideas previously discussed by Chaves [6], Thompson et al. [8], Shepherd et at. [9], Hill [10], Frost et al. [11], Shepherd and Simões-Moreira [12], Reinke [13], Reinke and Yadigaroglu [14], Simões-Moreira [15,16], Angelo et al. [17], and Stutz and Simões-Moreira [18]. Three states are defined in the analysis. The states are separated by a rarefaction wave (or fan), and then an evaporation wave. Figure 2 illustrates the defined states, waves and the control volume. State 0 (saturated liquid) is the initial pre-rupture state, located in front of the rarefaction wave. State 1 (superheated liquid) is the metastable liquid state, located behind the rarefaction wave but ahead of the evaporation wave. State 2 (two-phase equilibrium mixture) is located behind the evaporation wave. $T$ is the temperature, $P$ is the pressure, $V$ is the specific volume, $h$ is the enthalpy, $u$ is the velocity, and $\chi$ is the vapor mass fraction. A control volume that includes state 1 and state 2 is drawn around the evaporation wave. The evaporation wave is restricted to a narrow region [12]. The enthalpy used to evaporate a fraction of the liquid originates from the rapid depressurization from a saturated liquid state to a superheated state.

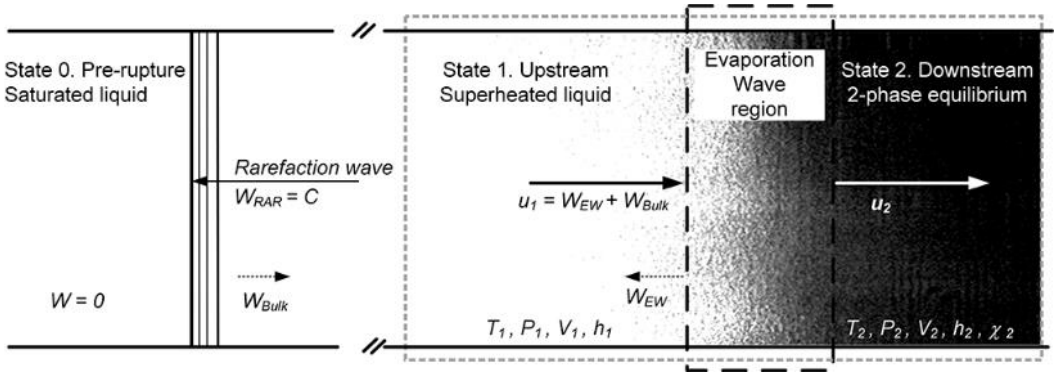


**Fig. 3.** Control volume that is used in the Rankine-Hugoniot analysis.

Some assumptions, which were described in [6-18], simplify the calculations. The method considers the evaporation wave as a steady-state jump from a metastable liquid state to a two-phase equilibrium state. Inviscid fluid flow is assumed with no heat transfer from the walls (adiabatic conditions). Heterogeneous nucleation on the wall surface ahead of the evaporation wave is neglected. Also, the gravitation force effects are neglected. The method assumes both mechanical equilibrium (no slip between vapor and liquid), and phase equilibrium (saturated vapor and liquid mixture) at state 2. The integral form of the conservation equations of mass, momentum, and energy in steady, one-dimensional flow can be formulated as:

$$\rho_1 u_1 = \rho_2 u_2 \tag{1}$$

$$P_1 + \rho_1 u_1^2 = P_2 + \rho_2 u_2^2 \tag{2}$$

$$h_1 + \frac{1}{2}u_1^2 = h_2 + \frac{1}{2}u_2^2 \tag{3}$$

The velocities $u_1$ and $u_2$ are defined relative to the evaporation wave (from the wave frame of reference). On the other hand, the evaporation wave velocity $W_{EW}$ and the liquid bulk velocity $W_{Bulk}$ ahead of the evaporation wave are both observed in a stationary lab frame. Then the velocity $u_1$ could be calculated by:

$$u_1 = W_{Bulk} + W_{EW} \tag{4}$$

$W_{Bulk}$ is approximated by the difference in liquid-phase speed of sound that results from the density ratio $\rho_0/\rho_1$ over the rarefaction wave. The Rayleigh line (equation 5) relates the velocity $u_1$ to the change in pressure and specific volume across the wave. A combination of equation 1 and 2 eliminates the velocity $u_2$.

$$u_1 = V_1 \left(\frac{P_2 - P_1}{V_1 - V_2}\right)^{1/2} \tag{5}$$

The solving for pressure $P_2$ gives a linear relation that connects $V_2$ and $P_2$ for a specific velocity $u_1$ and specified state 1. The negative slope of the Rayleigh line represents the mass flux squared, expressed by the squared ratio between the velocity $u_1$ to the specific volume $V_1$:

$$P_2 = -\left(\frac{u_1}{V_1}\right)^2 V_2 + \left[P_1 + \frac{u_1^2}{V_1}\right] \quad (6)$$

The Hugoniot curve (or evaporation adiabat) represents a locus of possible states behind the evaporation wave. The curve combines the conservation of mass, momentum, and energy in equations 1-3 to eliminate both the velocities $u_1$ and $u_2$:

$$h_2 - h_1 = \frac{1}{2}(P_2 - P_1)(V_2 + V_1) \quad (7)$$

The enthalpy available for adiabatic evaporation is the enthalpy difference between the expanded and saturated liquid at pressure $P_1$. At a sonic maximum velocity $u_2$, the Chapman-Jouguet solution represents a maximum mass flux. When state 2 is at phase equilibrium, mixture properties could express the specific volume and the enthalpy:

$$V_2 = (1 - \chi_2)V_{l,2} + \chi_2 V_{v,2} \quad (8)$$

$$h_2 = (1 - \chi_2)h_{l,2} + \chi_2 h_{v,2} \quad (9)$$

The subscripts *l,2* and *v,2* denotes saturated liquid and vapor at state 2. A combination of equations 7-9 gives the vapor mass fraction $\chi_2$ at state 2:

$$\chi_2 = \frac{2(h_1 - h_{l,2}) + (V_1 + V_{l,2})(P_2 - P_1)}{2(h_{v,2} - h_{l,2}) - (V_{v,2} - V_{l,2})(P_2 - P_1)} \quad (10)$$

The solutions at state 2, are specified as the intersections between the Rayleigh line and the Hugoniot curve.

The model inputs from the experimental tests are the pre-rupture pressure $P_0$, the pressure of the metastable liquid $P_1$, and the velocity $u_1$. State 1 is calculated by isentropic expansion from the pre-rupture pressure $P_0$ to the superheated liquid pressure $P_1$ by use of the Span Wagner technical equation of state [30]. Thermodynamic data from NIST [31] are supplied to calculate the state behind the evaporation wave (state 2). Figure 4a shows a PV diagram with two calculated examples from the Rankine-Hugoniot analysis. First, $u_1$ is specified as 30 ms$^{-1}$. The solutions at state 2 are the intersections between the Rayleigh line and the Hugoniot curve. The subsonic solution is named the non-CJ solution in Fig.4.a. Second, $u_1$ is specified as 36.5 ms$^{-1}$. The resulting solution at state 2 satisfies the CJ condition with the Rayleigh line being tangent to the Hugoniot curve. Figure 4b shows a PV diagram with a close-up of the region of interest.

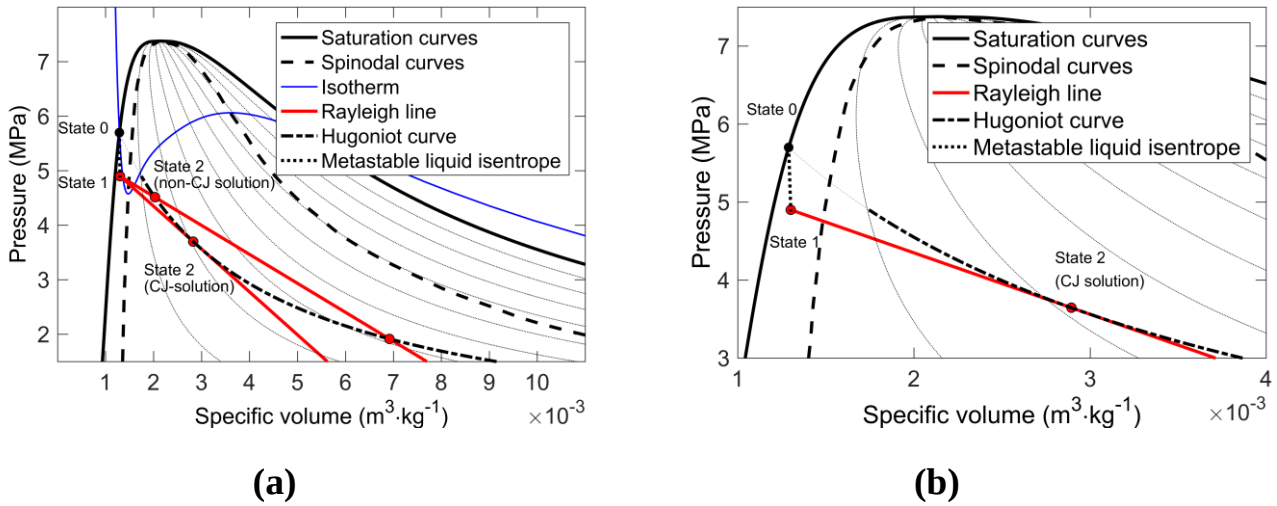


**Fig. 4.** PV diagrams of $CO_2$ that show the Rayleigh line, and the Hugoniot curve from the Rankine-Hugoniot analysis. The pressures at state 0 and 1 are 5.7 MPa and 4.9 MPa respectively. The temperature at state 0 is $T_0$ = 293 K. (a) The plot shows two solutions, one non-CJ solution ($u_1$ = 30 ms$^{-1}$), and one CJ solution ($u_1$ = 36.5 ms$^{-1}$). (b) PV-diagram that provides a close-up of the region of interest (CJ solution).

## 3. Results and discussion

Table 1 shows results from the four tests in the in the current study that include measured and calculated properties. The pressures at state 0 (saturated liquid), at state 1 (metastable liquid), at state 2 (two-phase equilibrium), and the evaporation wave velocity ($W_{EW}$) were measured. The Rankine-Hugoniot jump condition model produces the calculated properties. The available superheat energy caused by the rapid depressurization results in a vapor mass fraction $\chi_2$ in the range 0.21-0.23 at state 2.

**Table 1:** Measured and calculated velocities and state data. Three test setups (A-C) and four tests (1-4).

| | State | Symbol | Unit | Test 1 Setup A | Test 2 Setup A | Test 3 Setup B | Test 4 Setup C |
|---|---|---|---|---|---|---|---|
| **Measured properties** | | | | | | | |
| Pressure | *0* | $P_0$ | MPa | 5.84 | 6.27 | 5.70 | 3.40 |
| | *1* | $P_1$ | MPa | 5.05 | 5.60 | 4.90 | 2.00 |
| | *2* | $P_2$ | MPa | 3.6-3.8 | 4.15 | 3.5 | 1.2-1.4 |
| Velocity | *1* | $W_{EW,m}$ | $ms^{-1}$ | 35-40 | 42.4 | 32 | ~ 10* |
| **Calculated properties** | | | | | | | |
| Pressure | *2* | $P_2$ | MPa | 3.74 | 4.27 | 3.64 | 1.29 |
| Temperature | *0* | $T_0$ | K | 294.0 | 297.0 | 292.9 | 272.2 |
| | *1* | $T_1$ | K | 292.5 | 295.5 | 291.5 | 270.9 |
| | *2* | $T_2$ | K | 275.9 | 281.0 | 274.9 | 240.2 |
| Density | *0* | $\rho_0$ | $kgm^{-3}$ | 764.4 | 726.6 | 775.6 | 932.5 |
| | *1* | $\rho_1$ | $kgm^{-3}$ | 756.7 | 718.6 | 768.5 | 928.0 |
| | *2* | $\rho_2$ | $kgm^{-3}$ | 345.6 | 372.6 | 345.5 | 141.5 |
| Enthalpy | *0* | $h_0$ | $kJkg^{-1}$ | 258.7 | 270.2 | 255.2 | 197.3 |
| | *1* | $h_1$ | $kJkg^{-1}$ | 257.6 | 269.3 | 254.1 | 195.9 |
| | *2* | $h_2$ | $kJkg^{-1}$ | 254.9 | 266.6 | 251.5 | 193.0 |
| Velocity | *0* | $W_{Bulk}$ | $ms^{-1}$ | 3.3 | 3.2 | 3.1 | 2.6 |
| | *1* | $W_{EW,c}$ | $ms^{-1}$ | *35* | *41.4* | 33.4 | 9.1 |
| | *1* | $u_1$ | $ms^{-1}$ | 38.1 | 44.6 | 36.5 | 11.7 |
| | *2* | $u_2$ | $ms^{-1}$ | 83.5 | 86.1 | 81.2 | 76.9 |
| Vapor mass fraction | *2* | $\chi_2$ | - | 0.217 | 0.227 | 0.209 | 0.213 |
| Mass flux | | | $kgms^{-2}s^{-1}$ | 28 855 | 32 066 | 28 073 | 10 877 |
| **Deviation (Meas-Calc)** | | | | | | | |
| Pressure difference | *2* | $\Delta P_{2,dev}$ | MPa | *0.1* | *0.12* | *0.14* | *0.1* |
| Velocity difference | *1* | $\Delta W_{EW,dev}$ | $ms^{-1}$ | *< 5* | *1.0* | *1.4* | *~ 1.0* |

* *In the order of*

### 3.1 High-speed images, setup A

This sub-section describes observations and high-speed images from tests that were conducted in setup A. The presented images originated from several tests. This study includes two tests from the campaign that contained 80 tests. The initial pre-rupture condition was saturated liquid at room temperature (typically 5.5 - 6.3 MPa). Upon diaphragm rupture, a shock wave propagated outward from the opening (not visible in Fig.5). At the same time, a rarefaction wave propagated downward through the vessel. A series of schlieren images (Fig. 5b) captured the expansion wave that propagated at the speed of sound (typically 300 - 360 $ms^{-1}$) through the liquid phase. A jet of partially condensed $CO_2$ vapor followed the shock wave. Figure 5a shows the jet that propagated with an initial velocity of about 190 $ms^{-1}$.

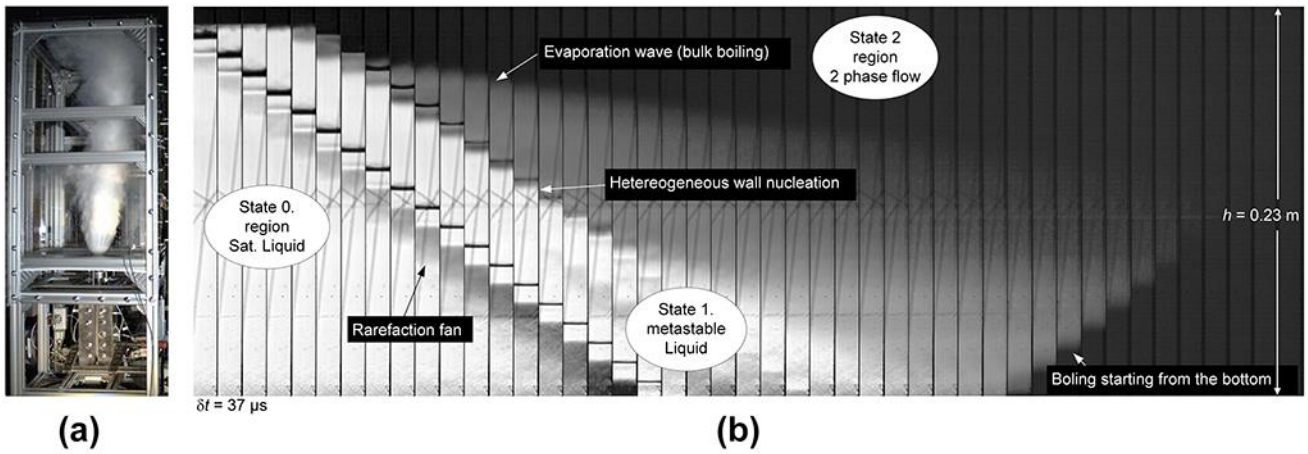


**Fig. 5.** High-speed images that originated from tests with setup A. (a) $CO_2$ jet from the high-pressure vessel. (b) Image-series from the schlieren setup that shows 1.5 ms of the rapid expansion and boiling process inside the vertical duct.

A contact surface that initially separated the liquid phase and the vapor headspace accelerated toward the high-pressure vessel exit plane (not visible in Fig.5). Figure 5b shows a 1.5-ms high-speed image sequence from the rectangular test section. The time that separated two subsequent images was ~ 37 µs. Because of the 0.7 - 0.9 MPa pressure reduction over the rarefaction fan, the liquid became superheated. After an induction period, rapid boiling started at the liquid/vapor interphase and continued downward into the superheated liquid. Heterogeneous nucleation was observed propagating at a velocity of 240-260 $ms^{-1}$ downward at the glass window surface (see Fig. 5b and Fig. 6.a-b). The wall nucleation that occurred in front of the evaporation wave limited the degree of superheat that was achieved in the current test setup. The rarefaction wave induced an upward flow on the liquid bulk that started to flow with a velocity $W_{Bulk}$ of about 3-5 $ms^{-1}$ (not visible in Fig. 5). An evaporation wave was observed that propagated downward from the liquid/vapor interphase with a velocity $W_{EW}$ of about 30-40 $ms^{-1}$ (see Fig 4.b and Fig 5.c). The rapid phase transition phenomena that are presented in the current study differed in appearance from the evaporation waves presented by Hill [10], Shepherd and Simões-Moreira [12], Reinke et al. [14], and Simões-Moreira [15, 16]. The presented images from the current setup did not resolve the front-details. One reason is the heterogeneous wall nucleation that occurred ahead of the evaporation wave. Another reason could be that the properties of $CO_2$ differ from the fluids studied by others, such as dodecane, propane, butane, water and refrigerant R114.

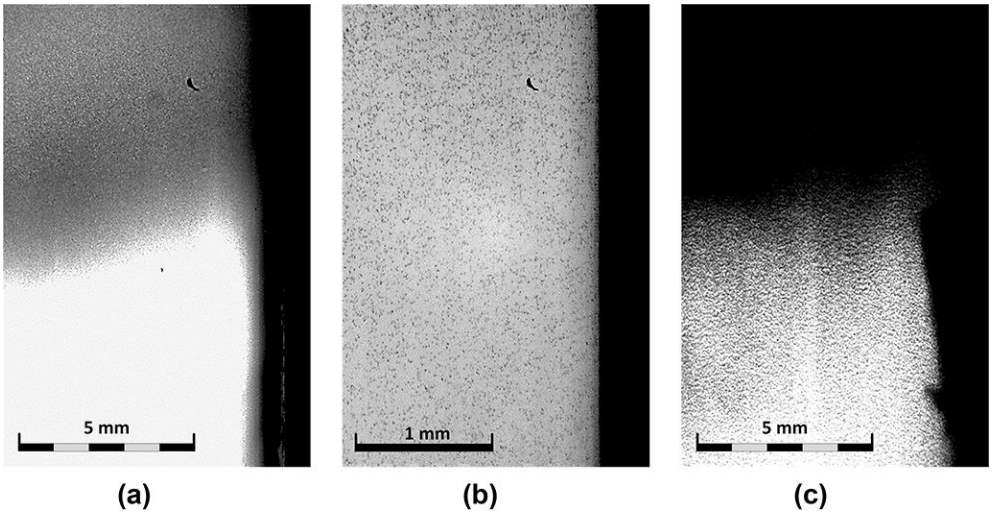


**Fig. 6**. High-speed images that were captured with a back-lit zoom-lens setup. (a) Heterogeneous nucleation propagating at the front glass. (b) Bubble growth at the front glass surface. (c) Evaporation wave propagating into the superheated liquid phase.

### 3.2 Experimental results versus calculated Rankine-Hugoniot solutions

Figures 7 - 9 show results from the Rankine-Hugoniot analysis and the experimental pressure histories in tests 1, 3 and 4. The three test setups (A, B and C) offered a range of initial conditions. A reasonable correspondence was found between the measured pressures and the calculated CJ-solutions at state 2. These results suggested that the Rankine Hugoniout relations could be used to model the rapid boiling of $CO_2$ as an evaporation wave. Results from three test designs in Figs.7-9. suggested that the findings were transferable to other situations.

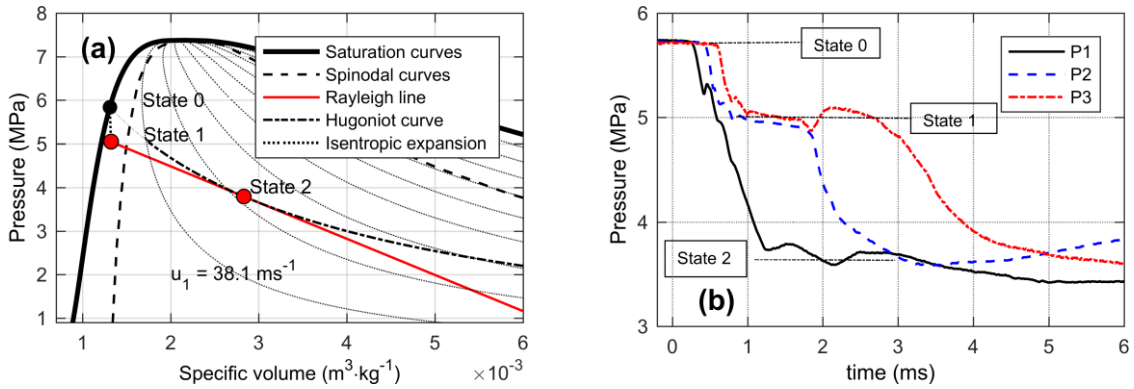


**Fig. 7.** Experimental data and calculated results from Test1, setup A. (a) PV diagram that shows the calculated CJ solution in the Rankine-Hugoniot analysis with $P_0$ = 5.8 MPa and $P_1$ = 5.0 MPa. (b) Experimental pressure histories from Test1 that show the pressures at level 1, 2 and 3. The pressure behind the evaporation wave showed reasonable correspondence with a CJ solution.

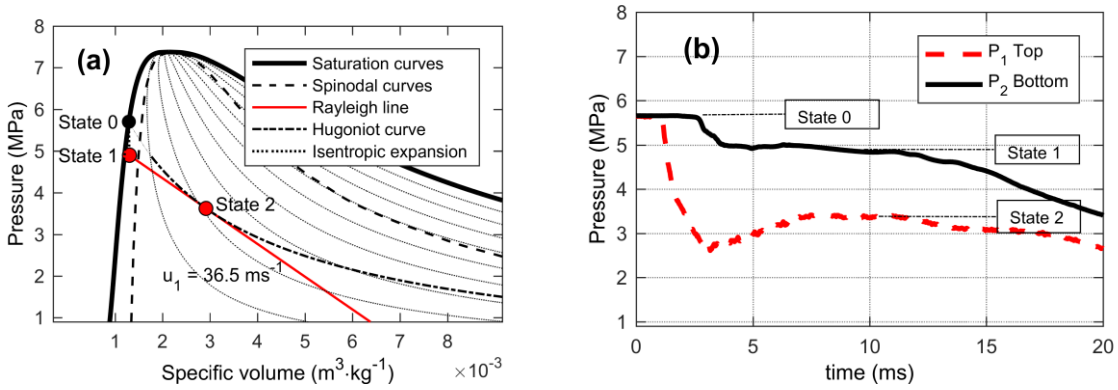


**Fig. 8.** Experimental data and calculated results from Test3, setup B. (a) PV diagram that shows the calculated CJ solution in the Rankine-Hugoniot analysis with $P_0$ = 5.7 MPa and $P_1$ = 4.9 MPa. (b) Pressure traces from Test3 that show the pressures at the top (P1) and bottom (P2) of the tube. The pressure at state 2 showed reasonable correspondence with a CJ solution.

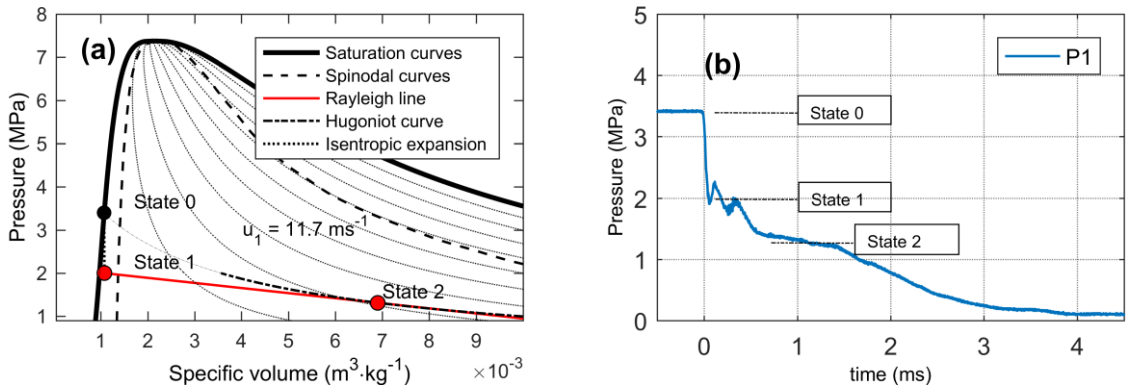


**Fig. 9.** Calculated results and experimental pressure histories from Test4, setup C. TR 4. (a) PV diagram that shows the CJ solution in the Rankine-Hugoniot analysis with $P_0$ = 3.4 MPa and $P_1$ = 2.0 MPa. (b) Pressure traces from TR 4 that show the pressure at the bottom of the tube. The pressure at state 2 showed reasonable correspondence with a CJ solution.

### 3.2 Chapman Jouguet (CJ) solutions from the Rankine-Hugoniot calculations

Figure 10 shows calculated properties ahead of and behind the evaporation wave. The plots show results from the Rankine-Hugoniot calculations that satisfy the CJ-solution for a range of pre-rupture pressures $P_0$ and superheat pressure drop ($P_0$ -$P_1$).

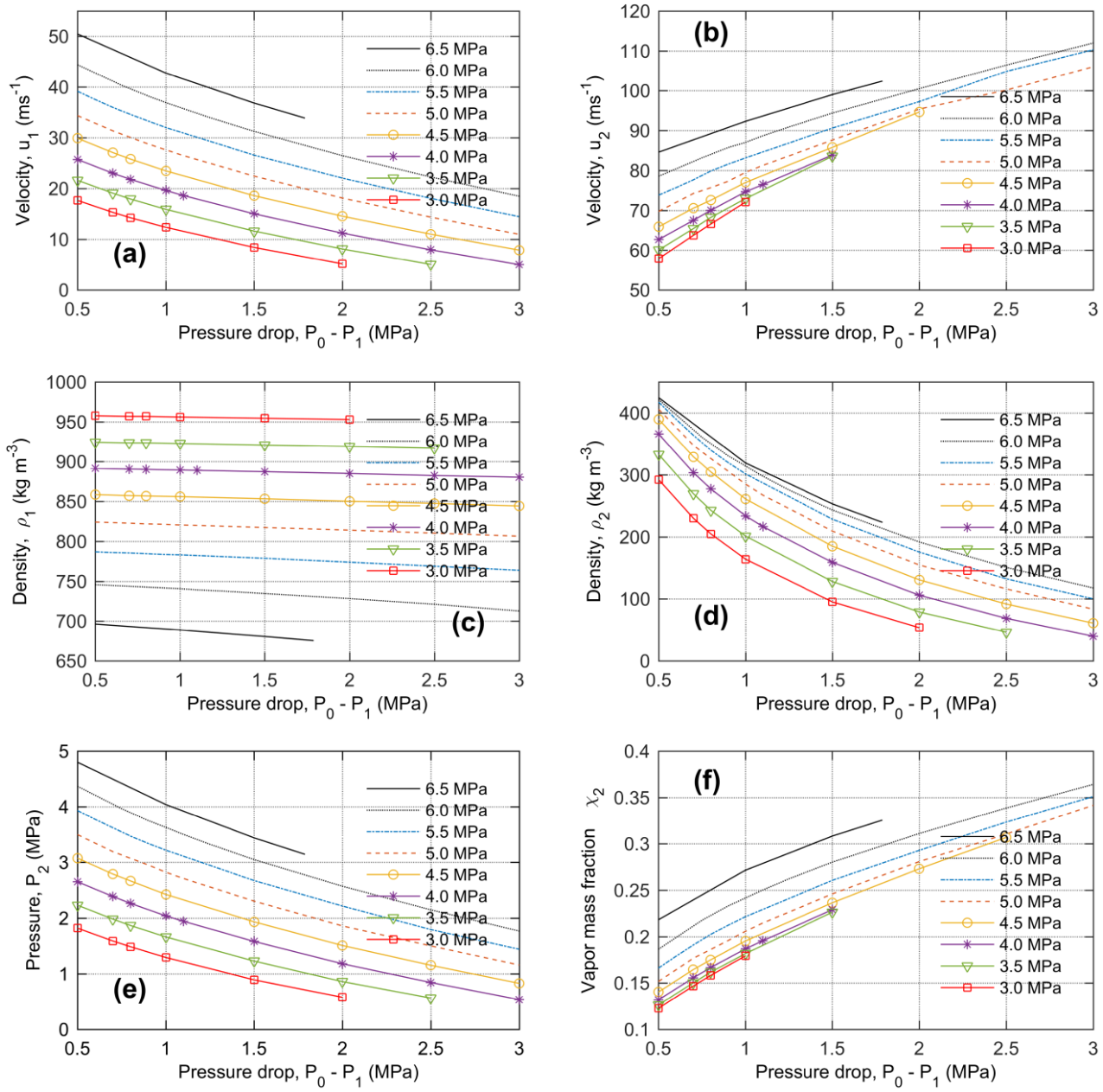


**Fig. 10.** Calculated CJ-solutions from the Rankine-Hugoniot analysis. Each line represents an initial pre-rupture pressure $P_0$. Six properties were plotted as a function of the superheat pressure drop $P_0$ - $P_1$. (a) velocity $u_1$. (b) velocity $u_2$. (c) density $\rho_1$. (d) density $\rho_2$. (e) pressure $P_2$. (f) vapor mass fraction $\chi_2$.

The plots in Fig. 10 provide rule-of-thumb calculations that can be used in simple flow and state predictions. The following example presents some possibilities: If saturated liquefied $CO_2$ at 5.5 MPa expands to 4.0 MPa in a rapid isentropic process, the calculated evaporation wave velocity is ~ 27 $ms^{-1}$ (see Fig10.a). The pressure drop across the evaporation wave accelerates the flow to a velocity of ~ 90 $ms^{-1}$ relative to the wave (Fig. 10b). The expansion across the wave decreases the density from ~ 790 to 230 $kgm^{-3}$ (see Figs. 10 c and d). Figure 10 e shows that the calculated pressure behind the wave is 2.7 MPa. The calculated vapor mass fraction behind of the wave is ~ 0.26 (Fig. 10f).

At metastable liquid pressures $P_1$ less than 2.5 MPa, the model shows increased sensitivity to numerical errors. A small change in the Rayleigh line gradient has a large impact on calculated properties such as the vapor mass fraction $\chi_2$ and multi-phase flow velocity $u_2$ behind the evaporation wave.

The findings in Figs.7-9, which suggest that the evaporation wave velocity corresponds with a CJ condition, do not exclude other solutions. Shepherd and Simões-Moreira [12] proposed that a range of evaporation wave velocities could be possible, depending on the pressure drop across the wave and degree of superheat of the liquid in front of the wave. In their setup, a variable pressure in the low-pressure reservoir (dump tank) controlled the degree of superheat. In the current study, the pressurized liquefied $CO_2$ was released to atmospheric pressure. A reason for the correspondence between the experimental results and the CJ solution in the current study could be because of choked flow conditions behind the evaporation wave. Further investigations should investigate the validity range of the modeled results.

### 3.3 Mechanical energy-release estimate

The present study suggests that the calculated vapor mass fraction $\chi_2$ from the Rankine-Hugoniot analysis can be used to estimate the mechanical energy released in a tank explosion. When the vessel contains a pressurized liquefied gas, the fraction of liquid that rapidly evaporates could have a significant influence on the energy released at the early stage of the explosion. Several methods exist [47-50] that estimates the burst energy in a BLEVE. The method proposed by Prugh [47], which calculates the isentropic expansion of an ideal gas at constant specific heat ratio, is the starting point of the present calculation example. The continued attraction of Prugh's method can be attributed to its simplicity [3]. A method proposed by Planas et al. [48] claims to be more accurate because it treats the vapor as a real-gas, and the expansion as an irreversible adiabatic process. Prugh's method tends to overestimate the energy released, hence produces conservative estimates [48]. This study suggests that the vapor mass fraction $\chi_2$ calculated by the Rankine-Hugoniot relations can be incorporated in Prugh's method to provide a less conservative energy estimate. The calculated vapor mass fraction behind the evaporation wave limits the energy-release. The calculated energy- release is restricted to the vapor expansion and the phase change caused by the adiabatic evaporation wave.

If a 1-$m^3$ tank that contains 85 vol% pressurized liquefied $CO_2$ at 5.5 MPa in equilibrium with a $CO_2$ vapor headspace suddenly bursts, the mechanical energy that is released at the early stage of the explosion could be estimated with the following method. A liquid expansion from 5.5 to 4.0 MPa gives a calculated vapor mass fraction of $\chi_2 = 0.26$ at the CJ-solution. The specified specific heat ratio used in the calculation is $\gamma = 1.3$. The degree of superheat in the liquid phase is considered "moderate," and heterogeneous nucleation is expected to initiate the evaporation. Thermodynamic properties of $CO_2$ from NIST [31] provide the density values. Equations 11-13 below show the calculations.

$$W_L = \rho_{0,L} \cdot V_T \cdot liquid\ volume\ fraction = 791 \frac{kg}{m^3} \cdot 1m^3 \cdot 0.85 = 672\ kg \tag{11}$$

$$V^* = V_T + W_L \left[\left(\frac{\chi_2}{\rho_{0,V}}\right) - \left(\frac{1}{\rho_{0,L}}\right)\right] m^3 = 1 + 672 \left[\left(\frac{0.26}{181}\right) - \left(\frac{1}{791}\right)\right] = 1.12\ m^3 \tag{12}$$

$$E = \frac{PV^*}{\gamma - 1}\left[1 - \left(\frac{P_{atm}}{P_0}\right)^{(\gamma-1)/\gamma}\right] = \frac{5.5 \cdot 1.12}{1.3-1}\left[1 - \left(\frac{0.101}{5.5}\right)^{(1.3-1)/1.3}\right] = 12.4\ MJ \tag{13}$$

$E$ is the energy released, $P_0$ is the initial pre-rupture pressure, $P_{atm}$ is the atmospheric pressure, $\gamma$ is the specific heat ratio, $V_T$ is the tank volume, $W_L$ is the mass of liquid in the tank, $\rho_{0,V}$ and $\rho_{0,L}$ are the initial densities of the vapor and liquid phase. $V^*$ is the total volume that includes both the original vapor volume plus the volume of the vapor generated by the rapid evaporation.

The calculated mechanical energy-release is 12.4 MJ. In comparison, isentropic expansion of a pure vapor produces an estimate of 11.1 MJ. In this example, calculated vapor mass fractions $\chi_2$ larger than 0.229 gives total volumes $V^*$ larger than the volume calculated from a pure vapor expansion. Figure 11 shows the calculated energy-release as a function of the degree of superheat and the resulting vapor mass fraction at state 2.

The energy estimate presented above gives ~ 55% of the energy calculated by the original Prugh method. The method by Prugh, which includes the full expansion from the initial pressure to the atmospheric pressure, calculates a vapor mass fraction $\chi_2$ of ~ 0.5, and an energy estimate of 22.2 MJ. A reason for this deviation is that the energy-release calculated by the Rankine-Hugoniot relations is restricted to the expansion of the vapor head-space and the vapor generated by the evaporation wave. In comparison, Abbasi and Abbasi [3] reported that the method proposed by Planas et al. [48] calculated ~ 40% of the energy-release estimated by Prugh. The significant deviation between the energy estimates calculated with the existing energy-release methods suggests that there is still a need for method validation.

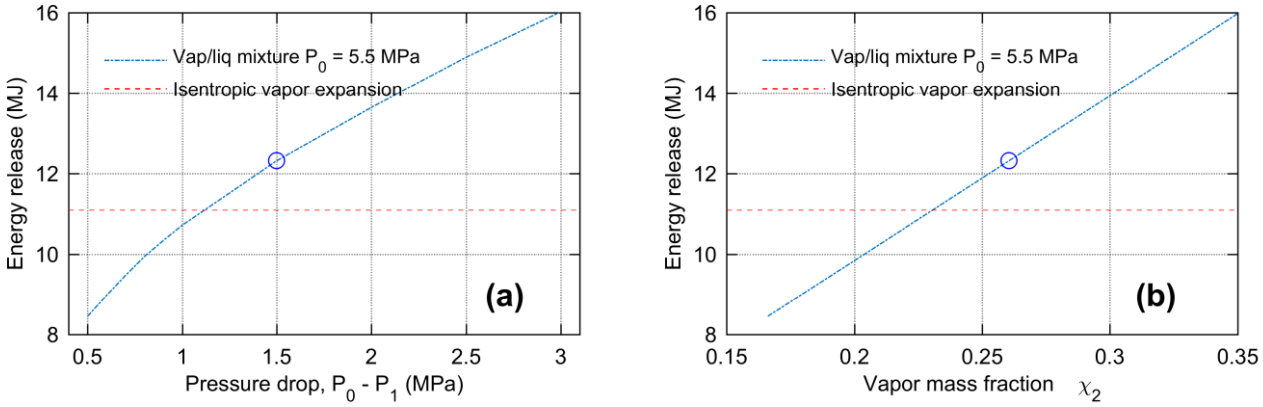


**Fig. 11.** The estimated mechanical energy released in an explosion of a vessel with a tank volume $V_T$ = 1 m$^3$ as a function of the superheat pressure drop. The liquid volume fraction was 85%, and the pre-rupture pressure was $P_0$ = 5.5 MPa. (a) Energy release as a function of the superheat pressure drop. (b) Energy-release as a function of the vapor mass fraction $\chi_2$.

The calculated energy-release in the current paper coincides with the blast observations in a previous study [37]. Hansen et al. [37] concluded that the evaporation process was too slow to contribute to the measured peak overpressure (15-20 kPa) in the presented test geometry. The calculated impulse in pure vapor and a liquid/vapor mixture was almost identical in the first 20 ms. The current study shows that a reason could be the low vapor mass fraction (~ 0.22) produced by the evaporation wave.

## Conclusion

This paper investigated the rapid expansion and phase transition of carbon dioxide ($CO_2$) in a vertical duct. The motivation was to quantify damage potential in scenarios such as $CO_2$ tank explosions. Results from small-scale experiments were compared with calculations from a Rankine-Hugoniot analysis. The Rankine-Hugoniot relations modeled the phase transition as an evaporation wave and calculated the fluid properties behind the wave. The model showed a good qualitative agreement with the experimental results that were sampled from three separate test setups. The measured evaporation wave velocities were 35 – 42 ms$^{-1}$ (setup A and B), and ~ 10 ms$^{-1}$ (setup C). The experimental results seemed to correspond with a Chapman Jouguet solution. At a specific CJ solution, the required model inputs were the initial pre-rupture pressure and the pressure of the metastable liquid ahead of the evaporation wave. Typically, the estimated vapor mass fraction behind the evaporation wave was in the range from 0.21 to 0.23. The paper presented a strategy to predict the energy released in a tank explosion based on the calculated vapor mass fraction.

## Acknowledgements

The funding for the presented work was granted by the University of South-Eastern Norway.

## References

[1] International Energy Agency. 20 years of carbon capture and storage; accelerating future developments. https://webstore.iea.org/20-years-of-carbon-capture-and-storage/, 2018 (accessed 12 April 2018).
[2] International Energy Agency. Technology Roadmap – Carbon Capture and Storage 2013. https://webstore.iea.org/technology-roadmap-carbon-capture-and-storage-2013/, 2018 (accessed 12 April 2018).
[3] T. Abbasi, S.A. Abbasi, The boiling liquid expanding vapour explosion (BLEVE): mechanism, consequence assessment, management, Journal of Hazardous Materials 141 (2007) 489–519.
[4] W.E. Clayton, M.L Griffin, Catastrophic failure of a liquid carbon dioxide storage vessel, Process Safety Progress 13 (4) (1994) 202-209.
[5] Y. Zhang, J. Schork, K. Ludwig, Revisiting the conditions for a $CO_2$ tank Explosion, Proceedings of the 2013 AIChE Spring Meeting and Ninth Global Congress on Process Safety, Curran Associates, San Antonio, Texas, 2013, pp. 109-120.
[6] H. Chaves, Phasenübergänge und wellen bei der entspannung von fluiden hoher spezifischer wärme, PhD thesis, Georg-August-Universität, Göttingen, Germany, 1984.
[7] H. Chaves, H. Lang, G. E. A. Meier, H.D. Speckmann, Adiabatic phase transitions and wavesplitting in fluids of high specific heat. In G. E. A. Meier & F. Obermeier (Eds.), Flow of Real Fluids (pp. 115-124). Berlin, Heidelberg: Springer Berlin Heidelberg (1985).
[8] P.A. Thompson, H. Chaves, G.E.A Meier, Y.G Kim, H.D Speckmann, Wave splitting in a fluid of large heat capacity, Journal of Fluid Mechanics 185 (1987) 385-414.

[9] J.E. Shepherd, S, McCahan, J Cho, Evaporation Wave Model for Superheated Liquids, In G. E. A. Meier & P. A. Thompson (Eds.), Adiabatic Waves in Liquid-Vapor Systems: IUTAM Symposium Göttingen, 28.8.–1.9.1989, Berlin, Heidelberg: Springer Berlin Heidelberg, 1989, pp. 3.12.
[10] L.G. Hill, An experimental study of evaporation waves in a superheated liquid. Ph.D. thesis, California Institute of Technology, Pasadena, CA, 1991.
[11] D.L Frost, J.H.S Lee, G. Ciccarelli, The use of Hugoniot analysis for the propagation of vapor explosion waves, Shock Waves 1(2), (1991) 99-110. doi:10.1007/BF01414905
[12] J.E. Shepherd, J.R. Simões-Moreira, Evaporation waves in superheated dodecane, Journal of Fluid Mechanics 382 (1999) 63-86. doi:10.1017/S0022112098003796
[13] P. Reinke, Surface Boiling of Superheated Liquid, Ph.D. thesis, ETH Zürich, 1997.
[14] P. Reinke, G. Yadigaroglu, Explosive vaporization of superheated liquids by boiling fronts, International Journal of Multiphase Flow 27 (2001) 1487–1516.
[15] J.R. Simões-Moreira, Adiabatic evaporation waves, Ph.D. thesis, Rensselaer Polytechnic Institute, Troy, NY, 1994.
[16] J.R. Simões-Moreira, Oblique evaporation waves, Shock Waves, 10 (2000) 229-234.
[17] J.R. Simões-Moreira, E. Angelo, D.B Barrios, Theory and occurrence of evaporation waves, Proceedings of the 18th international congress of mechanical engineering, Ouro Preto, MG, ABCM, 2005.
[18] B. Stutz, J.R. Simões-Moreira, Onset of boiling and propagating mechanisms in a highly superheated liquid – the role of evaporation waves, International Journal of Heat and Mass Transfer, 56 ( 2013) 683-693.
[19] P.A. Thompson, Compressible Fluid dynamics (1st edition). New York: McGraw-Hill, 1972.
[20] A.A. Avdeev, Theory of Boiling Shock in Bubble Systems (pp. 265-327). Cham: Springer International Publishing, 2016.
[21] V.V. Kuznetsov, I.A. Kozulin, O.V. Vitovsky, Experimental investigation of adiabatic evaporation waves in superheated refrigerants, Journal of Engineering Thermophysics 21 (2) (2012) 136–143.
[22] M.A. Gromles, H.K. Fauske, Axial propagation of free surface boiling into superheated liquids in vertical tubes, Proceedings of the Fifth International Heat Transfer Conference, Tokyo, 1974, Vol 4, pp. 30-34.
[23] R.J. Peterson, S.S Grewal, M.M. El-Wakil, Investigations of liquid flashing and evaporation due to sudden depressurization, International Journal of Heat and Mass Transfer 27 (2) (1984) 301-310.
[24] P.K. Das, G.S. Bhat, V.H. Arakeri, Investigations on the propagation of free surface boiling in a vertical superheated liquid column, International Journal of Heat and Mass Transfer 30 (4) (1987) 631-638.
[25] E. Hahne, G. Barthau, Evaporation waves in flashing processes, International Journal of Multiphase Flow 26 (2001) 531-547.
[26] A.M. Birk, C. Davison, M. Cunningham, Blast overpressures from medium scale BLEVE tests, Journal of Loss Prevention in the Process Industries 20 (2007) 194-206.
[27] C.R. Reid, Possible mechanism for pressurized-liquid tank explosions or BLEVE's, Science 203 (4386) (1979) 1263–1265.
[28] C.R. Reid, Some theories on boiling liquid expanding vapour explosions, Fire March (1980) 525-526.
[29] C.R. Reid, Superheated liquids, American Scientist 64 (2) (1976) 146-156.
[30] R. Span, W. Wagner, A new equation of state for carbon dioxide covering the fluid region from the triple-point to 1100 K at pressures up to 800 MPa, Journal of Physical and Chemical Reference Data, 25 (6) (1996) 1509–1596
[31] E.W. Lemmon, M.O. McLinden and D.G. Friend, "Thermophysical Properties of Fluid Systems" in NIST Chemistry WebBook, NIST Standard Reference Database Number 69, P.J. Linstrom and W.G. Mallard (Eds.), National Institute of Standards and Technology, Gaithersburg MD, 20899, doi:10.18434/T4D303, (accessed 3 January 2018).
[32] W. Ke, $CO_2$ BLEVE (Boiling Liquid Expanding Vapor Explosion), Master's thesis, Telemark University College, Porsgrunn, Norway, 2009.
[33] D. Bjerketvedt, K. Egeberg, W. Ke, A. Gaathaug, K. Vaagsaether, Boiling liquid expanding vapor explosion in $CO_2$ Small scale experiments, Energy Procedia 4 (2011) 2285–2292.
[34] S. Tosse, K. Vaagsaether, D. Bjerketvedt, An experimental investigation of rapid boiling of $CO_2$, Shock Waves 25 (2015) 277-282.
[35] S. Tosse, The rapid depressurization and evaporation of liquefied carbon dioxide, Ph.D. thesis, University College of Southeast Norway, Porsgrunn, Norway, 2017.
[36] P.M. Hansen, A.V. Gaathaug, D. Bjerketvedt, K. Vaagsaether, The behavior of pressurized liquefied $CO_2$ in a vertical tube after venting through the top, International Journal of Heat and Mass Transfer, 108 (2017) 2011-2020.
[37] P.M. Hansen, A.V. Gaathaug, D. Bjerketvedt, K. Vaagsaether, Blast from pressurized carbon dioxide released into a vented atmospheric chamber, Shock Waves (2018). https://doi.org/10.1007/s00193-018-0819-z
[38] M.M. van der Voort, A.C. van den Berg, D.J.E.M. Roekaerts, M. Xie, P.C.J. de Bruijn, Blast from explosive evaporation of carbon dioxide: experiment, modeling and physics, Shock Waves 22 (2012) 129-140.
[39] M.M. van der Voort, R.M.M. van Wees, J.M. Ham, M.P.N. Spruijt, A.C. van den Berg, P.C.J. de Bruijn, P.G.A. van der Ierschot, An experimental study on the temperature dependence of $CO_2$ explosive evaporation, Journal of Loss Prevention in the Process Industries 26 (2013) 830-838.
[40] G. Chiccarelli, J. Melguizo-Gavilanes, J.E. Shepherd, Pressure-field produced by the rapid vaporization of a $CO_2$ liquid column, Proceedings of the 30th International Symposium on Shock Waves, Tel-Aviv, 2015.
[41] M. Kim-E, R.C. Reid, The rapid depressurization of hot high pressure liquids or supercritical fluids, in M.E. Paulantis, J.M.L. Penninger, R.D. Gray, Jr, P. Davidson (Eds.) Chemical engineering at supercritical fluid conditions, Ann Arbor Science, Ann Arbor, Mich, 1983.

[42] W. Zheng, H. Mahgerefteh, D. Jamois, J. Hebrard, C. Proust, Modeling of Depressurization-Induced Superheating for Compressed Liquefied Gases, Industrial & Engineering Chemistry Research, 56 (2017) 5432-5442.
[43] M.Z. Li, Z.Y. Liu, Y. Zhou, Y. Zhao, X. Li, D. Zhang, A small-scale experimental study on the initial burst and the heterogeneous evolution process before $CO_2$ BLEVE, Journal of Hazardous Materials, 342 (2018) 634-642. doi:10.1016/j.hazmat.2017.09.002
[44] M.Z. Li, Q. Huang, Z.Y. Liu, Y. Zhao, Experimental study on solid CO2 BLEVE based on the superheat limit theory, in: 2016 Annual Reliability and Maintainability Symposium (RAMS), 2016, pp. 1-7.
[45] Y. Zhao, Z. Liu, X. Shi, X. Qian, Y. Zhou, D. Zhang, Q. Li, Numerical Simulation on BLEVE Mechanism of Supercritical Carbon Dioxide, Energy Procedia, 75 (2015) 880-885.
[46] Q. Huang, Z. Liu, Y. Zhou, D. Zhang, F. Wang, Study on Mechanisms of CO2 BLEVE Based on the Cusp-catastrophe Model, Energy Procedia, 61 (2014) 1343-1347.
[47] R.W. Prugh, Quantitative Evaluation of "Bleve" Hazards, Journal of Fire Protection Engineering, 3 (1991) 9-24.
[48] E. Planas-Cuchi, J.M. Salla, J. Casal, Calculating overpressure from BLEVE explosions, Journal of Loss Prevention in the Process Industries, 17 (2004) 431-436.
[49] CCPS, Guidelines for valuating the characteristics of Vapor Cloud Explosions, Flash Fires, and BLEVES. Center for Chemical Process Safety (CCPS), Published by the American Institute of Chemical Engineers, New York, 1994.
[50] C.J.H. van den Bosch, R.A.P.M. Weterings, Methods for the Calculation of Physical Effects: due to releases of hazardous materials (liquids and gases), Committee for the Prevention of Disasters, CPR 14E (TNO 'Yellow Book'), The Hague, The Netherlands, 1997.

# Paper D

# Phase Transition Rate in Rapid Boiling of $CO_2$

This paper was presented at 8th ISFEH (Eight International Seminar on Fire and Explosion Hazards) in Hefei, China on April 2016; and published in conference proceedings of 8th ISFEH, 2017. The paper was given a "Best student paper award" at the 8th ISFEH. ISBN 978-7-312-04104-4. DOI:10.20285/c.sklfs.8thISFEH.055

# Phase Transition Rate in Rapid Boiling of $CO_2$

**Hansen P. M.*, Vaagsaether K., Gaathaug A., Bjerketvedt D.**

*University College of Southeast Norway, N-3901 Porsgrunn, Norway*
**Corresponding author email: perha@usn.no*

## ABSTRACT

This paper presents phase transition rates and energy estimates based on small-scale experiments on the rapid boiling of compressed saturated $CO_2$ in a transparent tube. Estimated wave and bulk flow velocities are presented. To initiate the test runs, a diaphragm was punctured which led to the depressurization and boiling of the metastable $CO_2$. Initial conditions were saturated $CO_2$ (56-57 barg) at ambient temperatures (19-20 °C). The calculated rarefaction wave velocities were 192 m/s in the gas phase and 302-318 m/s in the liquid phase. The calculated condensation wave velocity was identical to the rarefaction wave velocity in the vapor phase (192 m/s). The evaporation wave had a diffuse boiling front with a propagation rate of about 32 m/s. Acceleration of the evaporation wave was probably caused by interaction with the reflection of the rarefaction wave. A contact surface between the vapor and vapor-liquid mixture was observed, accelerating out of the tube with an outlet velocity of 95 m/s. An liquid layer front propagated with a constant velocity of 8 m/s. The measured bulk flow velocities were 25 m/s before and 90 m/s after the expansion wave. The gas bubbles in the liquid phase moved with a constant velocity of 5-6 m/s after passage of the rarefaction wave. The high-speed camera did not capture the head of the rarefaction wave, but about 0.3 ms after the rarefaction wave passage, the camera detected changes that propagated with a constant velocity of 240 and 280 m/s through the liquid phase. The estimated phase transition rate was 27200 kg/(m$^2$·s). An estimate of the energy flux potentially released if the $CO_2$ was allowed to expand isentropic from the initial conditions to atmospheric conditions (1 atm, and a sublimation temperature of 173 K), was 2584 MJ/(m$^2$·s).

**KEYWORDS:** BLEVE, carbon dioxide, phase transition rate, rapid boiling.

## NOMENCLATURE

| | |
|---|---|
| $E$ | Energy (kJ) |
| $\dot{E}''$ | Energy flux (MJ/(m$^2$·s)) |
| $\dot{m}''$ | phase transition rate (kg/(m$^2$·s)) |
| $p$ | pressure (barg) |
| $s$ | evaporation wave velocity (m/s) |
| $T$ | temperature (K) |
| $t$ | time (s) |
| $v$ | velocity (m/s) |
| $u$ | Internal energy (kJ/kg) |

**Greek**

| | |
|---|---|
| $\Delta$ | difference |
| $\rho$ | mass density (kg/m$^3$) |

**Subscripts**

| | |
|---|---|
| $B$ | bulk |
| 0 | initial state |
| 1 | upstream state (expanded liquid) |
| 2 | downstream state (liq.-vap. mix) |

**Superscripts**

| | |
|---|---|
| $''$ | area flux |

## INTRODUCTION

The boiling liquid expanding vapor explosion (BLEVE) is a hazard that must be considered when designing and operating carbon dioxide ($CO_2$) storage tanks. Several definitions of a BLEVE exist. Birk et al. [1] proposed the following, which is used in the current publication: "*A BLEVE is the*

*Proceedings of the Eighth International Seminar on Fire and Explosion Hazards* (ISFEH8), pp. 547-557
Edited by Chao J., Liu N. A., Molkov V., Sunderland P., Tamanini F. and Torero J.
Published by USTC Press
ISBN:978-7-312-04104-4 DOI:10.20285/c.sklfs.8thISFEH.055

*explosive release of expanding vapor and boiling liquid when a container holding a pressure liquefied gas fails catastrophically*". A rupture of a vessel containing pressure liquefied $CO_2$ results in a sudden depressurization with rarefaction waves propagating through the fluid, followed by rapid boiling of the metastable liquid. Major BLEVE hazards include blast waves and flying fragments [2]. The consequences of a purely physical explosion in a non-reacting system can be severe, as was demonstrated by a 2008 ship accident in Yuhang, China [3] and a 1988 accident at a process plant in Worms, Germany [4]. According to Zang et al. [3], the transport ship in Yuhang, Hangzhou, carried 130 $m^3$ of liquid $CO_2$ at initial conditions of 23 bar and −15 °C. The ship was in dock when the $CO_2$ storage tank exploded, killing two workers and sinking two nearby ships carrying sulfuric acid and hydrogen peroxide. A brittle fracture and overfilling of a modified $CO_2$ tank were believed to be the causes of the accident. Modifications to the tank included work on the level indicator and locking of the relief valve [3].

The superheat limit theory proposed by Reid [5] is the standard theory to explain what triggers a BLEVE. Reid suggested that a BLEVE is initiated by homogenous nucleation at the superheat limit with vapor bubbles being spontaneously formed within the bulk liquid. If heterogeneous nucleation is suppressed during a rapid depressurization, the liquid will transgress the liquid saturation line and become superheated as it enters the metastable region inside the two-phase envelope. As the liquid continues to expand, it will eventually approach a limit of superheat, which is the lowest pressure it can exist as pure liquid for a given temperature. Then a vapor explosion will occur with rapid evaporation following the mechanism of homogenous nucleation. In the literature, a distinction between two different superheat limit temperatures is made, namely a thermodynamic superheat limit (TSL), derived from thermodynamic theory, and a kinetic superheat limit (KSL), derived from kinetic nucleation theory. The TSL is the upper limit of liquid stability, represented by the spinodal line, satisfying the criterion $(\partial\rho/\partial V)_T = 0$, approximated by any cubic equation of state. Experimental measurements of the superheat limit temperature is always the KSL [6]. According to the superheat limit theory, "*the temperature of the liquid must be above the superheat limit temperature at 1 atm, and the drop in tank pressure must be very rapid, [5]*". An experimental superheat limit temperature for $CO_2$ at 1 atm pressure is −6 ℃ [7]. However, the accident reports from Yuhang and Worms indicate that a $CO_2$ BLEVE could occur even if the initial temperature is below this superheat limit temperature at 1 atm [3]. This conclusion is supported by Bjerketvedt et al. [8] and Ke [9] in their work with small-scale $CO_2$ BLEVE experiments with initial temperatures below the superheat limit. Van der Voort et al. concludes from their experimental work with 40-liter $CO_2$ cylinders that BLEVE blasts do not disappear abruptly below the homogenous nucleation temperature, but instead shows a gradual decay [10, 11].

This article presents results from small-scale experiments on the rapid depressurization and boiling of carbon dioxide in a transparent expansion tube. An overall aim is to present phase transition rates and energy estimates based on the experimental data. Observed waves and calculated propagation velocities are presented. An application of these experimental results on $CO_2$ evaporative front propagation is the providing of validation data for the source terms in a 1D BLEVE simulation model. Several such models currently exists, that are capable of predicting the shock wave pressure and dynamics in a BLEVE. Interested readers are encouraged to seek out the work of Pinhasi et al. [12], and Xie [6] for further studies. Xie offers the most recent model among these two, with the ability to predict the onset of a BLEVE based on homogenous bubble nucleation. He builds on the work of Pinhasi, with improvements such as a model for nucleation, and a better thermodynamic basis. In addition, the work of Xie contains an extensive review of BLEVE related literature up to 2013. The experiments described in the current publication may not be classified as a true BLEVE according to the definitions in [1], since the test rig does not shatter during the test runs. However, the physical mechanisms of the expansion and boiling are believed to be similar to a BLEVE. Tøsse et al. [13] performed experiments on the same test rig and observed evaporation waves propagating at a near

constant velocity of 20-30 m/s inside the half-filled transparent tube. The present paper continues this experimental work, with the addition of phase transition rate and energy estimates.

## EXPERIMENTAL SETUP

An experimental study of the rapid boiling of $CO_2$ was performed on a test rig at Telemark University College. Fig. 1 shows an illustration of the experimental setup, a macro image of the rig, and a high-speed camera image. The test setup consisted of following main parts (1-8): (1) a Rexroth pneumatic actuator with a 5 cm piercing arrow to puncture the diaphragm; (2) a diaphragm consisting of two layers of PET polymer film; (3) a vertically oriented transparent polycarbonate tube with a visible region 32 cm long, an inner diameter of 9 mm, and a wall thickness of 1.5 mm; (4) a relief valve to evacuate air and carefully raise the liquid $CO_2$ level inside the tube; (5) two Kulite XTM-190 piezo resistive pressure sensors with range 0-1000 psig (P1 = top, P2 = bottom, spacing 43.5 cm); (6) an inlet valve to fill the rig from an external cylinder; (7) an emergency valve to safely release the pressure and empty the test rig in case of malfunction of the actuator device; and (8) a temperature sensor mounted at the bottom flange to measure the initial temperature. The test runs were conducted with the diaphragm and main outlet oriented at the top.

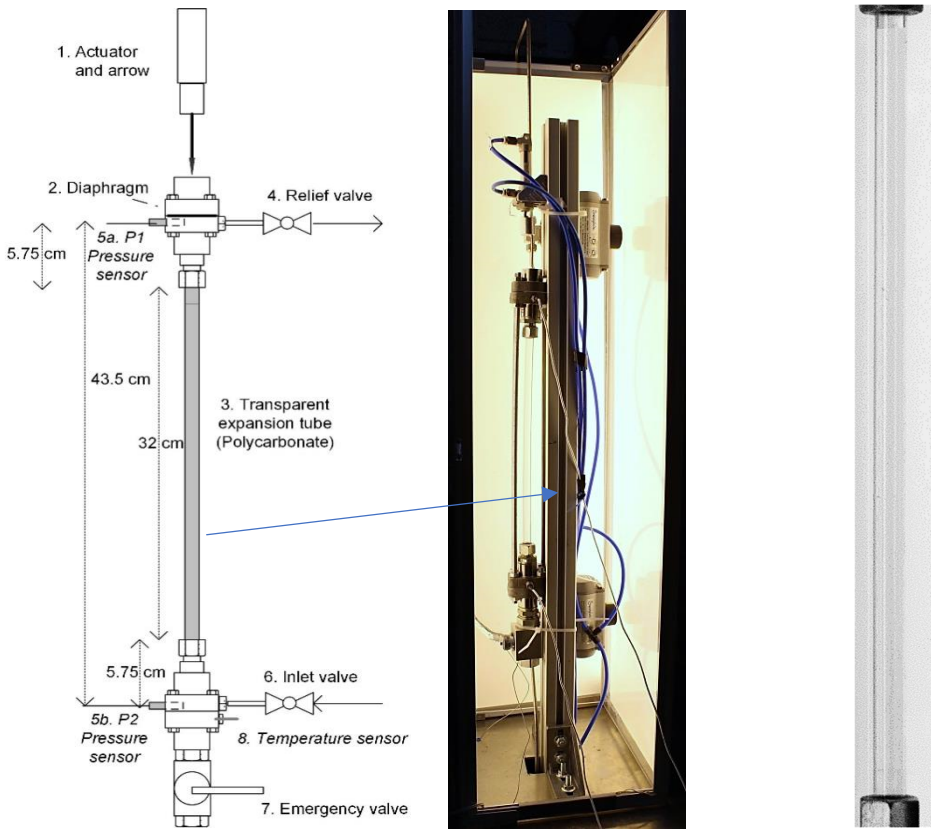


**Figure 1.** (a) Illustration of the test rig; (b) macro image of the rig; (c) cropped image from the high-speed camera with 1024 × 96 pixel resolution.

The main motivation for the use of a polycarbonate tube as opposed to glass (which offers a smother interphase towards the $CO_2$) was to withstand the high initial pressure (56-57 barg). The liquid $CO_2$ supply was a 40 liter cylinder with an internal riser pipe. The initial state was saturated liquid at ambient temperatures (19-21℃). A needle valve at the inlet and a pressure regulator at the outlet ensured controlled filling of the rig. A Photron Fastcam APX RS digital high-speed camera with a 50 mm Nikkor lens was used to capture the rapid boiling process. The experiments were initiated using a Quantum Composers 9500 series pulse generator that simultaneously triggered the arrow actuator and high-speed camera and initiated an HBM Quantum X data acquisition system.

## RESULTS AND DISCUSSION

Two test runs from the experimental series is presented in the article, denoted as TR1 and TR2. In addition, a reference test run with gas phase only is briefly commented, with respect to estimated rarefaction wave and condensation wave velocities. The initial conditions and calculated velocities are summarized in Table 1. The processed high-speed film images were plotted together with data from the pressure sensors. The observed evaporation waves, contact surfaces, and bulk flow velocities were identified and the wave and fluid velocities were calculated as a least squares fit using the *x-t* diagrams.

A method was developed to locate the observed waves from the high-speed film images and to calculate their velocities. The information from the digital high-speed images were imported into MATLAB and stacked next to each other to produce a position-time (*x-t*) plot. The original dimensions of the high-speed images were 1024 × 96 pixels with a typical tube width of 50 pixels. Fig. 1(c) shows an example of a high-speed camera image. The values of each pixel along the image width were combined in MATLAB, so that one combined pixel per image represents the entire tube diameter. The image dimensions were then reduced from 1024 × 96 pixels to 1024 × 1 pixels. Hence, a visualization of the boiling process was reduced to a 1-D phenomenon evolving in time, as illustrated in Fig. 2(b).

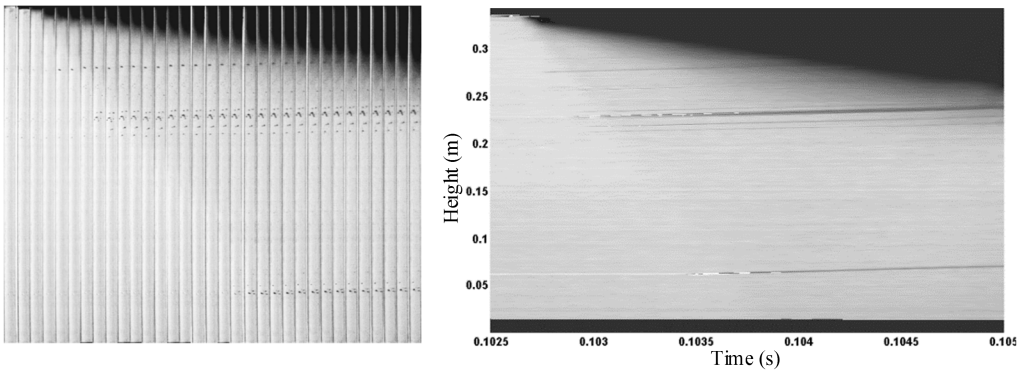


**Figure 2.** (a) A series of cropped high-speed images; (b) high-speed images processed in MATLAB.

Fig. 3 shows a schematic *x-t* diagram of the evaporation process with $CO_2$ vapor above the liquid phase. The diaphragm is punctured by the arrow at time $t = t_0$. An isentropic rarefaction wave then propagates through the tube. The vapor partially condenses (E) due to the pressure reduction, and enters the two-phase envelope. The liquid phase is temporarily in a metastable state for a few milliseconds after the passage of the rarefaction wave before the boiling starts at the phase boundary. An evaporation wave (B), assumed to be adiabatic, is observed propagating downward into the liquid phase, with a two-phase mixture downstream of the wave front. In literature, experimental studies of

evaporation waves in superheated liquids is well documented for a range of substances as presented in references [15-18]. However, this is not in the case for $CO_2$.

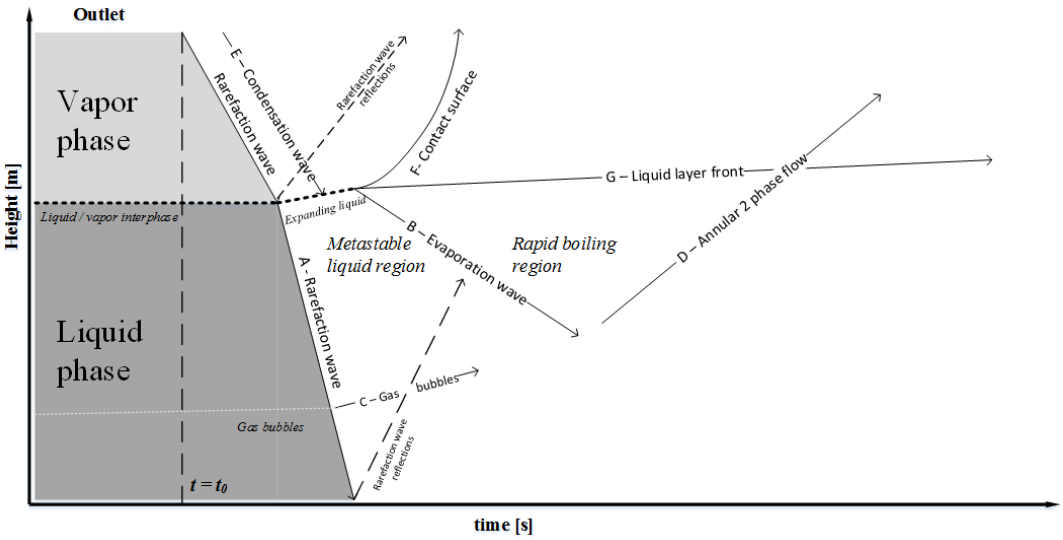


**Figure 3.** Typical schematic *x-t* diagram of the evaporation process with $CO_2$ vapor above the liquid phase.

In the current experiments, no clearly defined boiling front was observed. A contact surface (F) between the vapor and the two-phase vapor/liquid phase was observed, accelerating out of the test rig. At the phase boundary, a liquid layer front was observed, moving upward toward the outlet at a constant velocity. This wave is believed to be caused by choked flow conditions in the tube. The two-phase vapor/liquid mixture (D) then flows out of the tube. Some gas bubbles situated in the bulk (C) were observed moving upward after the passage of the rarefaction wave.

**Table 1.** Initial conditions and calculated wave velocities from the experiments.

| Description | Wave ID | | Reference | TR1 | TR2 |
|---|---|---|---|---|---|
| Liquid level (transparent section) | | % | 0 | 58 | 95 |
| Initial temperature | | °C | 21.7 | 19.5 | 19.7 |
| Initial pressure P2 (bottom) | | Barg | 57 | 56 | 57 |
| Rarefaction wave velocity, (Average, both gas and liquid phase based on pressure sensors P1 and P2) | | m/s | 192 | 240 | 280 |
| Rarefaction wave velocity, liquid phase (calculated from bubble condensation, in high-speed camera images) | | m/s | N/A | 318 | 302 |
| Evaporation wave velocity (linear section) | B | m/s | N/A | 32 | 32 |
| Gas bubble velocity (liquid bulk flow) | C | m/s | N/A | 5.2 | 5.4 |
| Bulk velocity two-phase flow below G | D | m/s | N/A | 25 | N/A |
| Condensation wave velocity,(vapor phase) | E | m/s | 192 | 190 | N/A |
| Contact surface velocity,(vapor-vapor/liquid, upper 6 cm) | F | m/s | N/A | 95 | N/A |
| Liquid layer front velocity | G | m/s | N/A | 8.0 | N/A |
| Bulk velocity two-phase flow above G | H | m/s | N | 90 | N |

Table 1 shows the initial values and calculated wave velocities for TR1-TR2 and a reference (vapor phase only). Blank cells labeled "N/A" in the data table denote that the wave or fluid velocity was either not observed or was not relevant for the given test run.

In TR1, the liquid level in the visual section was initially 58%. Fig. 4 shows a *x-t* plot of the processed high-speed film and a *p-t* plot from pressure sensors P1 (top) and P2 (bottom). The arrows labeled A-G indicate the velocities of the waves and the fluid flows in the *x-t* diagram. The pressure P1 started to drop at time $t$ = 95 ms from an initial value of 56 barg to a temporary minimum of 20 barg. After a 1.81 ms delay, the pressure P2 (bottom) started to decrease. This gave an average rarefaction wave velocity of 240 m/s, which is similar to the velocity 238 ±12 m/s calculated by Tøsse et al. [13]. The average speed of sound, based on interpolated values from the Span-Wagner equation of state [14] with saturated $CO_2$ at 19.5 ℃, was 258 m/s (196 m/s in the vapor phase and 344 m/s in the liquid phase). At time $t$ = 95.5 ms, the first visual changes was observed. Due to the rapid expansion of the saturated vapor, a condensation wave (E) propagated in the vapor bulk downward to the vapor/liquid interface with an average velocity of 190 m/s. A wave (A) was observed that propagated with a constant velocity of ~ 240 m/s. At first, this wave was thought to represent the head of the rarefaction wave, but further investigations of the high-speed film indicated that the propagation was too slow, compared to results from Span Wagner EOS. It was not possible to conclude from the footage whether the phenomenon originated in the bulk as the middle or the tail of the rarefaction wave, or as a boundary layer at the tube surface.

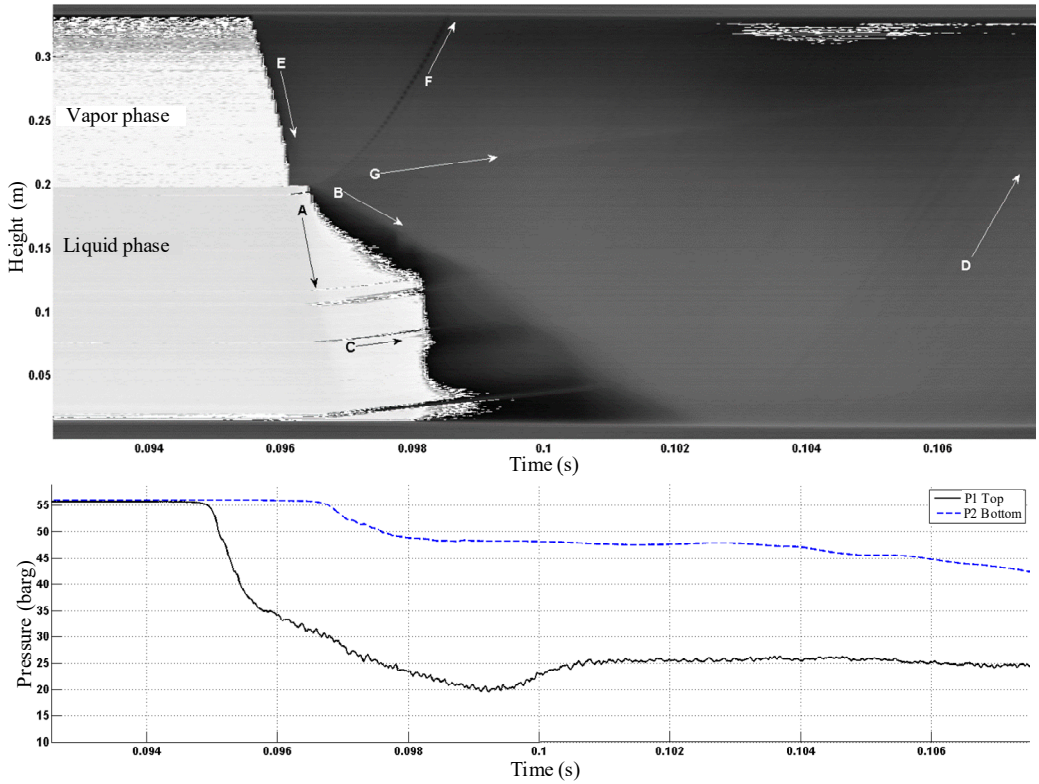


**Figure 4.** Experimental results from TR2 with 58% liquid level, showing an *x-t* plot of the processed high-speed film and a *p-t* plot from pressure sensors P1 (top) and P2 (bottom).

The presence of gas bubbles upstream in the liquid bulk phase could indicate non-equilibrium initial conditions. As the rarefaction wave passed by, these bubbles began to condense and entered the two-

phase region due to rapid expansion. The condensing gas bubbles (C) started to move toward the tube outlet with a constant velocity of 5.2 m/s. It is believed that the bubble velocity also represent the bulk liquid velocity, when assuming no velocity slip between the gas and the liquid phase. In this region, after the head of the rarefaction wave passed by and before the boiling started, the liquid was in a metastable superheated state. The estimated rarefaction wave velocity in the expanded liquid phase was 318 m/s. This calculation was based on position vs. time observations of the gas bubble condensation.

After an induction time of 0.3 ms from when the condensation wave (E) reached the liquid/vapor interface, the initiation of boiling was observed at the interface at time $t = 96.4$. The evaporation wave front (B) was rather diffuse and the current experimental setup did not permit the visualization of the front details. The velocity of the evaporation front was not constant but seemed to accelerate. As the boiling process continued behind the first diffuse evaporation front, the remaining $CO_2$ seemed to enter the two-phase region (B) at a nearly constant velocity of 32 m/s. At time $t = 98.2$ ms, the boiling front accelerated, probably caused by interaction with the reflection of the acoustic expansion wave. There were no sensors inside the visualization section, but the pressure was assumed to be between P1 and P2. The pressure P2 (bottom) decreased by about 8 bar, from 56 to 48 barg and was nearly constant during a boiling period of approximately 8 ms.

As the liquid started to boil at the interface, two additional wave fronts were detected. First, a front (F) was observed that is a contact surface between the vapor and the vapor/liquid phase. It started at the interface, and then it accelerated upward with a velocity ~95 m/s in the upper region. Second,

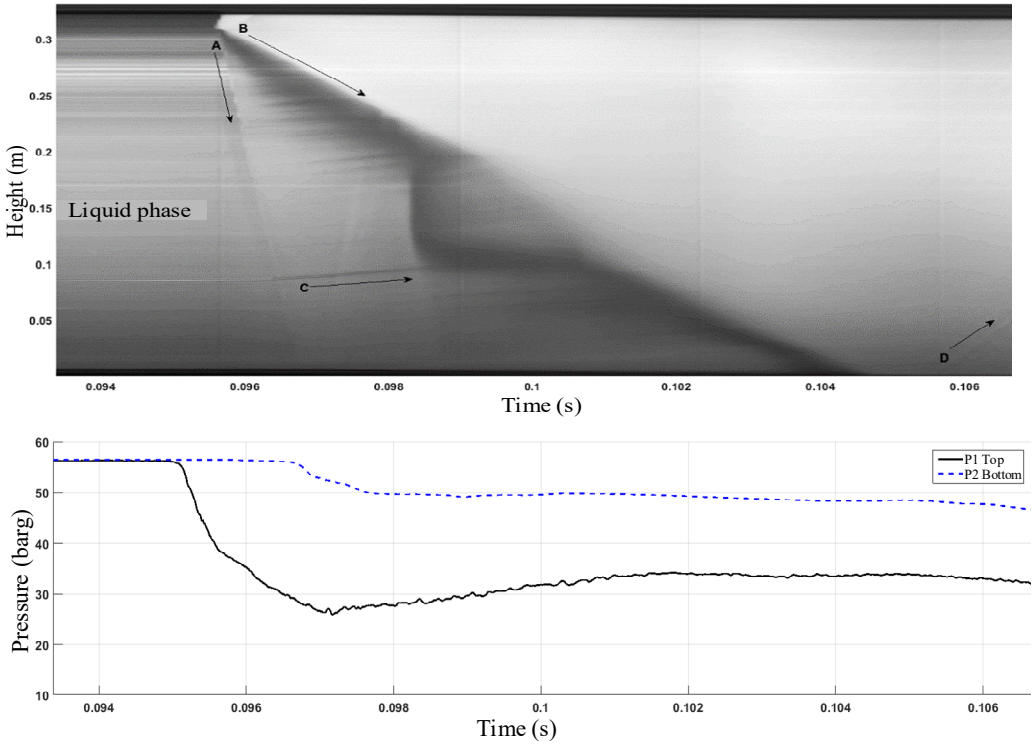


**Figure 5.** Experimental results from TR2 with 95% liquid level, showing an *x-t* plot of the processed high-speed film (MATLAB) and a *p-t* plot from pressure sensors P1 (top) and P2 (bottom).

a wave (G), probably an expansion wave originating at the liquid/vapor interface, was observed propagating with a constant velocity of 8.0 m/s toward the outlet. The reason for the occurrence of an expansion wave in this region was believed to be caused by choked flow conditions downstream of the evaporation inside the tube. The two-phase flow (D) seemed to accelerate toward the outlet. A calculated bulk velocity at time $t$ = 105.7 ms increased from 60 m/s (D) near the bottom to about 90 m/s (H) close to the outlet.

Fig. 5 shows an *x-t* plot of the processed high-speed film and a *p-t* plot from the pressure sensors in TR2. The initial liquid $CO_2$ level was 95%. Additional front illumination (Dedolight) was used compared to TR1, to provide more image details. The wave velocities in TR2 were similar to TR1. The results are presented in table 1.

The initial temperature in the current experiments was 19.5-19.7 ℃, hence above the experimentally determined [2] superheat limit temperature at 1 atm (−6 ℃). According to the original hypothesis proposed by Reid [5], homogenous nucleation could then occur during the expansion to atmospheric pressure if heterogeneous nucleation at the tube wall or in bulk impurities was suppressed. In a later publication [18], taking isentropic expansion into account, Reid proposed that liquid $CO_2$ would not allow attainment of a spinodal state in the expansion to 1 atm if the initial temperature was below 19 ℃. In the current experiments it is believed that heterogeneous nucleation occurred before reaching a spinodal state, hence no homogenous nucleation is assumed. The reason for this was the observation of vapor bubbles upstream of the evaporation wave.

## PHASE TRANSITION RATE AND ENERGY ESTIMATIONS

This section presents a simple phase transition rate estimate and an estimate of the energy potentially released if the $CO_2$ is allowed to expand from the initial state (saturated liquid at $T_0$ = 19.5 ℃, $P_0$ = 56 barg) to the end state ($T_2$ = −78.9 ℃, $P_2$ = 1 atm). This would be the case, for instance in a tank rupture. Isentropic expansion is assumed from the initial state (0) to the metastable state (1), where rapid boiling is initiated. Assuming adiabatic phase change, the latent heat of vaporization is supplied from the energy stored in the metastable liquid [5]. As the expansion continues below the triple point ($T_{tr}$ = −56.6 ℃, $P_{tr}$ = 5.18 bar), the $CO_2$ in the end state (2) will consist of a mixture of gas and dry ice. The vapor fraction at the end state and energy release will depend on whether the adiabatic evaporation is assumed reversible or irreversible. In these simplified calculations, the process is assumed isentropic, which probably will result in an overestimation of the energy release [12, 19]. Fig. 6 shows a sketch of the control volume as the evaporation wave is propagating through the liquid phase.

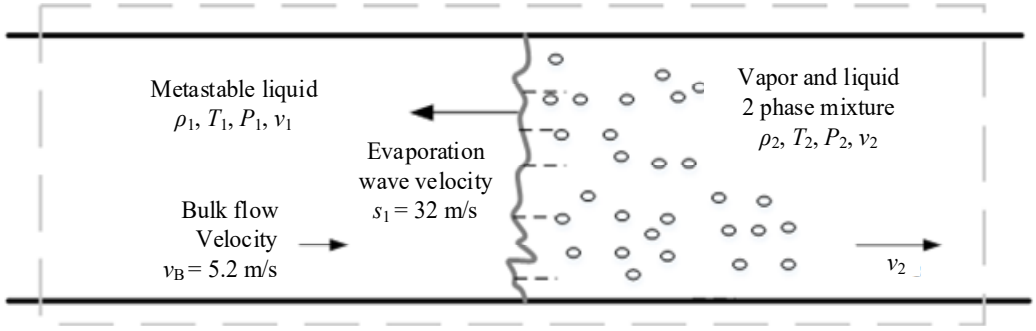


**Figure 6.** Control volume used in the calculations.

The velocity calculated in Eq. (1) is the calculated net velocity upstream $v_1$:

$$v_1 = s_1 + v_B = 32\left[\frac{\mathrm{m}}{\mathrm{s}}\right] + 5.2\left[\frac{\mathrm{m}}{\mathrm{s}}\right] = 37.2\left[\frac{\mathrm{m}}{\mathrm{s}}\right], \tag{1}$$

where $v_B$ (m/s) is the liquid phase bulk flow velocity and $s_1$ (m/s) is the evaporation wave velocity. The estimated phase transition rate presented in Eq. (2) is:

$$\dot{m}'' = \rho_1 \cdot v_1 = 731\left[\frac{\mathrm{kg}}{\mathrm{m}^3}\right] \cdot 37.2\left[\frac{\mathrm{m}}{\mathrm{s}}\right] \approx \underline{27200}\left[\frac{\mathrm{kg}}{\mathrm{m}^2 \cdot \mathrm{s}}\right], \tag{2}$$

where $\rho_1$ (kg/m$^3$) is an estimate of the density in the expanded, metastable liquid state ($T_1$ = 10 ℃, $P_1$ = 48 barg) calculated using the Span Wagner technical equation of state [12] and a T-S diagram. These numbers could be used as inputs in the validation of the source terms in a 1D BLEVE model.

An estimate of the energy potentially released if the $CO_2$ is allowed to expand from the initial state to the end state is presented in Eq. (3):

$$E_v = m \cdot (u_0 - u_2) = 0.017[\mathrm{kg}] \cdot (467 - 371)\left[\frac{\mathrm{kJ}}{\mathrm{kg}}\right] = 0.017[\mathrm{kg}] \cdot 95\left[\frac{\mathrm{kJ}}{\mathrm{kg}}\right] = \underline{1.6[\mathrm{kJ}]} \tag{3}$$

where $m$ (kg) is the mass of $CO_2$ originally present in the test rig, $u_0$ (kJ/kg) is the estimated internal energy at the initial state and $u_2$ (kJ/kg) is the estimated internal energy at the end state.

An estimate of the energy flux potentially released if the $CO_2$ is allowed to expand from the initial state to the end state is presented in Eq. (4):

$$\dot{E}'' = \dot{m}'' \cdot (u_0 - u_2) = 27200\left[\frac{\mathrm{kg}}{\mathrm{m}^2 \cdot \mathrm{s}}\right] \cdot 95\left[\frac{\mathrm{kJ}}{\mathrm{kg}}\right] = \underline{2584}\left[\frac{\mathrm{MJ}}{\mathrm{m}^2 \cdot \mathrm{s}}\right] \tag{4}$$

where $\dot{m}''$ (kg/(m$^2$·s)) phase transition rate, $u_0$ (kJ/kg) is the estimated internal energy at the initial state and $u_2$ (kJ/kg) is the estimated internal energy at the end state.

The calculations and results from the phase transition rate and energy estimations are summarized in Table 2.

**Table 2.** Data, phase transition rates and energy estimations.

| Description | TR1 |
|---|---|
| Initial mass of $CO_2$ , $m$ (g) | 17 |
| Density, expanded liquid phase, $\rho_1$ (kg/m$^3$) | 731 |
| Net evaporation wave velocity $v_1$ (m/s) | 37.2 |
| Internal energy, initial state $u_0$ (kJ/kg) ($T_0$=19.5 ℃, $P_0$=56 barg) | 467 |
| Internal energy, end state, $u_0$ (kJ/kg) ($T_2$=19.5 ℃, $P_2$=1 atm) | 371 |
| Phase transition rate, $\dot{m}''$ (kg/(m$^2$·s)) | 27200 |
| Energy potentially released in the expansion, $E_v$ (kJ) | 1.6 |
| Energy flux, potentially released in the expansion, $\dot{E}''$ (MJ/(m$^2$·s)) | 2584 |

## CONCLUSION

This article presents experimental results from two test runs, TR1-TR2, with rapid boiling of carbon dioxide in a transparent polycarbonate expansion tube. The experimental setup that included a high-speed camera and two pressure sensors was able to successfully identify the expected phenomena such as the acoustic rarefaction waves, the evaporation wave and a liquid /liquid-vapor contact surface. Calculated wave propagation velocities were presented. The evaporation wave velocity was constant in the upper part of the test section. No evaporation front details could be observed with the current setup. The experimental results did not show evidence of homogenous nucleation. An application of the experimental results on $CO_2$ evaporative front propagation is to provide model validation data for interfacial flux source terms in a 1D BLEVE simulation model. The net evaporation wave velocity (37.2 m/s) together with liquid density calculations (731 kg/m$^3$) was used to estimate the phase transition rate in the expanded, metastable liquid. The estimated phase transition rate based on the experimental data was 27200 kg/(m$^2$·s). An estimate of the energy flux potentially released if the $CO_2$ was allowed to expand from the initial state to the end state gave the result 2584 MJ/(m$^2$·s).

## REFERENCES


1. Birk, A. M., Davison, C., and Cunningham, M. Blast Overpressures from Medium Scale BLEVE Tests, Journal of Loss Prevention in the Process Industries, 20(3): 194-206, 2007.
2. Abbasi, T., and Abbasi, S. A. The Boiling Liquid Expanding Vapour Explosion (BLEVE): Mechanism, Consequence Assessment, Management, Journal of Hazardous Materials, 141(3): 489-519, 2007.
3. Zang, Y., Schork, J., and Ludwig, K. Revisiting the Conditions for a $CO_2$ Tank Explosion, Presented at the 2013 AIChE Spring Meeting, 2013.
4. Clayton, W. E., and Griffin, M. L. Catastrophic Failure of a Liquid Carbon Dioxide Storage Vessel, Process Safety Progress, 13(4): 202-209, 1994.
5. Reid, C. R. Possible Mechanism for Pressurized-Liquid Tank Explosions or BLEVE's, Science, 203(4386): 1263-1265, 1979.
6. Xie, M. Thermodynamic and Gasdynamic Aspects of a Boiling Liquid Expanding Vapour Explosion, Dissertation, Delft University of Technology, The Netherlands, 2013.
7. Abbasi, T., and Abbasi, S. A. Accidental Risk of Superheated Liquids and a Framework for Predicting the Superheat Limit, Journal of Loss Prevention in the Process Industries, 20(2): 165-181, 2007.
8. Bjerketvedt, D., Egeberg, K., Ke, W., Gaathaug, A., Vaagsaether, K., and Nilsen, S. H. Boiling Liquid Expanding Vapor Explosion in $CO_2$ Small Scale Experiments, Energy Procedica, 4: 2285-2292, 2011.
9. Ke, W. $CO_2$ BLEVE (Boiling Liquid Expanding Vapor Explosion), Master's Thesis, Telemark University College, Norway, 2009.
10. Van Der Voort, M. M., Van Wees, R. M. M., Ham, J. M., Spruijt, M. P. N., Van Den Berg, A. C., De Bruijn, P. C. J., and Van Ierschot, P. G. A. An Experimental Study on the Temperature Dependence of $CO_2$ Eexplosive Evaporation, Journal of Loss Prevention in the Process Industries, 26(4): 830-838, 2013.
11. Van Der Voort, M. M., Van Den Berg, A. C., Roekaerts., D. J. E. M., Xie, M., and De Bruijn, P. C. J. Blast from Explosive Evaporation of Carbon Dioxide: Experiment, Modeling and Physics, Shock Waves, 22(2): 129-140, 2012.
12. Pinhasi, G. A., Ullmann, A., and Dayan, A. 1D Plane Numerical Model for Boiling Liquid Expanding Vapor Explosion (BLEVE), International Journal of Heat and Mass Transfer, 50(23-24): 480-495, 2007.
13. Tϕsse, S., Vagsaether, K., and Bjerketvedt, D. An Experimental Investigation of Rapid Boiling of $CO_2$, Shock Waves, 25(3): 277-282, 2015.
14. Span, R., and Wagner, W. A New Equation of State for Carbon Dioxide Covering the Fluid Region from the Triple-Point to 1100 K at Pressures up to 800 MPa, Journal of Physical and Chemical Reference Data, 25(6): 1509-1596, 1996.
15. Hill, L. G. An Experimental Study of Evaporation Waves in a Superheated Liquid, Dissertation(Ph.D.), California Institute of Technology, 1991.
16. Shepherd, J. E., and Simões-Moreira, J. R. Evaporation Waves in Superheated Dodecane, Journal of Fluid Mechanics, 382: 63-86, 1999.

17. Reinke, P., and Yadigaroglu, G. Explosive Vaporization of Superheated Liquids by Boiling Fronts, International Journal of Multiphase Flow, 27(9): 1487-1516, 2001.
18. Kim-E, M. E., and Reid, R. C. The Rapid Depressurization of Hot, High Pressure Liquid or Supercritical Fluids, Chemical Engineering at Supercritical Fluid Conditions, Ann Arbor Science Publishers, 1983.
19. Planas-Cuchi, E., Salla, J. M., and Casal, J. Calculating Overpressure from BLEVE Explosion, Journal of Loss Prevention in the Process Industries, 17(6): 431-436, 2004.

# Paper E

# Blast from pressurized $CO_2$ released into a vented atmospheric chamber

This paper was presented at 26th ICDERS (26th International Colloquium on the Dynamics of Explosions and Reactive Systems in Boston, USA in August 2017. Submission number 826.

# Blast from pressurized $CO_2$ released into a vented chamber

Per Morten Hansen[a], Andre Vagner Gaathaug[a], Dag Bjerkedvedt[a], Knut Vaagsaether[a]
[a]University College of Southeast Norway
Porsgrunn, Telemark, Norway

## 1 Introduction

Accidental release of carbon dioxide ($CO_2$) from a high-pressure reservoir (a tank, or pipeline) into an atmospheric, vented room (laboratory, factory hall etc.) range from small releases (erroneous opening of a valve) to big, abrupt releases (complete tank rupture and BLEVE). Hazards associated with the larger $CO_2$ releases are related to both the harmful properties of the fluid (asphyxiation and frost injuries) and the energy release (phase transition rate, blast wave, accelerated fragments, dynamic loads on structures). The pressure buildup and impulse will be a function of the initial state of the fluid, the degree of superheat, the amount of mass released, the vent opening area and the volume ratio between the high-pressure reservoir and vented room / chamber. Zhang et al. [1] have discussed previous accidents involving $CO_2$ tank explosions.

This paper presents results from small-scale experiments on the release of saturated pressurized $CO_2$ from a high-pressure reservoir at ambient temperature (19 °C) into a vented, atmospheric chamber. The main goal was to investigate the effect of vent opening and initial liquid content on the measured pressure and calculated impulse response in the atmospheric chamber. In addition, an objective was to study if the volume increase resulting from the rapid boiling would contribute to shock strength in the current test geometry. The contribution includes experimental results from two different vent-opening areas (100 and 10 $cm^2$) and two different liquid portions (vapor only and a liquid/vapor mixture). Experimental results showing the release of $CO_2$ from a high pressure reservoir has been previously described by others [2,3,4,5,6], but not with a test rig geometry similar to the one presented here.

## 2 Materials and methods

Figure. 1 shows a schematic diagram of the experimental setup (a), and a photograph of the test rig (b). The test setup consisted of following main parts (1-5): (1) a high pressure reservoir with borosilicate windows at the front and back, sensor side ports and flanges at the main outlet; (2) an atmospheric chamber with an adjustable vent opening; (3) a pneumatic plunger actuator with a cross shaped knife; (4) a multi-layer aluminum foil diaphragm; and (5) a $CO_2$ supply system with two 40-liter industry grade cylinders. One cylinder supplied liquid phase feed while the other cylinder delivered vapor phase only. Pressure sensors and temperature sensors were installed at various positions on the test rig. Before each test run, the high-

Correspondence to: perha@usn.no

pressure chamber was flushed 3 times with vapor phase $CO_2$ at 10 bar to remove air initially present in the reservoir. The high-pressure reservoir was a custom-designed level gauge with a square channel rated at 100 barg. The maximum liquid fill volume was 0.13 $dm^3$ and the total volume was 0.19 $dm^3$. Sensors (temperature T1-T6 and pressure P1-P6) were mounted on the two sidewalls.

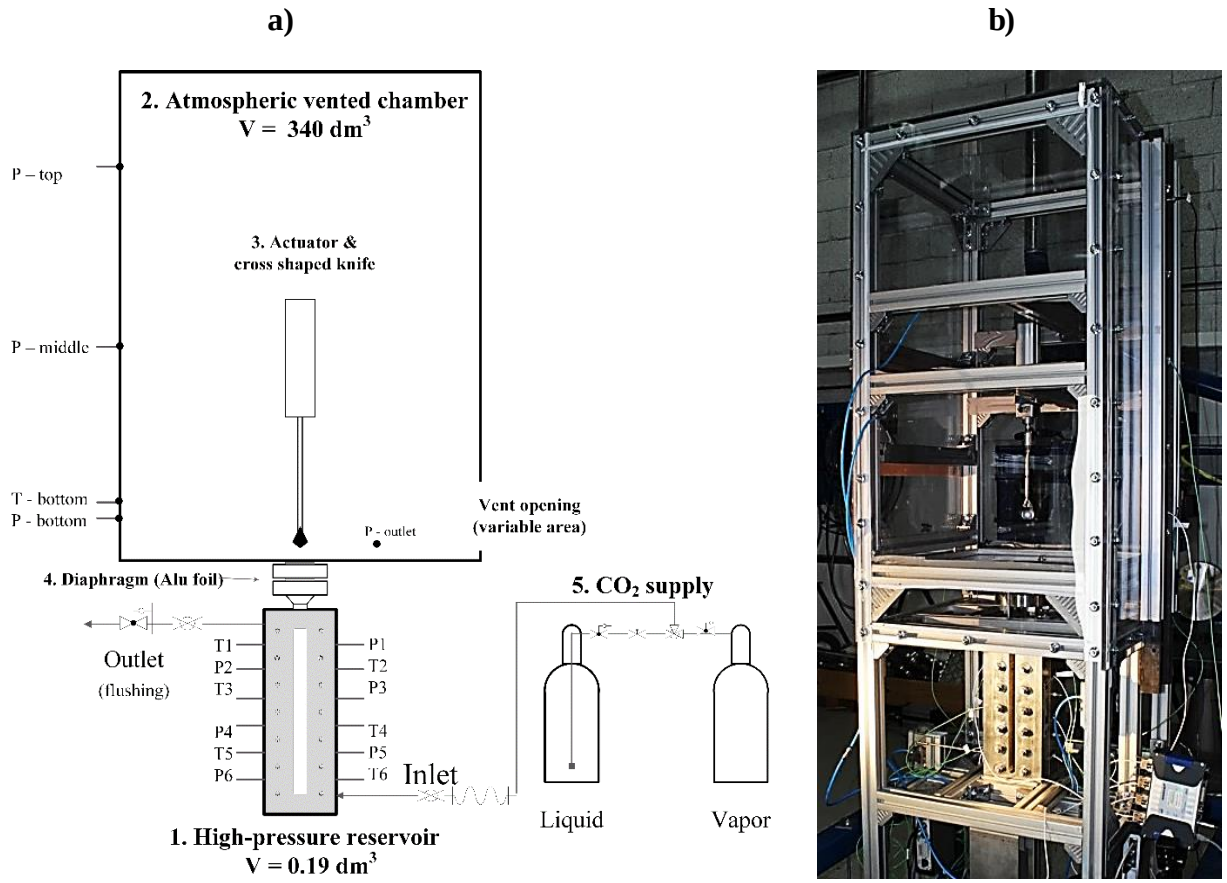


Figure 1. Left: a schematic diagram of the test setup; right a photograph showing the experimental test rig

The atmospheric vented chamber was equipped with transparent polycarbonate sidewalls enabling visual observation of $CO_2$ release. The chamber dimensions (width, depth and height) were 0.59 x 0.59 x 0.98 meter. The volume was 340 $dm^3$, after subtracting the volume of the actuator and aluminums profiles.

Four pressure sensors were installed inside the atmospheric vented chamber. Three sensors were mounted on a vertical U-channel steel beam at the rear sidewall while the last sensor was mounted on the sidewall close to the vent opening. A Kulite-XTM-190-100G piezoresistive transducer with a measuring range of 0-100 psig was installed in the steel beam bottom position. The remaining sensors were Kistler 7001 piezoelectric transducers with a measuring range of 0-250 barg.

A temperature sensor was installed close to the bottom pressure sensor on the steel beam. The temperature sensors were type –K thermocouples with a measurement error limit of ± 1.5°C.

A Photron Fastcam SA-1 high-speed camera operating at 5000 fps was used to record the release from the high-pressure reservoir into the vented chamber. High-speed movies with sensor data included were

prepared in MATLAB. The matching of the image observations with the sensor measurements provided a basis for interpretation of the experimental results. The measurements shown in Fig. 2 include temperature $T_1$ and pressure $P_1$, located in the high-pressure reservoir (0.13m below the outlet), pressure $P_{LP\ Chamber}$, located in the atmospheric vented chamber (0.18 m above the bottom), and calculated impulse of $P_{LP\ chamber}$ (time integrated pressure measurement). The rapid $CO_2$ expansion and phase transition processes in the high-pressure reservoir could be similar to the results published by Tosse et al. [2] and Hansen et al. [3]. These observations included well-known phenomena such as the rarefaction fan, a condensation wave, a contact surface and an evaporation wave.

## 3 Results and discussion

Table 1 shows test parameters and experimental results from the four presented test runs (TR1-TR4). The vent opening area and the liquid content in the high-pressure reservoir were the main varied parameters. Initial conditions were saturated $CO_2$ at ambient temperature (19°C).

Table 1: Test parameters and experimental results from the four presented test runs.

| Parameter \ Test run | TR1 | TR2 | TR3 | TR4 |
|---|---|---|---|---|
| Vent opening – atmospheric chamber ($cm^2$) | 100 | 10 | 100 | 10 |
| Liquid volume – high-pressure reservoir ($dm^3$) | 0 | 0 | 0.13 | 0.13 |
| Vapor volume – high-pressure reservoir ($dm^3$) | 0.19 | 0.19 | 0.06 | 0.06 |
| Mass of $CO_2$, estimated (g) | 35 | 35 | 110 | 110 |
| Pressure, initial (barg) | 53 | 52 | 55 | 55 |
| Temperature, initial (°C) | 19 | 19 | 19 | 19 |
| Pressure, peak – vented chamber bottom (barg) | 0.15 | 0.17 | 0.20 | 0.15 |
| Impulse, calculated at 100 ms (kPa·ms) | 55 | 149 | 346 | 426 |

Figure 2 shows three high-speed images from two different test runs (TR1 and TR3), captured at 20 ms and 100 ms after initiation. Initial time $t_0$ = 0 ms was defined as the time of diaphragm rupture. First, a jet of partially condensed vapor / dry ice was observed, moving out of the high-pressure reservoir and into the atmospheric vented chamber. The initial blast wave could not be observed with the current camera arrangement. The peak pressure from the initial blast wave ranged from 0.15 to 0.20 barg.

In the test runs containing a liquid / vapor mixture (T3 and T4), an increase in the jet intensity / mass flow rate was observed, about 3 ms after the diaphragm rupture. This was most probably the contact surface between liquid and liquid/vapor. The boiling liquid / expanding vapor then increased the intensity of the multi-phase jet flow, which completely filled the vented chamber with white mist.

The high-speed movies showed periodic wall oscillations due to pressure reflections inside the vented chamber. The Kulite sensor (bottom position) seemed to provide more reliable results than the Kistler sensors (top, middle and outlet) in the present experimental study. It seemed less sensitive to vibrations and could provide pressure measurements for a longer period due to the piezoresistive operation. Consequently, the presented pressure measurements from the vented chamber originate from the Kulite bottom sensor only.

Figure 3 shows an impulse plot and two pressure plots from the first 20-millisecond period. The pressure measurements suggested that the rapid phase transition (boiling) was too slow in the current test geometry to contribute to the initial shock strength. No additional peak or pressure increase could be related to the boiling liquid released from the high-pressure reservoir during this period (0-20 ms).

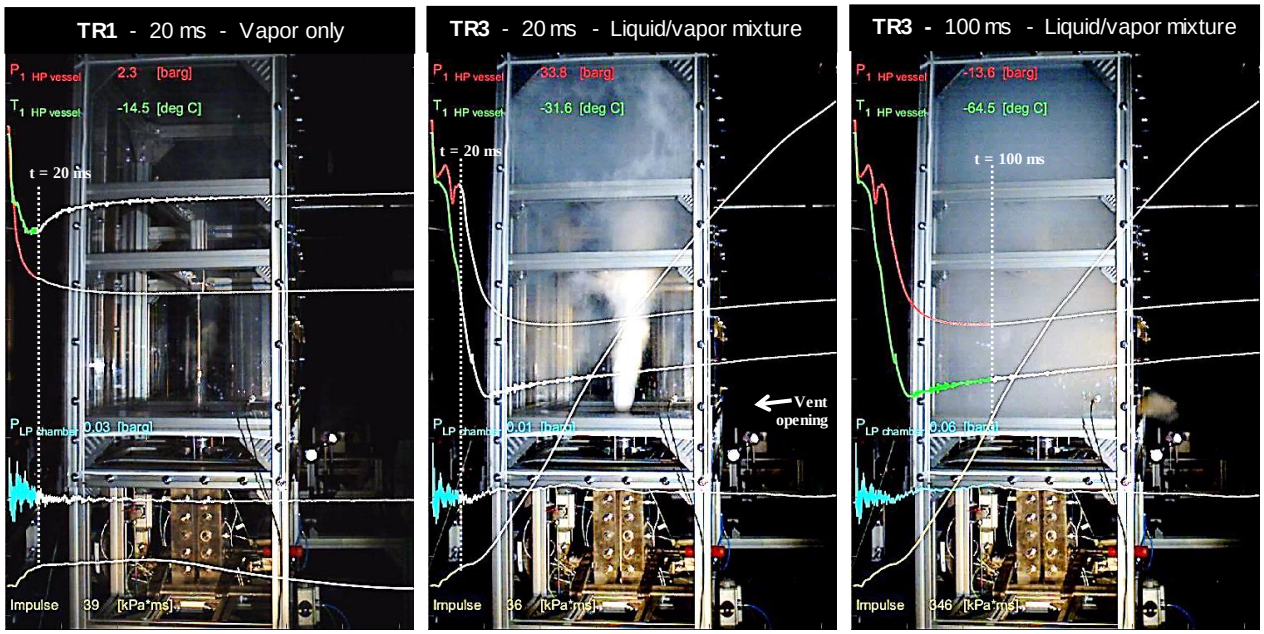


Figure 2. High-speed images and sensor data showing the release of $CO_2$ from the high-pressure reservoir into the atmospheric chamber with a 100 $cm^2$ vent opening. Left: After 20 ms, vapor only; Middle: After 20 ms, (liquid/vapor mixture); Right: After 100 ms, 100% (liquid/vapor mixture).

The calculated impulses from all four test runs were almost identical up to about 7.5 ms. Then, for a few milliseconds, the impulse in the vapor only test runs (TR1 and TR2) increased faster than in the liquid/vapor mixture test runs (TR3 and TR4). In the vapor only test runs (TR1 and TR2), the jet from the high-pressure reservoir decayed rapidly and was no longer visible after about 20 ms, as is shown in Fig.2 - left image. The middle image in Fig. 2 shows that an increased initial liquid content resulted in an increased duration of the $CO_2$ jet. The jet release then lasted about 40 milliseconds.

Figure 4 shows an impulse plot and pressure plot from the 0-500 millisecond period. The right plot shows a connection between the pressure response in the vented chamber with the liquid content in the high-pressure reservoir (vapor only or a liquid/vapor mixture). For the liquid / vapor mixture test runs (TR3 and TR4), a rise from zero to 0.05 – 0.07 barg in the vented chamber bottom pressure was observed, starting at about 30 ms. A high liquid content resulted in a longer period at an elevated pressure. Consequently, the calculated impulse was significantly larger when the high-pressure reservoir contained a liquid / gas mixture, as compared to vapor phase only. The duration of the liquid / vapor mixture test runs was longer than 100 ms, due to the time needed to push the cloudy mist of $CO_2$ in the vented chamber out through the vent opening.

An unexpected crossover in impulse history between TR3 and TR4 (both liquid / vapor mixture) was observed in Fig. 4 after about 150 milliseconds. One would expect that the smallest vent opening area (10 $cm^2$) should result in a higher calculated impulse than the 100 $cm^2$ opening due to a larger pressure buildup. A possible reason why this was not observed here could be an effect of the temperature dependency on the pressure measurements. As a conservative estimation, the impulse for the liquid/vapor mixture (TR3 and TR4) stated in table 1 was calculated at 100 ms. This is because a permanent offset originating from a thermal zero shift would result in a significant error contribution in the impulse calculations. The temperature decreased significantly both inside the high-pressure reservoir and inside the vented chamber, due to the rapid boiling and expansion.

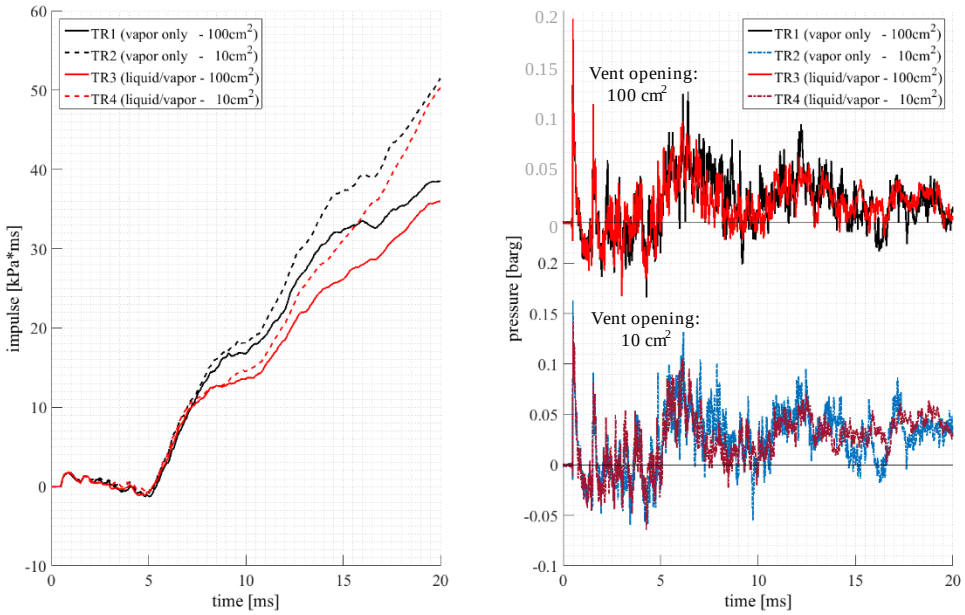


Figure 3. Impulse calculations (left) and pressure measurements (right) from the vented chamber bottom sensor showing the first 20 milliseconds after diaphragm rupture. There are four test runs (TR1-TR4) with two vent-opening areas (100 and 10 $cm^2$) and two different liquid/vapor proportions (vapor only and a liquid/vapor mixture).

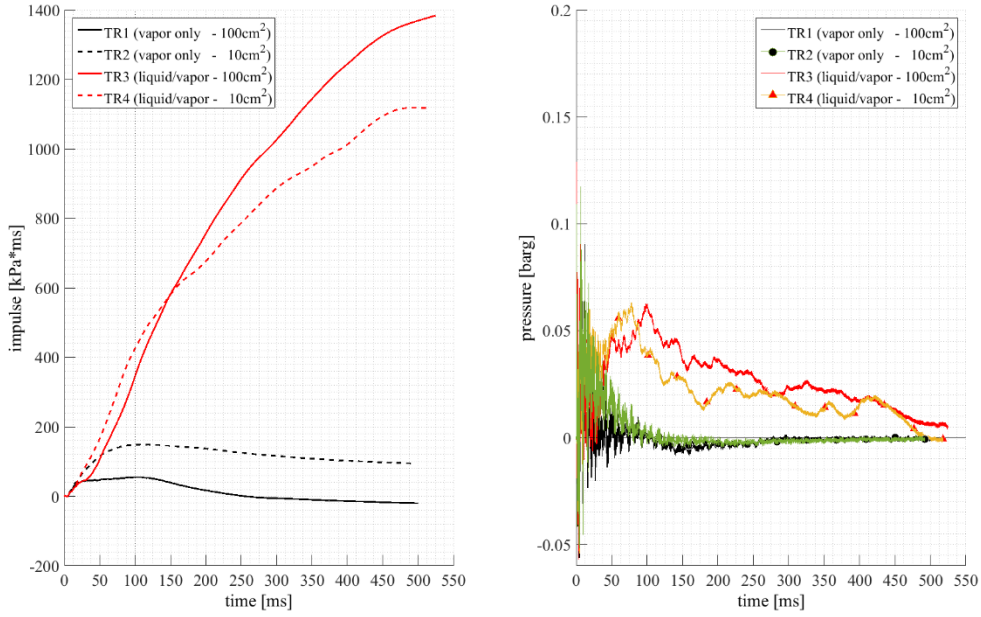


Figure 4. Impulse calculations (left) and pressure measurements (right) from the vented chamber bottom sensor showing the first 500 milliseconds after diaphragm rupture. There are four test runs (TR1-TR4) with two vent-opening areas (100 and 10 $cm^2$) and two different liquid/vapor proportions (vapor only and a liquid/vapor mixture).

The jet that formed at the exit of the diaphragm was under-expanded. The main part of the expansion occurred downstream of the diaphragm. The outlet section could probably influence the experimental results to some extent. With sonic conditions at the throat and by replacing the original straight slip-on flange to a divergent outlet section, the flow could be accelerated and then influence the outlet pressure and velocity. However, the mass flow rate was still believed to be unchanged for a period of time due to choking conditions at the throat upstream if the diaphragm. It would be desirable to achieve an instantaneous release of liquid $CO_2$ into the vented chamber, similar to the work by van der Voort et al. [6]. That would provide a better opportunity to investigate the effect of the rapid phase transition on blast wave pressure and calculated impulse.

Further investigations should include test runs with a reduced vapor headspace in the high-pressure reservoir, giving a liquid content closer to 100%. In addition, the volume of the vented chamber could be reduced, to study the response of venting opening area on the measured peak pressure inside the chamber.

## 4 Conclusions

This paper presents results from small-scale experiments on the blast effect of pressurized liquefied $CO_2$ released from a high-pressure reservoir into a vented atmospheric chamber. Some main findings are summarized below. The rapid phase transition (boiling) did not contribute to the initial shock strength in the current test geometry. The boiling process seemed too slow or the release rate from the high-pressure reservoir was too low to contribute to the measured peak pressure, which was in the range 0.15-0.20 barg. The test runs with a liquid/vapor mixture in the high-pressure reservoir, showed a significantly higher impulse (time integrated pressure response) compared to test runs with vapor phase only. Reducing the vent opening from 100cm$^2$ to 10cm$^2$ resulted in a slight increase in impulse calculated at 100 milliseconds. The effect of vent opening on the impulse was evident in the test runs with vapor only, but not so clear in the test runs with the liquid/vapor mixture.

## References

[1] Zhang Y, Schork J, Ludwig K. (2013). Revisiting the conditions for a $CO_2$ tank Explosion. Proceedings of the 2013 AIChE Spring Meeting and Ninth Global Congress on Process Safety, Curran Associates, San Antonio, Texas, 2013.

[2] Tosse S, Vaagsaether K, Bjerketvedt D. (2014). An experimental investigation of rapid boiling of $CO_2$. Shock Waves 25: 277.

[3] Hansen PM, Gaathaug AV, Bjerketvedt D, Vaagsaether K. (2017). The behavior of pressurized liquefied $CO_2$ in a vertical tube after venting through the top. Int. J. Heat Mass Transf. 108: 2011.

[4] Bjerketvedt D, Egeberg K, Ke W, Gaathaug A, Vaagsaether K. (2011). Boiling liquid expanding vapor explosion in $CO_2$ Small scale experiments. Energy Proc. 4: 2285.

[5] Chiccarelli G, Melguizo-Gavilanes J, Shepherd JE. (2015). Pressure-field produced by the rapid vaporization of a $CO_2$ liquid column. Proceedings of the 30th International Symposium on Shock Waves. Tel-Aviv, 2015.

[6] van der Voort MM, van den Berg AC, Roekaerts DJEM, Xie M, de Bruijn PCJ. (2012). Blast from explosive evaporation of carbon dioxide: experiment, modeling and physics. Shock Waves 22: 129.

# Paper F

# Modelling and Simulation of Phase Transition in Compressed Liquefied CO2

This paper was presented orally by Prasanna Kumara at the 9th EUROSIM (the 9th Eurosim Congress on Modelling and Simulation in Oulu, Finland on September 2016. The paper is published in the proceedings of the 9th EUROSIM. 2016.

Per Morten Hansen was a co-author on this conference paper. He provided the experimental results and prepared four of the figures in the paper. He also contributed to the interpretation and discussions of the results.

# Modelling and Simulation of Phase Transition in Compressed Liquefied $CO_2$

Sindre Tosse, Per Morten Hansen and Knut Vaagsaether
*Department of Process, Energy and Environmental Technology*
*University College of Southeast Norway*
*3918 Porsgrunn, Norway*
*Email: knut.vagsather@hit.no*

***Abstract*—A model and solution method for phase transition in compressed liquefied gases is presented. The model is a two-phase 6-equation model with a common flow velocity for the two phases. The numerical method for solving the model is based on the 2. order shock capturing MUSCL-scheme with a HLLC Riemann solver. The van der Waal cubic equation of state is used for closing the set of equations. The phase transition model is based on thermodynamic and mechanical relaxation between the phases. The goal of the work is to present a numerical model capable of resolving the two-phase flow situation in the depressurization of a vessel or pipe containing liquefied $CO_2$. Simulation of expansion and phase transition in pressurized liquefied $CO_2$ is presented and compared with experimental data. The simulations are with a one dimensional geometry and the experiments are performed in a narrow tube. Wall effects in the experiments are not captured in the simulations. The wave structure seen in the experiments is reproduced by the simulation although not quantitatively. The simulations show that the fluid is in the metastable region before it undergoes a phase transition. The level of expansion of the metastable liquid shown in the in the simulations is not seen in the experiments.**

***Keywords*-Phase transition, liquefied gas, BLEVE, van der Waal, MUSCL**

## I. Introduction

The focus of this paper is to present a numerical model capable of resolving the two-phase flow situation in the depressurization of a vessel or pipe containing liquefied $CO_2$. The methodology is attended for use with all types of liquefied pressurized gases. Sublimation of solid particles will not be addressed, since liquid-vapour interaction is the dominant process inside and in the immediate vicinity of the vessel. In order to get the necessary level of accuracy in the thermodynamic calculations, a non-monotonic equation of state is chosen. For $CO_2$, the most accurate liquid-vapour EOS available is the Span-Wagner multiparameter EOS [1]. It would be extremely challenging to implement this type of EOS into a numerical code, but the authors regards this as the end-goal of the present work. The usage of a non-monotonic EOS in a numerical solver raises a number of issues, since both the liquid and vapour states have a limited region of existence. In order to deal with these issues, the simplest form of a non-monotonic EOS, namely the cubic van der Waals EOS, is used in the development of a numerical code. Menikoff and Plohr [2] state that the Maxwell equal-area rule must be applied to modify the equation of state in order to avoid imaginary speed of sound in the van der Waals loop. Saurel et al. [3] propagate the misconception that the square speed of sound is negative in the spinodal zone. In the present work however, a less strict method is applied to allow metastable states, while maintaining a real speed of sound. While quantitatively inaccurate, the van der Waals equation of state provides a qualitative representation of every major feature of real gas behavior. Combined with its simple formulation, this makes it an often used EOS in model development and academic work. Using a non-monotonic equation of state in a numerical solver raises a number of issues. It is therefore necessary to develop robust solving algorithms that are capable of handling two phase flow in the vicinity of spinodal states. The van der Waals EOS is chosen to develop a proof of concept, because its simple formulation allows for analytical expressions for many thermodynamic parameters, e.g. the spinodal curve. Most compressible two-phase solvers use some form of stiffened gas equation of state or a more generalized Mie Gruneisen form equation of state. Even though it can be written on Mie-Gruneisen form, the van der Waals equation of state has been little used in the context of fluid dynamics. Slemrod [4] analyzed the dynamic phase transitions in a van der Waals fluid. Zheng et al. [5] used an interface capturing method with a generalized equation of state on the Mie-Gruneisen form where, among others, the van der Waals equation of state was used. To the authors knowledge, no solvers allowing metastable two-phase compressible flow with phase transition using the van der Waals equation of state exists.

Some work has been done to develop numerical models that are capable of describing evaporation waves. Saurel et al. [6] developed a Godunov method for compressible multiphase flow that was later applied to the subject of phase transition in metastable liquids [3]. They were able to qualitatively reproduce the evaporation front velocities measured by Simoes-Moreira and Shepherd [7]. In recent years, there have been several attempts to model BLEVE-type scenarios [8], [9], [10].

### A. Metastable liquids

Figure 1 shows the pressure-volume diagram of $CO_2$ calculated from the Span-Wagner EOS. The spinodal curve is defined as $\left(\frac{\partial p}{\partial v}\right)_T = 0$ and is seen as an absolute boundary for an expanding liquid state. In the region between the liquid saturation curve and the spinodal curve a metastable liquid can exist. A metastable liquid is not in an equilibrium condition and a fluid can only stay in such a state for very short times. During a rapid expansion

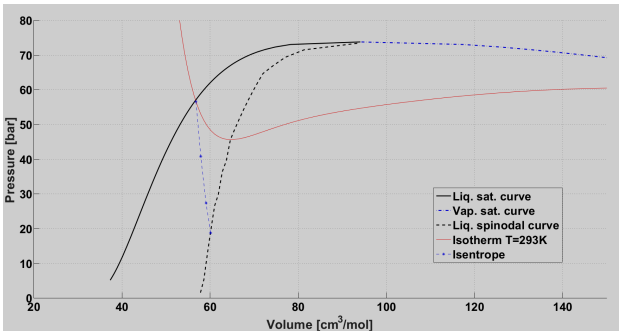


Figure 1. Pressure-volume diagram for $CO_2$ showing saturation curve, spinodal curve, an isotherm and an isentrope.

of a compressed liquefied gas metastable liquid states will occur behind propagating expansion waves before phase transition forces the thermodynamic state to change towards equilibrium conditions.

## II. Model for two phase flow and phase transition

The numerical model used in this work solves the two-pressure 6-equation model given by Saurel et al [11]. Without heat and mass transfer, the model reads:

$$\frac{\partial \alpha_1}{\partial t} + u\frac{\partial \alpha_1}{\partial x} = \mu(p_1 - p_2), \tag{1}$$

$$\frac{\partial \alpha_1 \rho_1}{\partial t} + \frac{\partial \alpha_1 \rho_1 u}{\partial x} = 0, \tag{2}$$

$$\frac{\partial \alpha_2 \rho_2}{\partial t} + \frac{\partial \alpha_2 \rho_2 u}{\partial x} = 0, \tag{3}$$

$$\frac{\partial \rho u}{\partial t} + \frac{\partial \rho u^2 + (\alpha_1 p_1 + \alpha_2 p_2)}{\partial x} = 0, \tag{4}$$

$$\frac{\partial \alpha_1 \rho_1 e_1}{\partial t} + \frac{\partial \alpha_1 \rho_1 e_1 u}{\partial x} + \alpha_1 p_1 \frac{\partial u}{\partial x} = -p_I \mu (p_1 - p_2), \tag{5}$$

$$\frac{\partial \alpha_2 \rho_2 e_2}{\partial t} + \frac{\partial \alpha_2 \rho_2 e_2 u}{\partial x} + \alpha_2 p_2 \frac{\partial u}{\partial x} = p_I \mu (p_1 - p_2). \tag{6}$$

The right hand side terms corresponds to pressure relaxation. $p_I$ is the interfacial pressure, estimated by

$$p_I = \frac{Z_2 p_1 + Z_1 p_2}{Z_1 + Z_2}, \tag{7}$$

where $Z_k = \rho_k c_k$ is the acoustic impedance of phase $k$. Where $\alpha_k$ is the volume fraction of phase k, $\rho_k$ is the density of phase k, $p_k$ is the pressure of phase k, $e_k$ is the specific internal energy of phase k, $Y_k$ is the mass fraction of phase k, $c_k$ is the speed of sound of phase k, $\mu$ is the dynamic compaction viscosity and determines the rate of pressure relaxation, $u$ is the flow velocity and an infinitesimal relaxation time, or large enough drag, is assumed leading to a common velocity between the phases. Phase 1 and phase 2 is vapour and liquid respectively. The mixture speed of sound used in this model is the frozen speed of sound,

$$c_f^2 = Y_1 c_1^2 + Y_2 c_2^2. \tag{8}$$

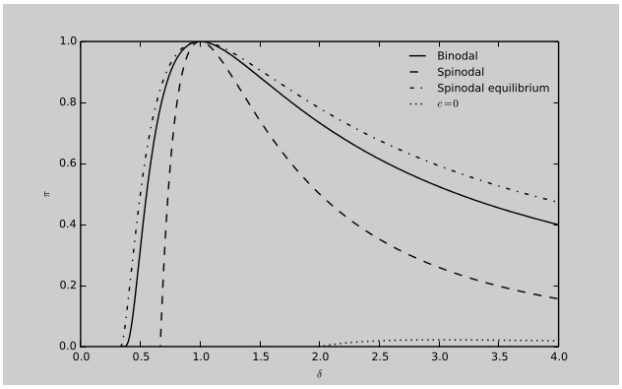


Figure 2. The binodal, spinodal and spinodal equilibrium curves of a van der Waals fluid in $\pi - \delta$ (reduced pressure and volume) space. The loci of zero speed of sound are also shown.

In the present work, we use stiff pressure relaxation ($\mu \to \infty$). As shown in [11], this means the recovery of the 5-equation model. Then the model is strictly hyperbolic with wave speeds $(u + c_f, u - c_f, u)$.

### A. The van der Waals equation of state

The van der Waals equation of state (vdW-EOS) is the simplest form of a cubic equation of state. It is classified as cubic because it can be written on the form

$$v^3 + a_2 v^2 + a_1 v + a_0 = 0 \tag{9}$$

where $v$ is the specific volume and $a_k$ are pressure and/or temperature dependent coefficients. The vdW-EOS can be derived from the ideal gas EOS by adding correction terms for the excluded volume occupied by finite-sized particles and inter-molecular forces. On its classical form, the vdW-EOS reads

$$\left(p + \frac{n^2 a}{V}\right)(V - nb) = nR_M T \tag{10}$$

where $n$ is the number of moles occupying the volume $V$ at pressure $p$ and temperature $T$. $R_M$ is the ideal gas constant. $a$ is a measure of the attraction between particles and $b$ is the volume excluded by one mole of particles (molecules). As the volume tends to infinity, the vdW-EOS converges to the ideal gas law. The special case of $V = nb$ corresponds to a situation where the volume $V$ is completely filled by the particles. At this point, the pressure tends to infinity. This implies that the van der Waals equation of state is only valid for $V > nb$. In terms of the volume at the critical point, this limit can be written as $\frac{v}{v_c} > \frac{1}{3}$.

Figure 2 shows the binodal, spinodal and spinodal equilibrium curves of a van der Waals fluid.

## III. Solver

The equation set is solved by the 2. order accurate shock capturing MUSCL-scheme (Monotone Upstream-centered Scheme for Conservation Laws) combined with a HLLC (Harten Lax vanLeer Contact) Riemann solver for the interfacial fluxes [12]. This solver is used for the

hyperbolic part of the equation set i.e. the left hand side of equations 2 to 6.

The shock capturing method with the approximate Riemann solver solves shock waves and contact surfaces as very steep gradients with a numerical diffusion of a shock or contact discontinuity thickness of usually three control volumes. The equation set is closed by the van der Waals equation of state. The time step is variable and controlled by the Courant-Friedrich-Levy number.

### A. Stiff pressure relaxation

The pressure relaxation step solves the equation set

$$\frac{\partial \alpha_1}{\partial t} = \mu(p_1 - p_2), \tag{11}$$

$$\frac{\partial \alpha_1 \rho_1 e_1}{\partial t} = -p_I \mu(p_1 - p_2), \tag{12}$$

$$\frac{\partial \alpha_2 \rho_2 e_2}{\partial t} = p_I \mu(p_1 - p_2) \tag{13}$$

in the limit $\mu \to \infty$. All other conserved variable groups are held constant during the relaxation step. According to [11], this system of equations can be replaced by

$$e_k(p, v_k) - e_k^0(p_k^0, v_k^0) + \hat{p}_I(v_k - v_k^0) = 0,\ k = 1, 2 \tag{14}$$

and the saturation constraint

$$(\alpha\rho)_1 v_1 + (\alpha\rho)_2 v_2 = 1 \tag{15}$$

where $(\alpha\rho)_k$ is constant during the relaxation step. The system can be closed by the van der Waal equation of state $e_k(\rho_k, p_k)$. Equation 14 can then be reformulated to $v_k(p)$ by using an estimate of $\hat{p}_I$. In the present work, the estimation $\hat{p}_I = p_I^0$ is used, but other estimates can also be used as shown by [11]. Finally, we insert the expressions for $v_k$ into eq. 15 and solve for $p$.

Since the pressure estimated by this method is not guaranteed to be in agreement with the mixture equation of state $p(\rho, e, \alpha_1)$, this pressure is only used to find the relaxed volume fraction $\alpha_1$. The relaxed pressure is then determined by the mixture equation of state and the internal energy from the redundant total energy equation. The conserved variables $(\alpha\rho e)_k$ are then re-initialized using the relaxed pressure and volume fraction. This ensures the conservation of mixture energy in the flow field.

Alternate relaxation methods can also be used. Both isentropic and isenthalpic relaxation methods has been tested with the same results as the method described here. This gives reason to assume that the thermodynamic relaxation path is of lesser importance, since it is only used to estimate the relaxed volume fraction. If the numerical method is expanded to a more complex EOS, this means that the pressure relaxation process most likely can be resolved with a less rigorous estimate of the thermodynamic relaxation path.

With the reduced vdW-EOS, eq. 14 can be written as

$$\pi(\delta_k) = \frac{2C_k\delta_k^2\hat{\pi}_I - 2\delta_k^3\hat{\pi}_I - 3\delta_k + 3}{\delta_k^2(3\delta_k - 1)}, \tag{16}$$

where

$$C_k = \delta_k^0 + \frac{1}{\hat{\pi}_I}\left[\frac{1}{2}(\pi_k^0 + \frac{3}{(\delta_k^0)^2})(3\delta_k^0 - 1) - \frac{3}{\delta_k^0}\right]. \tag{17}$$

Since we have no mass transfer, we can write

$$G_1\delta_1 + G_2\delta_2 = 1. \tag{18}$$

where $G_k = (\alpha\rho)_k v_c$. From this, we get

$$\delta_2(\delta_1) = \frac{1 - G_1\delta_1}{G_2} \tag{19}$$

The algorithm for stiff pressure relaxation solves the equation $f(\delta_1) = 0$ by the Newton-Raphson method, where

$$f(\delta_1) = \pi_1(\delta_1) - \pi_2(\delta_1),$$
$$\frac{\mathrm{d}\pi_k}{\mathrm{d}\delta_1} = \left(-\hat{\pi}_I\frac{6C_k - 2}{(3\delta_k - 1)^2} + \frac{6(3\delta_k^2 - 5\delta_k + 1)}{\delta_k^3(3\delta_k - 1)^2}\right)d_k,$$
$$d_1 = 1,\ d_2 = -\frac{G_1}{G_2}$$

Where $\pi$ is reduced pressure and $\delta$ is reduced volume.

### B. Stiff thermodynamic relaxation

The thermodynamic relaxation method used presently differs somewhat from the methods used by [3] and [13]. It is simpler in formulation and relatively easy to implement for any equation of state. We consider a two phase system with total density $\rho = \alpha_1\rho_1 + \alpha_2\rho_2$ and total internal energy $e = Y_1e_1 + Y_2e_2$. Since no mass or heat is added to the system during the relaxation step, these mixture properties are constant. We will consider the velocity of the two phases to be equal and constant during the relaxation step. Initially, the system is closed by the known variables $\rho_1, \rho_2, e_1, e_2$. In the numerical solver used presently, the two phases will be in mechanical equilibrium at the start of the relaxation step, but this is not a prerequisite of the procedure. The system can be uniquely determined by requiring complete thermodynamic equilibrium between the two phases:

$$p_1 = p_2 = p,\ T_1 = T_2 = T,\ g_1 = g_2 = g. \tag{20}$$

Where $g$ is the Gibbs free energy. Note that this requirement is not possible for all $\rho$ and $e$. This is indeed the case when there is only a single phase solution, that is when the limit of complete evaporation or condensation is reached. Since the numerical method is only valid for $\alpha_k > \xi$, where $\xi$ is some small number (typically $\xi = 10^{-6}$), the single phase limit of phase 1 will be determined by

$$p_1 = p_2 = p,\ T_1 = T_2 = T,\ \alpha_1 = 1 - \xi \tag{21}$$

and equivalent for the single phase limit of phase 2. If a cubic equation of state is used, even this is not possible for all $\rho$ and $e$. This will be the case when one phase reaches the spinodal state before thermal equilibrium is reached. If phase 2 is at the spinodal state, the system is determined by

$$\begin{gathered} p_1 = p_2 = p_{\mathrm{spin}}(v_2) = p, \\ T_1 = T(v_1, p),\ T_2 = T_{\mathrm{spin}}(v_2),\ \alpha_1 = 1 - \xi \end{gathered} \tag{22}$$

Table I
INITIAL SIMULATION CONDITIONS

| | $x < 0.25$ m | $0.25m \geq x$ $x < 0.5m$ | $x \geq 0.5m$ |
|---|---|---|---|
| $p\ [Pa]$ | $5.5 \cdot 10^6$ | $5.5 \cdot 10^6$ | $10^5$ |
| $u\ [m/s]$ | 0 | 0 | 0 |
| $\alpha$ | $10^{-6}$ | $1 - 10^{-6}$ | $1 - 10^{-6}$ |
| $\rho_1\ [kg/m^3]$ | 175.00 | 175.00 | 1.8794 |
| $\rho_2\ [kg/m^3]$ | 530.45 | 565.46 | 565.46 |

$v_2$ is determined by the mixture equation of state, and $v_1$ is determined by conservation of mass ($v = Y_1 v_1 + Y_2 v_2$). The subscript $spin$ denotes the thermodynamic spinodal state.

In the context of the van der Waals EOS, the three cases (20, 21 and 22) can be identified by the values of $\rho$ and $e$. A fourth case is theoretically possible, namely $e < e(\rho)_{T=0}$, but this is not likely to occur in numerical calculations and is therefore not further examined.

The stiff thermodynamic relaxation procedure was used when $p_l < p_{\text{sat}}(T_l)$. An additional criterion $\xi_I < \alpha_1 < 1 - \xi_I$ can be used, where $\xi_I$ represents the interface limit of the volume fraction (typically $\xi_I = 10^2\xi$ to $10^3\xi$). This last criterion is referred to as the interface criterion of the thermodynamic relaxation procedure and is used to allow for the formation of metastable liquid.

## IV. EXPERIMENTS

The capabilities of the model to predict phase transition in pressurized liquid $CO_2$ by expansion is validated by comparing simulation results with experimental results. The experimental results are presented in [14]. Figure 3 shows a drawing of a experimental apparatus for rapid expansion of liquefied $CO_2$. The expansion tube is 9 mm inner diameter, 1.5 mm wall thickness polycarbonate. Before the beginning of the experiment, the tube is filled to about half level with saturated liquid $CO_2$ at room temperature, about 20$^o$C. The pressure in the tube is then 5.5 MPa. The top of the tube is closed with a diaphragm which is punctured by an arrow, releasing $CO_2$ to the atmosphere. Expansion waves then propagates down the tube and starts a boiling process due to the falling pressure. The expansion tube is transparent and a high speed digital camera captures the expansion and boiling process on a high speed movie which is later analyzed. The camera operates at 20 000 fps for this experiment. Typical wave trajectories is shown in figure 4.

## V. SIMULATION SET-UP

The simulation domain is shown with initial conditions in figure 5. The calculation was run with an initial CFL number set to 0.2 for the first 200 time steps. The CFL number was then linearly increased to 0.5 over 50 time steps and was set to 0.5 for the rest of the calculation. The initial conditions for the simulation is shown in table I. The one dimensional domain was divided into 7000 control volumes with $10^{-4}$ m length.

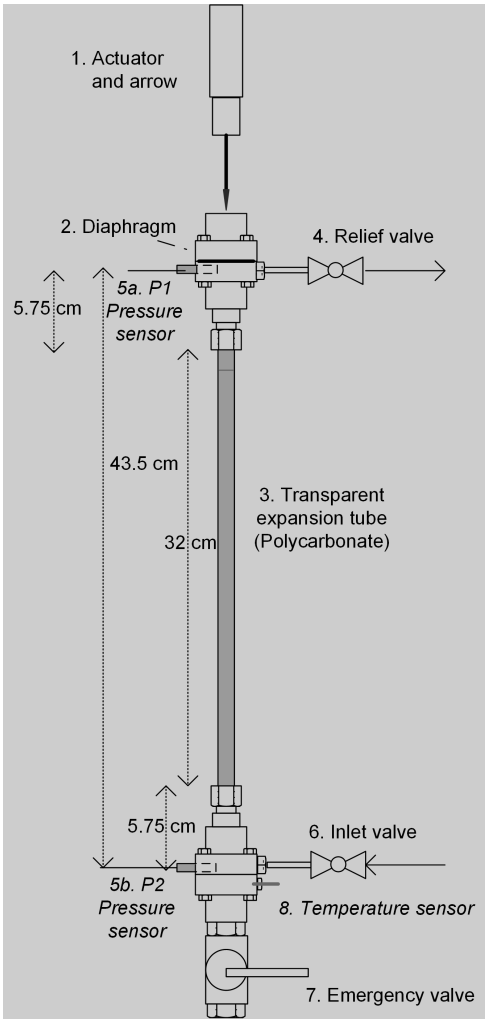


Figure 3. Experimental set-up.

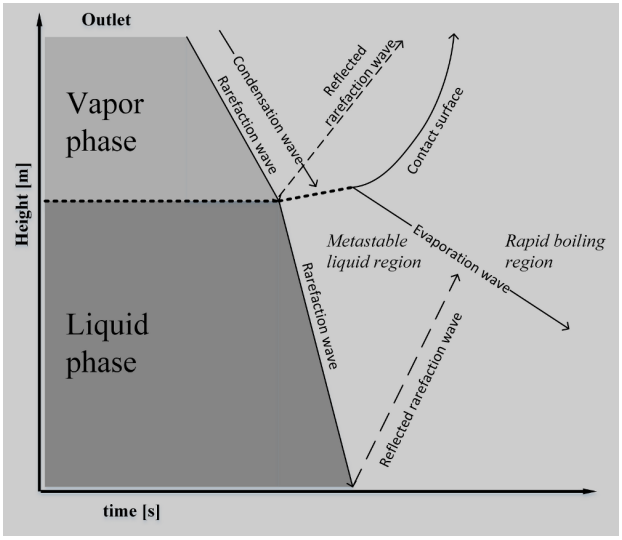


Figure 4. Schematic representation of the waves in the one dimensional expansion experiments.

## VI. RESULTS AND DISCUSSION

The van der Waal EOS is not able to reproduce the thermodynamical states quantitatively, especially close to

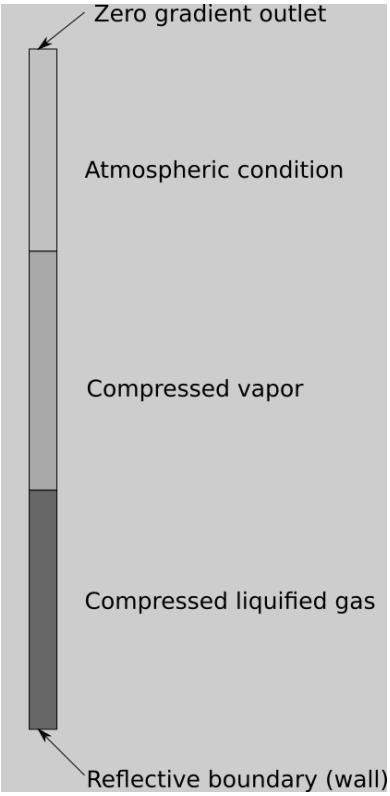


Figure 5. Initial and boundary conditions in the simulation domain.

saturation condition. The results are presented as scaled quantities to show the qualitative behaviour of the simulation method. The pressure is scaled with saturation pressure at initial temperature, ie. the initial pressure in the tube. The time is scaled by the average propagation time for an expansion wave along the total length of the pipe and the position is scaled by the tube length. The initial interphase in the experiments was 56 % of the tube length from the bottom. For comparison of the wave structures the interphase is moved to scaled position 0.5 like in the simulations. The wave structures in the experiments and simulations are shown as x-t diagrams. The experimental x-t diagram is extracted from the high speed movie. The pixel row from the central position of the tube is stacked along the time vector.

Figure 6 shows the simulated wave structure in the expansion tube. An initial expansion wave propagates downwards in the gas phase from scaled time 0. The expansion wave both reflects and transmits at the interphase, at scaled time 0.7, where the reflected wave is seen traveling upwards and the transmitted wave continues downwards into the liquid. A condensation phase transition occurs behind the reflected upwards traveling expansion wave. A phase transition in the liquid is initiated and the contact surface of the expanding liquid-gas mixture travels upwards following the reflected expansion wave. The expansion wave traveling through the liquid is reflected at the bottom of the tube and a faster phase transition is initiated there due to the high level of expansion. The phase transition initiated by the incident expansion wave is slow due to a

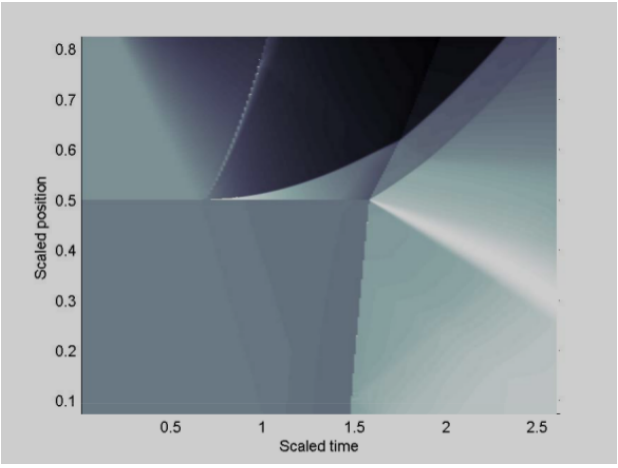


Figure 6. Scaled simulated density for expansion of $CO_2$ in 1D-domain. The results show the wave structure in the expansion process.

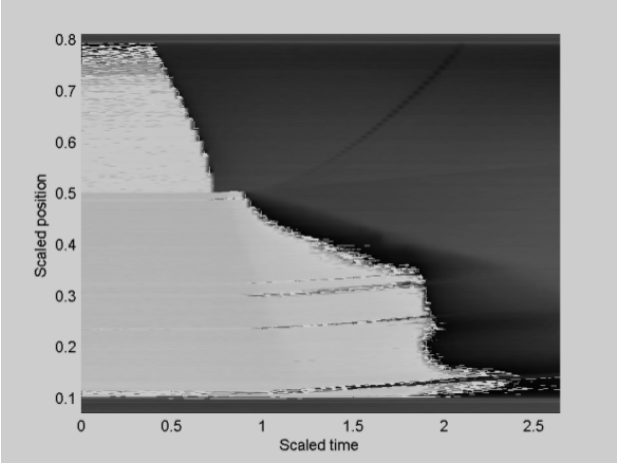


Figure 7. Experimental x-t diagram of expansion of $CO_2$ in a narrow tube. The results show the wave structure in the expansion process.

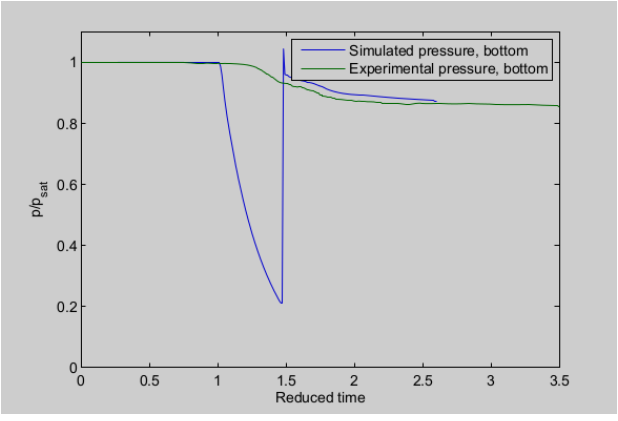


Figure 8. Simulated and experimental scaled pressure history at the bottom of the expansion tube.

low level of superheat. Once the expansion wave reflects at the bottom and again interactes with the initial interphase between liquid and vapour, at scaled time 1.6, a faster phase transition is triggered. Comparing these results to the experimental results seen in figure 7 shows the same

wave structures. In the experiments a condensation wave following the incident expansion wave occurs. This is not seen in the simulations. The reflected expansion wave is not clearly in seen in the experimental x-t diagram. The condensation seen in the simulations will not occur in experiments since the wave propagates into a two phase fluid.

Figure 8 shows the relative scaled pressure at the bottom of the tube vs. scaled time for simulation and experiment. The large drop in the simulated pressure, not seen in the experiments, is due to the expanding liquid. The thermodynamical state in the expansion wave is highly expanded metastable liquid. When the liquid pressure reaches the spinodal state at scaled time 1.5, a very rapid phase transition occurs and brings the pressure up towards equilibrium pressure. This creates a shock wave propagating upwards due to the fast expansion in the boiling. This shock is driven by a sudden change in thermodynamic state to equilibrium. This rapid phase transition propagates with the mesh speed, ie. $\Delta x/\Delta t$ and is an artefact of the phase transition model. The experimental pressure values does not drop as dramatically as the simulated pressure. The reason for this discrepancy can be that nucleation sites along the narrow tube will force a faster phase transition in the metastable liquid and keep the pressure at a higher level. The wall effects are not included in the simulation. After the rapid phase transition and formation of the shock wave the simulated pressure is close to the experimental pressure.

## VII. Conclusion

A model and solver for rapid phase transition in compressed liquefied gases is presented. The phase transition model uses a mechanical and thermodynamical relaxation approach for phase transition. The present model and solver is capable of handling the wave types that can occur in a depressurization process however the combination of the van der Waals equation of state and an ideal geometry in one dimension will not produce the quantitative values seen in the experiments. Wall effects and low accuracy of the EOS close to saturation conditions and in metastable state causes a higher degree of superheat before a rapid phase transition can occur in the simulations. When the metastable liquid reaches the spinodal state, the model produces an unphysically fast evaporation wave. Future work to improve the simulation method will be to develop a kinetic based phase transition model in highly expanded metastable liquids. Such a model can reduce the possibility of low pressures seen in the metastable liquid during the reflection of rarefaction waves. A kinetic based transition rate can include wall effects and effects from impurities in the liquid. For higher accuracy the present method can be extended to more complex equations of states, like the Span-Wagner EOS.

## References


[1] R. Span and W. Wagner, "A new equation of state for carbon dioxide covering the fluid region from the triple-point temperature to 1100 K at pressures up to 800 MPa", Journal of Physical and Chemical Reference Data, 25(6):1509–1596, 1996.

[2] R. Menikoff and B.J. Plohr, "The Riemann Problem for Fluid-Flow of Real Materials", Reviews of Modern Physics, 61(1):75–130, 1989.

[3] R. Saurel, F. Petitpas, and R. Abgrall, "Modelling phase transition in metastable liquids: application to cavitating and flashing flows", Journal of Fluid Mechanics, 607:313–350, 2008.

[4] M. Slemrod, "Dynamic phase transitions in a van der Waals fluid", Journal of Differential Equations, 52(1):1–23, 1984.

[5] H. W. Zheng, C. Shu, Y. T. Chew, and N. Qin, "A solution adaptive simulation of compressible multi-fluid flows with general equation of state", International Journal for Numerical Methods in Fluids., 67(5):616–637, 2011.

[6] R. Saurel, and R. Abgrall, "A multiphase Godunov method for compressible multifluid and multiphase flows", Journal of Computational Physics, 150(2):425–467, 1999.

[7] J.R. Simoes-Moreira and J.E. Shepherd, "Evaporation waves in superheated dodecane", Journal Of Fluid Mechanics, 382:63–86, 1999.

[8] G. A. Pinhasi, A. Ullmann, and A. Dayan, "1D plane numerical model for boiling liquid expanding vapor explosion (BLEVE)", International Journal of Heat and Mass Transfer, 50(23-24):4780–4795, 2007.

[9] M. M. Voort, A. C. Berg, D. J. E. M. Roekaerts, M. Xie, and P. C. J. Bruijn, "Blast from explosive evaporation of carbon dioxide: experiment, modeling and physics", Shock Waves, 22(2):129–140, 2012.

[10] M. Xie, "Thermodynamic and Gasdynamic Aspects of a Boiling Liquid Expanding Vapour Explosion", PhD thesis, Delft University of Technology, 2013.

[11] R. Saurel, F. Petitpas, and R. A. Berry, "Simple and efficient relaxation methods for interfaces separating compressible fluids, cavitating flows and shocks in multiphase mixtures", Journal of Computational Physics, 228(5):1678–1712, 2009.

[12] E. F. Toro, "Riemann solvers and numerical methods for fluid dynamics", Springer-Verlag, second edition, 1999.

[13] A. Zein, M. Hantke, and G. Warnecke, "Modeling phase transition for compressible two-phase flows applied to metastable liquids", Journal of Computational Physics, 229(8):2964–2998, 2010.

[14] P. M. Hansen, K. Vaagsaether, A. V. Gaathaug and D. Bjerketvedt, "$CO_2$ explosions - an experimental study of rapid phase transition", 8th International Seminar on Fire and Explosion Hazards, 25. – 28. April, Hefei, China, 2016.

Doctoral dissertation no. 13
**2018**

—

**Experimental and theoretical studies of rapid phase transitions in $CO_2$**

Dissertation for the degree of Ph.D

—

Per Morten Hansen

—

ISBN: 978-82-7206-487-6 (print)
ISBN: 978-82-7206-488-3 (online)

usn.no